UNIVERSITY OF SOUTHAMPTON

FACULTY OF ENGINEERING AND PHYSICAL SCIENCES

School of Engineering

EXPERIMENTAL AND COMPUTATIONAL CHARACTERISATION OF COMPOSITE LAMINATES SUBJECTED TO MULTIAXIAL LOADING

by

TOBIAS LAUX

ORCID: 0000-0003-4484-1699

Thesis for the degree of Doctor of Philosophy

Supervisors: Dr Khong Wui Gan, Prof. Janice M Dulieu-Barton, Prof. Ole T Thomsen

May, 2020

UNIVERSITY OF SOUTHAMPTON

ABSTRACT

FACULTY OF ENGINEERING AND PHYSICAL SCIENCES

School of Engineering

Thesis for the degree of Doctor of Philosophy

EXPERIMENTAL AND COMPUTATIONAL CHARACTERISATION OF COMPOSITE LAMINATES SUBJECTED TO MULTIAXIAL LOADING

By Tobias Laux

The constitutive response and failure mechanisms of fibre-reinforced polymer (FRP) composite laminates depends on the properties of the constituents and the laminate lay-up, as well as on the stress state. The dependency on the stress state implies that multiaxial experimental data is needed for a wide range of different material and loading configurations to gain a comprehensive understanding of the material response. However, only a limited amount of multiaxial experimental data exists in the literature, resulting in an incomplete understanding of the material response of FRP composites. Consequentially, the modelling frameworks used to predict failure in composites are not sufficiently validated, which severely limits their use in the design and certification of high-performance composite structures.

The aim of the work described in this thesis is to develop a multiaxial testing philosophy which enables to obtain experimental data that can be used to advance (develop, calibrate, validate) composite modelling frameworks. The thesis is focused on the modified Arcan fixture (MAF), which enables testing of FRP specimens subjected not only to combined tension-shear, as is possible on the original Arcan fixture, but also to compression-shear loading. Procedures based on the MAF, digital image correlation (DIC) and x-ray computed tomography (CT) are proposed to deliver the high-fidelity multiaxial experimental data needed.

As a starting point, an existing MAF was used in combination with butterfly specimens inspired by the original Arcan tests to investigate a range of glass/epoxy laminates. The MAF was limited to testing relatively weak laminates, since strong laminates could not be tested up to failure due to premature failure at the grips. Nonetheless, the data was useful to assess contemporary failure criteria (maximum stress, Tsai-Wu's, Puck's, LaRC03) against experimental failure envelopes, and to develop a new plasticity-based constitutive model that accounts for the nonlinear, pressure sensitive behaviour of UD composites. The superiority of a non-associative flow rule over an associative one has been confirmed, and new guidelines for the calibration of plasticity-based models have been proposed.

Following on from this, a new MAF was designed, which enabled the successful testing of strong FRP laminates up to ultimate failure. The new MAF was used in combination with stereo DIC to investigate laminate-lay-up effects on the tension/compression-shear open-hole specimen strength of quasi-isotropic carbon/epoxy laminates. It was found that ply thickness has a significant effect on the open-hole specimen strength under tension-shear loading, whereby thin ply specimens are up to 150% stronger than thick ply specimens, while this effect was negligible in compression-shear loading. Furthermore, no significant effect of the relative fibre orientation angle (angle between two adjacent plies) was observed.

The multiaxial open-hole data was then used for the validation of a meso-scale modelling framework developed at the University of Porto for the 'virtual testing' of laminated composites. The model discretises the laminate at the level of the UD plies modelled as anisotropic solids. Damage is predicted using a continuum damage model (CDM), where failure initiation is determined using approximation of the LaRC03/04 failure criteria, while damage propagation is governed based on the fracture energies of the ply. Inter-laminar damage (delamination) was modelled using cohesive zone models (CZMs) placed between the plies. The meso-scale model predicted the multiaxial open-hole specimen strength across all lay-up and loading configurations within a mean relative error of 10%. The validation study informs the direction of future developments to advance current 'virtual testing' frameworks.

Overall, the research in this thesis has successfully addressed the lack of multiaxial experimental data and has contributed to the advancement of FRP modelling frameworks. A significant step has been made towards an improved understanding of the behaviour, testing, and modelling of composites subjected to combined loading.

Table of contents

List of tables

List of figures

Academic thesis: declaration of authorship

I, Tobias Laux declare that this thesis and the work presented in it are my own and has been generated by me as the result of my own original research.

Integrated experimental and computational characterisation of advanced composite materials subjected to multiaxial loading

I confirm that:

1. This work was done wholly or mainly while in candidature for a research degree at this University;
2. Where any part of this thesis has previously been submitted for a degree or any other qualification at this University or any other institution, this has been clearly stated;
3. Where I have consulted the published work of others, this is always clearly attributed;
4. Where I have quoted from the work of others, the source is always given. With the exception of such quotations, this thesis is entirely my own work;
5. I have acknowledged all main sources of help;
6. Where the thesis is based on work done by myself jointly with others, I have made clear exactly what was done by others and what I have contributed myself;
7. Parts of this work have been published as:

K. W. Gan, T. Laux, S. T. Taher, J. M. Dulieu-Barton, and O. T. Thomsen. A novel fixture for determining the tension/compression-shear failure envelope of multidirectional composite laminates. *Compos. Struct.*, vol. 184, pp. 662–673, 2018. doi: 10.1016/j.compstruct.2017.10.030

T. Laux, K.W. Gan, J.M. Dulieu-Barton, O.T. Thomsen. A simple nonlinear constitutive model based on non-associative plasticity for UD composites – Development and validation using a Modified Arcan Fixture. *Int. J. Solids Struct.* vol. 162, pp. 135-147, 2019. doi: 10.1016/j.ijsolstr.2018.12.004

T. Laux, K.W. Gan, J.M. Dulieu-Barton, O.T. Thomsen. Ply thickness and fibre orientation effects in multidirectional composite laminates subjected to combined tension/compression and shear. *Compos. Part A Appl. Sci. Manuf.* vol. 133, 2020. doi: 10.1016/j.compositesa.2020.105864

Signed: ....

Date: ....

Acknowledgements

The journey which has brought me to writing up my PhD thesis in the field of composite materials has started a long time ago, way before I was made aware of the possibility of pursuing a PhD. Thus, there are many people to thank which have contributed indirectly to this work. Thanks to all of you! Most importantly my sincerest thanks go to my parents who have always fully supported me in following my passion even though on first sight the paths taken were far from the usual.

Throughout my PhD I felt the full support and great trust from my supervisors Dr Khong Wui Gan, Prof Janice Barton, and Prof Ole Thomsen. I am humbled and thankful for the opportunities you have given me and the guidance I have received. I am especially grateful to Prof Ole Thomsen and sincerely thank you for opening my eyes to the possibility of pursuing a PhD in the field of composite materials.

I am grateful to the sailing team INEOS Team UK and especially to Michel Marie for giving me the opportunity to introduce myself and my research and for generously providing some of the material used in this work. The initial discussion we shared and the collaboration with you has considerably shaped the course of my PhD project. I wish the team maximum success in their quest for the 36th America's cup!

I thank Prof Pedro Camanho for enabling my stay at the University of Porto and for sharing their expertise in simulating failure in composites. Thank you, Dr Carolina Furtado, Dr Rodrigo Tavares, and Dr Albertino Arteiro for the warm welcome received and for your scientific advice. The collaboration with you has significantly enhanced my research and the modelling work conducted in this thesis would not have been possible without you.

I am also very thankful to Dr Andy Robinson for his patience and advice in the TSRL laboratory. Without your magic power things would have been a lot harder. Further thanks go to Dr Dan Bull and Dr Mark Mavrogordato at μ-vis for their help with x-ray CT and their good company. Furthermore, thank you Dr Neha Chandarana and Kaspar Schlegel for your help with proofreading parts of my thesis. Geir, Jack, Jared, Tim, Vaggelis, Irene, and Sam, thank you for the many technical discussions and not to forget the gossip we shared during the past years. Thank you also to my examiners Prof Silvestre Pinho, Dr Lloyd Fletcher, Prof Fabrice Pierron, and Prof Mark Spearing for dedicating time to critically reviewing my work during internal and external examinations.

Nomenclature

Greek letters

α	MAF loading angle
α	IFF fracture plane angle in the LaRC03 failure criterion
α_0	IFF fracture plane angle under pure transverse compression
α_0	Half-height of a slit crack in the in-situ strength models
α_0^L	Half-length of the slit crack in the in-situ strength models
β	Mode-mixity ratio in CZM
γ_{12}, γ_{13}, γ_{23}	UD lamina (ply) engineering shear strains
γ_{xy}, γ_{xz}, γ_{yz}	Laminate engineering shear strains
γ_{12}^{fail}	Shear strain to failure
δ_1, δ_2, δ_3	Separations in shear, scissoring and normal opening modes in CZM
δ_1^0, δ_2^0, δ_3^0	Separations in shear, scissoring and normal opening modes at the onset of delamination failure in CZM
δ_1^f, δ_2^f, δ_3^f	Separations in shear, scissoring and normal opening modes at complete decohesion in CZM
δ_{sh}	Effective shear separation in CZM
δ_n	Normal separation in CZM
τ_{sh}	Effective shear traction in CZM
τ_n	Effective normal traction in CZM
δ_m, δ_m^0, δ_m^f	Mixed mode separation in CZM
ϵ_{11}, ϵ_{22}, ϵ_{33}	UD lamina (ply) normal strains
ϵ_{xx}, ϵ_{yy}, ϵ_{zz}	Laminate normal strains
$\boldsymbol{\epsilon}$	Strain tensor
$\boldsymbol{\epsilon}^e$	Elastic strain tensor
$\boldsymbol{\epsilon}^p$	Plastic strain tensor
$\overline{\epsilon}^p$	Effective plastic strain
ϵ_{11}^T	Fibre tensile strain to failure
ϵ_{11}^C	Fibre compressive strain to failure
ϵ_{22}^T	Transverse tensile strain to failure
ϵ_{22}^C	Transverse compressive strain to failure
$d\lambda$	Plastic multiplier
η^T	Transverse coefficient of influence (LaRC03)
η^L	Longitudinal coefficient of influence (LaRC03)

$\eta_{\text{B-K}}$	Benzeggagh-Kenane mixed mode interaction parameter in CZM
σ_{11}, σ_{22}, σ_{33}	UD lamina (ply) normal stresses
σ_{xx}, σ_{yy}, σ_{zz}	Laminate normal stresses
σ_{11}^m, σ_{22}^m, τ_{12}^m	Stresses in misaligned (kinked) fibres
$\boldsymbol{\sigma}$	Stress tensor
σ_h	Hydrostatic pressure
$\bar{\sigma}$	Effective stress
θ	Fibre orientation angle
θ	Sliding angle in LaRC04 kinking model
θ_{fp}	IFF fracture plane angle in Puck's failure criterion
τ_{12}, τ_{13}, τ_{23}	UD lamina (ply) engineering shear stresses
τ_{xy}, τ_{xz}, τ_{yz}	Laminate shear stresses
$\tau_{nl} = \tau^L$	Shear stress on the IFF fracture plane parallel to the fibres
$\tau_{nt} = \tau^T$	Shear stress on the IFF fracture plane transverse to the fibres
τ_{eff}^L	Effective shear stress on the IFF fracture plane parallel to the fibres
τ_{eff}^T	Effective shear stress on the IFF fracture plane transverse to the fibres
τ_{12c}	Shear stress at intersection of Puck's IFF mode B and C failure
τ_1, τ_2, τ_3	Tractions associated with shear, scissoring and normal opening modes in CZM
τ_1^0, τ_2^0, τ_3^0	Tractions associated with shear, scissoring and normal opening modes at the onset of delamination failure in CZM
φ	Fibre misalignment angle in fibre kinking model
φ^C	Critical fibre misalignment angle under uniaxial fibre compression
φ	Rigid body rotation angle of MAF specimen
Λ_{22}^0, Λ_{44}^0	Non-vanishing components of the crack tensor

Roman letters

d_i $i = 1, 2, 6$	Damage variable associated with fibre, matrix and shear failure
d_{1+}	Damage variable associated with fibre tensile failure
d_{1-}	Damage variable associated with fibre compressive failure
d_{2+}	Damage variable associated with matrix tensile failure
d_{2-}	Damage variable associated with matrix compressive failure
f_{XT}, f_{GT}	Shape parameters for softening law in longitudinal tension
f_{XC}	Shape parameter for softening law in longitudinal compression
g	Fracture toughness ratio
l^*	Characteristic element length (in CZM)

$p_{\perp\parallel}^{(+)}$, $p_{\perp\parallel}^{(-)}$, $p_{\perp\perp}^{(+)}$, $p_{\perp\perp}^{(-)}$	Slope parameters of the failure envelopes in Puck's IFF failure theory
t, t_{ply}, t_{lam}	Specimen thickness, UD ply thickness, laminate thickness
w	Specimen gauge section width
A	Specimen gauge section area
$\mathbf{C}$	Stiffness matrix
E_1	Longitudinal Young's modulus
E_{1c}	Longitudinal compressive Young's modulus
E_2	Transverse Young's modulus
E_{2c}	Transverse compressive Young's modulus
E_3	Through-thickness Young's modulus
F_1, F_2, F_{11}, F_{22}, F_6, F_{12}	Coefficients of Tsai-Wu failure criterion
G_{12}, G_{13}, G_{23}	Shear moduli
$G_{12}^{0°}$	In-plane shear modulus measured on $[0_{12}]$ specimen
$G_{12}^{90°}$	In-plane shear modulus on $[90_{12}]$ specimen
$G_I(i)$, $G_{II}(i)$	Mode I and II energy release rate in directions $i = T, L$
$G_{IC}(i)$, $G_{IIC}(i)$	Mode I and II fracture toughness in directions $i = T, L$
G_{IC}, G_{IIC}	Mode I and II fracture toughness of the interface in CZM
G_C	Effective fracture toughness under mixed mode loading in CZM
$\mathscr{G}_{1+}$	Ply fracture toughness for longitudinal tension
$\mathscr{G}_{1-}$	Ply fracture toughness for longitudinal compression
$\mathscr{G}_{2+}$	Mode I ply fracture toughness for transverse tension
$\mathscr{G}_{2-}$	Mode I ply fracture toughness for transverse compression
$\mathscr{G}_6$	Mode II ply fracture toughness for shear
$\mathbf{H}$	Compliance matrix
K_P	Shear incremental stiffness under 'plastic' flow
K_P	Penalty stiffness in cohesive zone model
N_y	Normal (y-direction) load component
N_{xy}	Shear (x-direction) load component
P	Load
$R_{\perp\perp}^A$	Fracture resistance in Puck's IFF theory
S_L	Shear strength in shearing longitudinal to fibres
$S_L^{0°}$	Apparent shear strength in shearing longitudinal to fibres measured on $[0_{12}]$ specimen

$S_L^{90°}$	Apparent shear strength in shearing longitudinal to fibres measured on $[90_{12}]$ specimen
S_T	Shear strength in shearing transverse to fibres
S_L^{is}	In-situ shear strength in shearing longitudinal to fibres
S_T^{is}	In-situ shear strength in shearing transverse to fibres
S_{LP}	Shear stress activating 'plastic' flow
v_{12}, v_{13}, v_{23}	Poisson's ratios
X_T	Longitudinal tensile strength
X_C	Longitudinal compressive strength
Y_T	Transverse tensile strength
Y_T^{is}	Transvers tensile in-situ strength
Y_C	Transverse compressive strength
Y_C^{is}	Transverse compressive in-situ strength
Y_{BT}	Biaxial transverse tensile strength
Y_{BC}	Biaxial transverse compressive strength

Frequently used sub- and superscripts

1, 2, 3	Lamina (or ply) coordinate system
c	critical
e	elastic
i, j	1, 2, 3
ini	Initial (failure load)
is	In-situ strength
k	1, 3, 4, … n
m	Associated with properties in the misaligned (kinked) fibre coordinate system
n, l, t	Fracture plane normal coordinate system
p	plastic
ult	Ultimate (failure load)
x, y, z	'Global' laminate coordinate system
C	Compression
L	Longitudinal
T	Tension, transverse or through-the-thickness

Abbreviations

ASTM	American society for testing and materials
B-K	Benzeggah-Kenane (fracture criterion)
CDM	Continuum damage model
CFRP	Carbon fibre reinforced polymer
CLT	Classical lamination theory
CT	Computed tomography
CZM	Cohesive zone model
DCB	Double cantilever beam test
DDM	Discrete damage model
DIC	Digital image correlation
ENF	End notched flexure test
FE	Finite element
FoS	Factor of safety
FRP	Fibre reinforced polymer
FI_F	Failure index for the fibre
FI_M	Failure index for the matrix
FF	Fibre failure
IFF	Inter fibre failure
GFRP	Glass fibre reinforced polymer
ISO	International organization for standardization
LaRC	Langley research centre
MAF	Modified Arcan fixture
M-C	Mohr-Coulomb (material model)
MD	Multidirectional (laminate)
MMB	Mixed-mode bending test
MPC	Multi Point Constraint
OHT	Open-hole tension
OHC	Open-hole compression
TSRL	Testing and structures research laboratory
UD	Unidirectional (laminate)
UoS	University of Southampton
UoSM	University of Southampton Malaysia
WWFE	World-wide failure exercise

Operators

$\langle \bullet \rangle$ Macaulay bracket; returns the argument $\bullet$ if positive or zero otherwise

∇ Gradient of a potential function resulting in a vector field

“Si tu veux construire un bateau,
ne rassemble pas les hommes pour aller chercher le bois, préparer les outils et distribuer les
tâches, mains enseigne-leur la nostalgie de l'infini de la mer”

“If you want to build a ship,
don't drum up people to collect wood and don't assign them tasks and work, but rather teach
them to long for the endless immensity of the sea.”

“Wenn du ein Schiff bauen willst,
dann trommle nicht Männer zusammen, um Holz zu beschaffen, Aufgaben zu vergeben und
die Arbeit einzuteilen, sondern lehre sie die Sehnsucht nach dem weiten, endlosen Meer.”

Antoine de Saint-Exupery

Chapter 1

Introduction

1.1   Background

Advanced composite materials are widely used in the design of lightweight structures across, for example the aerospace, transportation, marine, or energy industries, while substantial further growth of the composite market share is forecasted [1]. A wide range of different composite materials exist; for most stiffness-driven designs they constitute of a strong and stiff fibrous reinforcement material (*e.g.* glass, carbon or aramid fibres) embedded in a compliant thermosetting polymeric matrix material (*e.g.* epoxy resin) [2]. Usually unidirectional (UD) fibre-reinforced polymer matrix (FRP) materials are stacked together at different fibre orientation angles to form a multidirectional laminate. FRP laminates are valued for their high specific stiffness and strength, and for their excellent fatigue and corrosion resistance. Moreover, their mechanical, thermal or electrical properties can be optimised by tailoring the constituent materials themselves as well as the laminate lay-up to achieve high-performance, lightweight and in some cases multi-functional structural solutions. Due to their excellent mechanical properties, FRP composites have been used in the design of the world's most extreme structures such as in the largest wind turbine blades [3], in the payload fairings of the SpaceX Falcon Heavy rocket [4], or in the centre wing box of the Airbus A380 [5].

High-performance composite structures are designed and certified based on the 'building block' or the 'pyramid of tests' approach illustrated in Figure 1.1 as discussed by Rouchon [6] for composite aero-structures.
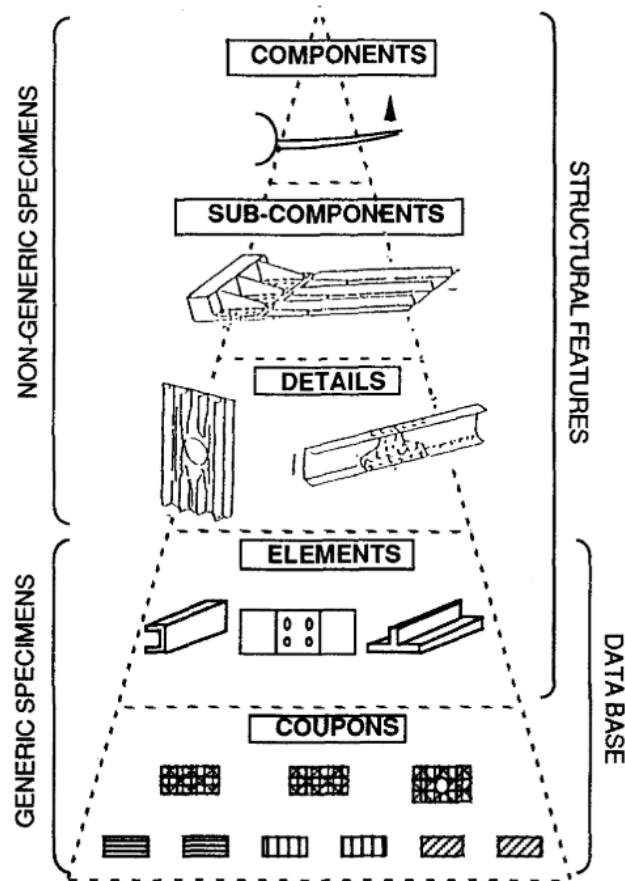
Figure 1.1, The pyramid of tests for the certification of composite aero-structures [6].

Structural integrity is established through a comprehensive, incremental programme of analysis and experimental validation using specimens of varying size and complexity, *i.e.* on the coupon, structural element, structural detail, sub-component and full structure level. Extensive experimental material characterisation is required due to the large number of possible material configurations, the properties of which are not only dependent on the constituent materials, the laminate lay-up, the manufacturing processes but also on the applied stress state [7]. Currently, the cost and complexity associated with the 'pyramid of tests' approach are exuberant and are limiting the uptake of composite solutions across industries. This in turn inhibits the development of more sustainable and economical structural concepts.

Over the past decades, modelling frameworks with promising predictive capability for a wide range of material and loading configurations have emerged (*e.g.* [8]–[20]). These modelling frameworks have the potential to replace physical material tests as part of the 'pyramid of tests' approach by defining 'virtual design allowables' through simulation [21]. 'Virtual testing' techniques offer the potential to explore novel material and structural solutions more rapidly and more cost effective than it is possible following the experimentally based 'pyramid of tests' approach. In the medium term, 'virtual testing' techniques could complement (or replace) tests on the coupon or structural details level and in the long run with the advent of ever more powerful computational power and better composite material models, they may also be entering higher

levels of the testing pyramid. However, the Achilles heel of these highly promising models is currently their insufficient validation against comprehensive experimental data with respect to material type, laminate lay-up and general loading configurations including multiaxial loading and stress states. This is related to the small amount of suitable experimental data available in the literature on different levels of the 'pyramid of tests' which would be suitable to validate such modelling frameworks. Therefore, experimental data is needed that allows a comprehensive validation of these modelling frameworks to establish their industry-readiness and to inform the future direction of model development. It has been proposed to validate 'virtual testing' techniques themselves based on the 'pyramid of tests' approach, *i.e.* initially they are experimentally validated on the coupon scale, before they are validated against more complex cases on higher levels of the 'pyramid of tests' [15], [17], [22]–[24]. Current state-of the-art models are being validated on the coupon scale and it will be imperative to facilitate their validation also for more demanding scenarios. To unleash the full potential of composite engineering in the future, thoroughly validated and improved modelling techniques, which can be employed at different levels of the 'pyramid of tests', are crucially important.

In this thesis, the lack of suitable experimental data for the advancement (development, calibration, validation) of high-fidelity modelling frameworks to predict damage initiation, progression and failure, is addressed. For this reason, multiaxial experimental data for a range of different material systems and laminate lay-ups is obtained to improve the understanding of the constitutive behaviour and failure of FRP composites. The thesis focuses on exploring the potential of a new multiaxial test fixture, the modified Arcan fixture (MAF), shown in Figure 1.2, for obtaining combined tension-shear and compression-shear experimental data, which can be used to advance composite modelling frameworks.
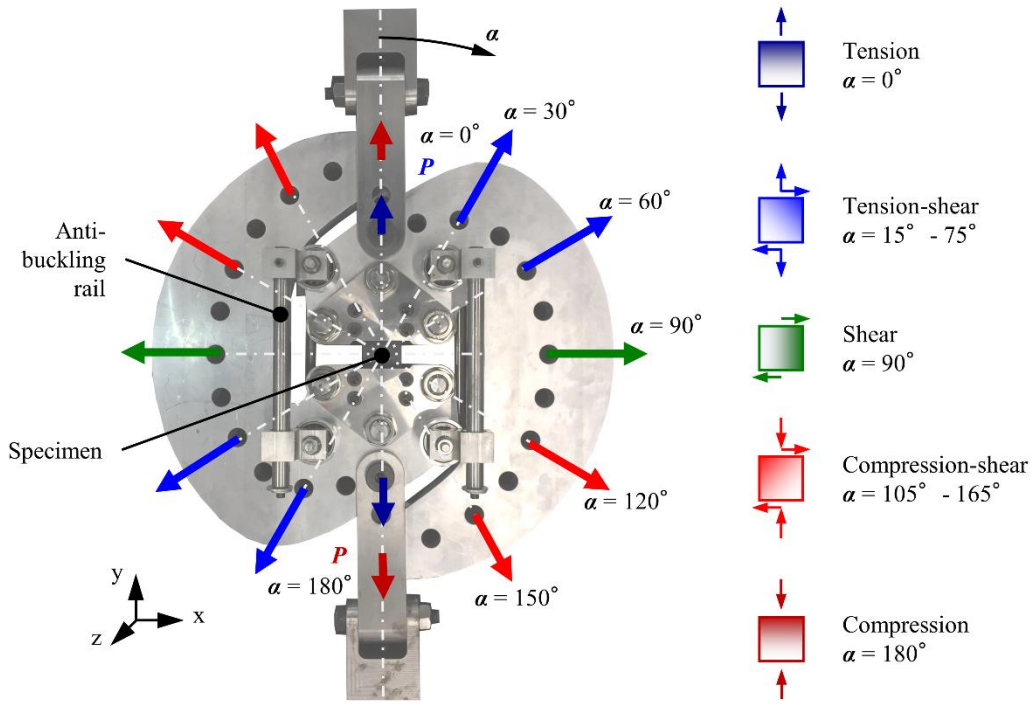
Figure 1.2, The new modified Arcan fixture (MAF) developed in this thesis, with indication of how different combined tension/compression-shear loading can be induced in the specimen by the choice of the loading hole pair designated by the loading angle α.

The novelty of the MAF developed in this thesis is that it enables testing of a wide range of composite laminates in the full tension-shear and compression-shear loading regimes. Combined compression-shear testing is not possible using the original Arcan fixture [14], [15], but is enabled using the MAF by anti-buckling rails (see Figure 1.2) that stabilise the rig against out-of-plane displacements. In this thesis, procedures based on the MAF in combination with advanced experimental techniques such as digital image correlation (DIC) [27] and x-ray computed tomography (CT) [28] are developed to obtain high-fidelity multiaxial experimental data. The data is then used for the development and validation of suitable composite modelling frameworks for the prediction of damage initiation and progression until failure. In summary, the research presented in this thesis advances the knowledge of composite mechanics, testing and modelling and addresses the increasing demand for improved and experimentally validated 'virtual testing' techniques that can be used in the design and certification of high-performance composite structures.

1.2   Aims and objectives

The aim of the work described in this thesis is to develop a new multiaxial testing methodology and the related experimental procedures that enable the acquisition of high-fidelity experimental data. The acquisition of multiaxial data is aimed at addressing the limited amount of such data reported in the literature, at improving the understanding of composite failure mechanics, and at

advancing the development, calibration and validation of composite modelling frameworks. The project is focused on the combined tension-shear and compression-shear loading regimes, which can be investigated experimentally on the MAF.

The first objective is to commission the MAF designed by Taher *et al.* [29] for a range of glass/epoxy material systems and to explore the potential and limitations of the MAF test set-up (Chapter 3). Based on a critical assessment of the initial testing the following research objectives have been defined to achieve the overall aim:

- To assess the predictive capability of contemporary failure criteria and modelling frameworks against the experimental data obtained using the MAF.
- To re-design the MAF used for the initial commissioning tests to enable the testing of high strength composite laminates exhibiting fibre driven failure modes, which is not possible with the MAF used for the initial testing.
- To develop a nonlinear material model for UD FRP composites that exploits the combined tension/compression-shear MAF/DIC test results.
- To investigate and characterise laminate lay-up effects on the strength of multidirectional composite laminates subjected to multiaxial loading.
- To establish the capability of a state-of-the-art FE-based meso-scale modelling framework ('virtual testing' technique) to predict the damage behaviour and strength of composite laminates subjected to multiaxial loading.

1.3   Novelties

The novelties of this research have largely been made possible by the development of a novel multiaxial test rig, the Modified Arcan Fixture (MAF), which enabled testing in the full combined tension-shear and compression-shear loading regimes.

This capability of the MAF has been exploited for the development of a new plasticity-based constitutive model that accounts for the nonlinear, pressure sensitive behaviour of UD composites. It has been demonstrated that the model fits experimental data better than previous similar models proposed in the literature. Furthermore, it has been confirmed that when a Drucker-Prager type yield function is used, a non-associative flow rule is required and that the use of an associative flow rule instead leads to the prediction of non-physical plastic transverse normal strains for pure shear and moderate combined compression-shear stress states. Moreover, the work has resulted in new guidelines for the calibration of plasticity-based models for UD composites: Firstly, it has been found that stress-strain curves obtained under three judiciously chosen biaxial stress states is enough for an accurate calibration of the model. This has been related to the physics of matrix failure where three distinct failure modes are observed and is a consequence of the mathematical/geometrical shapes of the yield and plastic potential ellipses.

Secondly, it has been demonstrated that the use of on-axis stress-strain curves for model calibration, as is often done in the literature, does not guarantee a good model fit. Even though the on-axis stress-strain curves may be accurately represented, the individual contributions of the transverse normal and shear plastic strains to the on-axis effective plasticity may be obscured. Therefore, it is recommended to experimentally obtain both the transvers normal and shear stress-strain curves individually, such that both the plastic transverse normal and shear stress/strains can be verified. DIC has proven a useful tool to this end, because it enables to fully characterise complex strain states without the need for multiple strain gauges, *e.g.* a strain gauge rosette.

A new MAF has been designed, which successfully enabled testing of strong laminates up to failure, which has not been possible with the existing MAF used for the initial research of this PhD project. New experimental procedures based on the MAF and stereo DIC have been proposed that enabled the investigation into the effect of laminate lay-up on the failure behaviour and strength of multidirectional composite laminates subjected to combined tension/compression-shear loading. In continuation of previous successful investigations into laminate lay-up effects, modified open-hole specimens were used. It has been shown that ply thickness has a significant effect on the open-hole specimen strength under tension-shear loading, where thin ply laminates were up to 150% stronger than thick ply laminates, while the effect is relatively small in combined compression-shear loading. Furthermore, no significant effect on the strengths between laminates with a 22.5° and a 45° relative fibre orientation angle between two adjacent plies (or pitch angle) was observed in the tests conducted. This study is amongst the first to investigate laminate lay-up effects under combined loading, especially in the rarely investigated compression-shear loading regime.

The unique multiaxial experimental data obtained using the new MAF enables the validation of predictive models for load cases for which they have never been validated before. Therefore, a meso-scale modelling framework developed for 'virtual testing' was assessed against the multiaxial open-hole data obtained using the MAF. The model discretises the laminate on the UD ply level, where each ply is modelled as an individual anisotropic solid. Intra-laminar damage is predicted using a continuum damage model (CDM) developed at the University of Porto [17]. Failure initiation is predicted using approximations of the LaRC03/04 failure theories [30], while damage propagation is governed by the fracture energies of the individual plies. A structured, fibre aligned mesh was used to mitigate some of the mesh-induced bias on the propagation of damage. Inter-laminar damage (delamination) is modelled using mixed-mode cohesive zones native to the FE software ABAQUS [31]. Similar models have previously been validated in uniaxial open-hole tension (OHT) and compression (OHC) [17] or filled-hole compression [17] tests, but never for multiaxial open-hole cases including combined compression-shear loading. Qualitatively, the model accurately predicted the ply thickness effects observed, *i.e.* the model predicted the thin ply laminate to be stronger in tension-shear than the thick ply laminate, while predictions were similar in compression-shear loading. However, quantitatively the model was

not able to predict the tension-shear open-hole specimen strength of the thin ply laminate. It was recommended that predictions could be improved by accounting for large shear deformation theory within the model formulations. Using an engineering solution to overcome the limitation of the used model, the multiaxial open hole specimen strength was predicted within a mean relative error across all investigated laminate and loading configurations of 10%. The results are promising, but highlight that further improvements are needed before the model can be used as a 'virtual testing' technique on general composite material systems within the design and certification of composite structures.

1.4   Thesis structure

The literature review in Chapter 2 aims to provide a fundamental understanding of the complex mechanical response and failure behaviour of FRP laminates. Alongside, an introduction to the state-of-the-art in simulating failure in FRP laminates is provided.

In Chapter 3, the initial MAF/DIC experiments on butterfly shaped glass/epoxy specimens are discussed. State-of-the-art failure criteria are calibrated and used to predict first-ply-failure in laminates with matrix driven failure modes. The potential and limitations of the MAF test set-up are discussed.

In Chapter 4, it is described how the biaxial experimental procedure and results from Chapter 3 are used to develop a plasticity-based nonlinear material model for UD.

The new MAF design is introduced in Chapter 5 along with the experimental set-up and procedures adopted to investigate laminate lay-up effects in multidirectional laminates. The carbon/epoxy laminates were provided through a collaboration with the sailing team INEOS Team UK and addressed. The experimental results obtained for the multiaxial open-hole specimen strength of three different quasi-isotropic carbon/epoxy laminates are discussed.

In Chapter 6, the state-of-the-art meso-scale model developed at the University of Porto for 'virtual testing' is used to predict the ply thickness effect on the multiaxial open-hole specimen strength observed in Chapter 5. The model is validated against the new experimental data and guidelines for the direction of future model developments are presented.

Finally, general conclusions are drawn and recommendations for future work are put forward in Chapter 7.

Chapter 2

Review of fibre-reinforced polymer matrix composites – constitutive response and modelling

2.1   Introduction

The research in this thesis is concerned with the experimental and numerical characterisation of unidirectional (UD) fibre-reinforced polymer matrix composites (FRP) and their laminates, as illustrated in Figure 2.1.

(a) Unidirectional (UD) lamina   (b) Multidirectional (MD) laminate
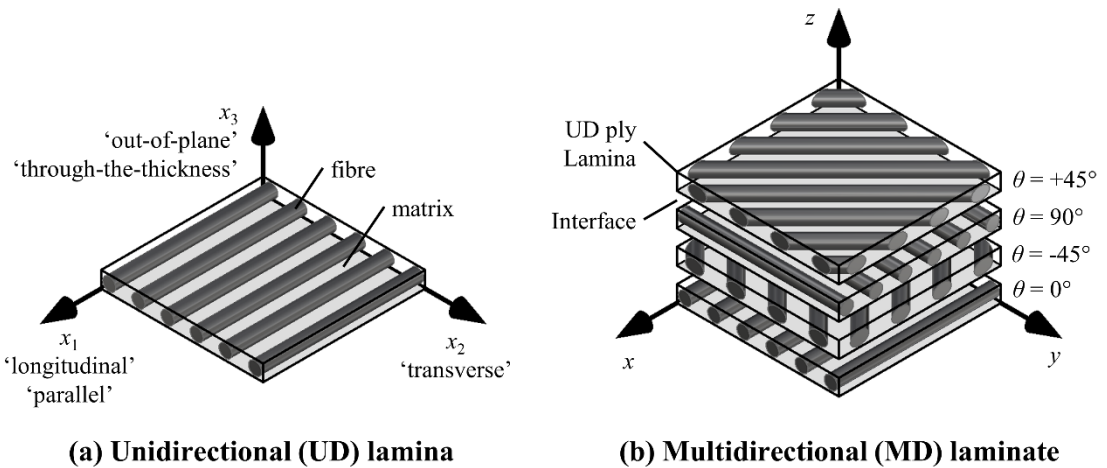
Figure 2.1, FRP composite materials: (a) Unidirectional (UD) lamina, and (b) multidirectional (MD) laminate.

A UD lamina (or ply) consist of the composite constituent materials, *i.e.* the fibre (*e.g.* glass, carbon) and the matrix (*e.g.* epoxy polymer resin) as shown in Figure 2.1 (a). A UD ply coordinate system (x_1, x_2, x_3) is introduced, where the x_1-axis is parallel to the fibres, the x_2-axis is transverse to the fibres, while the x_3 axis is perpendicular to the plane of the ply. From this point onwards the x_1-direction is also referred to as the 'longitudinal' direction, the x_2-axis as the 'transverse' direction and the x_3 axis as the 'out-of-plane' or 'through-the-thickness' direction. The subscripts 1, 2 and 3 will be associated with the axis of a UD composite as introduced in Figure 2.1 (a). When several UD plies are stacked together at different fibre orientation angles (θ) relative to a reference direction (here the *x*-axis), a multidirectional (MD) laminate is formed as illustrated in Figure 2.1 (b). In a multidirectional laminate, a 'global' *xyz* coordinate system is defined where

the *z*-axis is orientated perpendicular to the plane of the laminate. The *z*-axis is also referred to as the 'out-of-plane' or 'through-the-thickness' direction. The special case, where UD plies are stacked together at the same fibre orientation angles, is referred to as a UD laminate as opposed to a single UD ply lamina. The regions between plies of a laminate will be referred to as the 'interface' (see Figure 2.1 (b)). Therefore, failure events within the lamina are referred to as intra-ply or intra-laminar failure, while failure at the interface is referred to as inter-laminar failure. The heterogeneous and anisotropic properties of the UD composite in Figure 2.1 (a) and the layered morphology of a laminate in Figure 2.1 (b), result in complex nonlinear constitutive behaviours and various interacting failure modes, as well as preferred crack paths, which are often not intuitive. Therefore, the aim of this chapter is to provide an overview of the unique constitutive response and failure behaviour of FRP composites, based on which the state-of-the-art modelling techniques for progressive failure, from initiation to ultimate failure, are introduced.

The chapter starts with providing an overview of the nonlinear, pressure sensitive constitutive behaviour of UD composites with a focus on the matrix dominated properties. A brief introduction to the state-of-the-art of nonlinear constitutive modelling is then given. After introducing some of the most widely used failure criteria for FRP composites, the review focuses on the state-of-the-art physics-based LaRC03 failure criterion, by means of which the physics of failure in FRP materials is reviewed. The section is completed with a brief overview of damage models to predict progressive failure in multidirectional composites. Moving on, modelling techniques for the prediction of inter-laminar failure (delamination) are discussed, focusing on the cohesive zone model (CZM) which is a fracture mechanics-based technique that accounts for both delamination initiation and propagation. With the basic physics of failure introduced, laminate lay-up and size effects in multidirectional laminates are reviewed on the example of the open-hole tensile test. Following on, a brief overview of multiaxial testing on the coupon scale is provided. Finally, the key points from the literature review are summarised and opportunities for combined tension/compression and shear testing using the MAF test are highlighted.

2.2 Nonlinear constitutive response of UD FRP composites

2.2.1 Polymer matrix

Typical polymer matrix materials used for structural composites are polyester, vinyl ester or epoxy resins. Although their exact stress-strain behaviour depends on the type of the polymer, most engineering polymers initially respond linearly to low applied stresses, after which yielding with hardening occurs, as shown in Figure 2.2 [32].
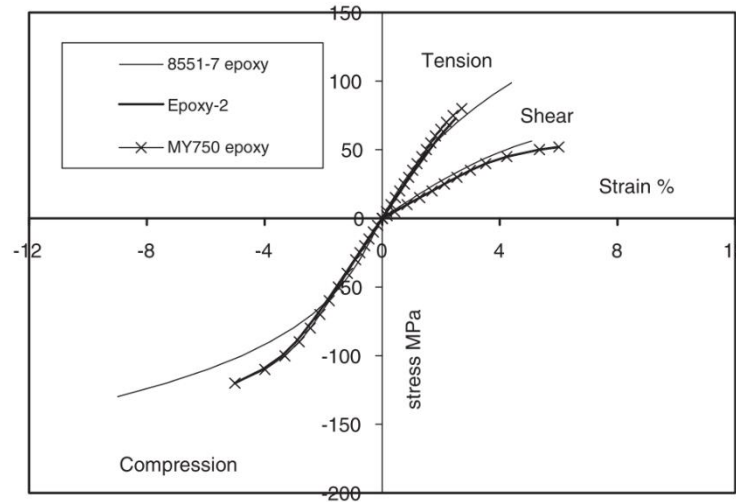
Figure 2.2, Tension, compression and shear stress-strain curves of three different types of epoxy resin [32].

While the response in tension is nearly linear and failure is brittle, the polymer exhibits a nonlinear response to compression and shear where plastic yielding takes place. In tension, existing microcracks open and propagate more easily and lead to brittle failure. In compression, microcracking is delayed, which allows the polymer to plastically deform before ultimate failure [33]. The failure behaviour of polymers is therefore governed by two competing failure mechanisms which are brittle fracture and yielding and their occurrence and interaction depends on the stress state applied. Polymers are also sensitive to hydrostatic pressure (σ_h) as shown by the compressive stress-strain curves in Figure 2.3 obtained on pure epoxy specimens subjected to σ_h up to 100 ksi (~690 MPa) [34].
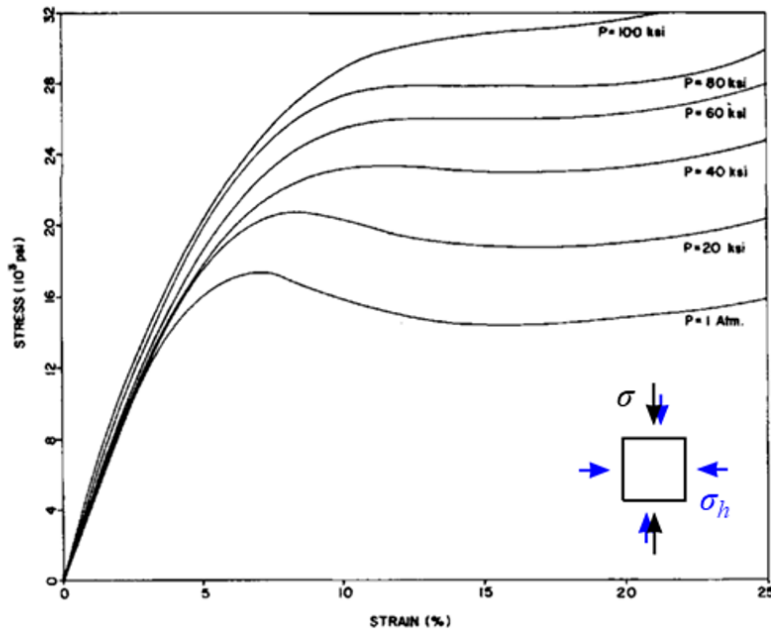
Figure 2.3, Effect of hydrostatic pressure on the compressive stress-strain curve of pure epoxy resin [34].

The pressure sensitivity was responsible for the distinctly different behaviour in tension and compression as shown in Figure 2.2. In addition, the compressive yield strength increases with σ_h as shown in Figure 2.3. The effect of pressure on the compressive behaviour is explained by Mears *et al.* [35] from a molecular perspective, arguing that the applied pressure reduces the mobility of the polymer chains, forces them closer together, and hence increases the intermolecular forces. Thus, a higher stress must be applied to initiate molecular mobility or in other words yielding. Furthermore, the application of σ_h also supresses crack growth and hence inhibits brittle failure and allows the polymer to yield.

2.2.2   UD composite laminate

The UD FRP composite inherits the nonlinear, pressure sensitive behaviour of the polymer. The constitutive response in the transverse to the fibre planes is especially effected by the properties of the resin: as for pure epoxy (see Figure 2.2), the transverse tensile and compressive stress-strain curves of a UD laminate are distinctly different as shown in Figure 2.4 (c), where the UD laminate is stronger in transverse compression than in tension and the compressive behaviour is distinctly nonlinear [36]. As for epoxy (see Figure 2.2), the shear stress-strain curves exhibit nonlinear behaviour as shown in Figure 2.4 (a) and (b).
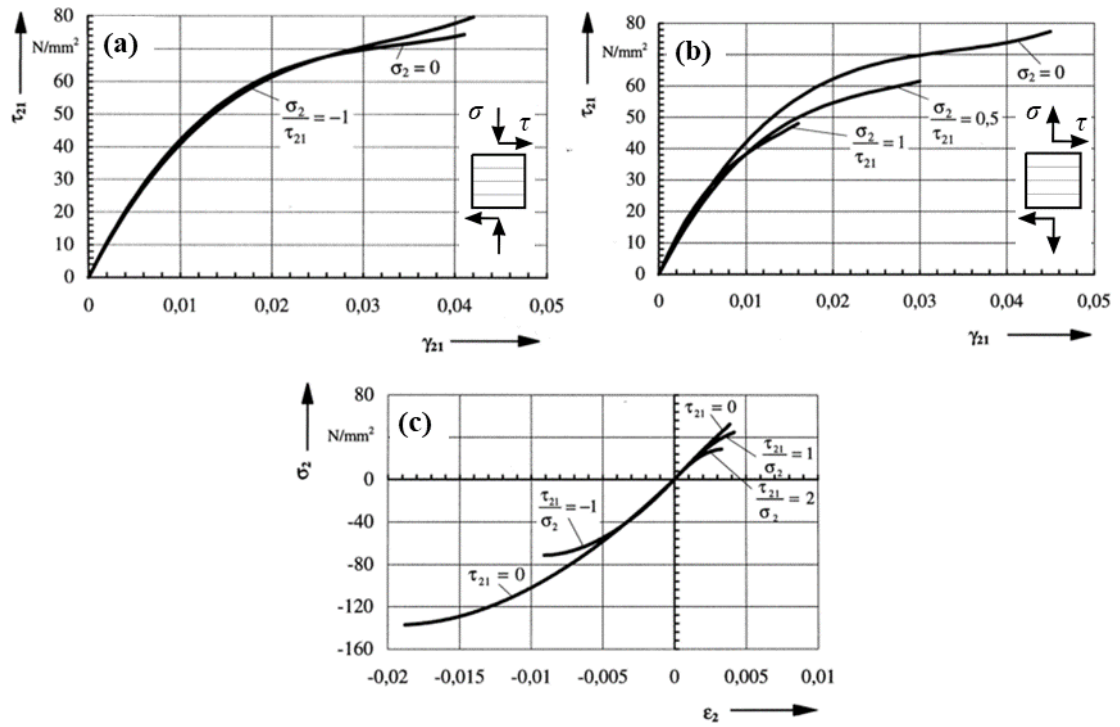
Figure 2.4, E-glass/epoxy subjected to combined transverse tension/compression and shear: (a) shear stress-strain curves under transverse compression, (b) shear stress-strain curves under transverse tension, and (c) transverse tensile and compressive stress-strain curves [36].

Shin *et al.* [37] showed that the shear behaviour of UD composites is also sensitive to hydrostatic pressure. Using hoop wound carbon/epoxy tubular specimens subjected to combined hydrostatic pressure and torsion, shear stress-strain curves were obtained as shown in Figure 2.5. They reveal that increasing hydrostatic pressure from atmospheric to 6 kbar almost doubles the shear stress at failure of the UD fibre-reinforced polymer-matrix composite.
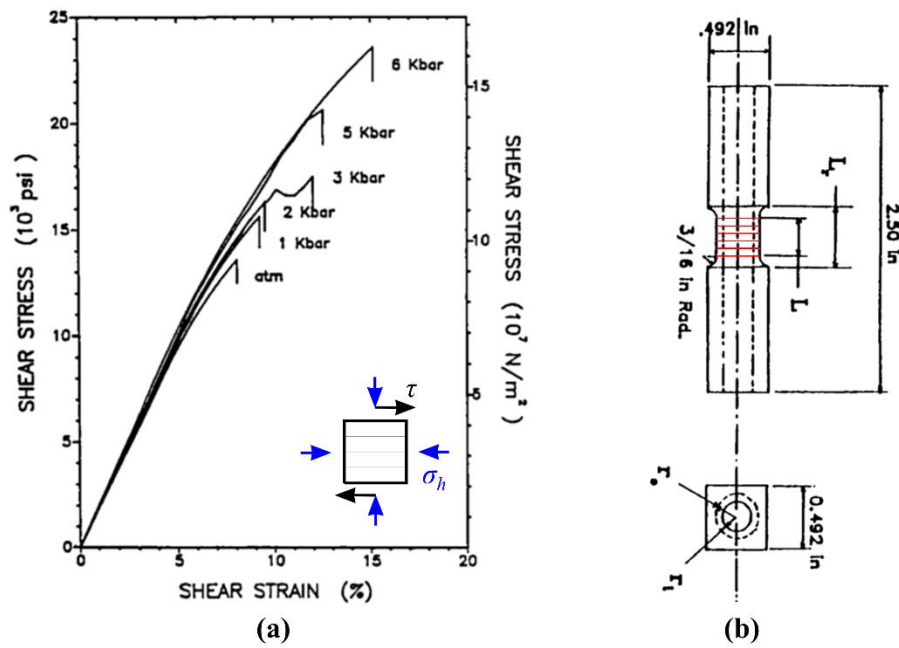
Figure 2.5, (a) Effect of hydrostatic pressure on the shear stress-strain curves and (b) the tubular specimen used in the test [37].

Subjecting hoop wound carbon/epoxy tubular specimens to combined torsion and axial tension/compression (instead of hydrostatic pressure in [37]), Swanson *et al.* [38] showed that the shear stress at failure depends on transverse compression in a similar way as on the hydrostatic pressure.
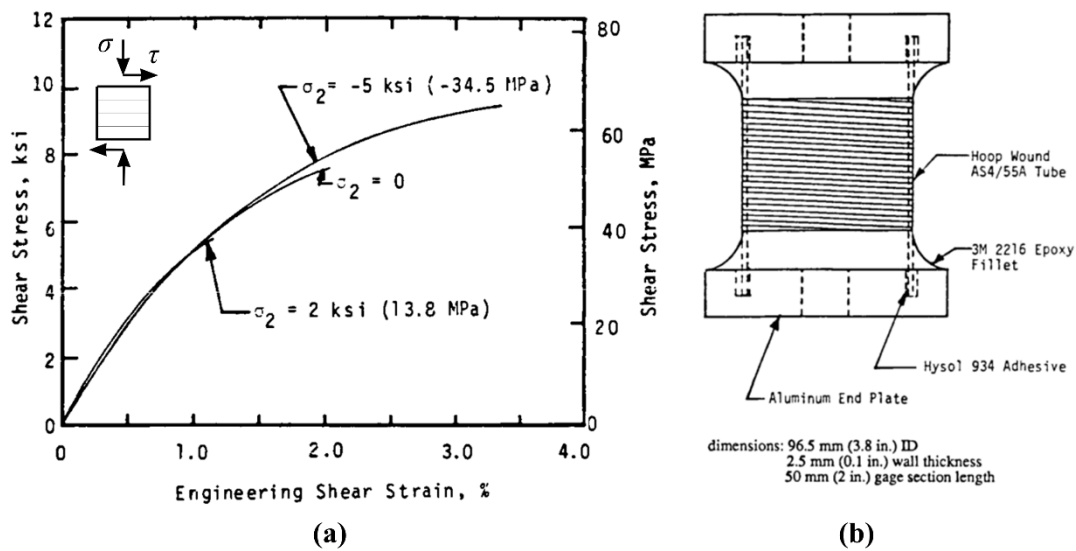
Figure 2.6, (a) Effect of transverse tension/compression on the shear stress-strain curve and (b) hoop wound tubular specimen used in [38].

As observed in Figure 2.6, applying transverse compressive stress significantly increases the shear stress at failure (similar to hydrostatic pressure), while applying transverse tensile stress reduces the shear stress at failure. The effect of transverse compression is therefore qualitatively similar to the effect of hydrostatic pressure. In continuum mechanics, hydrostatic pressure is defined as

a third of the trace of the stress tensor, which is an invariant. Therefore, an increase of transverse compressive stress also increases the hydrostatic pressure in the material, which supports the observation that transverse compression (see Figure 2.6) will have a similar effect on the constitutive response as hydrostatic pressure (see Figure 2.5).

2.2.3   Nonlinear modelling approaches

UD composites are generally modelled as transversely isotropic materials [39], [40], where the transverse plane is perpendicular to the fibre direction (x_1-axis), implying that the transverse-to-the-fibre response is equivalent to the through-the-thickness response as illustrated in Figure 2.7.
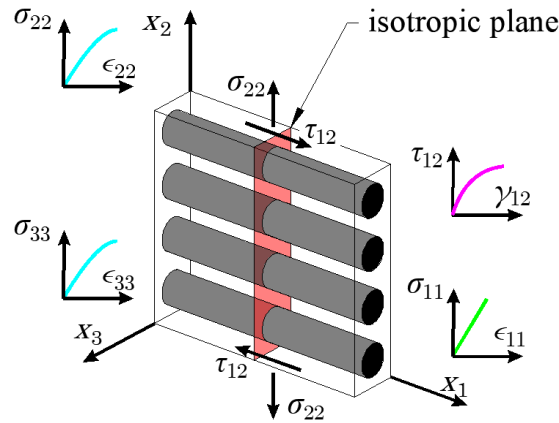
Figure 2.7, Illustration of a UD composite element showing the isotropic plane and the stress-strain behaviour in longitudinal (x_1), transverse (x_2) and through-thickness (x_3) directions.

While their response in the direction of the fibre is linear up to failure, it has been shown in Section 2.2, that the matrix dominated transverse properties exhibit nonlinear and pressure sensitive behaviour as shown in Figure 2.7. Despite these nonlinearities, many failure analyses of UD and multidirectional composites subjected to multiaxial stress states are simply based on linear elastic constitutive laws for the UD composite [18], [41]. This might lead to inaccurate predictions of the shear stresses and strains where the most significant nonlinear behaviour is observed. Therefore, to improve the models, the nonlinear stress-strain behaviour is often accounted for. In [17] it is approximated using a bilinear fit to the shear stress-strain curve, whereas the logarithmic Ramberg-Osgood fit [42] (*e.g.* in [15], [43]–[46]) or Hahn and Tsai's polynomial fit [47] (*e.g.* in [48], [49]) are also frequently used in the literature to describe the nonlinear shear behaviour. To account not only for the shear nonlinearity, but also for the nonlinearity in compression and the pressure sensitive behaviour, the modelling framework of plasticity has been proposed [50]–[55]. These models require biaxial experimental data in the tension/compression and shear stress space for calibration. Most often, tensile and compressive off-axis specimens are utilised [50]–[52], [55] but also custom built two-actuator biaxial testing facilities [56], [57] and tubular [54] specimens have been used. An in-depth discussion of the

mathematical framework and fundamental assumptions of the plasticity-based models applied to UD composites is provided in Chapter 4. In the chapter, a new nonlinear material model, similar to the models in [50]–[52], is developed using the MAF combined with DIC, which overcomes limitations of similar modelling frameworks proposed in the literature [50], [51].

2.3   Popular failure theories used in industry

The simplest failure theories, and according to Sun *et al.* [58] the most widely used theories by 1996 in industry, are the non-interactive maximum stress and maximum strain failure criteria. Non-interactive criteria do not take into account interactions between different stress/strain components, which typically leads to erroneous failure predictions when multiaxial states of stress occur in a structure [59]. For the case of plane stress ($\sigma_{33} = \tau_{23} = \tau_{13} = 0$), failure is predicted when the fibre longitudinal stress (σ_{11}), the transverse stress (σ_{22}) or the shear stress (τ_{12}), reached the strengths associated with fibre tensile (X_T) or compressive (X_C), matrix tensile (Y_T) or compressive (Y_C), or shear (S_L) failure [60]:

$$
\begin{aligned}
X_T &\geq \sigma_{11} \geq X_C \\
Y_T &\geq \sigma_{11} \geq Y_C \\
S_L &\geq |\tau_{12}|
\end{aligned}
\tag{2.1}
$$

The maximum strain theory is formulated similarly but is based on the strains to failure (ϵ_{11}^T, ϵ_{11}^C, ϵ_{22}^T, ϵ_{22}^C, γ_{12}^{fail}) instead of the failure stresses and on the strain field (ϵ_{11}, ϵ_{22}, γ_{12}) instead of the stress field as [60]:

$$
\begin{aligned}
\epsilon_{11}^T &\geq \epsilon_{11} \geq \epsilon_{11}^C \\
\epsilon_{22}^T &\geq \epsilon_{22} \geq \epsilon_{22}^C \\
\gamma_{12}^{fail} &\geq |\gamma_{12}|
\end{aligned}
\tag{2.2}
$$

Another popular failure theory is the Tsai-Wu failure criterion [61]–[63]. This criterion is representative of interactive, polynomial or tensorial failure theories, where failure is not associated with a specific failure mode but is instead described by a failure surface defined as a function of the material strengths. In the Tsai-Wu criterion [61]–[63], the failure envelope for orthotropic materials in a state of plane stress is given by the equation:

$$
F_1\sigma_{11} + F_2\sigma_{22} + F_6\tau_{12} + F_{11}\sigma_{11}^2 + F_{22}\sigma_{22}^2 + 2F_{12}\sigma_{11}\sigma_{22} = 1
\tag{2.3}
$$

where the stress symbols have their usual meanings and where the coefficients F_1, F_2, F_{11}, F_{22}, and F_6 can be determined from the uniaxial strength values:

$$F_1 = \frac{1}{X_T} - \frac{1}{X_C}, \ F_2 = \frac{1}{Y_T} - \frac{1}{Y_C},$$

$$F_{11} = \frac{1}{X_T X_C}, \ F_{22} = \frac{1}{Y_T Y_C}, \qquad (2.4)$$

$$F_6 = \frac{1}{S_L^{\ 2}}$$

F_{12} in Equation (2.3) is a biaxial stress interaction coefficient that is obtained in a tension-tension or compression-compression biaxial experiment. If no test data is available, Tsai recommends using $F_{12} = 0.5\sqrt{F_{11}F_{22}}$. The failure envelope is described by one closed polynomial equation, which means that *e.g.* compressive failure is not entirely independent from the tensile strength value and vice versa; a prediction that is contradicted by experimental evidence [64]. Moreover, different failure modes cannot easily be distinguished which is a significant disadvantage in the formulation of progressive failure models, where the type of failure mode ideally is used to inform the degradation of the elastic constants (see Section 2.4.4).

2.4   Physics-based intra-laminar failure models

The main failure modes in UD composites are now introduced by reviewing the LaRC03 [30] failure criterion for plane stress. More advanced three-dimensional versions are the LaRC04 [60] failure criterion, accounting for the nonlinear matrix behaviour in shear, and the LaRC05 [33] failure criterion, accounting for the nonlinear matrix behaviour in shear, and the transverse and through-the-thickness directions (see Section 2.2.2). The LaRC03 criterion is chosen for simplicity and to provide a (relatively) quick overview of physics-based composite failure modelling. Following Puck's [65], [66] and Hashin's [64] proposition to predict different failure modes separately, *i.e.* following a phenomenological approach, the LaRC03 failure criterion includes individual, in some cases physics-based, failure models for fibre and matrix tensile and compressive failure. The fibre compressive failure criterion is based on the fibre kinking models in [67], [68], while the criteria for matrix failure are based on Puck's inter-fibre failure (IFF) model [36], [69]. Furthermore, the LaRC03 criterion accounts for the in-situ strength effect using fracture mechanics based models developed by Dvorak and Laws [70]. Reviewing the LaRC03 criterion provides an excellent overview into the physics of failure and the associated state-of-the-art modelling approaches. However, many other failure criteria exist of which the World Wide Failure Exercises (WWFEs) [71]–[73] organised by Hinton, Soden and Kaddour provide an excellent overview.

2.4.1   Fibre tensile failure

Fibre tensile failure is mainly governed by the stress parallel to the fibre (σ_{11}) with no significant interaction effects from other components of the stress tensor. Failure is dominated by the

properties of the fibre with no significant dependency on the matrix constituent. Therefore, failure is predicted using the non-interactive maximum stress criterion as in Equation (2.1):

$$FI_F = \frac{\sigma_{11}}{X_T} \leq 1 \tag{2.5}$$

or using the non-interactive maximum strain criterion as in Equation (2.2):

$$FI_F = \frac{\epsilon_{11}}{\epsilon_{11}^T} \leq 1 \tag{2.6}$$

where FI_F is the failure index for the fibre. Fibre tensile failure is explosive due to the large amount of strain energy released, and typically causes catastrophic failure, *i.e.* it is associated with the ultimate strength of a laminate [33]. X_T in Equation (2.1) and ϵ_{11}^T in Equation (2.2) can be determined using the standard tensile test method [74].

2.4.2 Matrix failure

Puck's inter-fibre failure (IFF) theory

Puck *et al.* [36], [69] classified three distinctly different matrix failure modes for UD laminates (IFF mode A, B and C) as illustrated in Figure 2.8.
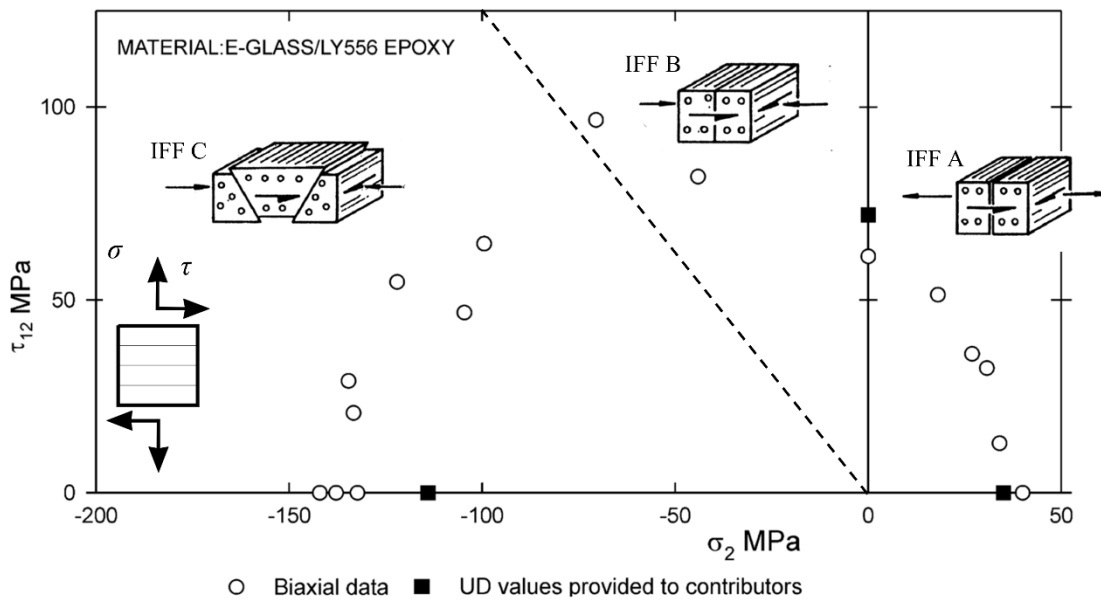
Figure 2.8, Failure envelope for UD glass/epoxy in the $\sigma_{22} - \tau_{12}$ stress space [75] with illustrations of the failure modes taken from [36].

IFF is governed by the transverse normal and shear stresses [75]: under transverse tension (IFF Mode A), the crack plane is perpendicular to the mid-plane of the laminate. Under moderate transverse compression the fracture plane is still perpendicular to the mid-plane of the laminates while a shear strength enhancement with increased transverse compression is observed in the

$\sigma_{22} - \tau_{12}$ failure envelope (IFF Mode B). When the transverse compressive stress becomes dominant, an inclined fracture plane is observed (IFF Mode C). The effect of transverse stress on the apparent shear strength can be related to the pressure sensitivity of the polymeric resin described in Section 2.2.

Puck's IFF criterion was adapted from Mohr-Coulomb's frictional yield model for brittle materials [76], stating that matrix failure is governed by the stresses acting on the fracture plane as shown in Figure 2.9.
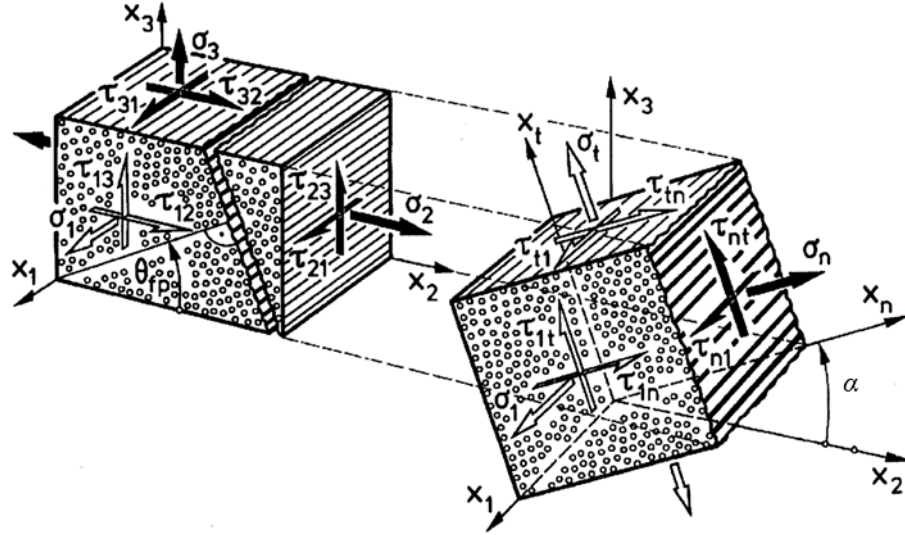
Figure 2.9, Three-dimensional stress state on a UD composite element and definition of the fracture plane inclined at an angle α[1] with respect to the transverse x₂-direction, and definition of the n-l-t coordinate system associated with the fracture plane [36].

It is assumed that IFF failure is independent from the stresses in the fibres, and that possible fracture planes are always located in the matrix and parallel to the fibres. The stresses on the fracture plane (σ_n, τ_{nl}, τ_{nt}) are linked to the stresses in the lamina coordinate system (σ_{22}, τ_{12}) through the stress transformation rules:

$$\sigma_n = \sigma_{22} \cos^2 \alpha$$
$$\tau_{nl} = \tau_{21} \cos \alpha = \tau^L \qquad\qquad (2.7)$$
$$\tau_{nt} = -\sigma_{22} \sin \alpha \cos \alpha = \tau^T$$

where α is the angle of the fracture plane with respect to the transverse x_2- direction. Note that later when the LaRC03 criterion is discussed, τ_{nl} and τ_{nt} are expressed by τ^L and τ^T, respectively.

---

[1] Note that Puck uses the symbol θ_{fp} to designate the fracture plane angle, while in the LaRC03 criterion the symbol α is used. To avoid confusion, the nomenclature from the LaRC03 criterion is adopted throughout this thesis.

Puck proposed fracture conditions based on the stresses on the fracture plane given in Equation (2.7) based on the Mohr-Coulomb fracture hypothesis [76]. Using several simplifying assumptions Puck then expressed the fracture criteria based on UD ply stresses (σ_{22}, τ_{12}) and the associated uniaxial transverse tensile (Y_T), compressive (Y_C) and shear (S_L) strengths. The fracture plane angle defining the stress state is the one maximising the failure index for which Puck suggested analytical closed-form solutions. For a more detailed discussion the reader is referred to the representative works by Puck *et al.*[36], [69].

The fracture plane angle α is given by:

$$\alpha = \text{acos}\left(\frac{R_{\perp\perp}^A}{-\sigma_{22}}\right) \tag{2.8}$$

where $R_{\perp\perp}^A$ is the fracture resistance of the action plane (superscript A denotes the action plane), which is the plane inclined at the angle α with the largest risk of fracture:

$$R_{\perp\perp}^A = \frac{Y_C}{2\left(1+p_{\perp\parallel}^{(-)}\right)} = \frac{S_L}{2p_{\perp\parallel}^{(-)}}\left(\sqrt{1+2p_{\perp\parallel}^{(-)}\frac{Y_C}{S_L}}-1\right) \tag{2.9}$$

In IFF Mode A, the tensile normal (σ_{22}) and shear (τ_{12}) stresses both promote fracture:

$$\sqrt{\left(\frac{\tau_{21}}{S_L}\right)^2 + \left(1-p_{\perp\parallel}^{(+)}\frac{Y_T}{S_L}\right)^2\left(\frac{\sigma_{22}}{Y_T}\right)^2} + p_{\perp\parallel}^{(+)}\frac{\sigma_{22}}{S_L} \geq 1, \ \left(\sigma_{22}\geq 0\right) \tag{2.10}$$

In IFF Mode B, the moderate compressive normal stress σ_{22} impedes fracture by increasing the resistance of the fracture plane against shear fracture:

$$\frac{1}{S_L}\left(\sqrt{\tau_{21}^2 + \left(p_{\perp\parallel}^{(-)}\sigma_{22}\right)^2} + p_{\perp\parallel}^{(-)}\sigma_{22}\right) \geq 1, \ \sigma_{22} < 0 \text{ and } 0 \leq \left|\frac{\sigma_{22}}{\tau_{21}}\right| \leq \frac{R_{\perp\perp}^A}{|\tau_{21c}|} \tag{2.11}$$

while in IFF Mode C, both σ_{22} and τ_{12} promote failure:

$$\left[\left(\frac{\tau_{21}}{2\left(1+p_{\perp\perp}^{(-)}\right)S_L}\right)^2 + \left(\frac{\sigma_{22}}{Y_C}\right)^2\right]\frac{Y_C}{-\sigma_{22}} \geq 1, \ \sigma_{22} < 0 \text{ and } 0 \leq \left|\frac{\tau_{21}}{\sigma_{22}}\right| \leq \frac{|\tau_{21c}|}{R_{\perp\perp}^A} \tag{2.12}$$

where τ_{12c} is the shear stress at the intersection between Mode B and C defined as:

$$\tau_{12c} = R_{\perp\parallel}^A\sqrt{1+p_{\perp\perp}^{(-)}} \tag{2.13}$$

$p_{\perp\parallel}^{(+)}$, $p_{\perp\parallel}^{(-)}$ are slope parameters in the $\sigma_{22}-\tau_{12}$, and $p_{\perp\perp}^{(+)}$, $p_{\perp\perp}^{(-)}$ in the $\sigma_{22}-\tau_{23}$ failure envelopes at pure shear ($\sigma_{22}=0$) in the tensile $^{(+)}$ and compressive $^{(-)}$ quadrants, respectively:

$$p_{\perp\parallel}^{(+)} = -\left(\frac{d\tau_{21}}{d\sigma_{22}}\right)_{\sigma_2=0} \text{ of } (\sigma_{22}, \tau_{21}) \text{ curve, } \sigma_{22} \geq 0 \tag{2.14}$$

$$p_{\perp\parallel}^{(-)} = -\left(\frac{d\tau_{21}}{d\sigma_{22}}\right)_{\sigma_2=0} \text{ of } (\sigma_{22},\ \tau_{21}) \text{ curve, } \sigma_{22} \le 0 \ (2.15)$$

$$p_{\perp\perp}^{(+)} = p_{\perp\perp}^{(-)} = p_{\perp\parallel}^{(-)}\frac{R_{\perp\perp}^{A}}{S^{L}} \tag{2.16}$$

These parameters can be determined experimentally or typical values from the literature can be assumed. Puck recommends for glass/epoxy $p_{\perp\parallel}^{(+)}$ =0.25, $p_{\perp\parallel}^{(-)}$ =0.3 and $p_{\perp\perp}^{(+)} = p_{\perp\perp}^{(-)}$ =0.2 – 0.25.

In-situ strength effect

To predict matrix cracking in a multidirectional laminate accurately, the 'in-situ' effect on the matrix dominated strengths must be accounted for in strength-based failure analyses, otherwise the failure initiation stresses are underpredicted [30]. 'In-situ' effects describe the phenomena, where assumed 'intrinsic' material properties measured on a UD laminate depend on the laminate lay-up (*i.e.* on the ply thickness, the stacking sequence, and the fibre orientations) when the UD ply is embedded in a multidirectional laminate. Parvizi *et al.* [77] was amongst the first to observe experimentally such an in-situ effect in tensile tests of cross-ply glass fibre-reinforced laminates. It was found that the transverse tensile strength (Y_T) is higher in thin embedded plies than in thick embedded plies, which eventually tends to the strength of the UD laminate for very thick embedded plies. Extending the study in [77], Flaggs *et al.* [78] showed that not only the ply thickness, but also the relative orientation of the constraining plies (θ in Figure 2.10) has an influence on the onset of transverse cracks in a carbon/epoxy laminate.
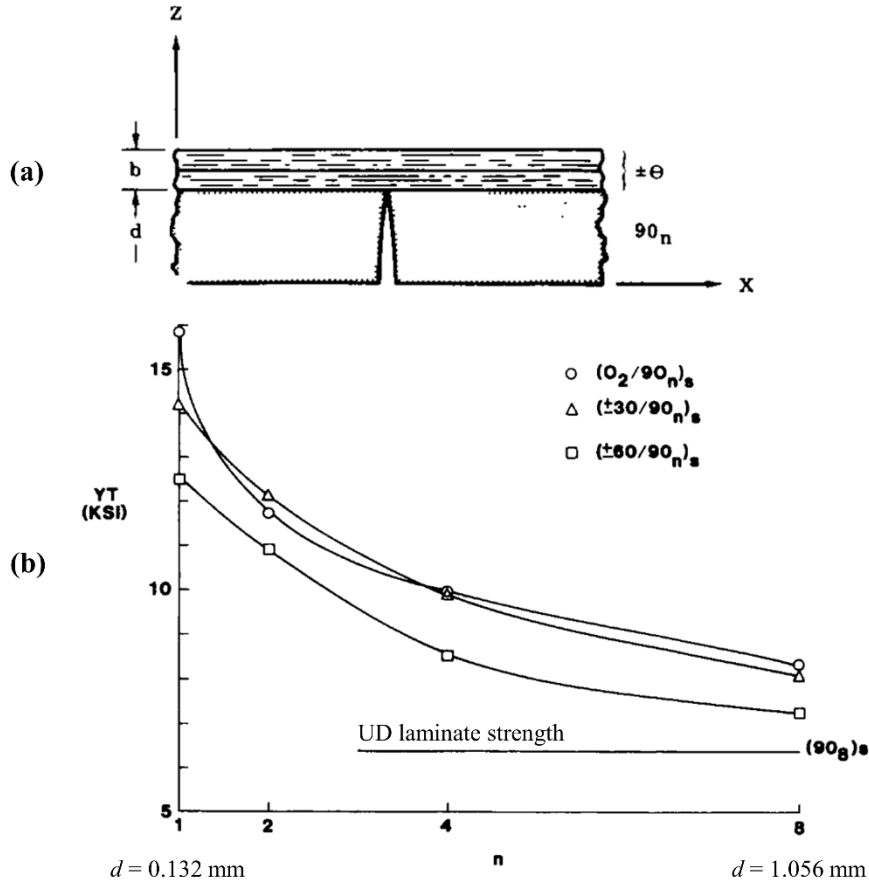
Figure 2.10, The effect of the thickness of the embedded ply (d) and the fibre orientation (or stiffness) of the constraining plies (θ) on the in-situ transverse tensile strength (Y_T^{is}): (a) specimen geometry, and (b) experimental results [78].

It is observed from Figure 2.10 that Y_T^{is} of thin plies ($d = 0.132$ mm) is more than twice as high than Y_T^{is} measured using a 2.12 mm thick UD laminate. Moreover, Y_T^{is} of the constrained ply is higher when the constraining plies are stiff in the direction perpendicular to the transverse crack opening in the embedded ply (*i.e.* in Figure 2.10 the transverse tensile strength is greatest for the $\theta = 0°$ laminate). In addition, Flaggs *et al.* [78] also showed that the fibre stresses σ_{11} have a negligible influence on the onset of matrix cracking and the in-situ effect. Using the rail shear test, Chang *et al.* [79] also showed that the shear strength (S_L) depends on the ply thickness and the orientation of the constraining plies. It was concluded that laminates with thin plies dispersed through the thickness are significantly stronger in shear than laminates where plies are clustered together. Arteiro *et al.* [80] investigated the effect of ply thickness on the transverse compressive strength (Y_C) of embedded plies using micro-mechanical models. The simulation results showed that Y_C is also subjected to an in-situ effect and that matrix cracking under transverse compression is delayed in thin plies.

Based on the experimental studies in [77]–[80], Dvorak and Laws [70], Camanho *et al.* [49], and Pinho *et al.* [33] argued that the matrix dominated strengths of the UD ply should not be

considered as 'intrinsic' material properties but rather as structural properties. This is further supported by the different boundary conditions in the fracture mechanics problems for crack growth, as shown in Figure 2.11, where the conditions for the propagation of micro-cracks are more favourable in a UD laminate (Figure 2.11 (a)) than in an outer ply of a multidirectional laminate (Figure 2.11 (b)), or in a thin (Figure 2.11 (c)) or thick (Figure 2.11 (d)) ply embedded in a multidirectional laminate.
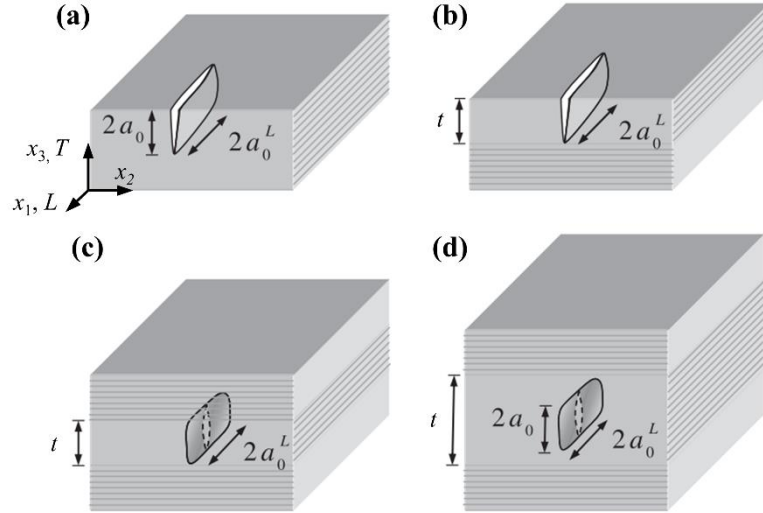
Figure 2.11, Fracture mechanics models for the derivation of the in-situ strengths: (a) slit crack in a UD laminate, (b) slit crack in a surface ply, (c) slit crack in a thin embedded ply, and (d) slit crack in a thick embedded ply [33].

Analytical expressions were proposed in [33], [49], [70] for the in-situ transverse (Y_T^{is}) and shear (S_L^{is}) strength of a UD fibre reinforced ply based on the fracture mechanics analysis of a slit crack, as initially proposed by Dvorak and Laws [70]. The cracks shown in Figure 2.11 are assumed to lie in the x_1-x_3 plane of the UD ply and have a height of $2a_0$ and a length of $2a_0^L$ along the fibre direction. These cracks represent physical defects in the material such as matrix-fibre debonds or voids which are the preferential location for the nucleation of matrix cracks. The derivation of the in-situ strength depends on the adopted stress-strain relationships. Particularly in shear, the response is nonlinear as was shown in Section 2.2. This nonlinearity requires special attention in the derivation of the shear in-situ strength, which is not accounted for in LaRC03 [30] and which is ignored for the sake of simplicity in this review. Therefore, for the following discussion of the in-situ strength concept, a linear shear stress-strain relationship is assumed. The reader is referred to [49], [60] on how to account for the nonlinear shear behaviour in the derivation of the in-situ strength.

Fracture mechanics differentiates between three types of cracks as shown in Figure 2.12: the normal opening mode is termed mode I (Figure 2.12 (a)), the shear mode is termed mode II (Figure 2.12 (b)), and the second shear-like scissoring mode is termed mode III (Figure 2.12 (c)).
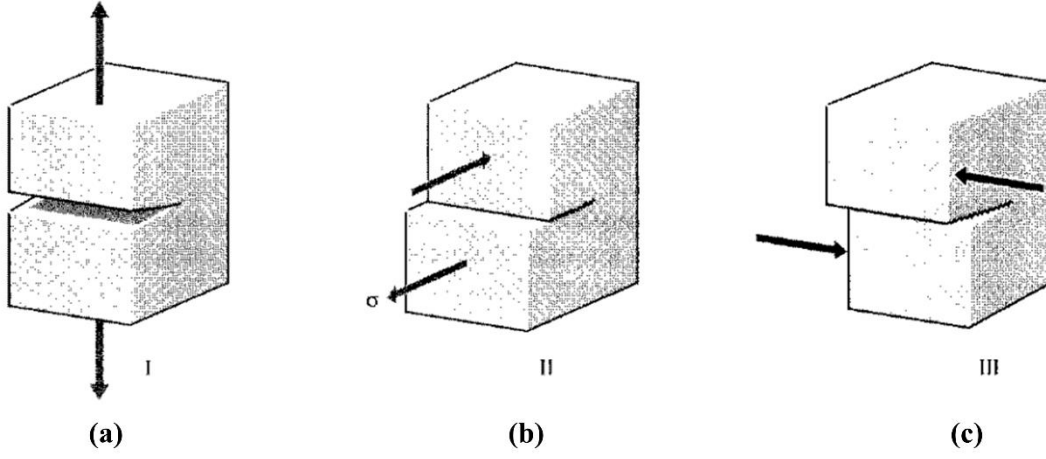
Figure 2.12, Fracture modes: (a) normal opening mode I, shear mode II, and scissoring mode III [81].

For crack growth in through-thickness direction in a laminate (along *T*-axis in Figure 2.11), a mode I ($G_I(T)$) and mode II ($G_{II}(T)$) energy release rate, corresponding to the fracture modes illustrated in Figure 2.12 can be defined as:

$$G_I(T) = \frac{\pi a_0}{2} \Lambda_{22}^0 \sigma_{22}^2 \tag{2.17}$$

$$G_{II}(T) = \frac{\pi a_0}{2} \Lambda_{44}^0 \tau_{12}^2 \tag{2.18}$$

while the energy release rate for crack growth in the direction of the fibres (along *L*-axis in Figure 2.11) are defined as:

$$G_I(L) = \frac{\pi a_0}{4} \Lambda_{22}^0 \sigma_{22}^2 \tag{2.19}$$

$$G_{II}(L) = \frac{\pi a_0}{4} \Lambda_{44}^0 \tau_{12}^2 \tag{2.20}$$

where Λ_{22}^0 and Λ_{44}^0 are non-vanishing components of the crack tensor as defined in [49]:

$$\Lambda_{22}^0 = 2\left(\frac{1}{E_2} - \frac{v_{21}^2}{E_1} \right) \tag{2.21}$$

$$\Lambda_{44}^0 = \frac{1}{G_{12}} \tag{2.22}$$

The corresponding components of the fracture toughness ($G_{IC}(i)$, $G_{IIC}(i)$ with $i = T, L$) are then given by the energy release rates in Equations (2.17) to (2.20) evaluated at the failure stresses (Y_T^{is} and S_L^{is}) as:

$$G_{IC}(T) = \frac{\pi a_0}{2} \Lambda_{22}^0 (Y_t^{is})^2 \tag{2.23}$$

$$G_{IIC}(T) = \frac{\pi a_0}{2} \Lambda_{44}^0 (S_L^{is})^2 \tag{2.24}$$

$$G_{IC}(L) = \frac{\pi a_0}{4} \Lambda_{22}^0 (Y_T^{is})^2 \tag{2.25}$$

$$G_{IIC}(L) = \frac{\pi a_0}{4} \Lambda_{44}^0 (S_L^{is})^2 \tag{2.26}$$

The in-situ strengths can now be determined using Equations (2.23) to (2.26) for the ply configurations as illustrated in Figure 2.11. As an example, consider the case of a thick embedded ply (Figure 2.11 (d)) for mode I loading: The crack can grow in both the transverse (T) and longitudinal (L) directions. By comparing Equations (2.17) and (2.19) it is observed that the crack will first propagate in the transverse direction because the energy release rate is twice as large. Therefore, Y_T^{is} can be obtained by re-arranging Equation (2.23):

$$Y_T^{is} = \sqrt{\frac{2G_{Ic}(T)}{\pi a_0 \Lambda_{22}^0}} \tag{2.27}$$

On the other hand, in a thin embedded ply, crack growth is constrained to the longitudinal direction (L), because $2a_0 = t$ as shown in Figure 2.11 (c). Therefore, the in-situ tensile strength for a thin embedded ply can be obtained by re-arranging Equation (2.25):

$$Y_T^{is} = \sqrt{\frac{8G_{Ic}(L)}{\pi t \Lambda_{22}^0}} \tag{2.28}$$

By comparing the in-situ strengths for thick and thin embedded plies in Equations (2.27) and (2.28) it is observed that the in-situ strength for thin plies is higher than for thick plies. Following similar arguments, also the remaining in-situ strengths for an outer ply and for mode II opening are obtained. A full set of derived in-situ strengths, assuming a linear shear stress-strain relationship, is provided in Table 2.1. For the full derivation of the in-situ strengths the reader is referred to [30], [33], [49], [70]. Note that for thick embedded plies, Equation (2.27) can be simplified to depend only on the measured UD transverse strength as reported in Table 2.1.

Table 2.1, Equations for the in-situ strengths assuming a linear shear stress-strain relationship.

Configuration	Transverse tensile strength	Shear strength
UD laminate	Y_T	S_L
Thick embedded	$Y_T^{is} = 1.12\sqrt{2}Y_T$ [49]	$S_L^{is} = \sqrt{2}S_L$ [49]
Thin embedded	$Y_T^{is} = \sqrt{\dfrac{8G_{Ic}}{\pi t \Lambda_{22}^0}}$ [49]	$S_L^{is} = \sqrt{\dfrac{8G_{12}G_{IIc}}{\pi t}}$ [49]
Thin outer	$Y_T^{is} = 1.78\sqrt{\dfrac{G_{Ic}}{\pi t \Lambda_{22}^0}}$ [17]	$S_L^{is} = 2\sqrt{\dfrac{G_{12}G_{IIc}}{\pi t}}$ [49]

where $\Lambda_{22}^0 = 2\left(1/E_2 - v_{12}^2/E_1\right)$

Matrix failure under transverse tension loading

In LaRC03, the criterion for matrix failure under transverse tension is based on the mixed mode fracture criterion proposed by Hahn *et al.* [82] expressed in terms of the mode I and mode II energy release rates in Equations (2.17) to (2.20) and the critical energy release rates in Equations (2.23) to (2.26) as:

$$(1-g)\sqrt{\frac{G_I(\mathrm{i})}{G_{Ic}(i)}} + g\frac{G_I(\mathrm{i})}{G_{Ic}(i)} + \frac{G_{II}(\mathrm{i})}{G_{IIc}(i)} = 1, \ i = T, L \tag{2.29}$$

where g is the ratio of the fracture toughness values:

$$g = \frac{G_{Ic}}{G_{IIc}} \tag{2.30}$$

Matrix failure under transverse tension ($\sigma_{22} > 0$) can then be expressed in terms of the stresses in the ply (σ_{22} and τ_{12}) and the in-situ strengths by substituting Equations (2.17) to (2.26) into Equation (2.29) resulting in:

$$FI_M = (1-g)\left(\frac{\sigma_{22}}{Y_T^{is}}\right) + g\left(\frac{\sigma_{22}}{Y_T^{is}}\right)^2 + \left(\frac{\tau_{12}}{S_L^{is}}\right)^2 \leq 1 \tag{2.31}$$

where FI_M is the failure index for the matrix. Failure is predicted when the inequality in Equation (2.31) is violated. The UD tensile and shear strengths (Y_T , S_L) required to compute the in-situ strengths according to Table 2.1 can be obtained using standard test methods. While Y_T can be obtained using the standard tensile test method [74], there is some ambiguity in the determination of the shear strength which is reflected by the existence of several standard test

methods. Either the +/−45° laminate tensile test [83], or the V-notched rail shear method [84], or the V-notched beam method (Iosipescu specimen) [85] can be used. The fracture toughness values can also be determined using established standard tests: the double cantilever beam (DCB) [86] test specimen is used to obtain the mode I fracture toughness (G_{Ic}), while the end notched flexure (ENF) [87] test specimen is used to obtain the mode II fracture toughness (G_{IIc}).

Matrix failure under transverse compression loading

The criterion for matrix failure under transverse compression is based on the concepts proposed by Puck *et al.* [36], [69] and uses the Mohr-Coulomb (M-C) failure hypothesis [76]: The M-C criterion is represented geometrically in Figure 2.13 (a) for a state of pure transverse compression where the fracture plane angle (α_0) is 53°. This is a typical value for glass and carbon FRP composites [30], [36] and an example is shown in Figure 2.13 (b).

Figure 2.13, Matrix failure in transverse compression: (a) Mohr's circle for uniaxial transverse compression [30], (b) specimen failed in uniaxial transverse compression [33], and (c) definition of stress state at the fracture plane [33].

The Coulomb fracture line *AB* in Figure 2.13 (a) is tangent to the Mohr's circle at point *A*; the location of which is defined by the transverse compressive strength (Y_C) and α_0. The M-C hypothesis postulates that fracture occurs for combined stress states, which are described by any

Mohr's circle tangent to the friction line *AB*. Recognising that the fracture plane can be subjected to both transverse and in-plane stresses, two effective shear stresses on the fracture plane can be defined:

$$\tau_{eff}^{T} = \left\langle \left| \tau^{T} \right| + \eta^{T} \sigma_{n} \right\rangle \tag{2.32}$$

$$\tau_{eff}^{L} = \left\langle \left| \tau^{L} \right| + \eta^{L} \sigma_{n} \right\rangle \tag{2.33}$$

where the Macaulay bracket $\langle \bullet \rangle$ returns the argument $\bullet$ if positive or zero otherwise and where η^{T} is the transverse friction coefficient which is defined directly based on the M-C hypothesis as:

$$\eta^{T} = \frac{-1}{\tan 2\alpha_{0}} \tag{2.34}$$

and where η^{L} is the longitudinal friction coefficient which is the slope of the $\sigma_{22} - \tau_{12}$ failure envelope in moderate transverse compression and shear (see *e.g.* Figure 2.8). It can be measured experimentally, or approximated otherwise by:

$$\eta^{L} = \frac{S_{L} \cos 2\alpha_{0}}{Y_{C} \cos^{2} 2\alpha_{0}} \tag{2.35}$$

σ_{n}, τ^{T}, and τ^{L} in Equations (2.32) and (2.33) are the stresses acting on the fracture plane as given in Equation (2.7) and shown in Figure 2.13 (c). Using Equations (2.7), the effective stresses in Equations (2.32) and (2.33) can be expressed as:

$$\tau_{eff}^{T} = \left\langle -\sigma_{22} \cos\alpha (\sin\alpha - \eta^{T} \cos\alpha) \right\rangle \tag{2.36}$$

$$\tau_{eff}^{L} = \left\langle \cos\alpha \left(\left| \tau_{12} \right| + \eta^{L} \sigma_{22} \cos\alpha \right) \right\rangle \tag{2.37}$$

Matrix failure under compression is then assumed to result from a quadratic interaction between the effective shear stresses on the fracture plane as:

$$FI_{M} = \left(\frac{\tau_{eff}^{T}}{S_{T}^{is}} \right)^{2} + \left(\frac{\tau_{eff}^{L}}{S_{L}^{is}} \right)^{2} \leq 1 \tag{2.38}$$

where S_{T} is the transverse shear strength which can be approximated by:

$$S_{T} = Y_{C} \cos\alpha_{0} + (\sin\alpha_{0} + \frac{\cos\alpha_{0}}{\tan 2\alpha_{0}}) \tag{2.39}$$

The fracture angle (α) in Equations (2.36) and (2.37) is not known a priori but will lie between $0°$ (fracture plane angle for a state of pure shear) and α_{0} (fracture plane angle for a state of pure transverse compression). It is determined by maximising FI_{M} in Equation (2.38) in the range $0° < \alpha < \alpha_{0}$. Y_{C} and α_{0} can be obtained using several standard test methods where compressive

stress states are induced into the laminates using shear loading [88], using combined shear and end (edge) loading (Wyoming fixture) [89], or by subjecting a sandwich beam to four-point bending [90]. For the determination of η^L failure stresses under a combined compression-shear stress state are required: The non-standard test methods are based on hoop wound tubular specimens subjected to combined axial compression and torsion [91] or Arcan type test [92], [93].

2.4.3   Fibre compressive failure (kinking or kink band formation)

Compressive fibre failure is the result of the formation of a kink band and the damage inflicted on the supporting matrix. The failure sequence of an embedded UD ply loaded in fibre compression is illustrated in the micrographs shown in Figure 2.14 for a T300/913 carbon/epoxy material system [33]: The kink band initiation is triggered by an initial fibre misalignment, which may be caused by a manufacturing defect, the residual stress mismatch between the fibre and the supporting resin, or simply by the occurrence of sub-critical damage. In Figure 2.14 (a), the failure initiates as a matrix crack in the neighbouring ply in (1). In Figure 2.14 (b) the first fibre-matrix splits in the vertical ply (1) and the first fibre breaks (2) are observed. Upon further loading, more fibres fail (2) and a kink band is observed, which is fully developed in Figure 2.14 (d). The compressive fibre strength of FRP composites is approximately 60% to 70% of the tensile strength [94]. Therefore, it is often the limiting design factor in high-performance composite structures such as in the aerospace industry [67]. For this reason, the fibre kinking mechanism was studied extensively, and fibre kinking models have been proposed, which showed promising results in the prediction of fibre compressive failure.
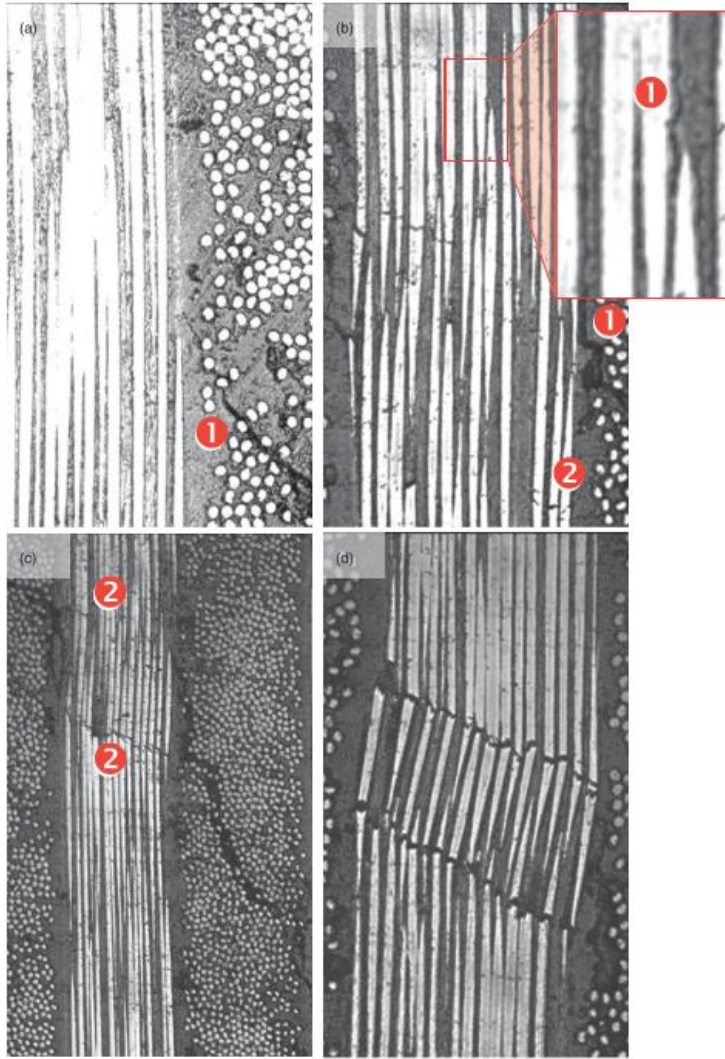
Figure 2.14, Sequence of compressive failure of a laminate loaded in the vertical direction according to [33]: (a) A small misalignment is induced into the vertical fibres by a transverse crack in the neighbouring ply (1), (b) occurrence of first matrix-fibre splits in vertically orientated ply (a) and first fibre breaks (2), (c) further fibre failure (2) with the initiation of a kink band, and (d) fully developed kink band.

The fibre kinking model proposed in the LaRC03 criterion is based on the works of Budiansky and Fleck [67] and Soutis *et al.* [68]. The failure criterion assumes that compressed fibres fail in fibre kinking where failure initiates as damage to the matrix. Thus, the matrix failure criteria in Equations (2.31) and (2.38) are linked to the fibre compressive stress through the introduction of the matrix stresses in the coordinate system associated with the misaligned fibre (or later kinked fibre). An initial idealized fibre misalignment is assumed as shown in Figure 2.15, where φ is the fibre misalignment angle and where the superscript m denotes the ply stresses in the coordinate system associated with the misaligned fibres.
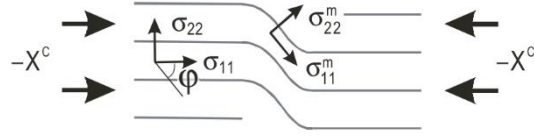
Figure 2.15, Idealized fibre misalignment (kink band) [30].

The stresses in the misaligned fibres are given by:

$$\sigma_{11}^m = \cos^2 \varphi \sigma_{11} + \sin^2 \varphi \sigma_{22} + 2\sin\varphi\cos\varphi |\tau_{12}|$$ (2.40)

$$\sigma_{22}^m = \sin^2 \varphi \sigma_{11} + \cos^2 \varphi \sigma_{22} - 2\sin\varphi\cos\varphi |\tau_{12}|$$ (2.41)

$$\tau_{12}^m = -\sin\varphi\cos\varphi \sigma_{11} + \sin\varphi\cos\varphi \sigma_{22} + (\cos^2\varphi - \sin^2\varphi)|\tau_{12}|$$ (2.42)

A critical fibre misalignment angle (φ^C) is defined as the misalignment angle at which the unidirectional fibre fails in kinking under a state of pure compression, where X_C is the fibre compressive strength. Inserting the pure compressive stress state at failure ($\sigma_{11} = -X_C$ and $\sigma_{22} = \tau_{12} = 0$) into Equations (2.40) to (2.42) and substituting the obtained σ_{22}^m and τ_{12}^m into the matrix failure criterion in Equation (2.38), and assuming that matrix failure in the kink is dominated by the in-plane shear stresses (*i.e.* $\tau_{eff}^T = 0$ and $\alpha = 0°$), the matrix failure criterion becomes:

$$\tau_{eff}^L = X_C (\sin\varphi^C \cos\varphi^C - \eta^L \sin^2 \varphi^C)$$ (2.43)

Assuming that failure occurs if $\tau_{eff}^L = S_L^{is}$ and solving for φ^C yields:

$$\varphi^C = \tan^{-1} \left(\frac{1 - \sqrt{1 - 4(S_L^{is}/X_C + \eta^L)(S_L^{is}/X_C)}}{2(S_L^{is}/X_C + \eta^L)} \right)$$ (2.44)

The misalignment angle φ in Equations (2.40) to (2.42) is obtained based on the applied ply level stress state, the shear stiffness G_{12}, X_C and φ^C as:

$$\varphi = \frac{|\tau_{12}| + (G_{12} - X^C)\varphi^C}{G_{12} + \sigma_{11} - \sigma_{22}}$$ (2.45)

where X_C can be obtained using the standard test methods for compression [88]–[90]. Substituting Equation (2.45) in Equations (2.40) to (2.42), the stresses in the local region of fibre misalignment are obtained which can be used to calculate matrix failure according to Equation (2.38) for compression-shear and Equation (2.31) for tension-shear, respectively. Thus, we obtain the

criterion for failure under longitudinal compression with transverse compression $(\sigma_{22}^m < 0)$ using the stresses in the misaligned coordinate system σ_{22}^m and τ_{12}^m as:

$$FI_F = \left\langle \frac{|\tau_{12}^m| + \eta^L \sigma_{22}^m}{S_{is}^L} \right\rangle \tag{2.46}$$

and for failure under longitudinal compression and transverse tension $(\sigma_{22}^m \geq 0)$ as:

$$FI_F = (1-g)\left(\frac{\sigma_{22}^m}{Y_{is}^T}\right) + g\left(\frac{\sigma_{22}^m}{Y_{is}^T}\right)^2 + \left(\frac{\tau_{12}^m}{S_{is}^L}\right)^2 \tag{2.47}$$

2.4.4   Intra-laminar failure and damage propagation

The failure models discussed in Sections 2.4.1 to 2.4.3 predict the initiation of failure. In a UD laminate, this also corresponds with ultimate failure and once failure is initiated, the laminate can no longer sustain higher stresses. However, in a multidirectional laminate an initial failure event (*e.g.* micro-cracking, fibre kinking, fibre breaks, *etc.*) in one of the plies does not necessarily lead to the total collapse of the laminate. Instead the stiffness of the failed ply degrades due to accumulation of damage which leads to stress redistribution to the neighbouring plies, enabling the laminate to continue carrying higher stresses before ultimate failure occurs [95]. Therefore, to predict damage evolution and ultimate strength of multidirectional laminates, failure criteria are insufficient and modelling frameworks accounting for the progressive nature of the damage are needed.

In the context of continuum mechanics, the initiation and accumulation of intra-laminar damage, as identified using a failure criterion such as the LaRC03 [30], can be represented by a local degradation of stiffness at the failed material points (*i.e.* the integration points in the elements of FE models). Assuming transverse isotropy ($E_3 = E_2$, $G_{13} = G_{12}$, $v_{13} = v_{12}$ $G_{23} = E_2 / (2(1 + v_{23}))$) with respect to the fibre direction (x_1-axis) and a state of plane stress, the typical UD composite lamina stress-strain relationship accounting for damage can therefore be described as:

$$\begin{bmatrix} \epsilon_{11} \\ \epsilon_{22} \\ \gamma_{12} \end{bmatrix} = \begin{bmatrix} \dfrac{1}{(1-d_1)E_1} & -\dfrac{v_{12}}{E_2} & 0 \\ -\dfrac{v_{12}}{E_2} & \dfrac{1}{(1-d_2)E_2} & 0 \\ 0 & 0 & \dfrac{1}{(1-d_6)G_{12}} \end{bmatrix} \begin{bmatrix} \sigma_{11} \\ \sigma_{22} \\ \tau_{12} \end{bmatrix} \tag{2.48}$$

where ϵ_{11}, ϵ_{22} and γ_{12} are the strain components, σ_{11}, σ_{22} and τ_{12} are the stress components, E_1, E_2, G_{12}, and v_{12} are the lamina elastic constants, while d_1, d_2 and d_6 are the scalar damage variables associated with fibre, matrix and shear damage, respectively. In the simplest progressive

failure models [96], [97], d_i are constant values between 0 and 1 which were determined using semi-empirical methods, *i.e.* by tuning the values to experimental results. Such approaches have for example been used to predict the strength of mechanically fastened joints [96], or the open-hole tensile strength [97], [98] in composite laminates. These simple models do not always accurately represent the actual damage process since the degradation methodology is semi-empirical and relies on the tuning of the d_i values rather than being based on measured material properties. Nevertheless, the approach captures the progressive nature of damage in multidirectional laminates and is simple to implement in *e.g.* a FE model. To improve failure prediction, intra-laminar damage evolution in composites has primarily been investigated using the framework of continuum damage mechanics (CDM) [10], [15], [17]–[20], [99]. In these models, the evolution of d_i is typically linked to the fracture toughness values combined with appropriate softening laws associated with the different damage modes. The CDM in [17] is used in Chapter 6 to predict the open-hole specimen strength in specimens subjected to combined tension/compression and shear loading. The resultant uniaxial stress-strain curves based on the CDM proposed in [17] are shown as an example in Figure 2.16. The CDM will be discussed in more details in Chapter 6.
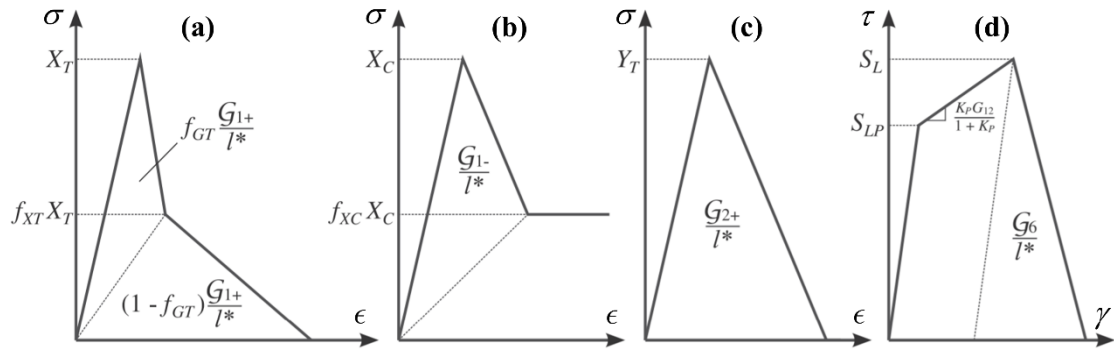
Figure 2.16, The uniaxial stress-strain responses in (a) longitudinal tension, (b) longitudinal compression, (c) transverse tension and compression and (d) in-plane shear [17].

Some of the fracture toughness values used in the CDM (see Figure 2.16) can be determined using standard tests. Note that the symbol $\mathscr{G}_i$ is used for the ply fracture toughness to differentiate it from the interface toughness (G_{Ic}, G_{IIc}). For example, the transverse tensile toughness $\mathscr{G}_{2+}$ in Figure 2.16 (c) is obtained using the DCB test, while the shear toughness $\mathscr{G}_6$ in Figure 2.16 (d) is obtained using the ENF test. The fibre longitudinal tensile ($\mathscr{G}_{1+}$ - see Figure 2.16 (a)) and compressive ($\mathscr{G}_{1-}$ - Figure 2.16 (b)) toughness values have both been measured using non-standardized approaches based on the compact tension (CT) [100] or double edge cracked (DEC) [101], [102] specimen tests. Damage evolution in CDMs is therefore linked to these measurable physical properties of the material, overcoming some of the limitations in the simple progressive damage models. They represent the physics of damage more closely than the models in [96], [97] and are more applicable to general material systems. However, experimental data on the intra-

laminar fracture toughness is rare and no consensus has been reached on standard characterisation methods. Furthermore, the softening laws used in the CDMs are typically controlled by additional shape parameters (f_{XC} , f_{XT} , f_{GT} - Figure 2.16) for which no experimental test methods exist yet and which are often obtained based on analytical or micromechanical models or inverse identification using iterative FE updating [17].

One of the limitations of the CDM approach is its dependence on the mesh: although mesh size dependency has been successfully addressed by Bažant's crack band theory [103], there remains a mesh induced directional bias on crack growth in UD FRP composites. This can be addressed with the use of fibre-aligned meshes which is not easy to achieve in all cases [15], [41]. A further limitation of the CDMs is their reduced capability to accurately describe the interaction effects between different failure mechanisms, *i.e.* between transverse matrix cracking and delamination, because the predicted failure patterns are not physical, *i.e.* matrix cracks are not represented discreetly. Instead, in CDMs the discrete damage is 'smeared' over the size of the element (in the FE modelling framework) [22]. For these reasons, mesh independent crack modelling techniques have recently been proposed, where evolving displacement discontinuities (*e.g.* cracks) in solids are modelled discretely, instead of 'smeared' as in the CDM approach. These discrete damage modelling (DDM) approaches are based on the concept of the eXtended FE method (x-FEM) and its variations [104]–[106]. These approaches do not need a priori knowledge of the location of a crack and they potentially can account for interaction effects between failure modes more accurately than CDMs.

2.5   Inter-laminar failure (delamination)

Due to the relatively weak inter-laminar strength of composites, failure at the interface between the plies (delamination - Figure 2.17) is a common type of damage in multidirectional laminates [107].

Figure 2.17, Example of a uniaxial tensile specimen that failed with excessive delamination [108].

Delamination occurs in situations where the through-thickness stresses are high, for example during an impact or due to high through-thickness stress concentrations at the free edges of a laminate, holes, notches, stiffener terminations, ply-drops, flanges, and joints [108], [109].

Delamination initiation is commonly predicted by a quadratic criterion based on the through-thickness normal (σ_3) and shear (τ_{13}, τ_{23}) stresses as in [110]:

$$\frac{\langle \sigma_3 \rangle}{N} + \frac{\tau_{13} + \tau_{23}}{S^2} = 1 \tag{2.49}$$

where N is the through-thickness normal strength and S is the interlaminar shear strength (ILSS) and where the Macaulay bracket ensures that only positive (or tensile) normal stresses trigger delamination. The inter-laminar normal and shear strengths can be measured using standard test methods: typically the flatwise tensile test [111] is used for determining the through-thickness normal strength, and the short beam shear (SBS) test [112] is used to measure ILSS. Other criteria are based on principal strains [113], or account for the shear strength enhancement (See also Section 2.4.2) when through-the-thickness pressure is applied [36], [69].

The analysis of delamination growth (progressive failure) is usually based on fracture mechanics methods [109]. One of which is the cohesive zone model (CZM), which is essentially a constitutive law for interfaces. The advantage of CZMs over alternative fracture mechanics methods, such as the virtual crack closure technique (VCCT) [114], is their capability to predict both the onset and propagation of delamination without previous knowledge of the crack location or the propagation direction within the cohesive zone. However, when CZMs are used, the potential delamination planes need to be known a priori, *i.e.* cracks will only initiate and grow within the cohesive zone defined during model set-up. In multidirectional composite laminates, the planes of delamination are well defined, *i.e.* CZMs can be placed at the interfaces of plies. Thus, CZMs are a powerful tool for the simulation of delamination in composite structures subjected to general loading configurations [109]. For intra-laminar damage, crack planes are not known a priori, making CZMs less attractive.

In the following, the CZM concept is introduced based on the models proposed by Camanho *et al.* [109] and Turon *et al.* [107]. The described model is native to the commercial FE software ABAQUS [115] and is used in Chapter 6 for the prediction of delamination in open-hole specimens subjected to combined tension/compression and shear. The CZM concept assumes that there is a fracture process zone forming ahead of the delamination crack tip as shown in Figure 2.18 for the example of single mode II, III (Figure 2.18 (a) and I (Figure 2.18 (b)) loading, respectively.

Fracture process zone

Fracture process zone

(a) Mode II and III loading

(b) Mode I loading
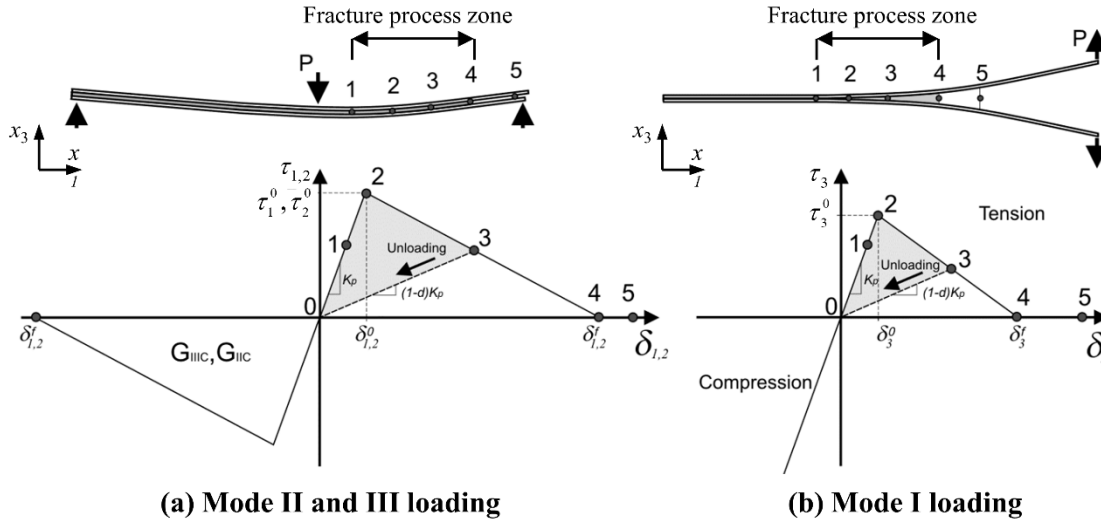
Figure 2.18, Cohesive zone model (CZM) concept: (a) Single mode II and III shear modes in an end notched flexure (ENF) test and associated constitutive law, and (b) single mode I opening mode in a cantilever beam (DCB) test and associated constitutive law [109].

Tractions (τ_i) and separations (δ_i) at the crack tip are introduced, where $i = 1, 2, 3$ denotes the shear, scissoring and normal opening modes. Initially, a high stiffness ('penalty' stiffness K_P) is used to represent the undamaged stiff bonding between the top and bottom faces of the cohesive interface (point $0 - 2$ in Figure 2.18). It is assumed that tractions are proportional to the separations of the faces and that they decrease from the stresses at crack initiation (τ_i^o) to zero within the fracture process zone (1 to 4 in Figure 2.18). Different shapes have been proposed for the softening law after the onset of damage (τ_3^o in Figure 2.18) ranging from simple linear, to bi-linear, to exponential laws [115]. The area under the traction-separation curves are associated with the respective mode I, II and III fracture toughness (G_{IC}, G_{IIC}, G_{IIIC}). Unloading is possible and follows along the line 3-0 in Figure 2.18 (b) with the slope corresponding to the damaged material stiffness $(1-d)K_P$ where d is a scalar damage variable. To account for mixed-mode loading (combination of opening, shear and scissoring modes), which is commonly the case in composite structures subjected to general loading, a mixed-mode traction-separation law must be defined, an illustration of which is shown in Figure 2.19.
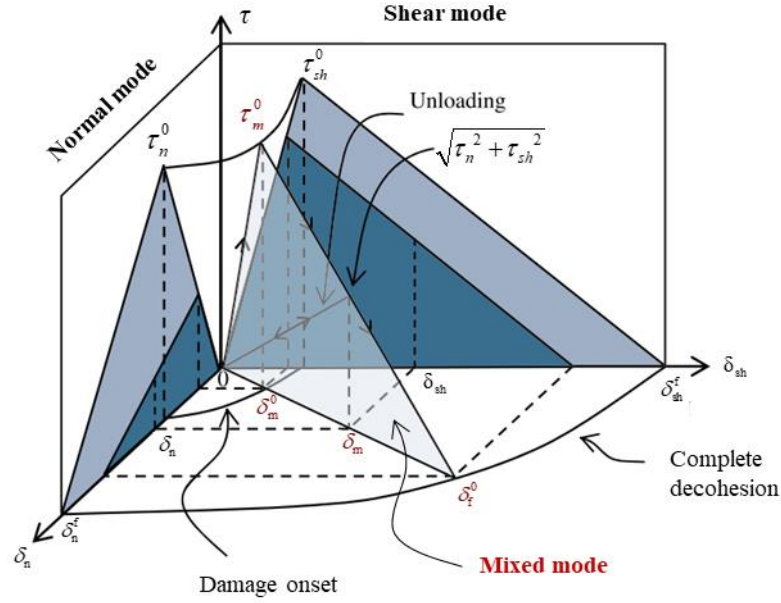
Figure 2.19, Mixed-mode traction-separation relationship and damage law for CZM [9].

The mixed-mode traction-separation law includes a mixed-mode damage onset criterion, which could for example be based on the quadratic interaction proposed in Equation (2.49) [115]. Other proposed delamination onset criteria also use the maximum stress criterion similar to Equation (2.1) or criteria based on the separations instead of the tractions at the interfaces. Upon onset of damage a mixed-mode damage evolution criterion and a fracture criterion which predicts complete decohesion of the interface are needed [115]. The formulations of the model used in Chapter 6 are introduced in the following. The traction-separation relationships are described by:

$$
\begin{aligned}
&\tau_1 = (1-d)K_P\delta_1 \\
&\tau_2 = (1-d)K_P\delta_2 \\
&\tau_3 = \begin{cases} (1-d)K_P\delta_3 & \text{if } \delta_3 > 0 \\ K_P\delta_3 & \text{otherwise} \end{cases}
\end{aligned}
\tag{2.50}
$$

where $d = 0$ when the interface is undamaged and where $d = 1$ at complete decohesion of the interface. Assuming a linear damage evolution law, d can be expressed as:

$$
d = \frac{\delta_m^f(\delta_m^{\max} - \delta_m^0)}{\delta_m^{\max}(\delta_m^f - \delta_m^0)}
\tag{2.51}
$$

where $\delta_m^{\max}$ is the maximum mixed-mode displacement in the loading history, δ_m^0 is the mixed-mode displacement at the onset of damage and δ_m^f is the mixed-mode displacement at complete decohesion of the interface – see Figure 2.19. Damage onset is predicted using a quadratic failure criterion based on the stresses at the interface similar to Equation (2.49):

$$
\left(\frac{\langle\tau_3\rangle}{\tau_3^0}\right)^2 + \left(\frac{\tau_2}{\tau_2^0}\right)^2 + \left(\frac{\tau_1}{\tau_1^0}\right)^2 = 1
\tag{2.52}
$$

The total mixed-mode relative displacement (δ_m) is introduced as:

$$\delta_m = \sqrt{\delta_1^2 + \delta_2^2 + \langle \delta_3 \rangle^2} = \sqrt{\delta_{sh}^2 + \langle \delta_n \rangle^2} \tag{2.53}$$

where δ_{sh} is the norm of the vector defining the combined in-plane shear and scissoring relative displacements between the faces and where τ_3 is from now on labelled as τ_n to differentiate the normal from the shear opening mode. The work-conjugate traction to δ_m is given by:

$$\tau_m = \sqrt{\langle \tau_n \rangle^2 + \tau_{sh}^2} \tag{2.54}$$

Based on the tractions before the onset of softening $\tau_i = K_P \delta_i$ and assuming $\tau_1^0 = \tau_2^0 = \tau_{sh}^0$, the single mode relative displacements at damage onset are:

$$\delta_n^0 = \frac{\tau_n^0}{K_P} \tag{2.55}$$

$$\delta_{sh}^0 = \delta_1^0 = \delta_2^0 = \frac{\tau_{sh}^0}{K_P} \tag{2.56}$$

The mixed-mode relative displacement at the onset of softening (δ_m^0) is then obtained by substituting Equations (2.53) to (2.56) into (2.52) and solving for δ_m^0, which yields:

$$\delta_m^0 = \begin{cases} \delta_n^0 \delta_{sh}^0 \sqrt{\dfrac{1+\beta^2}{(\delta_{sh}^0)^2 + (\beta \delta_n^0)^2}}, & \delta_n > 0 \\ \delta_{sh}^0, & \delta_n \leq 0 \end{cases} \tag{2.57}$$

where β is the mode-mixity ratio δ_{sh} / δ_n. When $\beta = 0$, Equation (2.57) returns $\delta_m^0 = \delta_n^0$ for single mode I loading and when $\beta \to \infty$ Equation (2.57) returns $\delta_n^0 = \delta_{sh}^0$ for single mode II loading. Complete decohesion is predicted by the Benzeggah-Kenane fracture criterion (B-K criterion), which is particularly useful when the fracture toughness values for shear and scissoring deformations are the same, as is usually assumed for delamination [109]:

$$G_C = G_{Ic} + (G_{IIc} - G_{Ic})\left(\frac{G_{II}}{G_I + G_{II}}\right)^{\eta_{B-K}} \tag{2.58}$$

where G_C is the effective fracture toughness under mixed-mode loading, G_I and G_{II} are the energy release rates for mode I and II, and $\eta_{B\text{-}K}$ is the mixed-mode interaction parameter. Based on the effective fracture toughness for mixed-mode loading in Equation (2.58), δ_m^f can be calculated as:

$$\delta_m^f = 2G_C / \tau_m^0 \tag{2.59}$$

where τ_m^0 is the traction at damage onset in mixed-mode loading given by Equation (2.54). Inserting Equations (2.57) and (2.59) into (2.51), the damage variable is now defined.

The model requires the input of the fracture toughness values (G_{IC} and G_{IIC}) which can be measured using the DCB [86] test for mode I and the ENF [87] test for mode II. η_{B-K} is measured using the mixed-mode bending (MMB) test specimen [116]. The standard tests recommend the use of UD laminates for the characterisation of the interface toughness, although the relative fibre orientation at interfaces in multidirectional laminates may influence toughness. Commonly these effects are ignored in the current modelling frameworks, while specialised tests to characterise angle-ply interfaces are being developed [117].

2.6 The open-hole tensile test: a small-scale structural test

The notched or open-hole strength of composite laminates is important to designers, since it can be a limiting factor for the integrity of a structure. Therefore, standard tests exist for the determination of both the open-hole tensile (OHT) [118] and compressive (OHC) [119] strengths. Experimental studies have shown that the laminate lay-up and the size of the hole in the open-hole tension (OHT) test have a significant influence on damage initiation, evolution and the open-hole strength of multidirectional composite laminates [120]. The presence of a stress raiser (notch or hole) causes a wide range of effects not present in unnotched material tests, but common to composite structures. The OHT test is therefore not a true material test but a small scale structural test which is useful to study complex interaction effects in the failure of laminates; the understanding of which is crucial to improve the strength and damage tolerance of composite structures [121], as well as for the development of progressive failure models as discussed in Sections 2.4.4 and 2.5.

Green *et al.* [120] conducted open-hole uniaxial tension tests on a family of quasi-isotropic carbon/epoxy laminates where a different number, n, of UD plies of the same fibre orientation were blocked together, *i.e.* ($[45_n/90_n/-45_n/0_n]_s$), or where sub-laminates were stacked together in a $[45/90/-45/0]_{ns}$ configuration, in which case the UD plies are dispersed through the thickness instead of blocked together. The blocked ply laminate will also be referred to as the 'thick' ply laminate, whereas the dispersed ply laminate will be referred to as the 'thin' ply laminate. Specimens as shown in Figure 2.20 with constant width to hole (w/D) and length to hole ratios (L/D) were tested with hole diameters ranging from 1.6 mm to 50.8 mm.
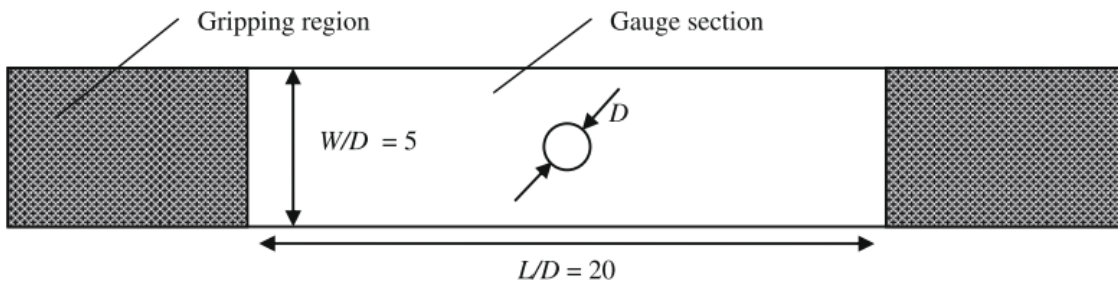
Figure 2.20, Open-hole specimen geometry used in [121].

Figure 2.21 illustrates the three distinctly different failure mechanisms observed across all laminate and hole size configurations. They are the results of a cascade of interacting failure events ranging from sub-critical matrix cracking, to delamination, to fibre failure [9], [108], [120].

| Brittle | Pull-out | Delamination |
| **(a)** | **(b)** | **(c)** |
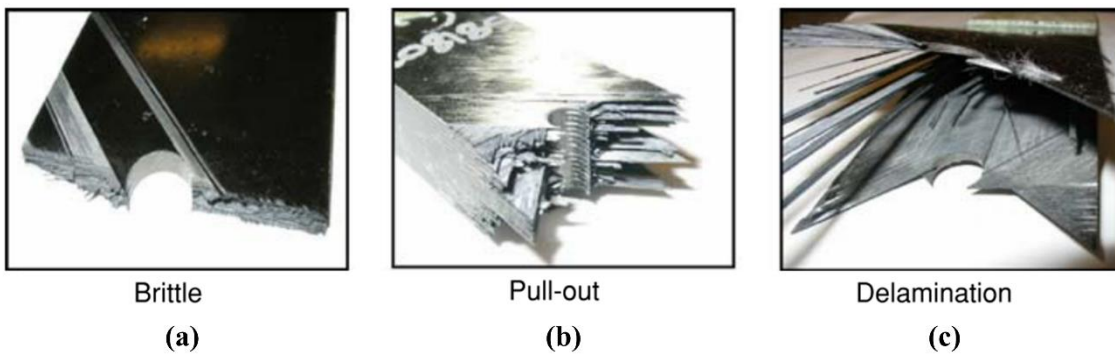
Figure 2.21, Failure mechanisms observed in OHT tests of quasi-isotropic carbon/epoxy laminates: (a) brittle failure for laminates with thin dispersed plies, (b) fibre pull-out failure for intermediate thick dispersed plies, and (c) delamination failure in Laminates with thick blocked plies [121].

The type of failure mechanism is directly related to the measured open-hole strength as a function of laminate lay-up and hole size as shown in Figure 2.22.
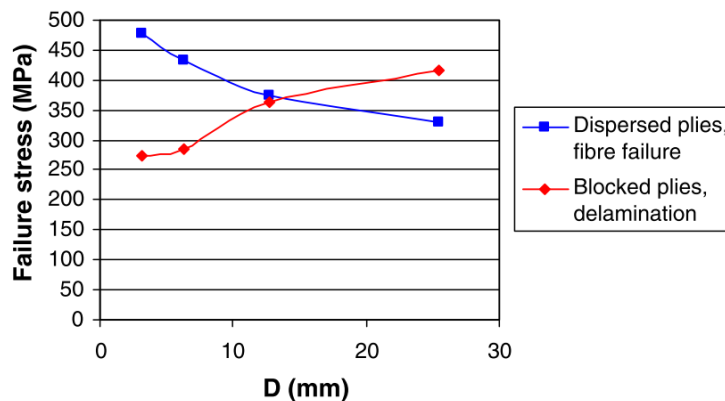
Figure 2.22, Effect of ply thickness and hole size on the OHT strength of 4 mm thick quasi-isotropic carbon/epoxy laminates with W/D = 5 [120].

The OHT strength increases in Figure 2.22 with hole size for blocked plies (thick plies) while it decreases for laminates with dispersed plies (thin plies). In thin ply laminates, the failure mechanism in specimens with small holes is a fibre pull-out type failure (Figure 2.21 (b)) and transitions into brittle failure (Figure 2.21 (a)) when the hole size is increased. Thick ply laminates fail predominantly in a delamination type failure (Figure 2.21 (c)) while for small holes the failure type transitions to a fibre pull-out type failure (Figure 2.21 (b)). Three main mechanisms have been identified that are responsible for the lay-up and the hole size effects observed in Figure 2.21 and in Figure 2.22:

1) Delamination propagates more easily for thick than thin plies, which is due to their higher delamination energy release rate [122]. Furthermore, delamination is often related to sub-critical matrix cracking, which is delayed in thin ply laminates as shown in Section 2.4.2. This implies that thick ply laminates are more prone to delamination failure than thin ply laminates which supports the observations from Figure 2.21.

2) The migration of delamination through-the-thickness of the laminate from one ply interface to another is supressed at the 0° plies. This means that the through-thickness migration of delamination is supressed in thin ply laminates where 0° plies acting as crack arrests are dispersed through-the-thickness [120].

3) Asymmetric fibre splits in the 0° plies to both sides of the hole, as shown in Figure 2.23, occur before ultimate load and lead to a redistribution of the stresses at the hole, which 'blunts' the stress concentration. The blunting effect is more significant in specimens with small holes than in specimens with large holes, where the longitudinal fibre splits in the specimens with the small hole (Figure 2.23 (a)) propagate further into the specimen [9].

(a)   (b)
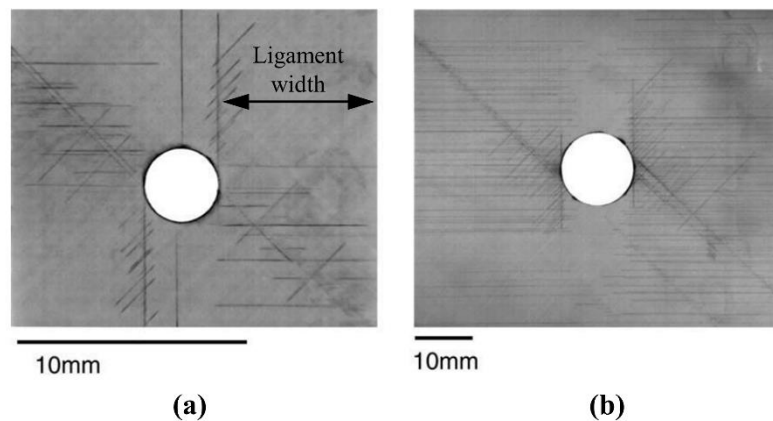
Figure 2.23, x-ray image for 4 mm thick ply-level scaled (thick ply) laminate with (a) 3.175 mm and (b) 12.7 mm holes loaded to 80% of their failure loads [9].

For thin ply specimens, the open-hole strength reduces with increased hole size (see Figure 2.22). This is directly related to the decreased blunting effect of large holes as described under 3) and shown in Figure 2.23. Because delamination in the thin ply laminates is supressed as described in 1) and 2), brittle failure susceptible to the notch blunting effect is governing the open-hole

strength. On the other hand, in thick ply laminates, the trend in Figure 2.22 is the opposite and the open-hole strength increases with hole size. Introducing the ligament width in Figure 2.23 (a) as the width of the undamaged part of the 0° plies after fibre splitting at the hole, Wisnom *et al.* [108] related the open-hole strength in thick ply laminates to the width of the ligament to ply thickness ratio. Specimens fail due to delamination propagating right across the width of the gauge, especially for small hole sizes with narrow ligaments. Therefore, delamination as the dominating failure mechanism gives rise to an increase in strength with hole size when the ratio of *W/D* is kept constant, because it is harder for the delamination to propagate across wider ligaments.

It has been shown that failure mechanisms and the strength in open-hole tests are dependent of the specimen geometry and the laminate lay-up. Thus, the test is rather a small-scale structural test instead of a 'true' material test [123]. Due to the size and lay-up effects observed experimentally, the test is challenging to simulate. Exactly for this reason, the test is an ideal validation case for advanced progressive failure models, *i.e.* 'virtual testing' techniques. Progressive failure in coupon specimens is typically simulated using FE-based models formulated on the meso-scale as shown in Figure 2.24, *i.e.* where the homogenised UD ply is the basic building block [17].
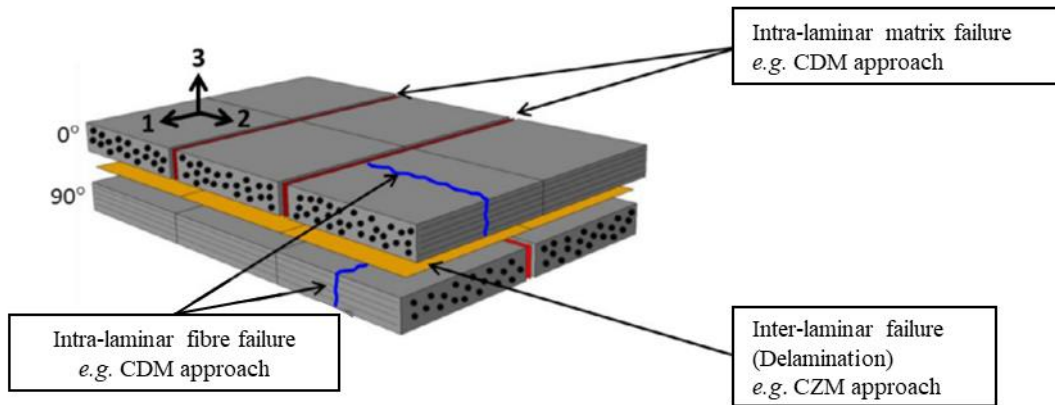
Figure 2.24, Typical meso-scale FE modelling framework to predict progressive damage in multidirectional laminates [23].

Intra-laminar damage is then predicted using intra-laminar failure and damage models similar to the one described in Section 2.4, while delamination is typically modelled using CZMs as introduced in Section 2.5. The discretisation of the laminate at the meso-scale is particularly useful because laminate lay-up effects can be accounted for, while most of the basic ply properties can be obtained with relatively simple mechanical tests [17]. Based on the conducted literature review, current progressive failure models, as shown for example in Figure 2.24, are able to predict the open-hole tensile strength of multidirectional laminates made from typical aerospace grade, autoclave consolidated, well characterised carbon/epoxy prepreg systems within a mean relative error of 10% [8]–[20]. It is observed from the literature, that commonly the same

carbon/epoxy prepreg material systems (*e.g.* IM7/8552, AS4/8552, T800/M21) are used to develop and validate such modelling frameworks. Although the models are physics-based and can be expected to be capable of dealing with a wide range of material systems, their predictive capability for other types of material systems, made from different fibres (*e.g.* glass, aramid, flax, *etc.*), different resins (*e.g.* thermoplastics instead of thermosets) or manufactured differently (*e.g.* using out-of-autoclave prepregs or resin infusion), are not well established.

2.7   Multiaxial testing on the coupon scale

Multiaxial coupon testing has led to a better understanding of stress interaction effects on the nonlinear constitutive response and failure behaviour of composites [124]. Early multiaxial testing was primarily carried out using tubular specimens subjected to combined axial tension/compression, torsion and/or internal/external pressure loading. The primary aim of multiaxial testing performed in [38], [91], [125]–[131] was to obtain failure envelopes that could be used to develop/validate failure criteria for FRP composites. Other studies were more concerned with the effect of combined stress states on the nonlinear constitutive response of FRP composites [37], [132]. Tubular specimens are versatile as it is possible to induce a large variety of relatively well-defined combined stress states (tension-tension, tension-compression, compression-compression, tension-shear, compression-shear, *etc.*) in the walls of the specimen due to the absence of free edges. However, to apply the multiaxial loading, complex and expensive custom-made experimental equipment is required. While tubular specimens are ideally suited to characterise material systems used in cylindrical components, *e.g.* made by filament winding, they are impractical to characterise the mostly flat and laminated composites used for primary structural components in *e.g.* the aerospace sector. The fibre architecture and geometry of filament wound tubes is not representative of flat and discretely layered laminates, *i.e.* their fibre architecture is inherently different, especially in the case of multidirectional laminates as was pointed out in [75]. Furthermore, the tubular specimens require specialised manufacturing procedures outside the production lines of composite manufacturers, which makes tubular specimens in many cases unsuitable for material characterisation.

Overcoming some of the limitations of tubular specimens, biaxial tests on flat and laminated material have been conducted using two-actuator biaxial testing machines. Different stress states have been investigated; Hsu *et al.* [56], [57] studied the nonlinear behaviour of AS4/PEEK subjected to combined transverse compression and shear, while cruciform specimens on two-actuator testing machines have often been used to subject composites to combined tension-tension, tension-compression or compression-compression loading [133]–[136]. The primary aim of the studies in [133]–[136] was to seek a method to measure the biaxial strength of the tested material to validate failure criteria. The need for a well-defined biaxial stress/strain state and the challenge to avoid spurious failure modes (*e.g.* failure at the specimen edges) has led to studies

focusing on shape optimisation of cruciform specimens [137]–[140]. Other studies, using biaxial testing machines, investigated the effect of through-thickness compression on the tensile strength [141] and on the inter-laminar shear strength [142]. Some researchers were less concerned with measuring the 'true' biaxial material strengths, but focused on the characterisation of the damage sequence of the specimen [41], [143], [144], using advanced experimental techniques such as DIC or x-ray CT combined with the multiaxial load frame. Their main aim was to provide validation data for advanced numerical techniques, *i.e.* 'virtual testing' techniques, under general loading conditions. For combined tension-shear and moderate compression-shear testing, several authors have used different variations of the original Arcan fixture [25], [26]. Compared to the tests on tubular specimens or on two-actuator biaxial testing machines, the Arcan fixture is relatively simple and can be easily fit in universal testing machines. Arcan type rigs have often been used to investigate material behaviour in the tension-shear stress space. The test method has been used to measure the shear modulus of AS4/PEEK [145], to obtain the through-thickness tension-shear failure envelope of UD glass/epoxy [146], to obtain the in-plane tension-shear failure envelope of pultruded FRPs [147] and discontinuous FRP composites [148], to investigate mixed-mode fracture toughness [149], [150], and to characterise the biaxial properties of polymer foam core materials [151]. Furthermore, Tan *et al.* [7], [152] used an Arcan rig to investigate lay-up effects on the tension-shear open-hole specimen strength of quasi-isotropic carbon/epoxy laminates. The focus of the test was on the characterisation of the damage sequence, employing x-ray CT and post-mortem de-ply techniques for the visualisation of damage. The data was then used for the validation of a progressive damage model. The combined compression-shear loading regime was not investigated in [7], [152].

In contrast to the combined tension-shear loading regime, the combined compression-shear loading regime has rarely been investigated using an Arcan type fixture, because compressive testing requires the rig to be stabilised against out-of-plane displacements (buckling). Petersen *et al.* [92] suggested to stabilise an Arcan type rig using the pillars of the universal testing machine as the 'anti-buckling guide rails' and measured the friction coefficients in Cuntze's [43] failure mode concept-based failure theory (see Section 2.4.2). The idea is similar to the one adopted for the MAF used in this thesis, where anti-buckling rails are mounted directly on the test rig itself (see Figure 1.2).

2.8   Summary and identified knowledge gaps

The literature review has shown that the nonlinear constitutive response and failure behaviour of FRP composites has been studied extensively over the last five decades and that the underlying physics is qualitatively well understood. However, the current predictive capability of state-of-the-art failure models for many composite material systems under general loading conditions is still relatively poor (*e.g.* in comparison to metals) and moreover not sufficiently well assessed.

Therefore, there is a clear need to validate and improve such models, which also requires the development of suitable test methods to generate the experimental data needed. Thus, the identified need for experimental data for model development and validation is addressed throughout the thesis.

The literature review has further shown that multiaxial testing has been a useful tool to study the nonlinear constitutive response, and stress state dependent failure modes of composite materials. The aim of several authors was to obtain 'true' material failure envelopes and stress-strain curves which should be equivalent/representative to the response of a single material point subjected to the investigated multiaxial stress state. Such data is suited for the calibration/validation of failure theories as discussed in Sections 2.3 and 2.4, or for fitting nonlinear material models as discussed in Section 2.2.3. In this multiaxial testing approach, it is desired that failure occurs in the gauge section under well-defined and uniform stress/strain states which is difficult to achieve. As there is no consensus reached on a preferable multiaxial test method to generate such data, the potential of the MAF will be assessed in Chapter 3 and 4 to calibrate and validate contemporary failure theories and to develop/calibrate a nonlinear constitutive model for UD composites.

The literature review has further shown that lay-up effects on the strength and failure behaviour of multidirectional laminates have commonly been investigated using uniaxial tests, while only few studies have considered the effect of laminate lay-up under multiaxial loading. This even though failure in composite laminates depends both on the laminate lay-up and the stress state. Thus, lay-up effects in laminates subjected to multiaxial loading are not sufficiently well understood and therefore the knowledge gap identified in the literature is addressed in Chapter 5.

Another motivation for multiaxial testing has arisen due to the advent of powerful predictive modelling frameworks, usually based on the FE method, for the 'virtual testing' of composites. The development of such 'virtual testing' techniques is the result of the vastly improved understanding of the physics of failure in FRP, in combination with the availability of increased computing power. It was shown in Section 2.6 that open-hole tests are a preferred validation case for 'virtual testing' techniques. This is because failure behaviour and open-hole specimen strength is influenced by the composite constituents, the laminate lay-up and the size of the specimen. It is therefore a demanding and thus valuable validation test case for 'virtual testing' techniques. State-of-the-art models show promising predictive capabilities (*e.g.* predict OHT strength within 10% of the experimental value [17]) and have the potential to be integrated in the design and certification of high-performance structures as part of the 'pyramid of tests' (see Figure 1.1). While the ability of the state-of-the-art 'virtual testing' techniques to predict lay-up and size effects on well-characterised material systems has been confirmed under uniaxial loading, their ability to predict the open-hole specimen strength in laminates subjected to multiaxial loading has rarely been assessed. This knowledge gap is addressed in Chapter 6 where a meso-scale modelling

framework similar to the one illustrated in Figure 2.24 is used to simulate the multiaxial tests conducted in Chapter 5.

In validation tests for 'virtual testing', the specimen can be regarded as a 'mini' structure and therefore a well-defined uniform stress/strain state within the specimen gauge is not as critical as in a material property characterisation test. Instead it is more important that failure events (often discrete in composites) can be observed and visualised. Multiaxial coupon tests have been identified as a simple means to increase the complexity of a test to further validate predictive tools. Thus, the potential of the multiaxial MAF test to advance the validation of modelling techniques through small-scale multiaxial coupon testing where the specimen is regarded as a mini structure, is explored in Chapter 6.

Chapter 3

Initial MAF testing – concepts, opportunities, and limitations

3.1   Introduction

In this Chapter, the modified Arcan fixture or MAF developed by Taher *et al.* [29] is used for combined tension/compression and shear testing for a range of FRP laminates. The MAF is commissioned on a unidirectional (UD), and two multidirectional [−/+60]$_{3s}$ and [+/−30]$_{3s}$ angle ply laminates made from UD glass fibre-reinforced epoxy plies. The aim of the initial testing program is to identify the opportunities and limitations of the MAF test set-up and to inform the future direction of the research in this thesis.

The chapter starts with a description of the initially proposed MAF test set-up. Inspired by the original Arcan test [25], [26], butterfly shaped specimens are used. A methodology is proposed to derive the apparent nonlinear shear and transverse normal stress-strain curves of the UD composite subjected to combined loading based on 2D digital image correlation (DIC). Furthermore, tension/compression and shear failure envelopes for both the UD and MD laminates were derived. Based on the UD laminate test results, the maximum stress [2], Tsai-Wu's [61]– [63], Puck's IFF [36], [69] and the LaRC03 [30] failure criterion are calibrated and used to predict first-ply failure in the tested multidirectional laminates. Stress/strain states calculated using linear elastic CLT [2] are used to inform the failure criteria, but also to better understand the failure behaviour observed in the multidirectional laminates. Predicted failure envelopes and failure modes for the multidirectional laminates are then compared against the experimental ones. To validate the predicted sub-surface failure modes, selected multidirectional specimens are also x-ray CT scanned post-mortem.

At last, opportunities and limitations of the MAF test-set up for the characterisation of FRP composites are discussed and determine the research carried out in the follow up Chapters of the thesis.

The work presented in this Chapter has contributed to the first journal paper published in Composite Structures (see Chapter 7, Section 7.3).

3.2 Experimental set-up

The front and side view of the modified Arcan fixture (MAF) [29] used in this chapter, is shown in Figure 3.1.
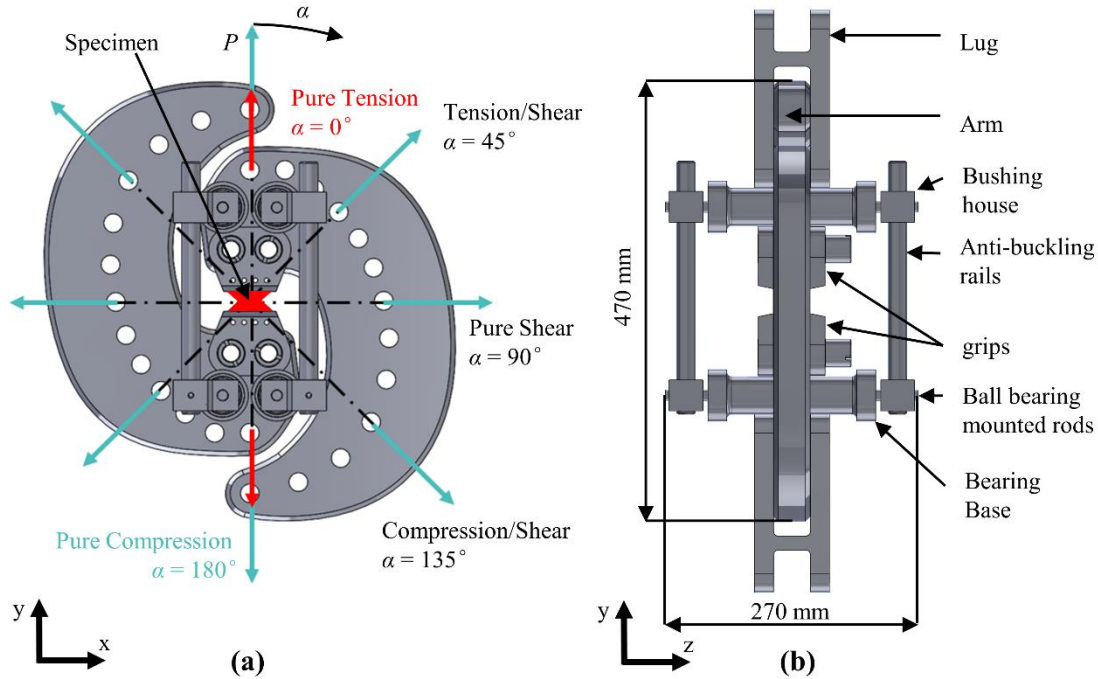
Figure 3.1, The modified Arcan fixture (MAF) designed by Taher et al. [29]: (a) front view, and (b) side view.

Its novel features in comparison to the original Arcan fixture [25], [26] are the anti-buckling rail assemblies and the boomerang shaped loading arms, which ensure that even in compressive test cases the load (*P*) applied to the MAF is always tensile (see Figure 3.1 (a)). Both features prevent out-of-plane displacements of the MAF under compressive loading and thus enable testing not only in the combined tension-shear but also in the combined compression-shear loading regime. The MAF arms are made of 40 mm thick high strength aluminium alloy Alumec 89. The specimen (shown in red in Figure 3.1) is secured to the fixture by mechanical friction grips made from Uddeholm Impax Supreme steel via four M6 bolts tightened to 5 Nm of torque (the recommended maximum value). The bolts providing the mechanical clamping force to grip the specimens go through the tabbed section of the specimen and help with the alignment of the specimen. The grips have knurled surfaces to increase the resultant gripping force. The anti-buckling rails are made from 20 mm diameter steel rods connecting the two loading arms. They are guided by friction bearings sitting in aluminium bushing houses. The bushing houses are attached to rods connecting the buckling rail assemblies on both sides of the MAF (Figure 3.1 (b)). The steel rods are ball bearing mounted within the bearing bases attached to the MAF arms. The design ensures that in-plane (*xy*-plane) displacements are unconstrained while out-of-plane displacements are supressed, so that the specimens can be loaded under an in-plane biaxial stress state according to

the choice of the pin hole pairs defined by the MAF loading angle α as shown in Figure 3.1 (a). The angle α can be adjusted in increments of 15° and controls the induced biaxial load case from pure tension ($\alpha = 0°$), over combined tension-shear ($\alpha = 15°$ - 75°), pure shear ($\alpha = 90°$), combined compression-shear ($\alpha = 115°$ - 165°), to pure compression ($\alpha = 180°$). The MAF is connected via two double-sided fork-lugs to a standard universal testing machine (see Figure 3.1 (b)). The MAF assembly is designed to a safe working load of 100 kN with a factor of safety against yielding of 1.5. For the experiments described in this chapter, butterfly specimens were used as shown in Figure 3.2.
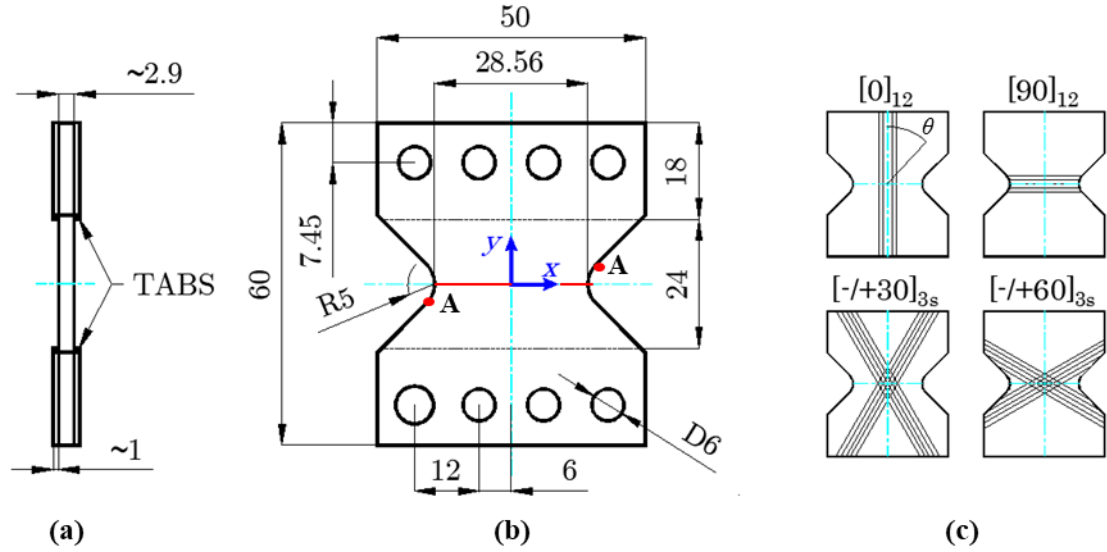
Figure 3.2, Butterfly-shaped specimen: (a) side view, (b) plane view, and (c) laminate lay-ups considered and definition of the fibre orientation angle θ. The representative gauges section is highlighted red. The dimensions are shown in mm.

The design choice of the butterfly-shaped specimen is similar to the specimen proposed by Arcan *et al.* [25], [26] and the specimens used for shear testing in the standardized V-notched rail shear [84], and the V-notched beam (Iosipescu) test methods [85]. The geometry provides a relatively uniform shear stress/strain state within the representative gauge section (red in Figure 3.2 (b)) and promotes failure at the waisted gauge. The gauge has a width (*w*) of 28.56 mm, an average thickness (*t*) of 2.9 mm, a gauge length (*l*$_g$) of 24 mm, whereas the notch radius is 5 mm. Plates were laminated from twelve layers of UD E-glass/epoxy RP-528 UT300 E00 M32 prepregs from PRF Composite Materials [153] according to the lay-ups shown in Figure 3.2 (c). The laminates were cured in the autoclave at 120 °C and a total pressure of 6.2 bar, according to the manufacturer's data sheet [153]. The plates were cut into stripes with the width equal to the total length of the specimen (60 mm), after which 1 mm thick glass/epoxy cross ply tabs were bonded to the stripes (see Figure 3.2 (a)) using thin film epoxy adhesive SA80 from Gurit [154]. The specimens were then waterjet cut from the tabbed stripes according to the drawing in Figure 3.2 (b).

Upon reflection, the described specimen manufacturing process has proven impractical: firstly, when specimens are water jet cut, the cutting material is preferably flat for the best cutting precision and minimal cutting costs, *i.e.* specimen should not be tabbed prior to cutting. Therefore, a manufacturing process where the specimens and tabs are assembled after water jet cutting would be preferred. The use of SA80 thin film has proven impractical as well: not only does the process require a lengthy 12h cure at 80 °C, but the post-cure also requires the tabbed stripes to be stabilised/supported in order to avoid thermally induced deformations. The use of thin film epoxy for specimen tabbing is therefore discouraged for future work, instead adhesive pastes should be considered. An improved alternative tabbing process is proposed in Chapter 5.

The experimental set-up is shown in Figure 3.3 and consists of the MAF installed on an Instron 100 kN 5800 servo-hydraulic test machine and two 2D DIC systems targeted at the front and the back side of the specimen, respectively.
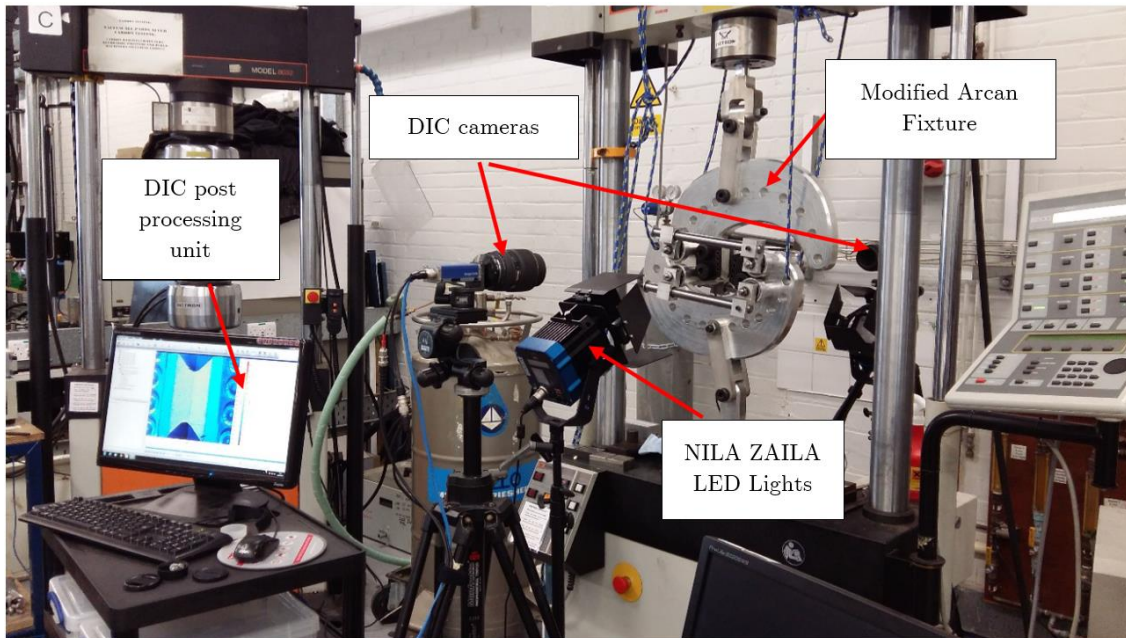
Figure 3.3, Experimental set-up with the MAF installed on the Instron test machine and the DIC equipment prepared (Image courtesy of Dr K.W. Gan).

Two white-light DIC cameras type 5 M Imager E-Lite with a 12 bit dynamic range equipped with C-mounts and Sigma 105 mm lenses were positioned approximately 750 mm away from the front and the back of the specimen. For image correlation, black speckles (approximate size 5 – 15 pixels) were spray painted on a white background. NILA ZAILA led lights were used for illumination. The DIC system specifications and the achieved displacement and strain resolutions are reported in Table 3.1. The displacement fields are exported from the DIC software Davis and are port-processed using a purpose-written python code, where the strains are obtained using the gradient function in Python, NumPy [155] which utilizes central differences in the interior and forward or backward differences at the edges of the data array.

Table 3.1, DIC system specifications for the measurement of the stress-strain curves.

Hardware (2D DIC)	
Camera	Imager E-lite 5M
Sensor and digitisation [pixels]	2448 × 2050, 12 bit
Lens	Sigma 105 mm f/2.8
Imaging distance [mm]	~ 750
Lighting	NILA ZAILA Led lights
Pixel resolution	~ 1 px = 22 μm
Magnification	0.123
Analysis parameters	
DIC Software	La Vision DaVis 8.3.1 [156]
Subset size [pixels] / Step size [pixels]	51 / 25
Interpolator	6th order spline
Spatial pre-filtering of displacements	None
Strain calculation	Using gradient function from Python, NumPy library (central difference scheme) [155]
System performance[2]	
Displacement noise floor [px]	$u \approx 0.004$ / $v \approx 0.006$
Strain noise floor [%]	$\epsilon_{xx} \approx 0.006$ / $\epsilon_{yy} \approx 0.006$ / $\gamma_{xy} \approx 0.011$

Before the start of a test, the MAF was pre-tensioned to approximately 0.2 kN to take up initial slack in the pin fittings. Image acquisition was then triggered at a rate of 2 Hz before the specimen was loaded in displacement control at a rate of 1 mm/min.

---

[2] The system performance (precision) values reported are only indicative. The precision varies from test to test due to DIC system realignment and the quality of the spray painted speckle patterns.

3.3 Derivation of stress-strain curves based on DIC measurement

Apparent normal and shear stress-strain curves were derived for the UD $[90]_{12}$ laminate (see Figure 3.2 (c)) in the full combined tension/compression and shear loading regimes based on the average stresses and strains in the specimen's gauge section (red in Figure 3.2 (b)). The average normal $(\bar{\sigma}_{22})$ and shear $(\bar{\tau}_{21})$ stresses are obtained based on the applied load (P), the loading angle (α), the gauge section width (w) and thickness (t) as:

$$\bar{\sigma}_{22} = \bar{\sigma}_{yy} = \frac{N_y}{wt} = \frac{P}{wt}\cos(\alpha)$$

$$\bar{\tau}_{21} = \bar{\tau}_{yx} = \frac{N_{yx}}{wt} = \frac{P}{wt}\sin(\alpha)$$

(3.1)

where N_y is the normal and the N_{yx} is the shearing component of P. In case of a multidirectional laminate, the stress/strain components derived from the applied loading, are expressed in the global coordinate system designated by the xy- subscripts as shown in Figure 3.4. In the case of a UD [90] laminate, the local material x_1-x_2- coordinate system is equivalent with the global xy- coordinate system and is conveniently used to describe the induced stress state. During testing, the DIC cameras were always aligned with the specimen xy- coordinate system as shown in Figure 3.4. Thus, the DIC cameras had to be realigned and rotated by the loading angle α for each biaxial load case. The realignment procedure improved the spatial resolution of the images of the specimens within the camera field of view.
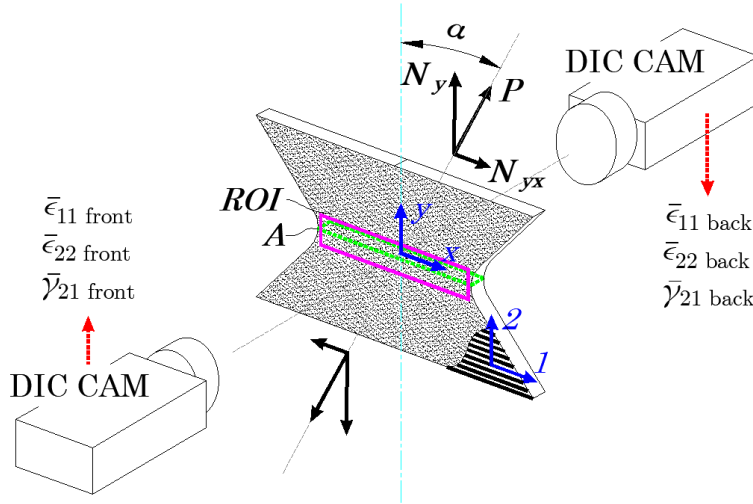
Figure 3.4, DIC system set-up with the DIC cameras aligned with the specimen xy- coordinate system.

Considering now the UD $[90]_{12}$ laminate, typical strain fields obtained on the front side of specimens loaded to approximately 75% of their ultimate failure loads for a transverse tension ($\alpha = 0°$) and a shear ($\alpha = 90°$) load case are shown in Figure 3.5.
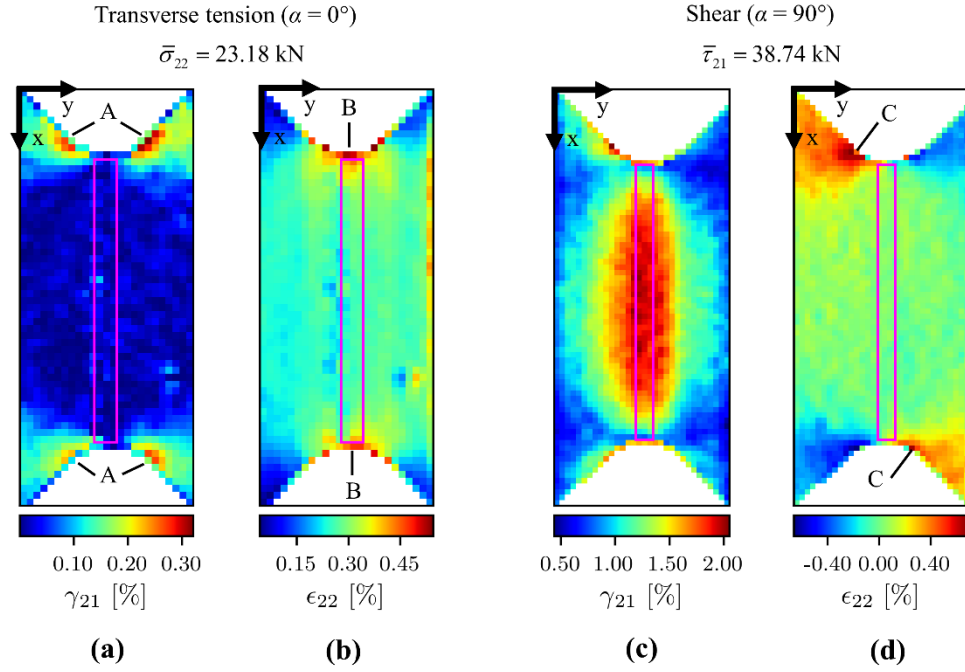
Figure 3.5, Example DIC strain maps with the ROI (purple box) indicated for a UD [90]$_{12}$ specimen subjected to transverse tension (α = 0°) (a) and (b), and shear (α = 90°) (c) and (d).

These two load cases are chosen, because the strain fields in the combined load cases are superpositions of the fields shown, *i.e.* the maps in Figure 3.5 show the relevant features (strain concentrations) observed across all the biaxial tests. It is observed from Figure 3.5 (a), that the shear strain in the gauge section of a specimen loaded in tension is approximately zero and constant across the gauge width, while shear strain concentrations exist to both sides of the notches (A in Figure 3.5 (a)). The normal strains are constant across most part of the gauge section, with high strain gradients in the vicinity of the notches (B in Figure 3.5 (b)). Hence, a complex stress state around the notches exist with high transverse normal and shear strains. When the specimens are loaded in shear (Figure 3.5 (c)), relatively constant shear strains develop in the centre part of the gauge section, while the shear stresses reduce to zero at the notches. Lastly, high tensile and compressive transverse strains develop at the sides of the notches (C in Figure 3.5 (d)).

For the derivation of the apparent stress-strain curves, the average normal $(\bar{\epsilon}_{22})$ and engineering shear $(\bar{\gamma}_{21})$ strains were extracted from the DIC strain fields measured on both sides of the specimen in a narrow strip spanning the whole width of the gauge section, excluding the data points right at the edges of the specimen (purple boxes in Figure 3.4 and Figure 3.5). The edge data was excluded because it is corrupted unless a special numerical treatment is applied [157]. Using the average strain across the whole width of the gauge in combination with the average stresses in Equation (3.1) yields accurate stress/strain relationships as long as the material response is linear elastic, despite the nonuniform strain state in the gauge section as observed in Figure 3.5. After the onset of material nonlinearities, the stress-strain curves derived are only approximations of the 'true' material stress/strain behaviour. The rectangular region of interest

(ROI) in Figure 3.4 and Figure 3.5 was chosen to be 3 DIC steps[3] high and roughly 50 DIC steps wide, depending on the optical magnification of the DIC system which varied slightly from test to test due to system realignments. The number of data points in the y-direction (see Figure 3.5) may have a small effect on the extracted stress-strain curve in the nonlinear region only and was not considered in the current work. The strains extracted from the front ($\overline{\epsilon}_{22}^{front}$, $\overline{\gamma}_{21}^{front}$) and backside ($\overline{\epsilon}_{22}^{back}$, $\overline{\gamma}_{21}^{back}$) of the specimen where then averaged as:

$$\overline{\epsilon}_{22}^{avg} = \frac{1}{2}(\overline{\epsilon}_{22}^{front} + \overline{\epsilon}_{22}^{back}) \tag{3.2}$$

$$\overline{\gamma}_{21}^{avg} = \frac{1}{2}(\overline{\gamma}_{21}^{front} + \overline{\gamma}_{21}^{back}) \tag{3.3}$$

where $\overline{\epsilon}_{22}^{avg}$ and $\overline{\gamma}_{22}^{avg}$ are the average gauge section strains. $\overline{\epsilon}_{22}^{avg}$ and $\overline{\gamma}_{22}^{avg}$ are then combined with the average gauge section stresses in Equations (3.1) to construct the stress-strain curves. Averaging the strains across both sides of the specimen, accounts for rigid out-of-plane body motions of the MAF/specimen assembly which may otherwise induce spurious strains into the 2D DIC strain measurement. The set-up also averages out the effects of possible through-thickness material variability. In comparison to using a stereo DIC system, the two camera 2D DIC system has the advantage of the higher spatial resolution (decreased in stereo DIC due to the required stereo angle) and that no stereo calibration, which induces additional uncertainty, is required. On the other hand, no out-of-plane displacements maps can be obtained, out-of-plane displacements (*e.g.* out-of-plane bending and through-the-thickness displacement discontinuities) cannot easily be identified, and two independent camera systems on both sides of the experimental set-up are needed, which may not be practical. It should be noted that there were little differences between the strain values obtained from the front and back faces.

3.4 Experimental results

3.4.1 [90]₁₂ UD laminate

Figure 3.6 presents the apparent stress-strain curves derived for the UD [90]₁₂ laminates tested on the MAF. Three specimens per loading angle were tested apart from $\alpha = 30°$, $135°$ and $165°$, where only two data sets were included in the analysis. Each stress-strain curve shown in Figure 3.6 was obtained as a polynomial fit to the three (or two) measured stress-strain curves for each loading angle. The experimental raw data, supporting Figure 3.6, is provided in Appendix A. Averaged stress-strain curves were derived, because they conveniently illustrate the constitutive,

---

[3] In DIC, the subset 'element' for which the correlation algorithm tracks the displacement. The step defines the overlap of the subsets where a step size equal to the subset size would mean no overlap.

stress state dependent response of the UD composite across the full combined tension/compression-shear loading regime. Furthermore, the averaged curves are used in Chapter 4 for the calibration of the plasticity-based nonlinear constitutive model.
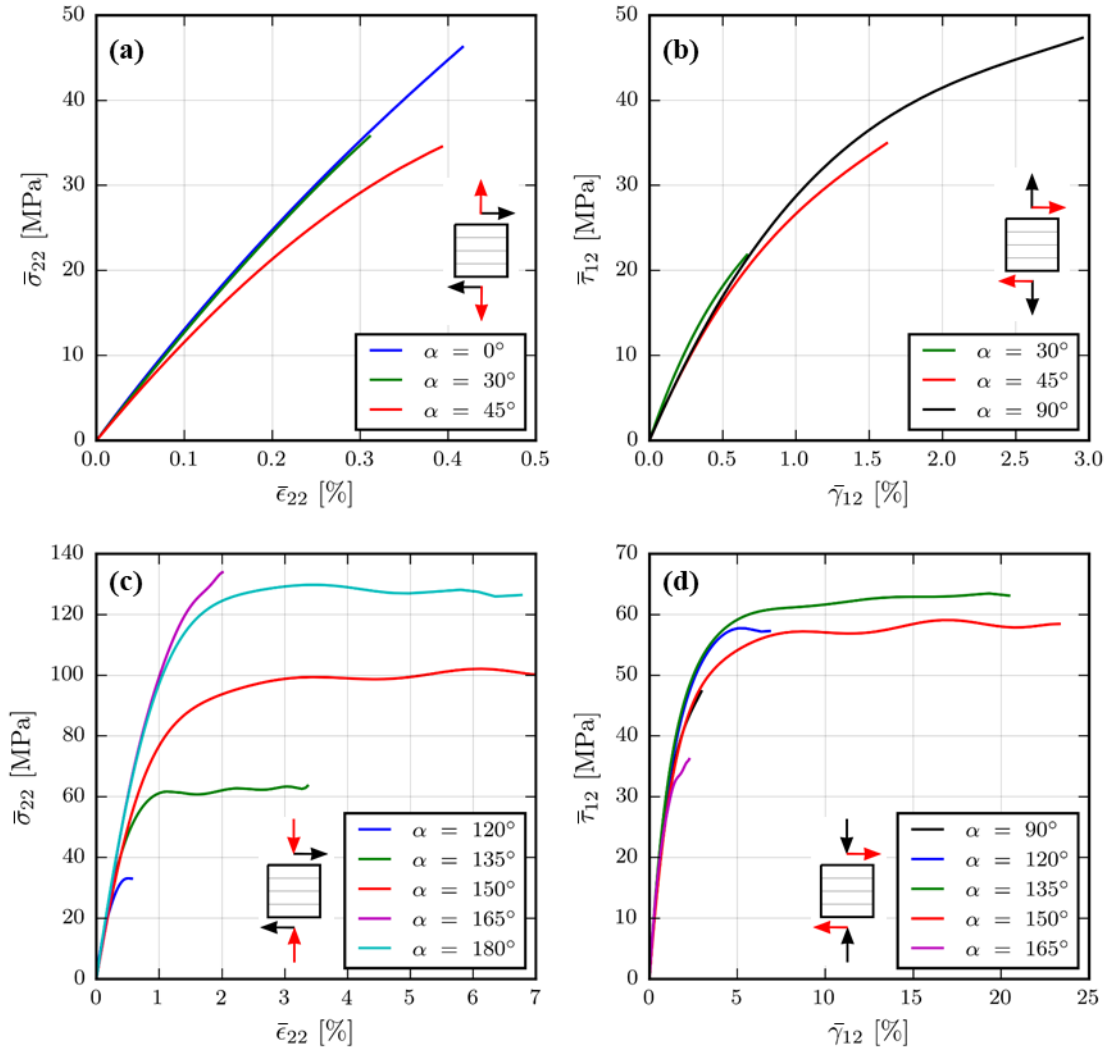
Figure 3.6, Apparent stress-strain curves obtained with the MAF for different biaxial stress states for the [90]₁₂ UD laminate: (a) transvers normal stress-strain curves for the tensile load cases, (b) shear stress-strain curves for the tensile load cases, (c) transvers normal stress-strain curves for the compressive load cases, and (d) shear stress-strain curves for the compressive load cases.

The normal $\bar{\sigma}_{22}/\bar{\epsilon}_{22}$ and shear $\bar{\tau}_{21}/\bar{\gamma}_{21}$ stress-strain curves derived for the tensile load cases ($\alpha = 0°$, $30°$, $45°$) are shown in Figure 3.6 (a) and (b), while the stress-strain curves for the compressive load cases ($\alpha = 120°$, $135°$, $150°$, $165°$, $180°$) are shown in (c) and (d), respectively. The uniaxial shear stress-strain curve ($\alpha = 90°$) is plotted with both the tensile and compressive load cases (Figure 3.6 (b) and (d)) for comparison. It is observed from Figure 3.6 (a) that the response to combined tension-shear is close to linear for the tensile dominated cases $\alpha = 0°$ and $30°$. Generally, it is assumed that the stress-strain relationship remains unchanged regardless of the combined state of stress (here different combined σ_{22}/τ_{21} stress states). However,

counterintuitively, for $\alpha = 45°$, the apparent normal stress-strain curve deviates from the curves obtained in the $\alpha = 0°$ and $30°$ load cases. This deviation is also observed in similar experimental data obtained using hoop wound tubular specimens (see Figure 2.4). Puck *et al.* [36] argued that the $\bar{\sigma}_{22}/\bar{\epsilon}_{22}$ curve is affected by the higher proportion of shear stress applied which induces damage into the matrix which softens not only the shear but also the transverse normal stress-strain curves. The shear stress-strain curves for the tensile load cases are shown in Figure 3.6 (b) and are distinctly nonlinear which is in agreement with similar experimental data in the literature (see Figure 2.4). From the stress-strain curves obtained in the compressive load cases in Figure 3.6 (c) and (d), it is observed that very large strains develop (up to 7% normal strain and up to 25% engineering shear strains) before catastrophic failure of the specimen. The apparent stress-strain curves within the plateau regions should be interpreted as the response of the specimen and the MAF rig together, rather than the response of a 'true' material point, because rigid body rotations are large and discrete cracks occurred at this point. Note that some of the apparent oscillations in the plateau regions are due to the curve fitting approach and occur due to different failure strains of the individual specimens. Furthermore, it is observed from Figure 3.6 (d) that the maximum sustained shear stresses increase firstly with superimposed compression (compare $\alpha = 90°$, $120°$, $135°$) before they reduce when compression becomes the dominant load component ($\alpha = 150°$, $165°$). This shear strength enhancement at moderate compression is due to the pressure sensitivity of the UD composite, which is accounted for in Puck's IFF theory [36], [69], or in the LaRC03 failure criterion [30] (see Chapter 2, Section 2.4.2). All $[90]_{12}$ specimens failed by matrix failure around the waist with a flat fracture plane parallel to the fibre direction as shown in Figure 3.7.
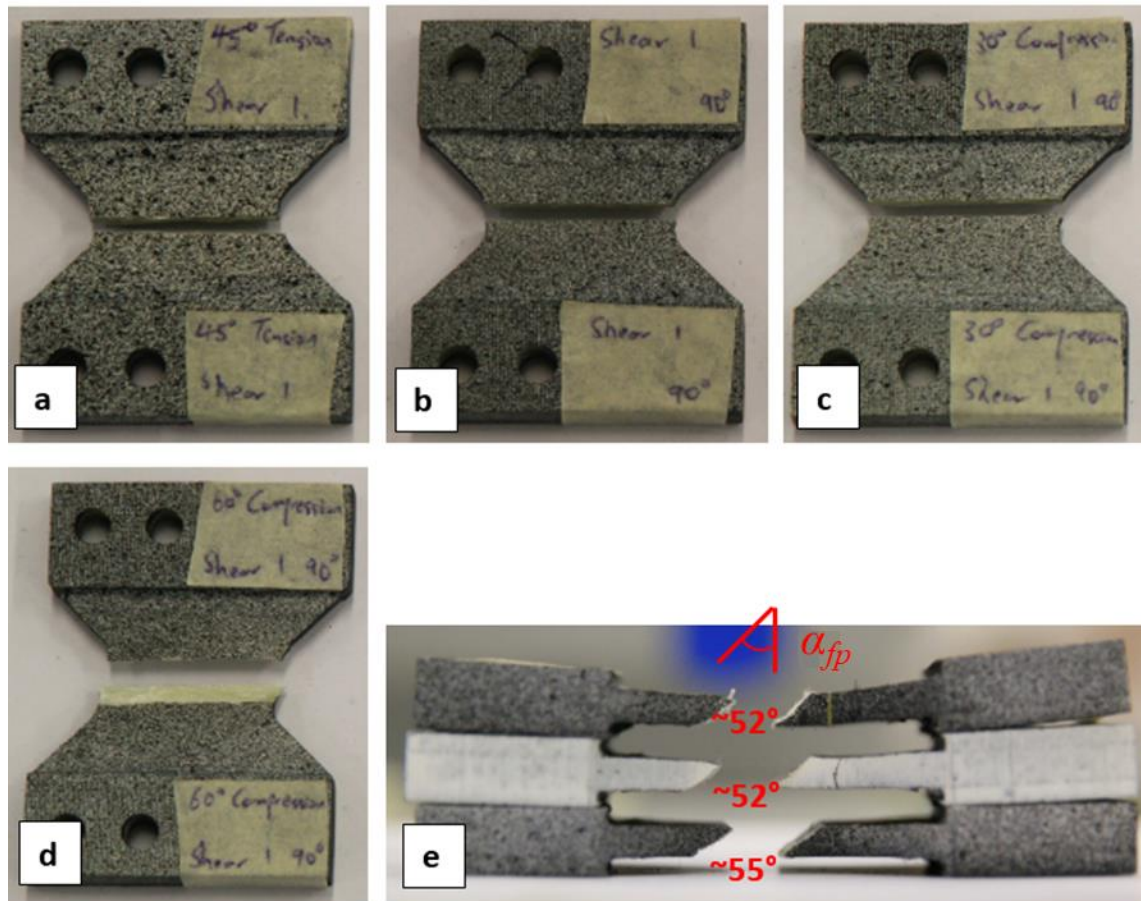
Figure 3.7, Failure of the [90]₁₂ specimens under (a) combined tension-shear (α = 45°), (b) pure shear (α = 90°), (c) combined compression-shear (α = 120°), and (d) combined compression-shear (α = 150°) loading configurations. (e) The fracture plane of the specimen in (d) generally inclines at an angle about 53° (Photo courtesy of Dr K.W. Gan).

The specimens loaded in tension-shear (α = 0° - 45°), pure shear (α = 90°) and moderate compression-shear (α = 120° and 135°) failed with a fracture plane perpendicular to the laminate mid-plane. The fracture plane was between 29 and 30 mm wide and was vertically located where the notch radius transitions into a straight line (see point A in Figure 3.2). This indicates that the position of the fracture plane is dictated by the tensile ϵ_{22} stress/strain concentration in the vicinity of the notch (see Figure 3.5 (d)). Under compression dominated loading (α = 150° - 180°) the fracture plane was inclined at an oblique fracture plane angle (α) as shown in Figure 3.7 (e), which is in agreement with observations made by Puck *et al.* [36], [69] (see Figure 2.8). The measured ultimate failure loads (P_ult), failure stresses calculated using Equations (3.1), and the observed fracture plane angles are reported in Table 3.2.

Table 3.2, The average load at failure and the corresponding average gauge section normal and shear stresses in the [90]$_{12}$ unidirectional laminates for the tested biaxial load cases (α = 0°, 30°, 45°, 90°, 120°, 135°, 150°, 165°, 180°).

(α) Load case	P_{ult} [kN] (c.v.)	$\bar{\sigma}_{22}$ at failure [MPa]	$\bar{\tau}_{21}$ at failure [MPa]	α [deg]
(0°) Pure tension	3.77 (8.21%)	46.98	0	0°
(30°) Tension-shear	3.40 (10.12%)	36.48	21.06	0°
(45°) Tension-shear	3.58 (11.27%)	29.97	29.97	0°
(90°) Pure shear	3.90 (4.50%)	0	46.76	0°
(120°) Compression-shear	5.47 (0.38%)	-31.73	55.00	0°
(135°) Compression-shear	7.41 (0.80%)	-62.56	62.56	3°
(150°) Compression-shear	9.22 (4.05%)	-96.32	55.61	53°
(165°) Compression-shear	11.52 (3.44%)	-135.36	36.27	54°
(180°) Pure compression	10.74 (3.03%)	-134.47	0	59°

3.4.2   [−/+60]₃ₛ angle ply laminate

Photographs of the failed [−/+60]₃ₛ specimens are shown in Figure 3.8 where the painted speckle patterns were removed using acetone to inspect the damage pattern of the specimen's surface.
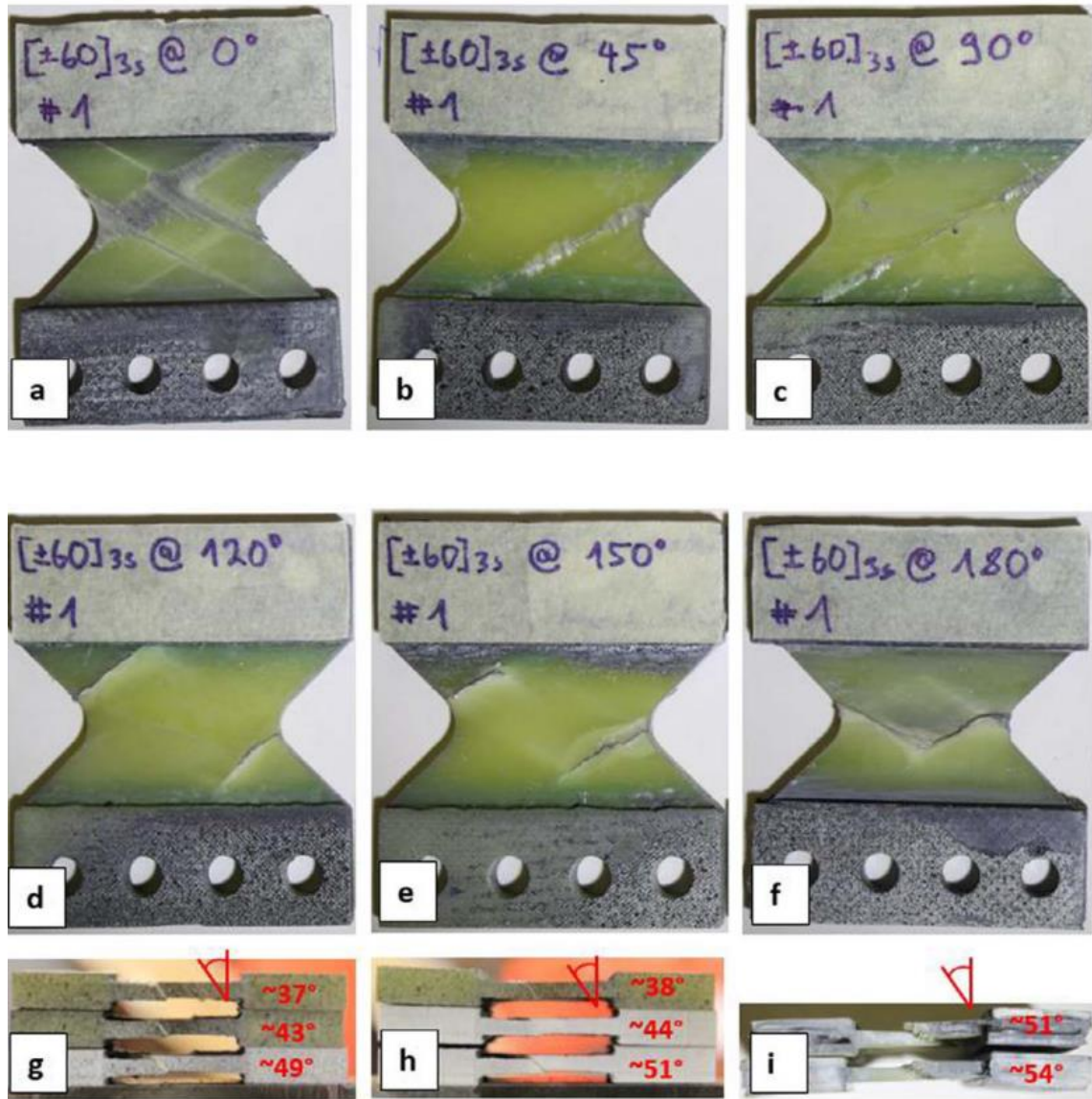
Figure 3.8, Failure of the [−/+60]₃ₛ specimens under (a) pure tension (α = 0°), (b) combined tension-shear (α = 45°), (c) pure shear (α = 90°), (d) combined compression-shear (α = 120°), (e) combined compression-shear (α = 150°), (f) pure compression (α = 180°) loading configurations. Photographs (g) to (i) show the side-views of the specimens in (d) to (f) with an inclined fracture plane at an angle between 37° and 54°.

From Figure 3.8 it is observed that failure for all specimens initiated in the waisted gauge region, but no well-defined fracture plane was formed as was the case for the [90]₁₂ specimens (see Figure 3.7). Instead, the macroscopic (laminate level) fracture planes follow the morphology of the material, *i.e.* the macroscopic cracks initiate in the vicinity of the notches and follow the −/+ 60° orientated fibres into the tab regions.

In tension (Figure 3.8 (a)), macroscopic cracks initiate at the notch and run symmetrically up- and downwards along the +60° and –60° fibre directions into the tabs. Plies aligned with the macroscopic crack direction show a distinct matrix crack, whereas the plies intercepting the macroscopic crack are rotated in the area of the crack. Very large fibre rotations are observed in the −60° surface plies at one of the macroscopic cracks. CLT predicts high transverse tensile stresses in both plies, which are likely the critical stresses leading to the transverse matrix cracks observed in both plies, which then determine the locations and orientations of the macroscopic cracks.

In combined tension-shear (Figure 3.8 (b)), only a single macroscopic crack appears which initiates at the right edge of the specimen where the notch radius meets the straight-line edge, following the +60° direction into the tabs. To investigate the sub-surface damage mechanisms, a selected specimen was x-ray CT scanned in the μ-VIS X-Ray Imaging Centre at the University of Southampton. A Nikkon/Xtek 160 kVp benchtop scanner was used with a spot size of 3 µm and a flat panel detector of 1248 × 1248 pixels. The CT images were reconstructed using the open image processing software ImageJ [158] as shown in Figure 3.9.
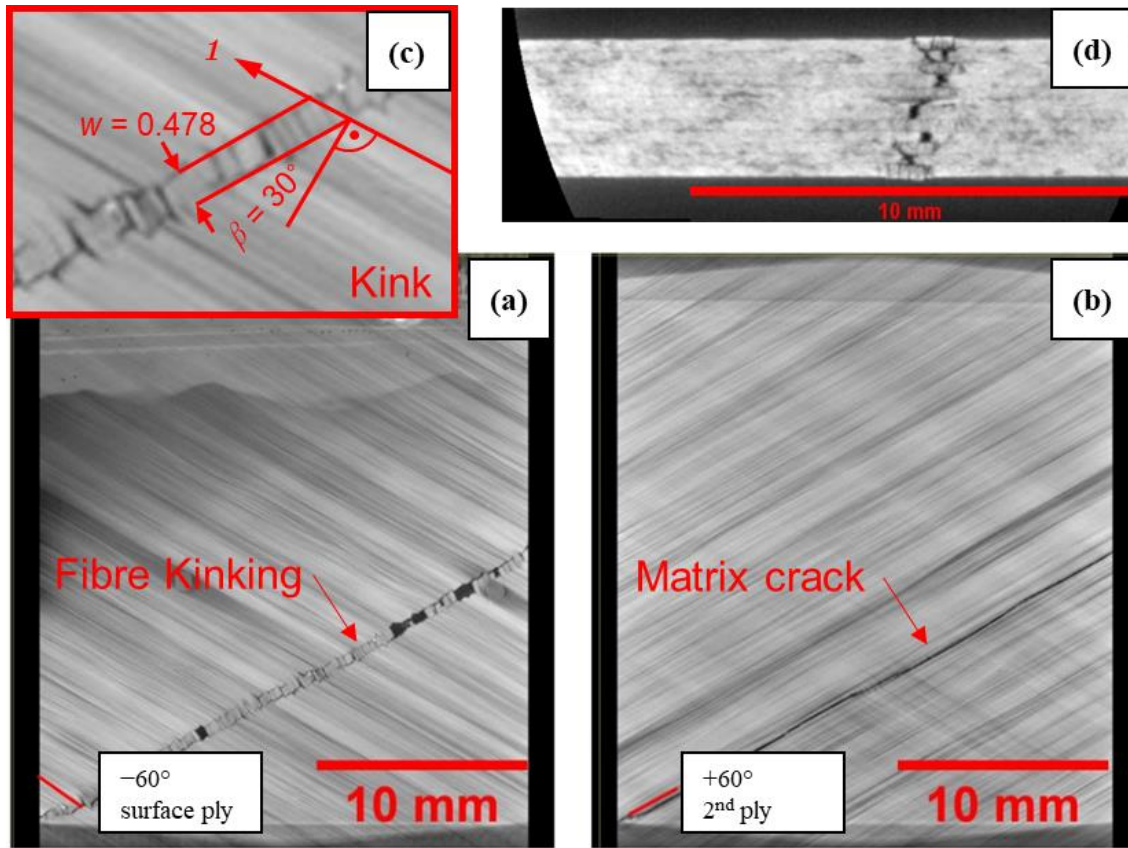
Figure 3.9, Failure modes of the [−/+60]$_{3s}$ specimen under combined tension-shear (α = 45°) loading: (a) fibre kinking in −60 ply, (b) matrix crack in +60 ply, (c) kink ban geometry, and (d) through-thickness view. Resolution: 1 px = 0.0257 mm.

Firstly, it is observed from Figure 3.9 that the failure modes within the macroscopic crack are the same in plies with the same fibre orientation, *i.e.* all −60° plies failed in fibre kinking (Figure 3.9 (a)) while all +60° plies showed a distinct matrix crack (Figure 3.9 (b)). The formation of the kink band in the −60° plies is a result of the compressive fibre stresses, as also predicted by CLT, induced by the shear load component applied to the laminate. The kink geometry is shown in detail in Figure 3.9 (c); the formed kink band has a width (*w*) of 0.478 mm and its inclination angle relative to the direction perpendicular to the fibres (*β*) is approximately 30°. This indicates that the kink band propagates along the direction of the fibres in the neighbouring plies within the multidirectional laminate.

In shear (Figure 3.8 (c)), the failure pattern looks similar to the combined tension-shear case. However, the macroscopic fracture zone does not initiate at the transition from the notch to the straight edge, but instead within the straight-line edge itself. To investigate the sub-surface failure modes, a selected specimen was x-ray CT scanned as well as shown in Figure 3.10.
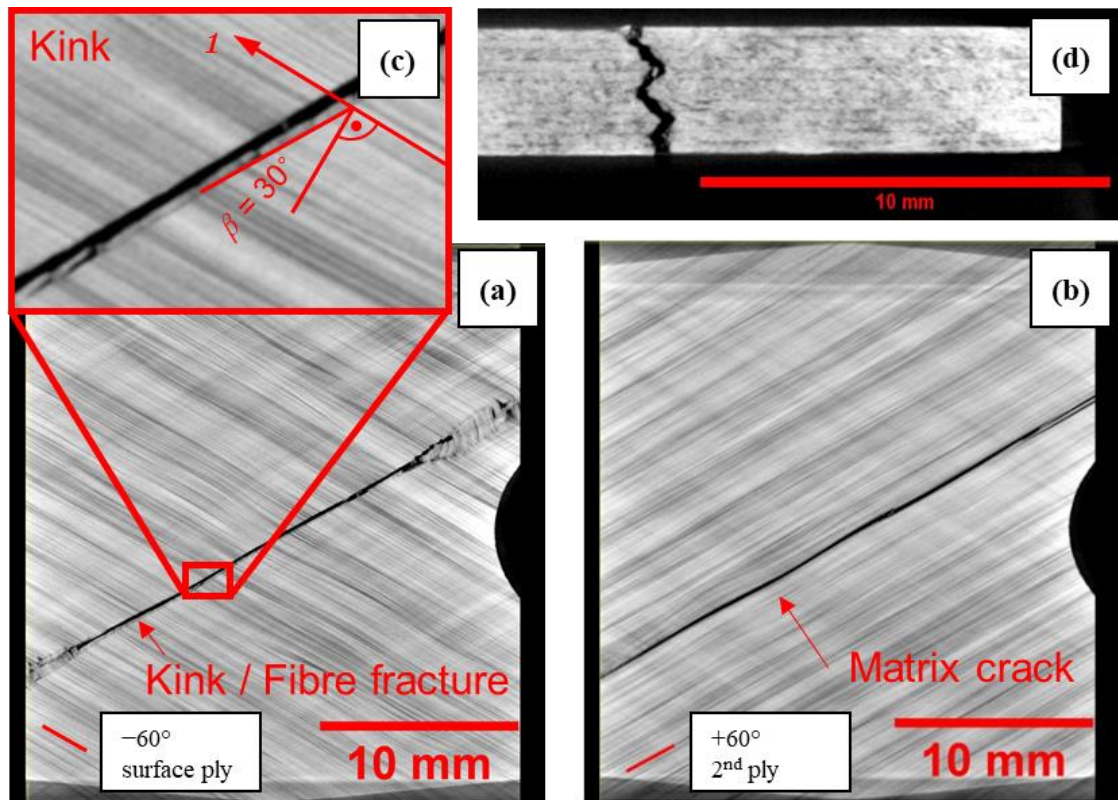
Figure 3.10, Failure modes of the [−/+60]$_{3s}$ specimen under pure shear (α = 90°) loading: (a) fibre kinking in the −60° ply, (b) matrix crack in +60° ply, (c) kink details, and (d) through-thickness view. Resolution: 1px = 0.0257 mm.

It is again observed from Figure 3.10 that the failure modes in plies with the same fibre orientation exhibit the same failure modes through-the-thickness of the laminate within the fractured zone: distinct matrix cracks are seen in all the +60° plies (Figure 3.10 (b)) whereas again fibre kinking is evident throughout the −60° plies (Figure 3.10 (a)) which is caused by the high compressive

stresses induced by the shear component of the load applied. The compressive fibre stresses in the −60° plies are also predicted by CLT. Interestingly, the kink band inclination angle β in Figure 3.10 (c) is identical with the one observed in the tension-shear case shown in Figure 3.9 (c), supporting the idea that the kink band aligns with the fibres of the neighbouring plies, regardless of the applied load case. If this still holds true when the load cases are significantly different, remains to be investigated.

In the combined compression-shear load cases (Figure 3.8 (d) and (e)) the macroscopic failure patterns are distinctly different from the tension-shear and shear cases: fracture zones initiate at the notch and run only along the +60° plies into the tab areas. From visual inspection it is seen that the −60° surface plies have failed with a relatively clean fracture without a visible kink band. Furthermore, distinctly white regions (see Figure 3.8 (d)) indicate that some of the interfaces have delaminated. CLT predicts high compressive stresses in the −60° plies, which are likely driving the failure. It is further observed from Figure 3.8 (g) and (h), that the macroscopic fracture planes are oriented at oblique through-the-thickness angles of 37° to 51°.

In uniaxial compression (Figure 3.8 (f)), macroscopic fracture lines initiate at the notches and run along both plies into the top and bottom tabs. The fracture zones show distinct matrix cracks in both plies. Furthermore, zones of fibre fracture in the +60° plies are oriented at −60° relative to the vertical y-axis and vice versa. CLT predicts high transverse compressive stresses in both plies which are likely governing the failure behaviour of the laminate, *i.e.* causing matrix cracks under transverse compression.

Across all investigated load cases, it is observed that the fracture planes were not aligned with the designed minimum gauge section and that the failure behaviour is affected by the geometry of the specimen and the morphology of the laminate. This highlights the difficulty in designing a suitable test specimen for the characterisation of multidirectional laminates. As the fracture plane is not aligned with the minimum gauge section, it is difficult to determine a 'true' limiting stress state. However, for this initial study the average normal $(\overline{\sigma}_{yy})$ and shear $(\overline{\tau}_{yx})$ stresses acting on the waisted gauge section were nevertheless calculated based on the maximum failure load (P_{ult}) and Equations (3.1) as reported in Table 3.3.

Table 3.3, The ultimate failure loads, the average normal and shear stresses at the gauge section and the observed fracture plane angles for different load configurations of the [−/+60]$_{3s}$ laminate.

(α) Load case	P_{ult} [kN] (c.v.)	$\bar{\sigma}_{yy}$ [MPa]	$\bar{\tau}_{yx}$ [MPa]	α [deg]
(0°) Pure tension*	8.17 (1.59%)	112.67	0	0
(45°) Tension-shear	8.32 (3.48%)	71.03	71.03	0
(90°) Pure shear	13.15 (0.87%)	0	158.71	0
(120°) Compression-shear	17.06 (1.68%)	-102.99	178.38	43.0
(150°) Compression-shear	15.01 (7.13%)	-156.95	90.61	44.3
(180°) Pure compression*	13.33 (1.09%)	-183.79	0	52.5

* The width of the second-batch specimen's waist is 25mm (instead of 28.56 mm).

3.4.3   [+30/−30]$_{3s}$ angle ply laminate

The response of the [+/−30]$_{3s}$ specimens is fibre dominated and hence the loads to fail the gauge section are significantly higher than for the [90]$_{12}$ and the [−/+60]$_{3s}$ laminates where ultimate failure modes are to a large extent governed by the matrix properties. For loading angles $\alpha = 45°$, 90° and 120°, shear-out and bearing failure initiated prematurely at the pin holes of the specimens well before failure at the gauge section due to the high stiffness and strength of the laminate. This indicates that specimen slippage in the grips has occurred, due to an insufficient friction force generated by the specimen clamping/gripping mechanism. The tests were stopped when pin hole failure occurred as it was not possible to load the specimen any further, so these load cases are not discussed here. However, three specimens were successfully tested for the combined compression-shear ($\alpha = 150°$) load case. Ultimate failure occurred at a load of 23.67 kN (+/−3.45%). The specimen showed a complex fracture pattern (Figure 3.13 (a)) with four parallel macroscopic cracks running along the −30° ply direction (denoted C1) and one crack running along the +30° direction (denoted C2). From the sequence of DIC strain images in Figure 3.12, it is shown that the C1 cracks are clearly associated with the initial failure event and that the C2 crack is catastrophic and associated with the ultimate failure of the specimen.
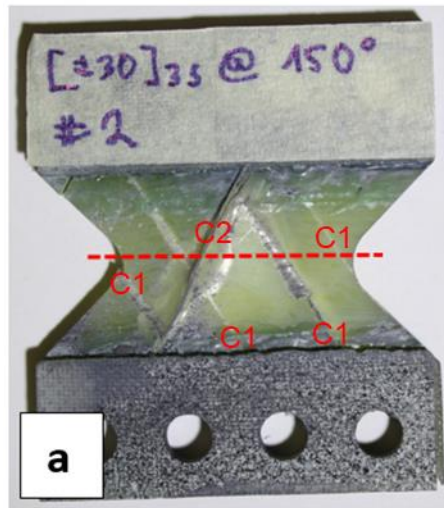
Figure 3.11, Failed [+/−30]₃ₛ specimen in combined compression-shear (α = 150°).
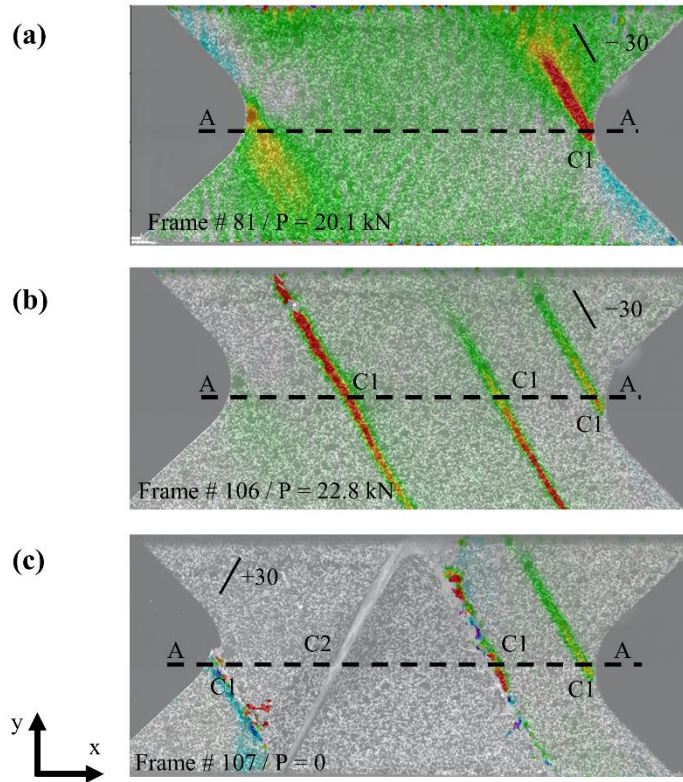
Figure 3.12, DIC strain maps illustrating the sequence of failure: (a) initial macroscopic cracks (C1) along the −30° direction originating at the notches, (b) more macroscopic C1 cracks along the −30° direction within the gauge section, and (c) ultimate failure associated with the macroscopic crack C2 running along the +30° fibre orientation.

The failure sequence illustrates that failure in the [+/−30]₃ₛ laminate is progressive. Initial failure of the specimen was determined as the occurrence of the first macroscopic cracks in C1 at the notches at $P_{ini} = 18.75$ kN. Due to the complex failure pattern, the specimen was CT scanned: the

scan in Figure 3.13 confirms that the failure modes in the form of C1 cracks are the same in all plies with the same fibre orientation: All +30° plies show fibre kinking/rotation (Figure 3.13 (a)), while the −30° plies exhibit a distinct matrix crack (Figure 3.13 (b)). CLT predicts that both plies are loaded in fibre compression: additionally, the −30° plies are also subjected to relatively high transverse tensile stresses which may be responsible for the clear C1 matrix crack seen in Figure 3.13 (b). The C2 crack in Figure 3.13 (c) shows compressive crushing failure with several different interacting failure events, including matrix cracking, delamination, and fibre breaks. In the C2 crack, no distinct ply-by-ply repetition of failure modes is observed.
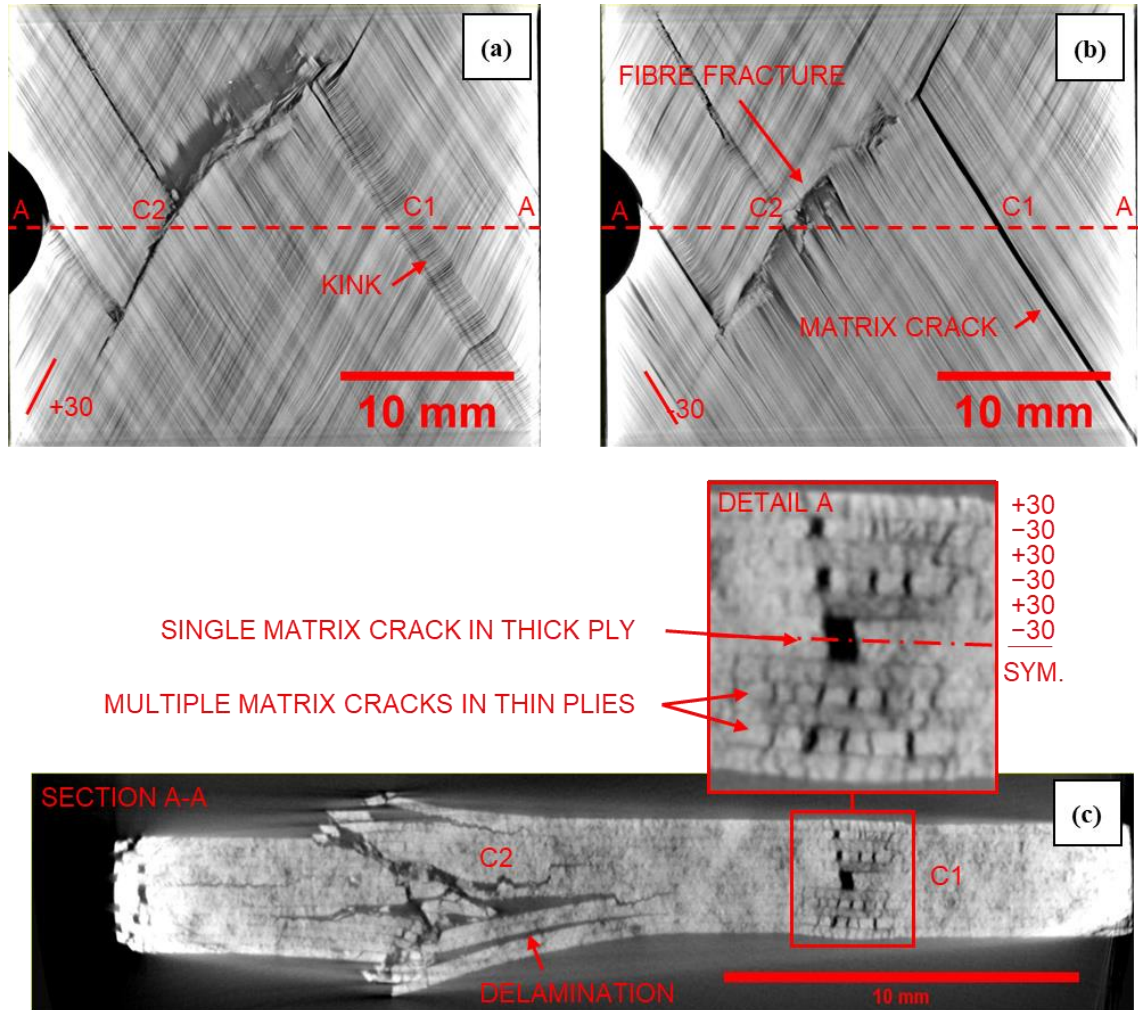
Figure 3.13, CT-scan of [+/−30]₃ₛ specimen loaded in combined compression-shear (α=150°): (a) fibre kinking in +30° ply, (b) matrix crack in −30° ply, and (c) through-thickness view with detail of matrix cracks. Resolution: 1px = 0.0232 mm.

An interesting observation can be made in Figure 3.13 (c): the thick double ply at the centre of the laminate fails with a single distinctive crack whereas all thin single plies fail in multiple smaller cracks. The same can be observed in a similar damage zone just on the left-hand side of Section A-A conforming that this is a repetitive feature. This supports the in-situ strength concept

as introduced in Chapter 2, Section 2.4.2, according to which the fracture behaviour of thin and thick plies is distinctly different.

3.5 Prediction of strength and failure modes

The investigated maximum stress, Tsai-Wu's, Puck's IFF and the LaRC03 criteria are calibrated based on the UD test results and are evaluated based on the CLT ply-by-ply stress/strain predictions. The details of the failure criteria are provided in Chapter 2, Sections 2.3 and 2.4. The maximum stress and the LaRC03 criterion predict fibre and matrix failure modes separately and the failure theories are complete, *i.e.* all failure modes are accounted for within the framework of the theory. Tsai-Wu's theory is also complete, *i.e.* it is expected to predict general failure under any given stress/strain state. In case of Puck's theory, only the inter-fibre failure (IFF) failure functions are implemented in the CLT code, although the theory also includes fibre failure modes. It should be noted that the simple failure analysis conducted in this Chapter aims to assess the capability of the contemporary failure theories to predict initial failure and failure modes but ignores the nonuniformity of the stress/strain fields within the specimen, the nonlinear constitutive behaviour of the UD composite, and the progressive nature of failure of multidirectional laminates.

3.5.1 Calibration of failure criteria

The CLT code is informed by the elastic properties of the UD ply as reported in Table 3.4.

Table 3.4, RP-528 glass/epoxy elastic properties.

Elastic properties		Strain range (%)	
E_1 [GPa] (c.v.)	41.33 (0.99%)	0.1-0.3	ASTM 3039 [74]
v_{12} (c.v.)	0.317 (2.52%)		
E_2 [GPa] (c.v.)	11.51 (1.65%)		
E_{2c} [GPa] (c.v.)	12.38 (1.30%)	0.05-0.5	$[90]_{12}$ MAF test
$G_{12}^{90°}$ [GPa] (c.v.)	3.48 (4.59%)	0.05-0.5	

The fibre longitudinal Young's modulus (E_1) and the Poisson's ratio (v_{12}) were obtained using an uniaxial standard test [74], whereas the transverse tensile (E_2), compressive (E_{2c}) and the shear (G_{12}) moduli were derived from the apparent stress-strain curves obtained using the MAF on $[90]_{12}$ specimens as shown in Figure 3.6. Uniaxial strength properties are further needed to inform the failure criteria. Limit stress states were derived from the MAF tests and from the uniaxial standard tests on $[90]_{12}$ and $[0]_{12}$ laminates as reported in Table 3.5.

Table 3.5, RP-528 glass/epoxy strength properties.

Material Property	Standard Test	MAF Test	% Difference between the test results
X_T [MPa] (c.v.)	996 (4.11%)	-	-
Y_T [MPa] (c.v.)	54.91 (6.63%)*	46.98 (8.21%)	15.5
Y_C [MPa] (c.v.)	122.49 (0.73%)	134.47 (3.03%) *	9.3
$S_L^{90°}$ [MPa] (c.v.)	45.58 (5.80%)	46.76 (4.50%) *	2.55
$S_L^{0°}$ [MPa]	-	70 * [93]	-
X_C [MPa]	790 [153]	-	-
η^L	-	0.304	-

* Used to inform failure criteria

The fibre longitudinal strength (X_T), the transverse tensile (Y_T) and compressive (Y_C) strengths were determined using standard tension [74] and compression [88] tests, respectively. The transverse strengths were also compared against the limit stresses obtained using the MAF test for $\alpha = 0°$ and $\alpha = 180°$, as reported in Table 3.2. The average transverse tensile stress at failure in the MAF test is 15.5% lower than the strength obtained on straight-sided specimens following the standard test in [74]. Failure in transverse tension is brittle and the complex stress state at the notches of the butterfly specimen initiates failure prematurely (Figure 3.5 (a) and (b)), reducing the average gauge section stress at failure. Therefore, Y_T obtained using the standard test is considered a more accurate measurement and will be used for the failure analysis. In transverse compression, the MAF specimen failed with the typical oblique fracture plane as shown in Figure 3.7 (d) and (e), whereas the uniaxial compression specimen failed prematurely in buckling, despite its gauge length being determined according to [88]. Interestingly, the same observation is made in Figure 2.8, where tubular test results are compared to uniaxial standard tests. In the standard test, the gauge section could be reduced further to delay buckling and to promote material failure. However, the butterfly specimen appears to be a good choice for transverse compressive testing. While the 'wings' of the butterfly stabilise the specimen against buckling, failure induced due to the complex stress state around the notches does not lead to premature gauge section failure, as in the tensile load case, because the compressive normal stresses prevent and delay micro-cracking. Therefore, Y_C obtained using the MAF test was used for the further analysis. The average shear stresses at failure were obtained using specimens with the fibres parallel $(S_L^{90°})$ and perpendicular $(S_L^{0°})$ to the gauge section. The specimens with the fibres parallel to the gauge section give lower bound values for the shear strength because they are prone to premature brittle failure due to the transverse tensile stress/strain concentrations at the notches. According to [159],

shear strength is more accurately determined using specimens where the fibres are perpendicular to the gauge section (*i.e.* $[0]_{12}$ laminates), because they are less sensitive to the transverse stress/strain concentrations at the notches. Due to the difficulty in accurately determining the shear strength, failure analyses in the multidirectional specimens were conducted with both a lower bound shear strength $(S_L^{90°})$ and an upper bound shear strength $(S_L^{0°})$. The $S_L^{90°}$ shear strength was also obtained according to the V-notched beam standard (Iosipescu) test [85] and agreed within 2.55% with the MAF test results. Both the LaRC03 and Puck's criterion require the longitudinal friction coefficient (or coefficient of influence) (η^L) to be determined experimentally to account for the shear strength enhancement when transverse pressure is applied. Fitting a straight line to the biaxial failure stresses from Table 3.2 for $\alpha = 90°$ and $120°$, η^L was determined as 0.304. Puck recommends η^L for glass/epoxy is 0.25, which is of the same order of magnitude but slightly smaller [69]. Although the MAF measurements show the shear enhancement with transverse pressure, specimen failure is influenced by the transverse tensile stresses developed at the notches. The shape of the failure envelope is affected and therefore also the derivation of η^L. While specimens in shear fail prematurely due to the transverse stress/strain concentrations developed at the notches (see Figure 3.5 (d)), the compressive stresses induced in the combined compression-shear ($\alpha = 120°$) case are delaying premature failure. Because failure is premature in shear, η^L determined using the MAF and the butterfly specimens used can be considered an upper bound value. However, given the lack of other suitable tests, $\eta^L = 0.304$ was used for the following failure analysis. The fibre compressive stress (X_T) was taken from the material data sheet [153]. The calibrated maximum stress, Tsai-Wu's, Puck's and LaRC03 failure criterion, using both the lower and upper bound shear strengths, are plotted against the biaxial and uniaxial experimental results in Figure 3.14 for the $\sigma_{22} - \tau_{21}$ stress space.
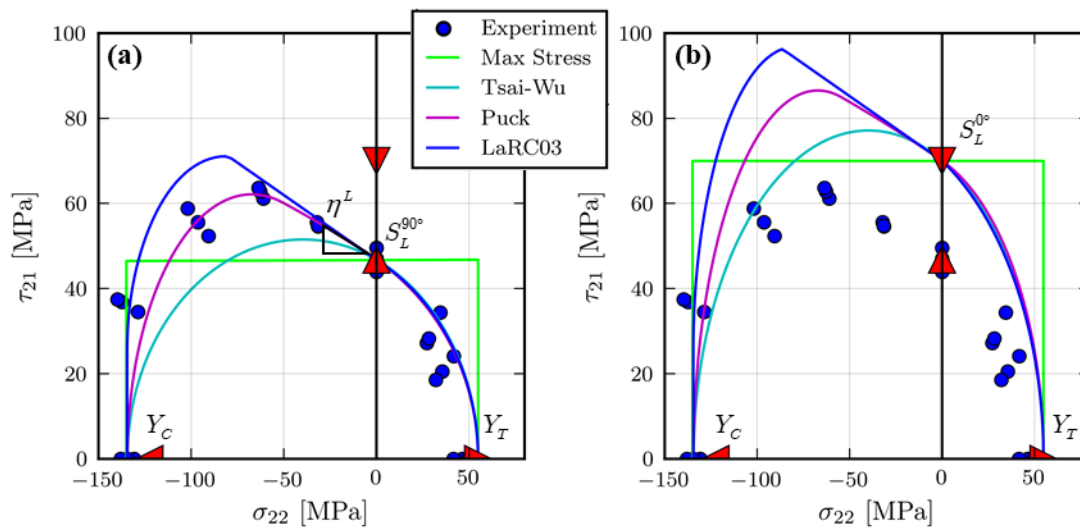
Figure 3.14, Calibrated failure criteria for RP-528 glass/epoxy: (a) using lower bound, and (b) using upper bound shear strength values.

Note that the aim of Figure 3.14 is not to validate the failure criteria against the biaxial experiment results for the UD composite, but to illustrate the different calibrated failure envelopes which result from considering different judiciously chosen model input parameters, *i.e.* strength data. It is not clear at this stage which calibration will yield the better failure predictions. In any case, for an accurate prediction of failure in multidirectional laminates, the in-situ effect on the matrix strength properties has to be accounted for (see Chapter 2, Section 2.4.2). The in-situ strengths calculated according to the Equations summarised in Table 2.1 are reported in Table 3.6.

Table 3.6, Thick ply in-situ strengths for RP-528 [30].

Y_T^{is} [MPa]	$(S_L^{is\ 90°})$ [MPa]	$(S_L^{is\ 0°})$ [MPa]
87	66	99

Note that the plies in the investigated laminates would be categorised as thin plies (transition from thin to thick for glass/epoxy is defined at 0.7 mm according to [70]) but the required fracture toughness values to compute them are not available. For thick plies however, the elastic properties are sufficient to calculate the in-situ strengths, hence they are used for the analysis. The in-situ strengths for thick plies are lower than those for thin plies and hence the prediction is expected to be conservative.

3.5.2 [−/+60]₃ₛ angle ply laminate

The failure envelopes for the [−/+60]₃ₛ angle ply laminate were computed using the lower and upper bound shear strength with and without accounting for the in-situ strength effect as shown in Figure 3.15.
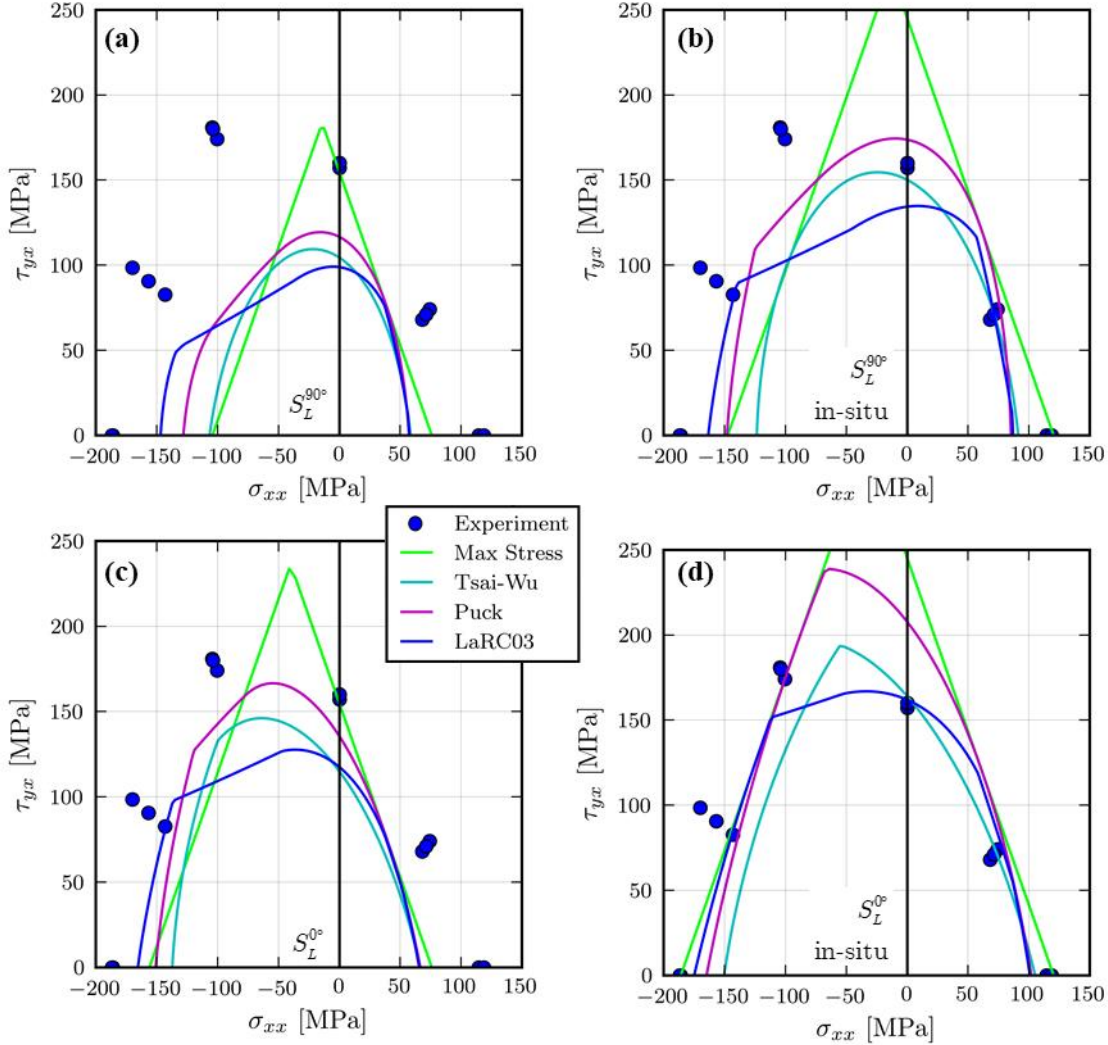
Figure 3.15, Predicted vs experimental failure envelopes using (a) lower bound shear strength $(S_L^{90°})$ without in-situ strengths, (b) lower bound shear strength $(S_L^{90°})$ with in-situ strengths, (c) upper bound shear strength $(S_L^{0°})$ no in-situ strengths, and (d) upper bound shear strength $(S_L^{0°})$ with in-situ strengths.

Using the lower bound shear strengths without accounting for the in-situ strength effect (Figure 3.15 (a)), all failure criteria yield conservative failure predictions. Accounting for the in-situ strengths (Figure 3.15 (b)), Puck's, Tsai-Wu's and the LaRC03's predictions in the tension-shear ($\alpha = 0°$ - $90°$) and the highly compressive load cases ($\alpha = 150°$, $180°$) are improved, while (especially LaRC03) still underpredicts the strength in the combined compression-shear case ($\alpha = 120°$). However, the maximum stress criterion now severely overpredicts the shear strength of the laminate and is therefore non-conservative. Using the upper bound shear strength (Figure

3.15 (c)), the agreement between the predicted and experimental failure envelopes are improved; however, apart from the maximum stress theory, all failure criteria are still conservative. Accounting for the in-situ strengths while using the upper bound shear strength (Figure 3.15 (d)), Puck's and the maximum stress criterion are non-conservative and over predict the strength especially in shear. While the maximum stress criterion is simply not capable of accurately predicting the complex physics of failure, Puck's criterion is over predicting the strength because no fibre compressive failure criterion is included, although it has been shown in Section 0 that fibre kinking plays an important role in the failure behaviour. On the other hand, Figure 3.8 (d) shows that the LaRC03 criterion is in reasonable agreement with the experimental data. Therefore, the failure modes predicted by the LaRC03 criterion, as shown in Figure 3.16, are further discussed and compared to the experimental failure modes characterised in Section 3.4.
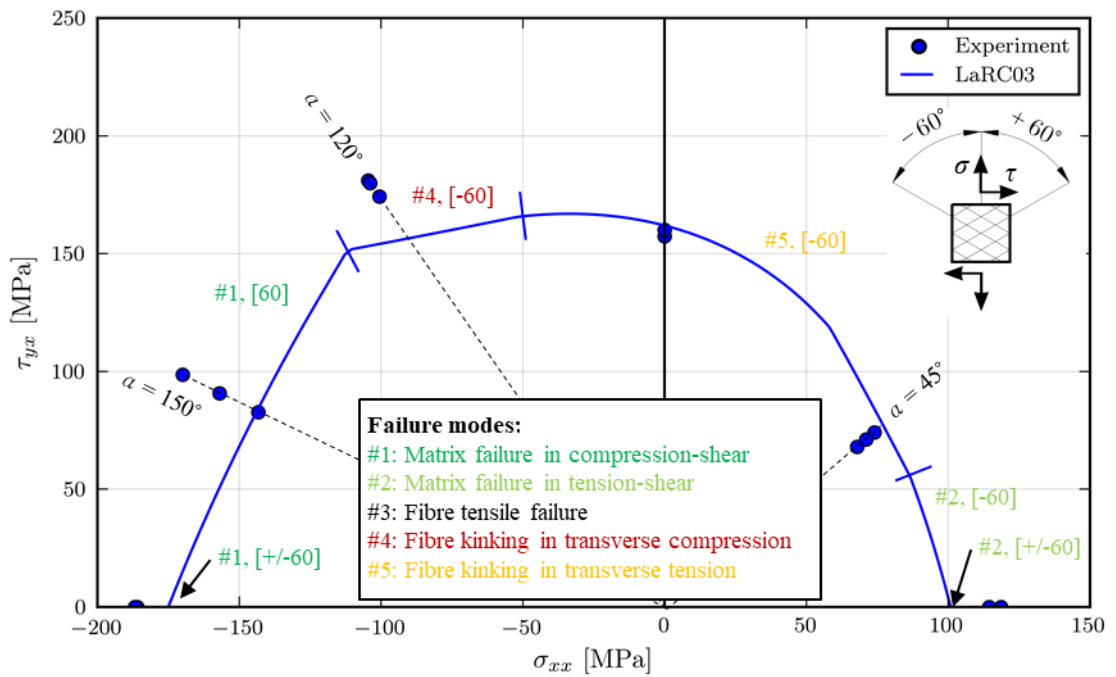
Figure 3.16, Comparison of LaRC03 failure envelope and failure modes against experimental results.

For the tension load case ($\alpha = 0°$) LaRC03 predicts tensile matrix failure in both plies, which agrees with experimental observations (see Figure 3.8 (a)). For the combined tension-shear ($\alpha = 45°$) and the shear ($\alpha = 90°$) load case, LaRC03 predicts fibre kinking failure in the −60° plies, which is in excellent agreement with experimental data in Figure 3.8 (b) and (c), as well as the x-ray CT scans in Figure 3.9 and Figure 3.10. For the combined compression-shear case ($\alpha = 120°$), LaRC03 predicts fibre kinking of the −60° ply. Although kinking is not evident in the tested specimen by visual inspection (Figure 3.8 (d)), fibre fracture under compression in the −60° plies is observed which supports the predicted failure mode. In the compressive dominated cases ($\alpha = 150°$ and 180°), LaRC03 predicts simultaneous failure of both plies by transverse matrix

cracking under compression. Experimentally, this prediction is supported by the appearance of macroscopic fracture zones which are aligned with transverse matrix cracks in both plies (see Figure 3.8 (e) and (f)).

3.5.3   [+/−30]$_{3s}$ angle ply laminate

The predicted first-ply failure loads and modes for the [+/−30]$_{3s}$ laminate subjected to combined compression-shear ($\alpha = 150°$) are compared against the experiment in Table 3.7.

Table 3.7, Experimental and predicted failure loads and modes for the [+/−30]$_{3s}$ laminate subjected to combined compression-shear ($\alpha = 150°$).

	P_{ini} [kN]	P_{ult} [kN]	Initial failure mode
MAF experimental	18.75	23.67	Macroscopic cracks along the −30° fibre direction. Matrix crack in −30° plies and fibre rotation in +30° plies.
Maximum stress	27.17	-	+30° ply fails in shear
Tsai-Wu's	19.39	-	−30° ply (no failure mode prediction)
Puck's IFF	27.17	-	+30° ply fails with matrix crack under moderate transverse compression and shear (crack plane perpendicular to laminate midplane)
LaRC03	18.87	-	−30° ply fails in fibre kinking under transverse tension

In the experiment, the average initial failure load (P_{ini}) of 18.75 kN is associated with the occurrence of macroscopic cracks orientated along the −30° fibre direction (see Figure 3.12). From the CT scan in Figure 3.13 it is observed that the −30° plies exhibit distinct matrix cracks, whereas the +30° ply shows fibre rotations following paths aligned with matrix cracks in the neighbouring −30°. The initial failure load predicted by the maximum stress criterion overpredicts even the ultimate load, and the failure is predicted in the +30°. The criterion is therefore unable to accurately predict the initial failure in the tested laminate and leads to non-conservative results. Tsai-Wu's criterion predicts failure of the −30° ply with an initial failure load of 19.39 kN, which is in agreement with the occurrence of the C1 macroscopic cracks where distinct matrix cracks are observed in the −30° plies (see Figure 3.13 (b)). Puck's IFF predicts failure in the +30° ply

and over predicts the initial failure load significantly. Using Puck's IFF alone predicts first-ply failure incorrectly and the result is non-conservative. On the other hand, LaRC03 predicts initial failure at 18.87 kN due to fibre kinking under transverse tension in the −30° ply. The associated failure function utilises the tensile matrix failure criterion informed by the stresses in the misaligned fibre frame (see Chapter 2, Section 2.4.3). The distinct matrix cracks observed in the fracture zones C1 in Figure 3.11 and Figure 3.13 therefore support the predictions. Initial failure prediction using Tsai-Wu's and LaRC03 failure criteria is therefore reasonably accurate. Both theories predict the −30° plies to fail first, while LaRC03 predicts failure of the matrix in the misaligned frame which aligns with the experimental evidence. To predict the ultimate load accurately, the progressive nature of failure of the laminate needed to be accounted for using a damage model as discussed in (see Chapter 2, 2.4.4), which is beyond the scope of this chapter.

3.6   Opportunities, limitations, and way forward

The MAF has successfully enabled combined tension/compression-shear testing of UD and MD FRP laminates, which was not possible using the conventional Arcan fixture. While the relatively weak $[90]_{12}$ and $[-/+60]_{3s}$ laminates, which exhibit matrix dominated/driven failure modes (matrix cracking and fibre kinking) were successfully tested using the MAF up to failure, the much stronger $[0]_{12}$ and $[+/-30]_{3s}$ laminates, which exhibit not only matrix but also fibre failure modes, could not be tested up to failure for all load cases. To achieve failure in the gauge section of strong laminates displaying fibre dominated failure modes, it will be necessary to induce sufficiently high stresses to break the fibres. The observed premature failure event at the pin holes indicates that the frictional forces generated by the clamps were insufficient to stop the slippage of the specimens. Thus, to enable testing of laminate configurations with fibre dominated response characteristics, a re-design of the MAF is required; this will be addressed in Chapter 5.

The proposed MAF/DIC approach allowed the derivation of apparent normal and shear stress-strain curves for UD composites under biaxial loading. They are based on the average stress and strain within the gauge section where the average strain was conveniently extracted from the DIC strain maps. Due to the averaging approach which ignores the nonuniform stress/strain distribution in the specimen, the method only yields accurate stress-strain curves, while the material response is linear with respect to the applied load. After the onset of material nonlinearities, the obtained stress-strain curves are only approximations. Despite the approximate nature of the stress-strain curves, their overall behaviour agrees reasonably well with similar experimental data reported in the literature (see Figure 2.2) obtained using tubular or off-axis specimens. Therefore, the experimental data is used in Chapter 4 to develop a new nonlinear plasticity-based constitutive model for UD composites.

Failure envelopes have been defined based on the average stress in the gauge section. However, failure has often occurred outside the gauge due to stress/strain concentrations at the edges and

has than propagated along morphologic features of the laminate instead of across the waisted gauge section. This implies that the measured failure envelopes are structural failure envelopes of the specimen rather than true material failure envelopes. This means that the measured failure envelopes have limited use for the calibration of point failure criteria, as a well-defined stress state would be required (see Chapter 2, Section 2.8). However, the structural failure envelope is still useful for the validation of model predictions. When the specimen is regarded as a 'mini' structure, then the nonuniform stress/strain state is not an issue, in fact it may even be preferable as it adds complexity to the test, which may be desired for model validation (similar as in OHT/OHC tests as described in Section 2.6). The quality of the model validation then depends more on the sophistication of the used modelling framework, rather than on the ambiguity in the definition of the failure envelope. In this chapter, a very simple modelling framework based on CLT was used. The model ignores the nonuniform stress state, assumes linear elastic material behaviour and does not account for the progressive nature of failure in laminated composites. In Chapter 5 and 6 the idea is further pursued to regard the multidirectional laminate specimen as a mini structure where the UD plies are the basic building blocks (or sub-components) of the mini structure.

Despite the simplifying assumptions adopted for the modelling presented in this Chapter, the failure criteria have been assessed against the biaxial experimental data obtained and conclusions regarding their predictive capability and the calibration could be drawn. Overall, the LaRC03 and Tsai-Wu theory predicted initial failure in the $[-/+60]_{3s}$ and $[+/-30]_{3s}$ laminates in reasonable agreement with the experimental data when the upper bound shear strength where used and when the in-situ strength effect was accounted for. For the determination of the failure modes, x-ray CT has proven a useful tool. LaRC03 did not only predict the first-ply failure loads in agreement with the experimental data but also the failure modes. On the other hand, Puck's IFF theory overpredicted the strength of the laminates in load cases where fibre kinking was observed, because no fibre kinking/compressive failure criterion was included. This demonstrated that fibre kinking failure plays an important role, especially in the shear dominated load cases and must be accounted for in an accurate failure prediction. The use of simple theories such as the maximum stress theory in combination with in-situ strengths should be discouraged as this can lead to highly non-conservative failure predictions. The LaRC03 criterion will be further used in Chapter 6.

Chapter 4

A nonlinear plasticity-based constitutive model for UD composites

4.1   Introduction

High-fidelity failure prediction in laminated composites requires accurate constitutive models that account for the nonlinear, pressure sensitive behaviour of UD composites. Amongst other approaches (see Chapter 2, Section 2.2.3), the modelling framework of plasticity has been proposed by several researchers to cumulatively account for the nonlinear effects, which include plasticity (in the resin), micro-cracking, as well as fibre rotation [51]. To calibrate/validate such models, multiaxial experimental data is needed due to the stress state dependent nonlinear behaviour of UD composites. Following on from this, the terminology 'plastic' or 'plasticity' is used in this chapter to conveniently represent the cumulative nonlinear material response and does not only refer to pure plastic behaviour.

In this Chapter, a plasticity-based material model is developed based on the MAF/DIC experimental procedures proposed in Chapter 3. The relative simplicity of the biaxial MAF test in comparison to alternative test methods such as using tubular specimens [132], conducting tests in a high-pressure apparatus [160], off-axis tests with a different specimen configuration for each biaxial stress state [51], [161] or the use of additional hydraulic actuators [57], makes the MAF test a promising candidate for identification of biaxial material parameters. Furthermore, the combined compression-shear test data which has been obtained using the MAF is crucial for this work because the most pronounced nonlinearities are observed in the transverse compression-shear stress domain. It is shown how the MAF can be used to calibrate plasticity-based models. Furthermore, it is demonstrated that a non-associative flow rule is required and that the use of an associative flow rule lead to the prediction of non-physical plastic strains/stresses. Moreover, guidelines for the calibration of plasticity-based nonlinear models are established.

The model is applied to the RP-528 glass/epoxy prepreg system [153] characterised using the MAF [93] and also to off-axis test results available in the literature for two other material systems (T800/3633 carbon/epoxy [51] and infused glass/epoxy laminates [161]). The model is also implemented in the FE software ABAQUS/Explicit [115] as a user defined material (VUMAT). The constitutive equations are discretised and the VUMAT is verified using single element FE models compared to the nonlinear analytical solution (see Appendix B).

The work presented in this Chapter has led to the second journal publication in the *International Journal of Solids and Structures* (see Chapter 7, Section 7.3).

4.2   Plasticity-based constitutive models for UD composites

Sun and Chen [50] developed a one-parameter associative plasticity model to simulate the response of UD composites where the material behaviour is plastic in transverse and shear loading and linear elastic in the fibre direction. In an associative model, the plastic strain tensor is assumed to be normal to the yield surface, whereas in a non-associative model the plastic strain tensor is assumed to be normal to a potential function, which is different from the yield function. The associative model predictions in [50] agreed well with the measured nonlinear response of boron/epoxy and carbon/epoxy specimens in off-axis tensile tests. Noting that the transverse stress/strain behaviour in tension and compression is distinctly different, and that the one-parameter quadratic yield function used in [50] could not account for this, Yokozeki *et al.* [51] extended the model by including a Drucker-Prager type [162] linear dependency of the hydrostatic pressure in the yield function. Despite the use of an associative flow rule, good agreement between model predictions and off-axis tensile and compressive test results were reported. Gan *et al.* [52] adopted a similar plasticity framework to predict the nonlinear biaxial response of carbon/epoxy subjected to combined through-thickness compression and inter-laminar shear. The yield function in [52] was constructed based on the stress invariants for transversely isotropic material [39], [40], and assuming negligible plasticity in the fibre direction. All models discussed so far assume the existence of an intrinsic effective plastic stress/strain relationship (or hardening rule) independent of the stress state, which accounts for the cumulative nonlinearity in the transverse and shear stress-strain curves. In both [50] and [52] the shear stress-strain curve was used to derive the effective plastic stress/strain relationship, whereas in [51] the effective plastic stress/strain relationship was obtained by collapsing all experimentally obtained effective plastic stress-strain curves at different off-axis angles into one 'master curve' using a least-squares optimisation procedure to determine the best fit yield and hardening parameters. These simple plasticity models discussed so far have adopted associative flow rules and isotropic hardening laws with a minimum number of plasticity parameters. A more complex plasticity model, based on the stress invariants for a transversely isotropic material, was proposed by Vogler *et al.* [53], [22]. A non-associative flow rule was adopted, where the direction of the plastic flow was taken as the gradient of a plastic potential function that differs from the yield function as the pressure dependent yielding term is omitted. It was argued that the non-associative flow rule allows accurate prediction of the effective plastic Poisson's ratio and the volumetric plastic strains which is not possible with an associative model. The plasticity model was calibrated based on standard tests, hydrostatic pressure compression tests [160], and results from computational micromechanics due to the lack of appropriate experimental data. Often, the parameters were deduced by scaling from similar

materials and the lack of multiaxial experimental data was emphasised as a major difficulty in calibrating the model. Vyas *et al.* [54] proposed a similar non-associative plasticity model to [53] which retained the linear hydrostatic pressure term in the plastic potential in a modified form to ensure an accurate representation of the effective plastic Poisson's ratio and volumetric strain. The model also accounted for stiffening of the elastic properties (E_2 and G_{12}) with applied hydrostatic pressure. The plasticity model was calibrated with biaxial experimental data obtained from filament wound tubular specimens subjected to shear and hydrostatic pressure [132] and off-axis tests under hydrostatic pressure [163]. Further, Hsu *et al.* [56] modelled the combined transverse compression and shear response of carbon/PEEK composites using a micromechanical finite element model where a non-associative Drucker-Prager type plasticity model was prescribed to the matrix. The PEEK matrix material model was calibrated by tests conducted on a custom designed biaxial testing facility using a standard test machine and an additional hydraulic actuator [57]. It can be concluded from the discussion above that multiaxial experimental data is needed to develop and calibrate nonlinear material models for UD composites.

In summary, current plasticity models, which assume transverse isotropy, neglect plasticity in the fibre direction and use a Drucker-Prager type yield function, are generally able to predict the nonlinear, pressure sensitive transverse and shear stress-strain curves in good agreement with experimental data. Most of the simple plasticity models (*e.g.* [51], [50] and [52]) have adopted associative flow rules, whilst others [53], [54], [56] adopted more complex non-associative flow rules. However, no consensus has been reached whether an associative or non-associative flow rule should be used to model the nonlinear, pressure sensitive response of UD composites.

4.3   Non-associative elasto-plastic material model

The total strain tensor ϵ is decomposed into the sum of an elastic and a plastic strain component tensor following the classical plasticity theory as in *e.g.* [164]:

$$\epsilon = \epsilon^e + \epsilon^p \tag{4.1}$$

where the superscripts *e* and *p* denote elastic and plastic components, respectively. The elastic constitutive law for a plane stress condition is expressed as:

$$\epsilon^e = \mathbf{H}^e \boldsymbol{\sigma} \tag{4.2}$$

where $\mathbf{H}^e$ is the elastic compliance matrix for plane stress of an orthotropic composite lamina and where ϵ^e is the elastic strain and $\boldsymbol{\sigma}$ is the stress tensor [2]. To model the plastic response of a transversely isotropic UD lamina, a yield function $f(\sigma_{ij})$ is defined based on stress invariants that remain unchanged for arbitrary rotations about the symmetry axis (*i.e.* the fibre x_1- direction) [52], [43], [48]:

$$I_1 = \sigma_{11}$$
$$I_2 = \sigma_{22} + \sigma_{33}$$
$$I_3 = \tau_{12}^{\ 2} + \tau_{13}^{\ 2}$$
$$I_4 = (\sigma_{22} - \sigma_{33})^2 + 4\tau_{23}^{\ 2}$$
$$I_5 = (\sigma_{22} - \sigma_{33})(\tau_{13}^{\ 2} - \tau_{12}^{\ 2}) - 4\tau_{12}\tau_{13}\tau_{23}$$

(4.3)

where the indices *1*, *2* and *3* refer to the directions parallel to the fibres, in-plane transverse to the fibres and out-of-plane transverse to the fibres, respectively (see Figure 2.7). Based on the experimental observation that the constitutive response of a typical UD composite laminate is quasi linear elastic in the fibre direction, I_1 is excluded from the formulation of the yield function. From physical reasoning, the yield criterion should not depend on the sign of the shear stresses and therefore I_5 is excluded as well. Thus, for a general three-dimensional case, the following yield function similar to the Drucker-Prager model is proposed [52]:

$$f(\sigma_{ij}) = \sqrt{H(\sigma_{22} - \sigma_{33})^2 + L\tau_{23}^{\ 2} + M(\tau_{12}^{\ 2} + \tau_{13}^{\ 2})} + J(\sigma_{22} + \sigma_{33})$$

(4.4)

Equation (4.4) can be simplified for a 2D plane-stress condition by setting all out-of-plane stresses to zero, thus yielding:

$$f(\sigma_{ij}) = \sqrt{H\sigma_{22}^{\ 2} + \tau_{12}^{\ 2}} + J\sigma_{22}$$

(4.5)

Where H and J are plastic material coefficients that must be determined experimentally. According to [50], the shear coefficient M can be set to one without loss of generality. H controls the ellipticity of the yield surface in the σ_{22} versus τ_{21} stress space, *i.e.* when $H = 1$, the yield surfaces are circular. The coefficient J controls the sensitivity to hydrostatic stress and leads to a different response in transverse tension and compression. The special case of $J = 0$ implies that the material exhibits no pressure sensitivity, and thus that the transverse compressive and tensile yield behaviour are identical. To model plastic deformation and hardening in a complex three-dimensional stress state, a scalar effective plastic stress can be defined using the yield function:

$$\bar{\sigma} = f(\sigma_{ij})$$

(4.6)

A non-associative plastic flow potential (*i.e.* plastic flow potential $g \neq$ yield function f) is proposed and defined in a similar way to the yield function in Equation (4.5), neglecting the pressure sensitive J term, *i.e.*:

$$g(\sigma_{ij}) = \sqrt{H\sigma_{22}^{\ 2} + \tau_{12}^{\ 2}}$$

(4.7)

The gradient of the potential function g defines the direction of the plastic flow increment (or plastic strain component vector) $d\epsilon_{ij}^p$:

$$d\epsilon_{ij}^p = \frac{\partial g(\sigma_{ij})}{\partial \sigma_{ij}} d\lambda \tag{4.8}$$

where $i, j = 1, 2, 3$ and where $d\lambda$ is the plastic multiplier.

For the pressure sensitive fibre-reinforced polymer material, a non-associative flow rule is chosen over a simpler associative flow rule as the latter induces a non-physical constitutive behaviour for shear-dominated combined compression-shear stress states. This is illustrated in Figure 4.1 by considering the case of pure shear loading (loading along vertical axis), chosen for clarity: when an associative flow rule is used, the resultant plastic strain vector as per definition will be normal to the yield surface (∇f), and non-physical positive plastic transverse strains, ϵ_{22}^p (red horizontal arrow in Figure 4.1), are induced even for a pure shear stress state where no plastic transverse strains would be expected. Erroneous predictions will also be made for shear dominated combined compression-shear stress states (indicated by the transparent red triangle area in Figure 4.1), since tensile rather than compressive plastic transverse strains are predicted. This physical inconsistency can be eliminated by adopting a non-associative flow rule (red ellipse in Figure 4.1) by which the resulting plastic flow direction (∇g) will be aligned purely along the vertical axis for pure shear stress states, and, as expected, the plastic transverse strains for shear dominated combined compression-shear stress states will be compressive. An experimental example of this will be demonstrated and discussed in Section 4.5 of this Chapter. Thus, based on physical reasoning it is argued that an appropriate simple potential function for pressure sensitive materials, such as UD composites, should satisfy the symmetry condition:

$$\frac{\partial g(0, \tau_{12})}{\partial \sigma_{22}} = 0 \tag{4.9}$$
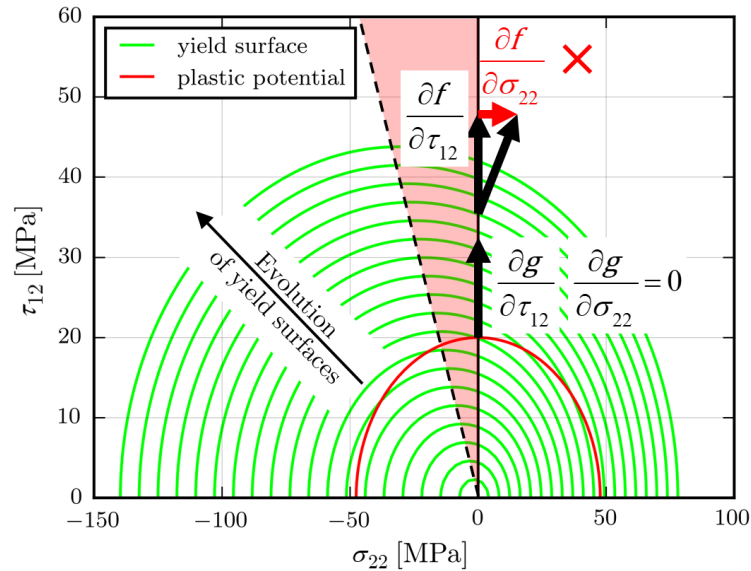
Figure 4.1, Yield surfaces and plastic potential function of the non-associative plasticity model. Note that the number of yield surfaces shown, and the relative size of the potential and yield surfaces are purely illustrative.

Using the definition of the effective stress, $\bar{\sigma}$, given by Equation (4.6), the increment of equivalent plastic work per unit volume dW_P is expressed as:

$$dW_p = \sigma_{ij}d\epsilon_{ij}^p = \bar{\sigma}d\bar{\epsilon}^p \tag{4.10}$$

where $d\bar{\epsilon}^p$ is the increment of the effective plastic strain, and repeating indices imply Einstein summation. The plastic multiplier, $d\lambda$, can be found by substituting the plastic flow rule given in Equation (4.8) into Equation (4.10):

$$\sigma_{ij}\frac{\partial g(\sigma_{ij})}{\partial \sigma_{ij}}d\lambda = \bar{\sigma}d\bar{\epsilon}^p \Rightarrow g(\sigma_{ij})d\lambda = f(\sigma_{ij})d\bar{\epsilon}^p \tag{4.11}$$

Upon rearranging, $d\lambda$ is found as:

$$d\lambda = \frac{f(\sigma_{ij})}{g(\sigma_{ij})}d\bar{\epsilon}^p. \tag{4.12}$$

After inserting $d\lambda$ back into the plastic flow rule in Equation (4.8), and evaluating the partial derivatives of the potential function, the incremental plastic strain components, $d\epsilon_{ij}^p$, are obtained as follows.

$$\begin{Bmatrix} d\epsilon_{11}^p \\ d\epsilon_{22}^p \\ d\gamma_{12}^p \end{Bmatrix} = \begin{Bmatrix} 0 \\ (H\sigma_{22}^2 + \tau_{12}^2)^{-0.5}H\sigma_{22} \\ (H\sigma_{22}^2 + \tau_{12}^2)^{-0.5}\tau_{12} \end{Bmatrix}\frac{f(\sigma_{ij})}{g(\sigma_{ij})}d\bar{\epsilon}^p. \tag{4.13}$$

It is implicitly assumed in the adopted plasticity model that a master effective plastic stress-strain curve (or hardening rule) exists, from which $d\bar{\epsilon}^p$ can be computed knowing $\bar{\sigma}$ from Equation (4.6). The relationship is approximated with the Ramberg-Osgood equation [42]:

$$\bar{\epsilon}^p = (\frac{\bar{\sigma}}{K})^{1/m} \tag{4.14}$$

Thus, by substituting Equations (4.14) into (4.13), all the plastic strain components can be evaluated based on the stress state alone. The yield parameters (*H, J*) and the hardening parameters (*K, m*) remain to be determined experimentally. It should be emphasized that the adoption of a Ramberg-Osgood type description for the effective stress/strain relationship is merely based on phenomenological (rather than physically based) considerations to include the cumulative effects of (actual) material plasticity, micro-cracking and geometrically nonlinear effects as stated in Section 4.1. Thus, Equation (4.14) does not represent 'hardening' in a conventional sense in the proposed formulation, but merely is a suitable nonlinear relation between stress and effective plastic strain.

4.4 Model calibration using the MAF

The model is calibrated using the transverse and shear stress-strain curves shown in Figure 3.6. Firstly, the apparent elastic properties of the tested UD laminate under different biaxial stress configurations were extracted from the stress-strain curves. The parameter E_2^α is used to denote the apparent transverse modulus for each loading angle and is plotted against α in Figure 4.2 and was calculated using a linear fit to the representative stress-strain curves in Figure 3.6 in the strain range of $0.05 - 0.25\%$. The strain range was selected because it conveniently covered the linear region of the apparent stress-strain curves in Figure 3.6.
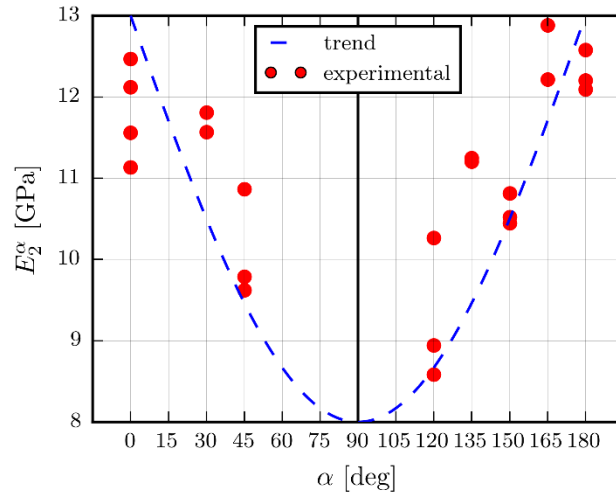
Figure 4.2, Dependency of the apparent transverse modulus on the loading angle α.

The apparent transverse modulus is highest for the pure tension and pure compression stress states (*i.e.* $\alpha=0°$ and $180°$ - see Figure 4.2). For combined stress states where shear stress is applied in addition to tension/compression (loading angle α: $30°$, $45°$, $120°$, $135°$, $150°$ and $165°$ - see Figure 4.2), the apparent transverse modulus is reduced. Opposed to this, it was observed from the tests that there is no significant change of the measured/apparent shear modulus when transverse tension/compression stresses are superimposed. The reason for the scatter in the data in Figure 4.2 is not fully understood, however it is due to the sensitivity of the tested UD material in combination with the test set-up. The elastic properties of the UD composite and the characterisation method used are reported in Table 3.4. Overall, the nonlinear constitutive response and the stress interaction effects measured using the MAF agreed well with similar biaxial experimental data found in the literature measured on tubular specimens [36], [38]. The plastic strain components, $d\epsilon_{22}^p$ and $d\gamma_{12}^p$, are then extracted from the total strains according to Equations (4.1) and (4.2) where the apparent Young's moduli as shown in Figure 4.2 are used to compute the compliance matrix **C** for each individual biaxial load case. The effective plastic strain increment, $d\bar{\epsilon}^p$, can now be expressed as a function of H and J and based on the experimentally

extracted plastic strain components upon rearranging the second and third rows respectively in Equation (4.13) to give:

$$d\bar{\epsilon}^p = \frac{d\epsilon_{22}^p}{(H\sigma_{22}^2 + \tau_{12}^2)^{-0.5} H\sigma_{22}} \frac{g(\sigma_{ij})}{f(\sigma_{ij})}$$

$$= \frac{d\gamma_{12}^p}{(H\sigma_{22}^2 + \tau_{12}^2)^{-0.5} \tau_{12}} \frac{g(\sigma_{ij})}{f(\sigma_{ij})}$$

(4.15)

Note that by using Equation (4.13), two effective plastic strains (and thus two effective plastic stress-strain curves or hardening curves) can be defined for each load case based on the respective transverse and shear stress-strain curves. In an ideal scenario following the theory, the extracted effective plastic strains from both equations would be identical and would exactly follow the effective plastic stress-strain curve defined in Equation (4.14). Thus, an optimisation procedure is adopted to find the best set of model parameters where the extracted effective plastic stress-strain curves both collapse on the same hardening curve. Therefore, a cost function is defined as the vector of the differences between the effective plastic strains extracted from the experimental stress-strain curves of every load case according to Equation (4.15) and the analytical effective plastic strains given by Equation (4.14). The optimised effective plasticity coefficients are then found by minimising the least-squares error of the cost function. In other words, the model is calibrated when the effective plastic stress-strain curves as a function of H and J collapse onto the hardening curve described by Equation (4.14). The optimisation was carried out using a purpose written Python code embedded in a least-squares optimisation algorithm [165].

Referring to Figure 3.6, it is shown that the stress-strain curves obtained for compressive loading exhibit a distinct plateau region. The plateaued regions of the stress-strain curves were excluded from model calibration by visual identification of a strain cut-off point at the beginning of the plateau region as tabulated in Table 4.1. The exclusion of data points above the strain cut-off points is justified based on the fact that the adopted plasticity model framework loses its applicability (or physical suitability) at very large strains where macroscopic damage occurs due to stress concentrations around the notches of the specimen or out-of-plane geometrical instabilities.

Table 4.1, Total strain cut-off points for stress strain curves defined under compressive loading.

α [deg]	120°	135°	150°	165°	180°
Transverse strain cut-off point	0.5%	0.9%	3.0%	-	2.0%
Shear strain cut-off point	5.0%	7.5%	7.5%	-	N/A

Figure 4.3 shows the effective plastic stress-strain curves for the optimised/calibrated yield parameters where the experimental stress-strain curves of all load cases are included in the optimisation process (see No. 1 in Table 4.2). Figure 4.3 (a) and (b) show the effective plastic stress-strain curves obtained from the transverse stress-strain curves and the shear stress-strain curves, respectively.
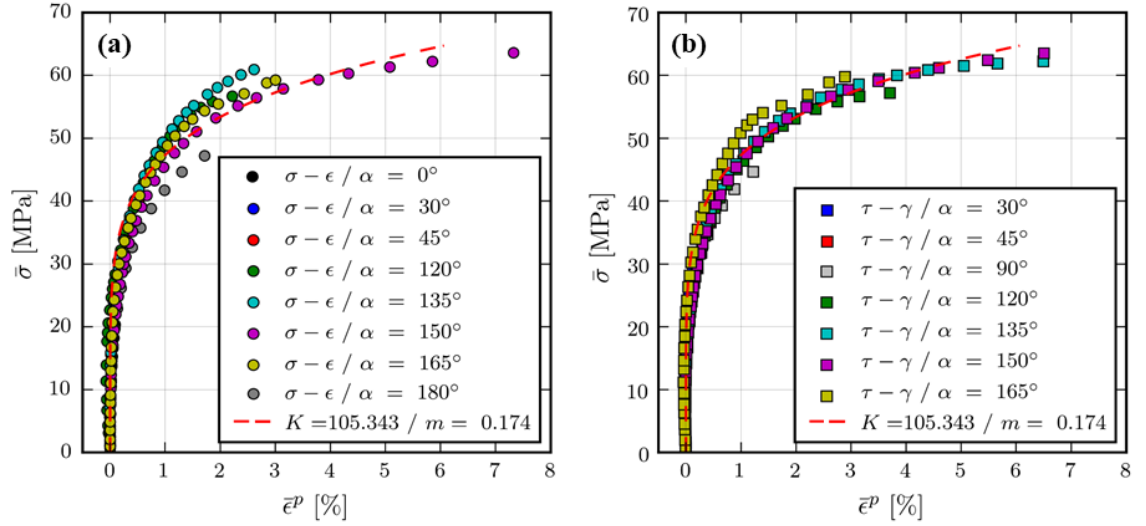
Figure 4.3, Effective plastic stress-strain curves for all load cases obtained based on the transverse (a) and shear (b) stress-strain curves collapsed into a single master curve using the yield parameters from Table 4 (No. 1).

The assumption of the existence of a master effective plastic stress-strain curve, which is independent of the biaxial stress state characterised by the loading angle α, is generally confirmed by the plots in Figure 4.3. It is possible to fit a Ramberg-Osgood equation similar to [51], [50] and [52], to the data with a correlation coefficient of $R^2 = 0.925$, thus demonstrating the suitability of the Ramberg-Osgood equation to describe the effective plastic stress-strain curves. The acquisition of transverse normal and shear strains using DIC allows the computation of two effective plastic stress-strain curves per biaxial load case (see Figure 4.3 (a) and (b)) which allows the verification of both plastic strain components individually. This is a major difference and improvement in comparison to the off-axis tests reported in the literature [51], [50], where only the on-axis stress-strain relationships in the direction of the applied load was obtained and verified. The individual contributions of the plastic transverse normal and shear strains are therefore obscured and cannot be fully verified independently. Having both the transverse and shear stress-strain curves is particularly important to highlight the superiority of the proposed non-associative flow rule over the associative one which will be demonstrated on experimental data in Section 4.5.

Table 4.2 presents the results of a sensitivity analysis investigating the influence of the choice of the load cases included in the optimisation procedure to identify the resultant plasticity model parameters and the corresponding model's predictive capability as indicated by the R^2 value. In

calibration set No. 1 in Table 4.2, the stress-strain curves of all tested load cases were included in the optimisation procedure. In the cases of calibration sets No. 2 to 10, the number of load cases was systematically reduced to identify (i) the lowest number of load cases needed, and (ii) the most suitable load cases to include in the model calibration to give good predictive capability. Furthermore, the sets No. 11 to 14 report the calibrated model parameters and predictive capability of using only uniaxial load cases.

Table 4.2, Sensitivity of the nonlinear material model parameters and the 'goodness of fit' on the choice of experimental data sets included in the parameter calibration/optimisation.

No	α's included	No. of α's	H [-]	J [-]	K [MPa]	m [-]	R^2
1	All	9	0.190	0.069	105.3	0.174	0.925
2	All but 0°, 90°, 180°	6	0.183	0.058	108.4	0.178	0.916
3	30°, 120°, 135°, 150°, 165°	5	0.181	0.053	107.5	0.175	0.921
4	45°, 120°, 135°, 150°, 165°	5	0.183	0.058	108.4	0.178	0.916
5	45°, 120°, 150°, 165°	4	0.192	0.082	101.2	0.170	0.930
6	45°, 135°, 150°, 165°	4	0.197	0.075	95.7	0.146	0.940
7	45°, 135°, 150°	3	0.202	0.066	95.7	0.141	0.936
8	45°, 135°, 165°	3	0.189	0.083	95.7	0.148	0.917
9	45°, 135°	2	0.124	0.151	95.7	0.182	0.455
10	45°, 165°	2	0.207	0.137	94.832	0.175	0.882
11	0°, 90°, 180°	3	0.213	0.087	125.1	0.235	0.864
12	0°, 90°	2	0.306	0.175	105.5	0.200	0.812
13	90°, 180°	2	0.211	0.084	125.1	0.235	0.661
14	0°, 180°	2	0.463	0.072	95.686	0.048	N/A

Table 4.2 shows that the calibration sets No. 1 to 8 yield similar model parameters ($H = 0.181 - 0.202$, $J = 0.053 - 0.083$, $K = 95.7 - 108.4$, $m = 0.141 - 0.178$) with a high predictive capability ($R^2 > 0.9$). This indicates that not all experimental data needs to be included in the optimisation. However, the sensitivity study has shown that it is advantageous to include at least three judiciously chosen load cases, *i.e.* one in tension-shear ($\alpha = 30° - 45°$), one in moderate compression-shear ($\alpha = 120° - 135°$) and one in compression dominated compression-shear ($\alpha = 150° - 165°$). This is because UD composites exhibit three distinctly different failure modes within the transverse tension/compression and shear stress space (*e.g.* the three inter-fibre failure modes as defined by Puck *et al.* [36], [69]). Therefore, to achieve a good model calibration, it is necessary to select load cases which yield stress-strain curves that adequately represent the three

distinct mechanical responses and failure mechanisms. Further, recalling the plasticity model framework in Figure 4.1 and the yield function in Equation (4.5), it is clear that to determine the hydrostatic term *J*, which describes the offset of the centre point of the yield ellipse from the origin, it is required to include a tension-shear and a compression dominated load case to accurately locate the origin of the yield ellipse. On the other hand, to determine the coefficient *H*, which describes the ellipticity or transverse/shear anisotropy, a shear dominated load case is needed in addition. In summary, stress-strain curves derived for different biaxial stress states are required, which comprise different information regarding the mechanisms that generate nonlinearity, to achieve a robust and overall accurate model calibration. The point is further demonstrated by the calibration sets of No. 9 to 14 in Table 4.2. Calibration set No. 9 fails to include sufficient information on the pressure sensitivity due to the omission of compression dominated load cases, resulting in poor predictive capability. Similarly, set No. 10 yields poor predictive capability because a shear dominated compression-shear load case is omitted and the ellipticity is not captured well in the included data. Calibration set No. 11, which includes all three uniaxial load cases, is also insufficient as the overall predictive capability is still poorer than when three biaxial load cases are used instead. The reason for this is that a uniaxial load case provides only one stress-strain curve for model calibration compared to two stress-strain curves for a biaxial load case. Finally, calibration sets No. 13, which does not include a tension-shear load case, and No. 14, without a shear dominated load case, both produce low R^2 values (*i.e.* poor model fit) due to insufficient information regarding the pressure sensitivity or anisotropy, respectively.

The calibrated stress-strain curves, using the optimised parameters from No. 1 in Table 4.2, are compared against the experimental data in Figure 4.4. The model normal and shear stress-strain curves match generally well with the experimental data. In the cases of combined tension-shear (Figure 4.4 (a) and (b)) the model plastic strains are generally slightly lower than the experimental ones. However, in comparison to linear elastic analysis, the strain prediction is greatly improved, and the general behaviour is well captured, *i.e.* the level of plasticity increases with increased loading angle α. For combined compression-shear stress states, the transverse stress-strain curves for $\alpha = 120°$ and $165°$ are in excellent agreement with the experimental data. For $\alpha = 135°$ the model plastic strains are slightly higher, while for $\alpha = 180°$ and $\alpha = 150°$ slightly lower (see Figure 4.4 (c)) than the experimental plastic strains. The model shear stress-strain curves are generally in good agreement with the experimental data except for pure shear ($\alpha = 90°$) where the model plastic shear strains are lower than the experimental plastic strains (see Figure 4.4 (b) and (d)).
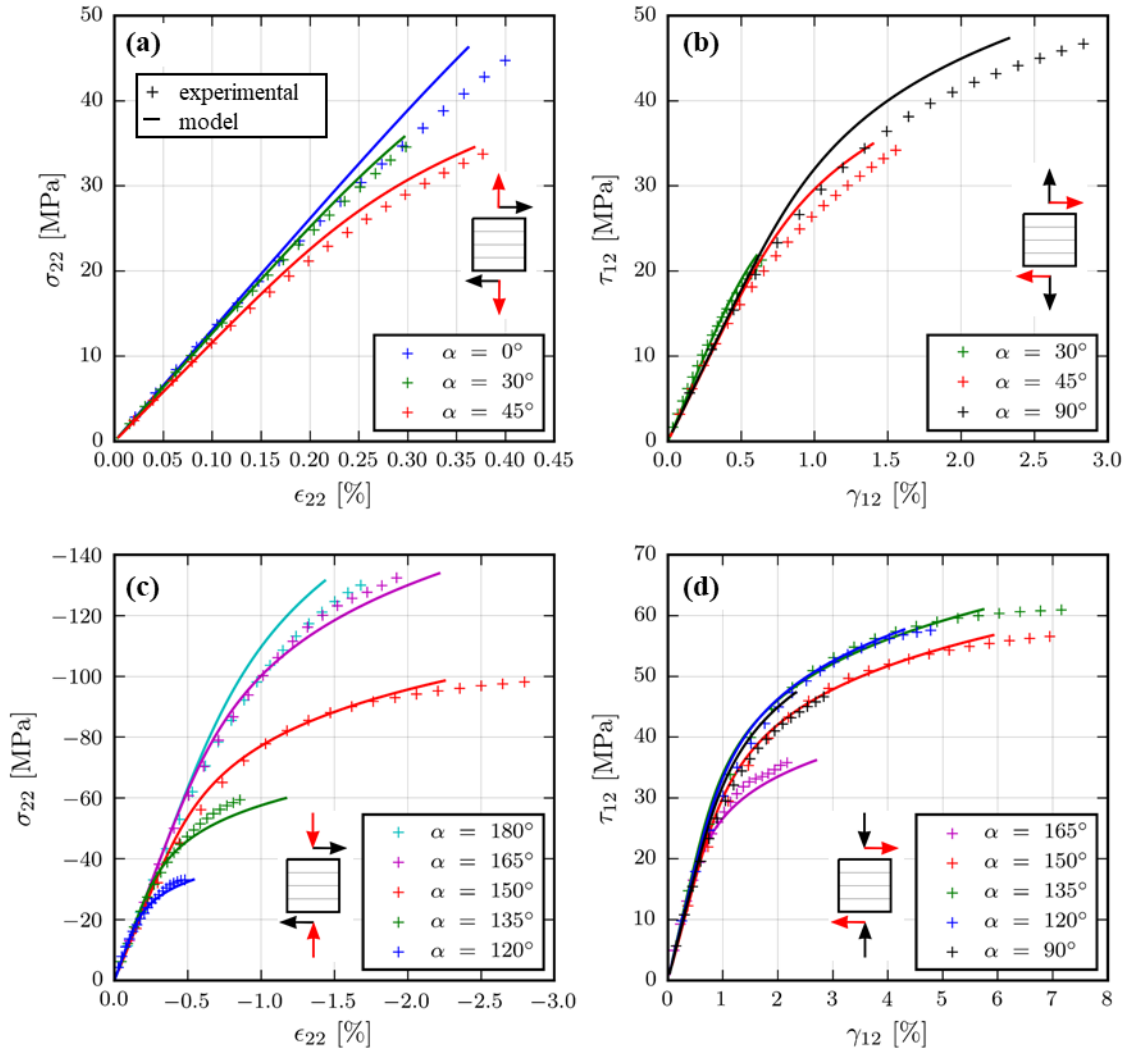
Figure 4.4, Non-associative plasticity model predictions in comparison to MAF experimental data. Note that the small figure inserts illustrate the stress state, while the corresponding strain component is highlighted in red.

4.5   Model calibration using off-axis test results from the literature
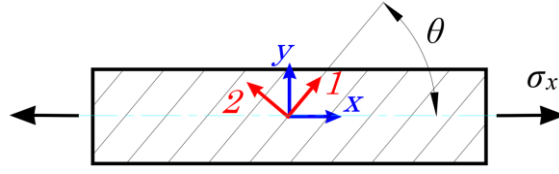
Figure 4.5, Illustration of an off-axis test and definition of the off-axis angle θ and the nominal stress σ_x.

In this section, the non-associative plasticity model was applied to off-axis tension/compression experimental data for T800/3633 carbon/epoxy [51] and infused glass/epoxy [161], respectively. Figure 4.5 illustrates a uniaxially loaded off-axis UD specimen where the off-axis angle θ relates the nominal stress σ_x to the local (lamina) stress state through:

$$
\begin{aligned}
\sigma_{11} &= \sigma_x \cos^2(\theta) \\
\sigma_{22} &= \sigma_x \sin^2(\theta) \\
\tau_{12} &= -\sigma_x \sin(\theta)\cos(\theta)
\end{aligned}
\tag{4.16}
$$

The off-axis angle θ determines the biaxial stress state similar to the MAF loading angle α (see Figure 1.2), which is related to θ through the following relationship:

$$
\theta = \begin{cases} 90° - \alpha, \sigma_x \geq 0 \\ -90° + \alpha, \sigma_x \leq 0 \end{cases}
\tag{4.17}
$$

where small off-axis angles θ correspond to shear dominated load cases and MAF loading angles α close to pure shear loading ($\alpha = 90°$). The reported stress-strain curves for various off-axis angles were digitised. The plasticity models were then calibrated by collapsing all the effective plastic stress-strain curves from the different load cases (stress states) into one master curve to which Equation (4.14) was fitted. To calibrate the developed material model using off-axis tests, the measured stress σ_x and strain ϵ_x^{tot} in the loading direction (see Figure 4.5) need to be related to the effective plastic stress, $\overline{\sigma}$, and strain. The derivation of this relationship closely follows [51] but differs due to the adoption of a non-associative rather than an associative flow rule. The experimentally measured plastic strain in the loading direction ϵ_x^p is obtained as:

$$
\epsilon_x^p = \epsilon_x^{tot} - \frac{\sigma_x}{E_x}
\tag{4.18}
$$

where E_x is the laminate modulus in the loading direction. The off-axis plastic strain ϵ_x^p can be expressed based on the local (lamina) strain components as:

$$
\epsilon_x^p = \epsilon_{11}^p \cos^2(\theta) + \epsilon_{22}^p \sin^2(\theta) - \gamma_{12}^p \sin(\theta)\cos(\theta)
\tag{4.19}
$$

To simplify the derivation, $h(\theta)$ is defined by inserting the stress transformation rules in Equations (4.16) into the yield function in equation (4.5):

$$h(\theta) = \begin{cases} \sqrt{H \sin^4(\theta) + \sin^2(\theta)\cos^2(\theta)}, \sigma_x \geq 0 \\ -\sqrt{H \sin^4(\theta) + \sin^2(\theta)\cos^2(\theta)}, \sigma_x \leq 0 \end{cases} \tag{4.20}$$

Note, that by multiplying $h(\theta)$ with σ_x the yield function is retrieved.

The individual plastic strain components ϵ_{11}^p, ϵ_{22}^p and γ_{12}^p in Equation (4.19) can be substituted by the expressions given in Equation (4.13). Then the transformed stresses from Equation (4.16) and $h(\theta)$ defined in Equation (4.20) can be substituted and $\bar{\epsilon}^p$ is obtained as a function of σ_x, $h(\theta)$, and $g(\sigma_{ij})$ upon rearranging:

$$\bar{\epsilon}^p = \frac{\epsilon_x^p}{h(\theta)} \frac{g(\sigma_{ij})}{f(\sigma_{ij})} \tag{4.21}$$

where

$$\frac{g(\sigma_{ij})}{f(\sigma_{ij})} = \frac{h(\theta)}{h(\theta) + J \sin^2(\theta)} \tag{4.22}$$

Inserting equation (4.22) into equation (4.21) one obtains:

$$\bar{\epsilon}^p = \frac{\epsilon_x^p}{h(\theta) + J \sin^2(\theta)} \tag{4.23}$$

Similarly, the effective plastic stress can be obtained as a function of σ_x, as follows:

$$\bar{\sigma} = (h(\theta) + J \sin^2(\theta))\sigma_x \tag{4.24}$$

The model can now be optimised based on the derived effective plastic stress-strain curve in equation (4.23) and (4.24). Figure 4.6 shows the best fit effective plastic stress-strain curves obtained with the optimised plasticity parameters given in Table 4.3, where 't' and 'c' in the legends represent tensile and compressive off-axis test data, respectively.
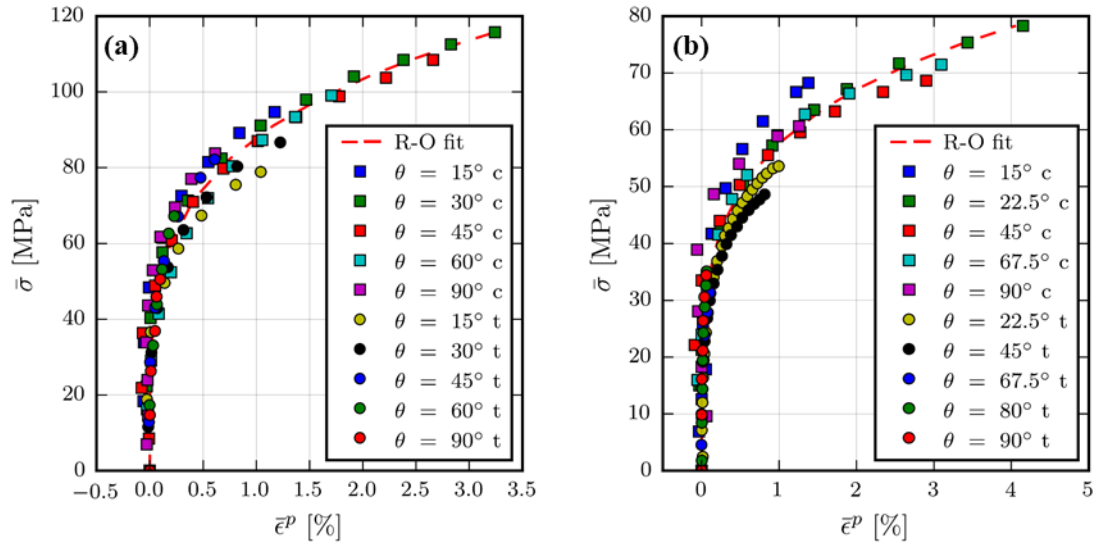
Figure 4.6, Effective plastic stress-strain curves after least-squares optimisation for (a) T800/3633 carbon/epoxy [51], and (b) infused glass/epoxy [161], showing the Ramberg-Osgood fit (R-O fit).

Table 4.3, Calibrated plasticity parameters for the developed non-associative model.

Material	H [-]	J [-]	K [MPa]	m [-]	R^2
T800/3633 [51]	0.319	0.132	257.346	0.233	0.978
glass/epoxy [161]	0.355	0.212	151.149	0.209	0.950

From Figure 4.6, and based on the R^2 values of 0.978 and 0.950 given in Table 4.3, it is clearly shown that the predicted master effective plastic stress-strain curve fits the experimental stress/strain data well for both material systems, and thus is suitable to describe their nonlinear behaviour. For the case of the off-axis tests presented in [51] and [161], only one effective plastic stress-strain curve can be extracted per off-axis angle from the experimentally obtained stress-strain curve (σ_x versus ϵ_x) in the global loading direction. This is different to the MAF/DIC approach discussed in the previous section, where the effective plastic stress-strain curves can be obtained from the transverse and shear stress-strain curves independently (see Equation (4.15) and Figure 4.3). The additional information allows verification of not only the overall induced nonlinear behaviour, but also of the prediction of the individual plastic strain components, which is not possible when only on-axis test data is available.

For comparison, the associative plasticity model proposed in [51] was also calibrated using the same data sets and the optimum plasticity parameters are given in Table 4.4 adopting the notation as defined in [51], where *a1* and *a66* are yield parameters similar to *H* and *J*, and *A* and *n* are fitting parameters similar to *K* and *m*.

Table 4.4, Calibrated plasticity parameter for the associative model [51].

Material	$a1$ [-]	$a66$ [-]	A [1/MPa]	n [-]	R^2
T800/3633 [51]	0.090*	2.700*	3.140e-13*	4.190*	0.979
glass/epoxy [161]	0.129	3.931	1.528e-13	4.510	0.947
* Values directly taken from [51]					

4.6 Non-associative vs. associative plasticity

Both the predictions of off-axis stress-strain curves by the proposed non-associative plasticity model and the reference associative model [51] are plotted and compared against experimental results for carbon/epoxy [51] in Figure 4.7 and for vacuum infused glass/epoxy in Figure 4.8 [161].
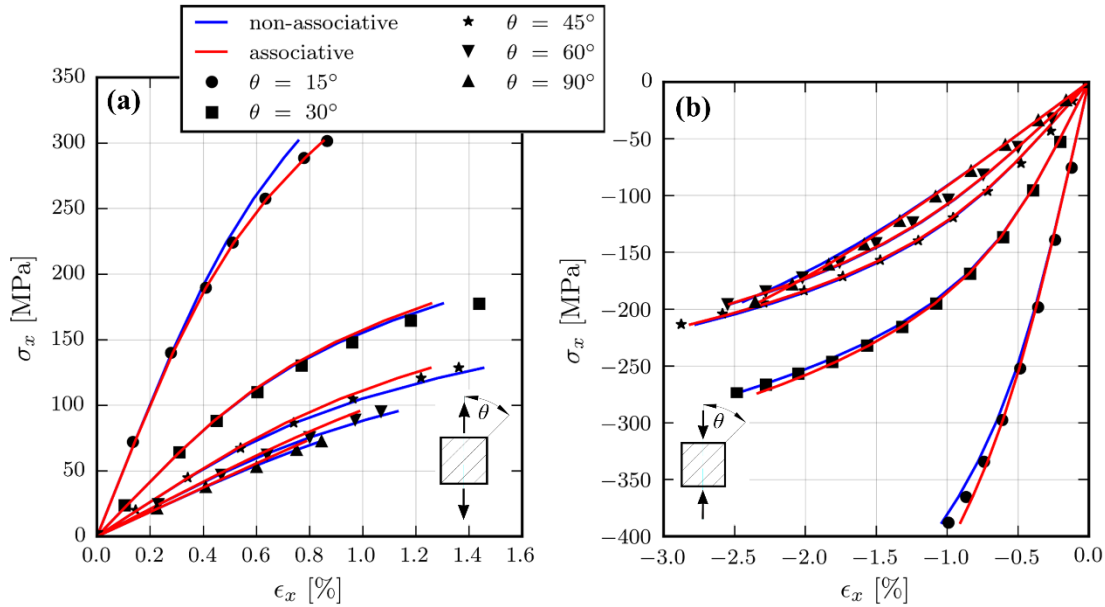
Figure 4.7, Carbon/epoxy T800/3633 (a) tensile and (b) compressive off-axis experimental results (data points) [51] compared against model fit (solid lines).
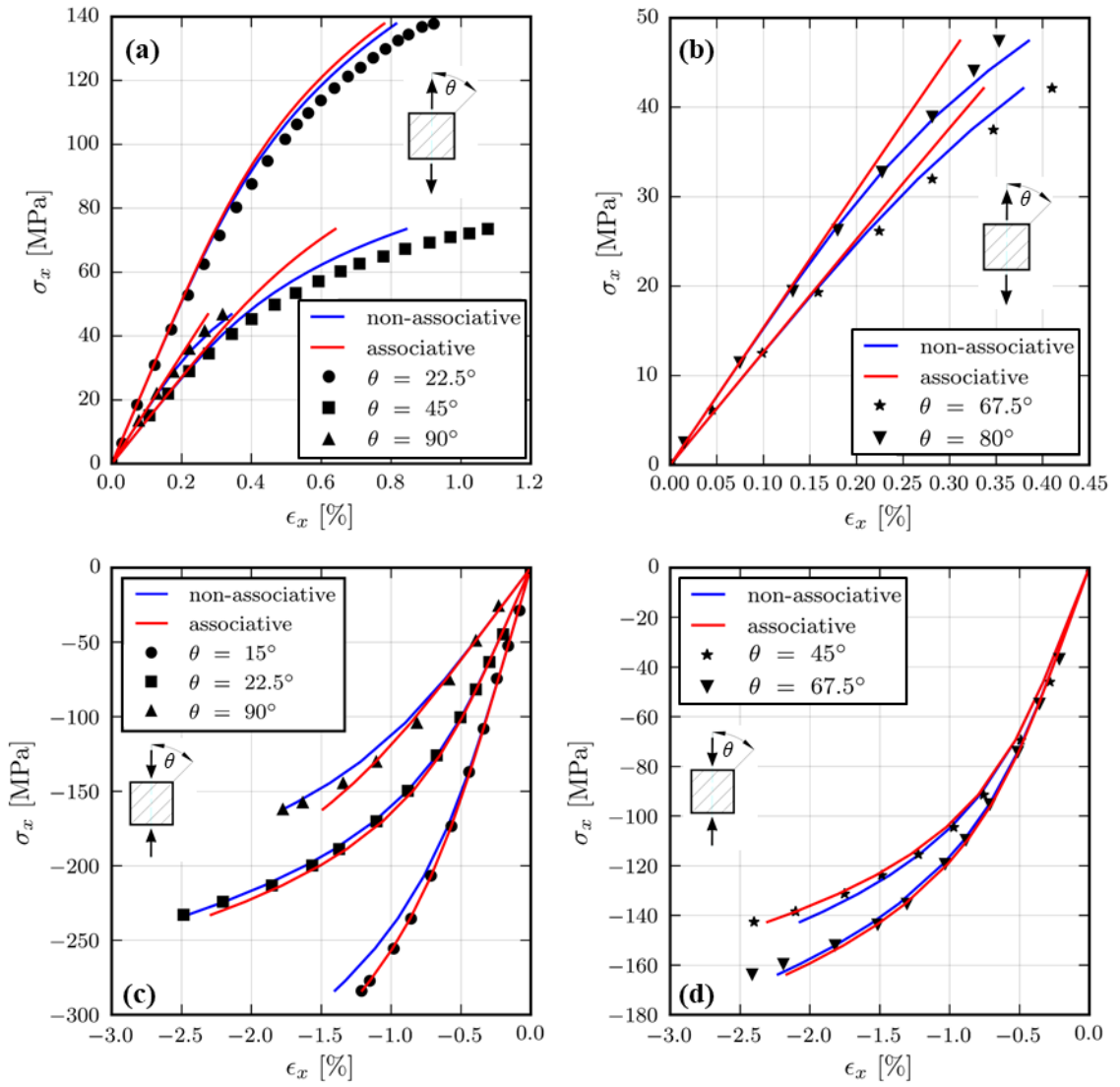
Figure 4.8, Vacuum infused glass/epoxy tensile (a and b) and compressive (c and d) off-axis experimental results (data points) [161] compared against model fit (solid lines). The curves are plotted in different figures for clarity. The small figure inserts illustrate the stress state and the off-axis angle.

Figure 4.7 *and* Figure 4.8 show that both models (associative and non-associative) fit the nonlinear off-axis stress-strain curves for both material systems in good agreement with the experimental data and with a similar degree of accuracy (see R^2 in Table 4.3 and Table 4.4). It is not apparent that the proposed non-associative plasticity model gives better predictions than the associative model as the subtle differences are obscured in the on-axis plastic strains, which are a function of the transverse normal and shear strain components in the local x_1,x_2- coordinate system. To illustrate the advantages and physical consistency of the proposed non-associative plasticity model over the associative models, the components of the plastic strains (ϵ_{22}^p and γ_{12}^p) predicted by the proposed non-associative model and the associative model of [51] are plotted individually against the off-axis stress σ_x in Figure 4.9 for selected compressive load cases for carbon/epoxy T800/3336 (same qualitative results apply to glass/epoxy). Both models predict

similar plastic shear strain components γ_{12}^p (Figure 4.9 (b)), with the associative model giving slightly lower values. However, the plastic transverse strains ϵ_{22}^p predicted by the two models are different (see Figure 4.9 (a)). The associative model predicts tensile plastic transverse strains although the loading is compressive for off-axis angles $\theta = 15°$ and $\theta = 45°$, which is clearly non-physical. In contrast, the non-associative model predicts the plastic transverse strain to be compressive, as would be expected under compressive loading. This non-physical characteristic of the associative flow rule when used together with a Drucker-Prager type yield surface was also explained and illustrated in Figure 4.1 (Section 4.3), and is a consequence of the negative slope of the yield surfaces in the case of pure shear and shear-dominated combined compression-shear stress states. Thus, adoption of an associative flow-rule forces the prediction of non-physical transverse strains for these stress states, hence a non-associative flow rule is required.
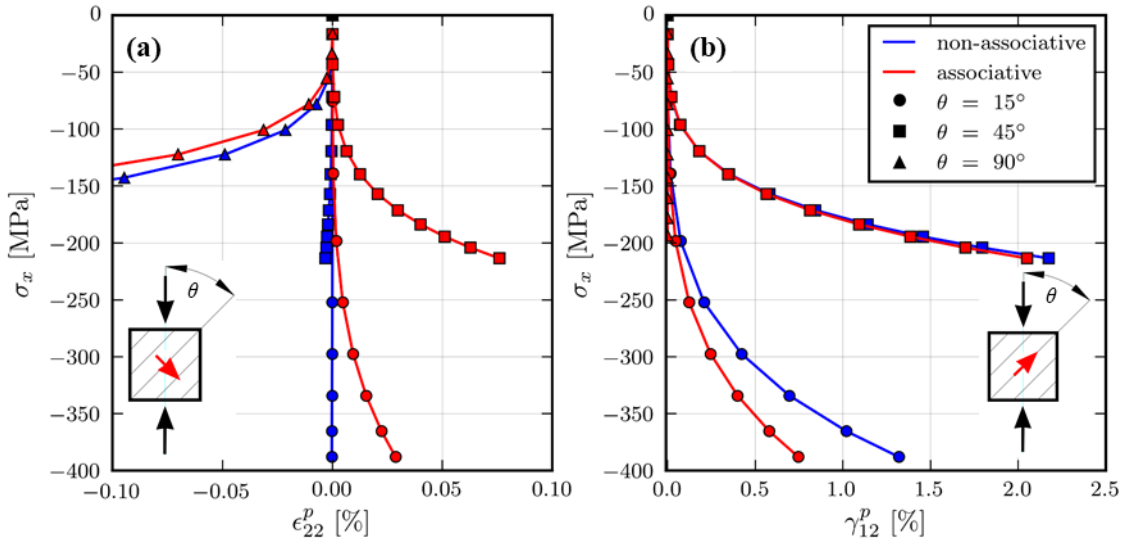
Figure 4.9, Plastic component strains ϵ_{22}^p (a) and γ_{12}^p (b) as predicted by the non-associative (blue) and associative (red) models for compressive off-axis test on T800-3633 carbon/epoxy [51].

The comparison between the individual strain components predicted by the non-associative and the associative models in off-axis tests has clearly shown that the use of a non-associative flow rule is crucial to predict the effective plastic component strains correctly when a Drucker-Prager type yield surface is adopted. Furthermore, the study has demonstrated that it is important to obtain all the strain components experimentally, as facilitated by the MAF combined with DIC which provides full-field strain maps. This enables full scrutiny, calibration and verification of nonlinear constitutive models, whereas simple axial and transverse strain measurements reported in most off-axis tests [51], [161] cannot achieve this.

4.7   Conclusions

A non-associative plasticity model based on the invariants of transverse isotropy has been developed for UD composite materials subjected to multiaxial in-plane loading. The model accounts for the cumulative nonlinear response due to resin plasticity, micro-cracking and geometrically nonlinear effects in the transverse and shear stress-strain curves, while assuming linear elastic behaviour in the fibre direction. The pressure dependent responses for transverse tension and compression stress states are accounted for using a Drucker-Prager type yield function.

It has been shown that the MAF/DIC approach used is a viable alternative to conventional off-axis tests, experiments using tubular composite specimens, experiments in high-pressure chambers, or experiments involving multiple actuators, to generate biaxial experimental data for nonlinear constitutive model calibration. The model is calibrated by minimising the difference between the experimentally extracted effective plastic stress-strain curves and the nonlinear relationship between stress and effective plastic strain described by the Ramberg-Osgood equation. It has been found that at least three judiciously chosen biaxial load cases should be used for model calibration; one in tension-shear, one in moderate compression-shear, and one in compression dominated compression-shear.

The model has been applied to a glass/epoxy prepreg material system tested using the MAF. The analysis of the MAF experimental data has shown that the nonlinearities in all the measured transverse and shear stress-strain curves corresponding to different biaxial stress states can be reduced into a single effective plastic stress-strain curve. Furthermore, it is demonstrated that an associative flow rule, when used with a pressure sensitive Drucker-Prager type yield function, can induce incorrect, non-physical plastic transverse strains for pure shear and shear-dominated combined compression-shear stress states. However, the issue can be resolved by adopting a non-associative model. The research conducted has shown the importance of measuring all the strain components experimentally for full model calibration, *e.g.* using a full-field DIC approach, to ensure that all the predicted individual plastic strain components can be verified.

The model was further calibrated based on off-axis experimental data from the literature for an infused glass/epoxy and a carbon/epoxy material system. The off-axis stress-strain curves of the model agreed well with the experimental ones, thus demonstrating that the proposed non-associative plasticity model is applicable to a wide range of advanced composites.

Chapter 5

Lay-up effects in multidirectional laminates subjected to multiaxial loading

5.1   Introduction

The literature review in Chapter 2 has shown that laminate lay-up significantly effects the strength and failure modes of multidirectional laminates (see in-situ effect in Sections 2.4.2 and OHT tests in Section 2.6). Further, Tan *et al.* [7], [152] showed that multiaxial loading also alters the failure modes and open-hole specimen strengths. Nonetheless, lay-up effects in composite laminates subjected to multiaxial loading, especially in the compression-shear loading regime, have rarely been addressed in the open literature and require further investigation. Thus, in this chapter the clear gap identified in the literature is addressed by experimentally assessing lay-up effects in multidirectional laminates subjected to combined tension/compression-shear loading. Therefore, three quasi-isotropic laminates with different lay-ups, as shown in Figure 5.1, are studied.
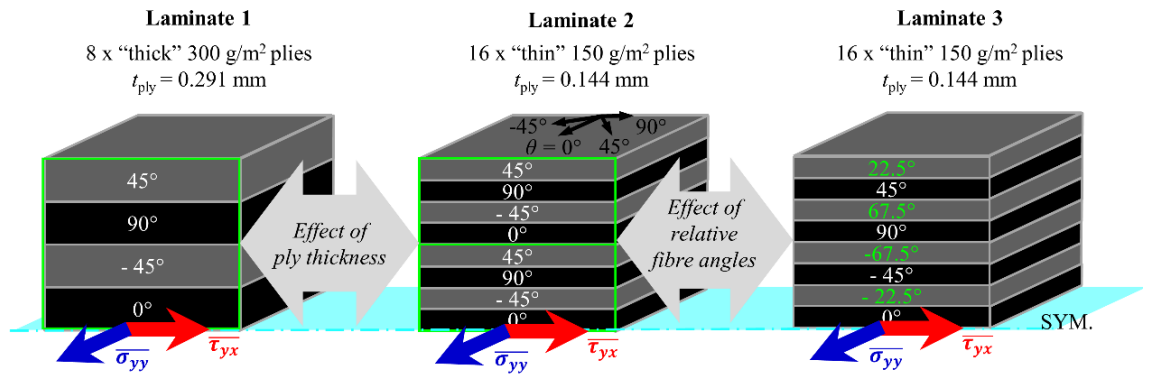
Figure 5.1, Quasi-isotropic carbon/epoxy laminates subjected to combined tension-shear and compression-shear loading.

Laminates 1 and 2 are made from UD plies with different thickness (*i.e.* 0.291 and 0.144 mm respectively), while Laminates 2 and 3 feature different relative fibre orientation (or pitch) angles (*i.e.* 45° and 22.5° respectively). However, all three laminates exhibit the same overall laminate thickness and equivalent homogenised elastic stiffness properties according to classical lamination theory (CLT) [2].

To enable the investigation of the strong laminates in Figure 5.1 up to failure, a new MAF is designed. A procedure based on stereo DIC is used to identify damage evolution in the open-hole specimens based on the full-field displacement and strains. DIC is also used as a biaxial

extensometer to derive decoupled normal and shear load-extension curves from the biaxially loaded specimens. Failure envelopes are constructed and used to assess the failure behaviour and multiaxial open-hole specimen strength. The results from the three tested laminates, enable a comparative assessment of the effects of ply thickness and fibre orientation on the failure behaviour of quasi-isotropic laminates, contributing to understanding the effects of laminate lay-up on the failure of composite laminates subjected to multiaxial loading. Furthermore, the full-field experimental data provides a challenging high-fidelity means of validating composite damage and failure modelling frameworks.

The laminated carbon/epoxy plates were manufactured and provided by the sailing team INEOS Team UK, the British challenger for the 36th America's cup. The detailed UD material specification cannot be disclosed at the time of writing. The work presented in this Chapter led to the third journal publication which has been published in *Composites Part A: Applied Science and Manufacturing* (see Chapter 7, Section 7.3).

5.2   Design of new MAF and experimental set-up

Figure 5.2 provides an overview of the new MAF, which is similar in concept to the previous version of the MAF in [93], [166] used for initial testing in Chapter 3, but with important key design alterations that allow larger loads to be applied for general composite materials testing.
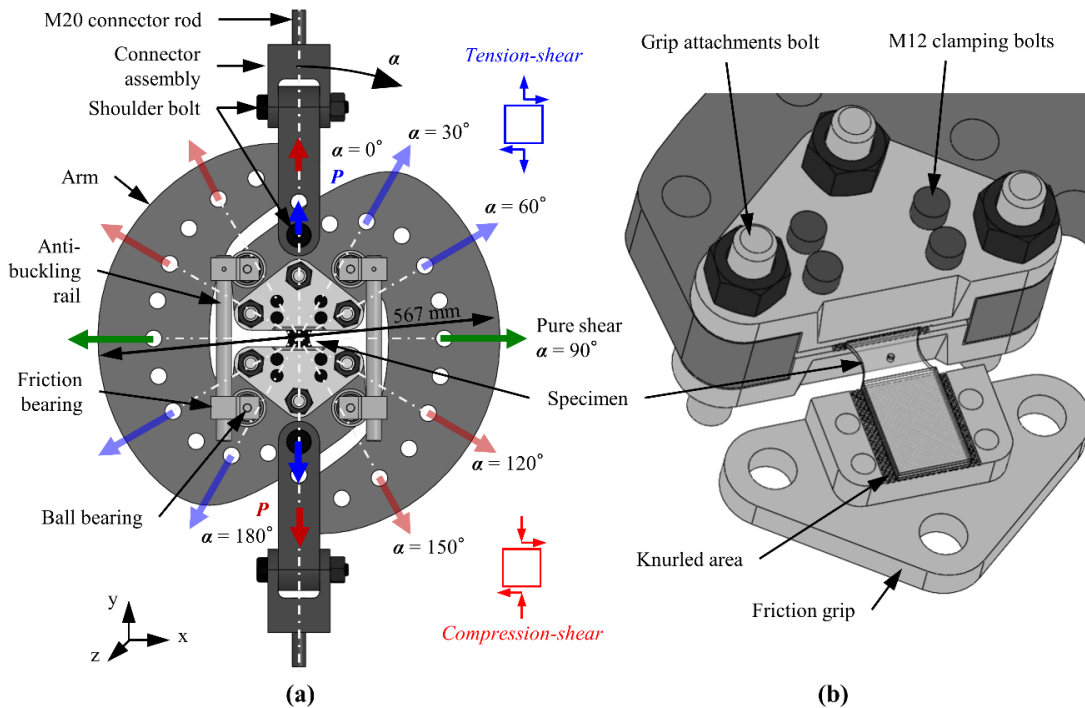
Figure 5.2, (a) The new MAF, with indication of how different combined tension/compression-shear loading can be induced in the specimen by the choice of the loading hole pair designated by the loading angle α, and (b) the re-designed specimen friction grip arrangement.

Premature failure of the specimens at the grips was successfully eliminated by upsizing the clamping bolt diameters (from M6 to M12) to induce greater clamping and thus friction forces to delay specimen slippage. Furthermore, the clamping bolts were positioned outside of the specimen tabs as shown in Figure 5.2 (b) to eliminate premature shear out failure at the bolt holes. The new MAF as shown in Figure 5.2 (a) consists of two boomerang shaped arms with loading holes positioned at increments of $15°$, the anti-buckling rail assembly, the top and bottom connector assemblies, the grip attachment bolts, and the friction grips shown in detail in Figure 5.2 (b). By connecting the new MAF via the connector assemblies to a tensile test machine as shown in Figure 5.3, using the different pairs of loading holes designated by the loading angle (α) different mean combined tension/compression-shear stress states can be induced in the specimen, ranging from tension ($\alpha = 0°$) to tension-shear ($\alpha = 15° - 75°$), to shear ($\alpha = 90°$), to compression-shear ($\alpha = 105° - 165°$) and to compression ($\alpha = 180°$).
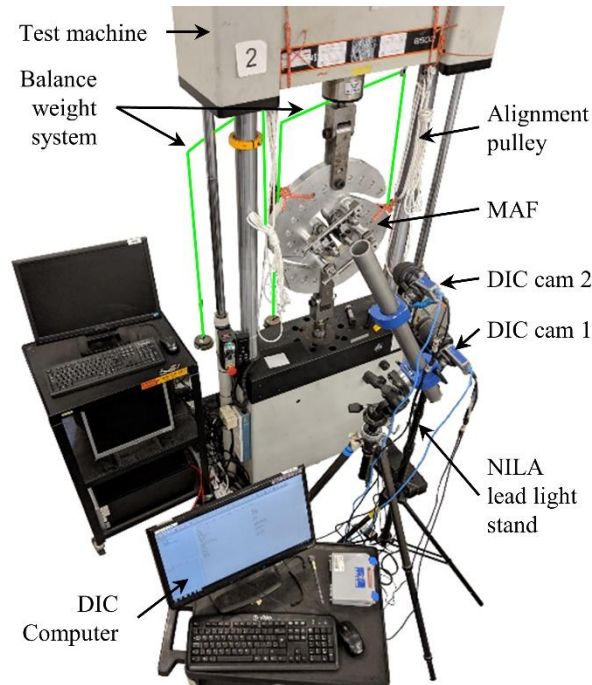
Figure 5.3, Experimental set-up showing the MAF attached to a universal test machine, the alignment pulleys, the balance weight system and the stereo DIC system.

The MAF arms are made from 40 mm thick high strength aluminium alloy Alumec 89. The top and bottom connector assemblies consist of two pin joint lugs made from P20 tool steel, two 24 mm diameter shoulder bolts and a M20 threaded steel rod. The connectors allow the MAF to freely rotate in both the *xy-* (in-plane) and *yz-* (transverse) planes due to the two integrated shoulder bolts per plane. This ensures that the rig and specimen are free from out-of-plane constraints, potentially arising from test machine misalignment, which may induce spurious out-of-plane bending stresses/strains in the specimen. The grips are connected to the arms via the three 24 mm diameter grip attachment bolts made from stainless steel 17-4HP-A. The knurled friction grips are made from stainless steel 17-4PH-H900, hardened to Rockwell hardness C 45

to increase their durability in contact with the specimen. The knurls are 2 mm high pyramids with square bases. The four M12 bolts per grip, shown in Figure 5.2 (b), generate the required apparent friction force by applying allowable torques up to 150 Nm. Out-of-plane displacements are prevented by an anti-buckling rail assembly similar to the one used for the previous MAF in [93]. All parts were designed to withstand a safe working load of 100 kN with a factor of safety against yielding of 1.5. The arms, grips, grip attachment bolts and the connector lugs were dimensioned using detailed FE analyses. The threaded connector rod and the M12 clamping bolts were dimensioned analytically according to the tensile strength requirement in [167], and the minimum thread engagement length requirement in [167], [168], whereas the shoulder bolts were dimensioned according to [169]. The manufacturing drawings of the new MAF are attached in Appendix F.

Two pulleys were suspended from the test machine crosshead and attached to the MAF arms to facilitate changing the loading angle α to set up different combined loading states as defined in Figure 5.2 (a). Further, a balance weight system (highlighted in green in Figure 5.3) was installed to counteract the moment generated by the weight of the two MAF assembly halves (17 kg per combined arm and grip assembly), which otherwise would induce additional in-plane bending stress/strains into the specimen.

Stereo DIC was used for the assessment of the full-field deformation of the specimens, where u is the horizontal, v the vertical and w the out-of-plane displacement, respectively. The strain state (vertical ϵ_{yy} and horizontal ϵ_{xx} normal strains and shear strains γ_{xy}) was derived by the DIC software in terms of the logarithmic strain tensor. The full-field deformation data was used to assess the load response of the specimens as well as to identify the initial failure sites and subsequent damage evolution. The stereo DIC system was positioned approximately 500 mm away from the specimen's front side and was realigned and calibrated for each combined load case such that the camera xy- coordinate system corresponded with the principal axes of the undeformed specimen. Camera 1 was thereby always aligned perpendicular to the specimen surface whereas Camera 2 was positioned at an angle of approximately 20°. The DIC system specifications are listed in Table 5.1.

Table 5.1, DIC system specification, processing parameters and system performance.

Hardware (stereo DIC)	
Cameras	$2 \times$ Imager E-Lite 5M
Sensor and digitization	2448×2050, 12 bit
Lens	Sigma 105 mm f/2.8
Imaging distance [mm] / Stereo angle [deg]	~ 500 / 20
Lighting	$2 \times$ NILA ZAILA LED lights
Pixel resolution	~ 50.62 pixel/mm
Field of view [mm]	~ 40×48
Analysis parameters	
DIC Software	DaVis 10, LaVision [156]
Subset size [pixels] / Step size [pixels]	51 / 10
Shape function / Correlation Criterion	Quadratic / LSM
Spatial pre-filtering of displacements	Gaussian smoothing (3×3 kernel)
Strain tensor	Logarithmic
System performance[4]	
Displacement noise floor [μm]	$u \approx 0.443$ / $v \approx 0.288$ / $w \approx 0.688$
Strain noise floor [μm/m]	$\epsilon_{xx} \approx 99$ / $\epsilon_{yy} \approx 87$ / $\gamma_{xy} \approx 102$

To perform the DIC, the specimens were spray painted with white speckles on a black background. Using a black instead of a white background requires less paint to be applied to the already black carbon/epoxy specimens, thus resulting in a thinner layer of spray paint on the surface of the specimens. Five static images were taken before each test, which were averaged and used as the first image in the image sequence of the loaded specimen to reduce the influence of camera noise on the displacement and strain measurements. To spatially resolve the steep strain gradients expected at the hole, and to account for the small diameter hole, a small step size of 10 pixels (0.198 mm) was selected. To select an appropriate subset size, the first image of the loaded image sequence was correlated against the averaged static image using subset sizes of 21, 31, 51 and 71 pixels. The reported noise floors were then determined as the standard deviation of the correlated static displacement and strain fields [170]. At a subset size of 51 pixels (1.008 mm), the critical noise in the strain fields was reduced to the commonly adopted acceptable level of approximately 100 με. A subset size of 51 pixels and a step size of 10 pixels were therefore chosen for the analysis.

---

[4] The system performance (precision) values reported are only indicative. The precision varies from test to test due to DIC system realignment, recalibration, and the quality of the spray-painted speckle patterns.

5.3   Specimen design and manufacturing

Plates were laminated according to the lay-ups in Figure 5.1 by INEOS Team UK using an out-of-autoclave UD carbon/epoxy prepreg system. The laminate lay-ups were selected so that ply thickness and fibre orientation effects could be investigated. To this purpose Laminate 1 consists of 8 'thick' plies, whereas Laminates 2 and 3 consist of 16 'thin' plies, where the 'thin' plies are approximately half the thickness of the 'thick' plies. The plies in Laminates 1 and 2 are orientated at the standard quasi-isotropic fibre orientation angles, $0°$, $90°$ and $+/- 45°$, so that any differences in their failure behaviour can be related to the effect of ply thickness ($t_{ply} = 0.291$ mm versus $t_{ply} = 0.144$ mm). To study the effect of the relative ply orientation angle, also referred to as the pitch angle, Laminate 3 features more dispersed fibre orientation angles with the addition of the non-standard fibre angles, $+/- 22.5°$ and $+/- 67.5°$. As Laminate 2 and 3 have the same ply thicknesses, differences in their failure behaviour and multiaxial strengths can be attributed to the relative fibre orientation angle ($45°$ versus $22.5°$).

The nature of damage initiation and evolution in multidirectional laminates makes the identification of an ideal specimen design for multiaxial testing challenging. The severity of stress concentrations and their locations are influenced by the combined load case, while the initial failure modes, strengths and the evolution of damage is strongly dependent on the laminate lay-up. Therefore, it is difficult to find a specimen shape which enables the comparative assessment of the failure loads across all laminate lay-ups and load cases investigated in this work. The specimen shape should promote failure at an observable location within the gauge section away from the tabs in all lay-ups and loading configurations. A way of increasing the chance of failure initiation at a preferable location regardless of laminate lay-up and load case is the use of an artificial stress raiser such as a small hole in the gauge of the specimen [121]. Apart from the work in [7], [152], where straight-sided open-hole specimens were used for combined tension-shear testing, there is no guideline on an ideal open-hole specimen design used with an Arcan fixture for combined tension/compression-shear testing of multidirectional laminates.

A preliminary stress and failure analysis has therefore been conducted using the commercial FE code ABAQUS 6.14 [115] to study the effect of specimen shape and to find a specimen geometry which promotes failure at the hole. Failure initiation was predicted using the LaRC03 failure criterion [30] as discussed in Section 2.4. Different specimen shapes were considered ranging from the butterfly specimen, inspired by the original Arcan test [25], to lightly waisted specimens, to straight-sided specimens with central holes. The overall conclusion was that straight-sided specimens subjected to shear dominated load cases are prone to damage occurring at the top right and bottom left corners of the specimen due to the high y- direction normal stresses developing (see Figure 5.9 (b)) and that the predicted probability of failure at the hole for lightly waisted specimens is improved. It is concluded that the lightly waisted specimen with a hole offers the best compromise with respect to promoting failure initiation at the hole across all laminate lay-

ups and load cases. Pilot tests with the lightly waisted specimen geometry as shown in Figure 5.4 were conducted and showed promising results. Therefore, the specimen shape was adopted for the experiments presented in this Chapter.
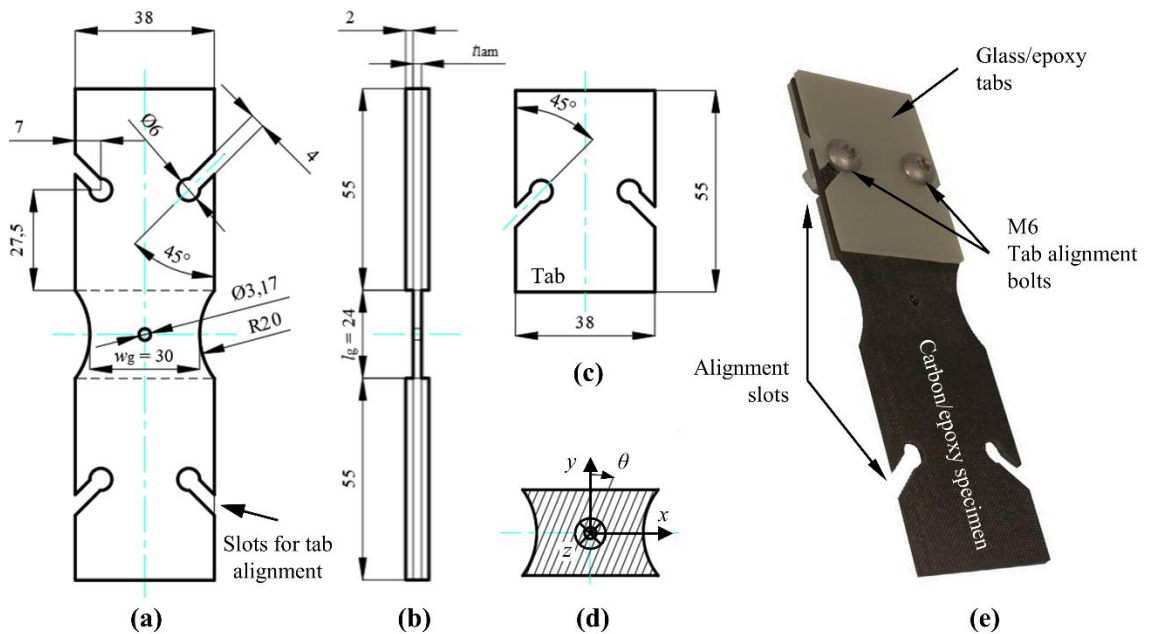
Figure 5.4, Specimen design; (a) in-plane view and (b) side view of the assembled specimen, (c) glass/epoxy tab, (d) definition of fibre orientation angle, θ, and (e) tabbing procedure using alignment slots and bolts. Dimensions given in mm.

Prior to bonding the end tabs, a large batch of specimens was water jet cut following the dimensions in Figure 5.4 (a). Water jet cut tabs as shown in Figure 5.4 (c), made from 2 mm thick quasi-isotropic glass/epoxy circuit board material [171], were bonded to the carbon/epoxy using aerospace grade epoxy adhesive Araldite 2015 [172]. To facilitate the bonding process, slots were integrated into the specimen shape as shown in Figure 5.4 (a) and (c). The tabs were aligned using M6 bolts as shown in Figure 5.4 (e), ensuring an accurate alignment and bond line thickness. The alignment bolts were removed prior to testing. The fibre orientation was defined with respect to the y-axis perpendicular to the waistline as shown in Figure 5.4 (d) of the undeformed specimen, such that the surface ply was orientated at an angle of $\theta = +45°$ for Laminates 1 and 2 and at $\theta = +22.5°$ for Laminate 3. After water jet cutting, the central hole was drilled using a tungsten carbide drill bit on a pillar drill. Due to the limited amount of material supplied in combination with the large number of tests needed for multiaxial testing, the specimens were pre-screened using x-ray CT with a voxel resolution of 30 μm as shown in Figure 5.5.
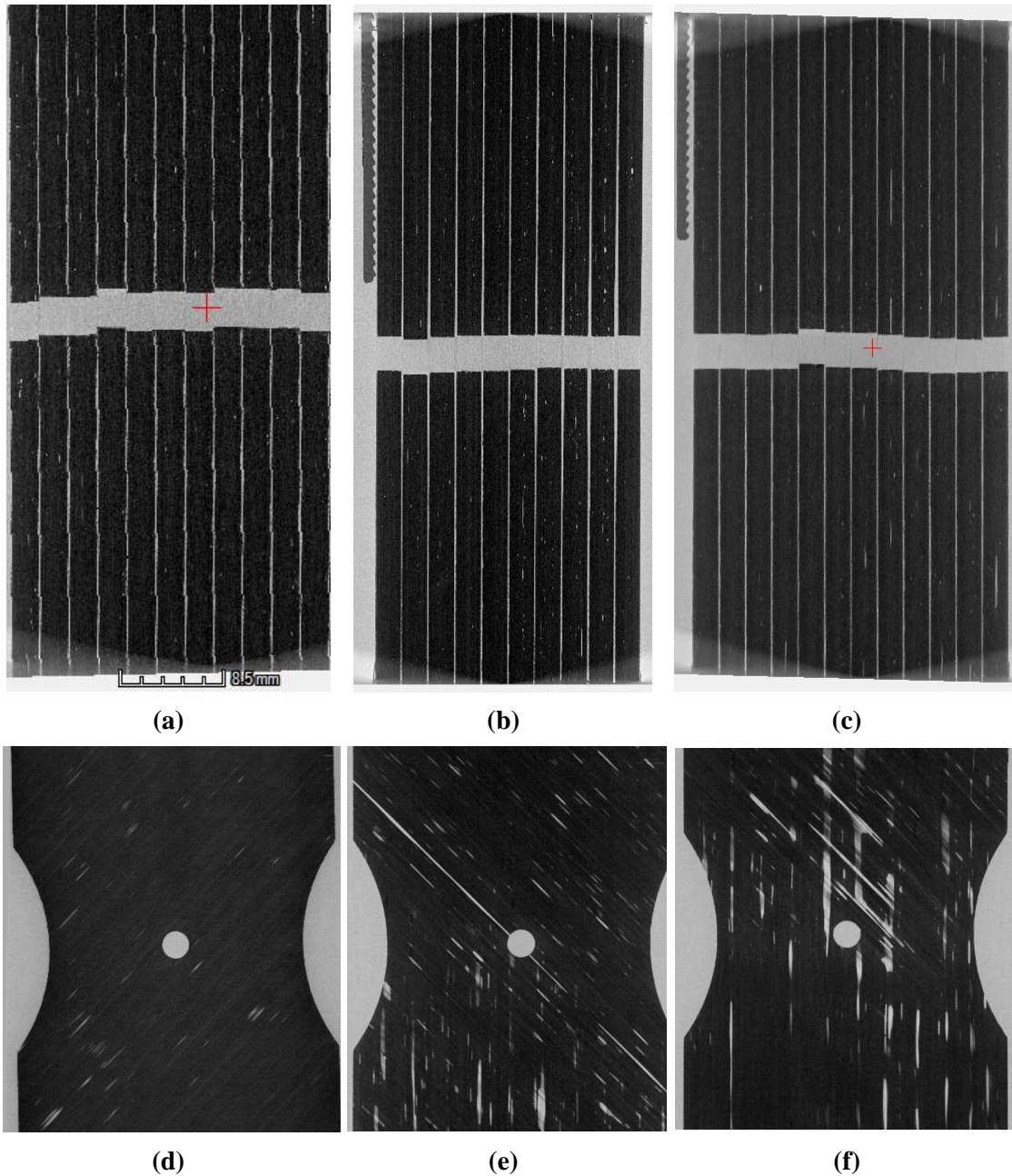
Figure 5.5, x-ray CT scan examples: (a) Through thickness slices of laminate 1 specimens, (b) of laminate 2 specimens, (c) of laminate 3 specimens, and in plane slices of d) a "good" ply, e) a ply with a "butt joint" and (f) a ply with major inter ply defects (Resolution 1 pixel =30 μm).

A maximum of 14 specimens were stacked together and scanned at the same time on the custom 450/225 kVp Hutch CT system in the μ-vis x-ray imaging centre at the University of Southampton. The CT images were reconstructed using VGStudioMAX. Based on visual inspection of the scans, the best specimens with the least manufacturing induced defects (*e.g.* inter/intra ply voids from lamination process or damage to edges due to the water jet cutting and drilling of holes) were selected for testing, to reduce the expected experimental scatter and thus justifying reduced numbers of test specimens per load and laminate configuration.

To improve the precision of the DIC measurements, an attempt was made to remove the peel ply pattern on the specimen surface which can adversely influence the correlation algorithm. Both sides of Laminate 2 specimens were therefore carefully sanded, but the attempt was stopped upon realisation that it is impossible to remove the peel ply pattern completely without damaging the fibres of the surface plies. The surface plies of Laminate 2 specimens are therefore thinner than the rest of the plies. The total laminate thickness, t_{lam}, variation is reported in Table 5.2 as measured using a micrometre at three locations along the gauge section.

Table 5.2, Measured mean thicknesses of the specimens.

	Laminate 1	Laminate 2	Laminate 3
t_{lam} [mm]	2.326	2.133	2.301
% CoV	1.29%	2.71%	1.08%

5.4   DIC based biaxial extensometer

Load-extension curves provide a direct means of assessing the specimen load and failure response. In biaxial experiments such as in the MAF experiment, the test machine extension is only of limited use because the combined tension/compression and shear deformation is not separated. Furthermore, the test machine extension measurement is affected by the compliance of the test machine and additionally of the MAF assembly, which varies for the different loading angles (α) thus making direct comparisons between test cases difficult. Therefore, an alternative method of measurement of the specimen deformation is required that decouples the tension/compression and shear responses, and further is not affected by the compliance of the test set-up. In the following, a DIC based biaxial extensometer which overcomes these limitations is described. The derived load-extension curves are then used in Section 5 to discuss the load and failure response of the tested laminates. Figure 5.6 illustrates the principle of the biaxial extensometer based on DIC measurements.
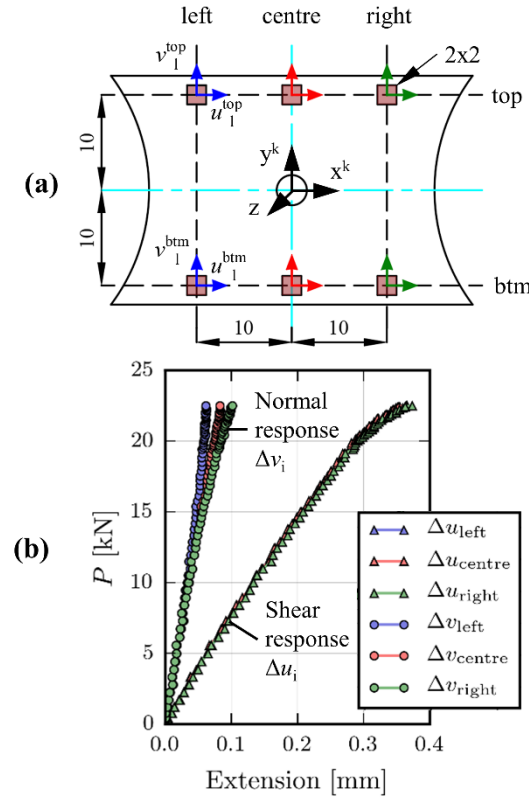
Figure 5.6, Principle of the DIC based virtual extensometer: (a) Location of displacement extraction points and (b) example of derived load-extension curves for a Laminate 3 specimen loaded in combined tension-shear (α = 45°). Dimensions given in mm.

Vertical, *v*, and horizontal, *u*, displacements are extracted from the corresponding displacement fields near the top and bottom edges of the specimen averaged within 2 mm × 2 mm reference areas (red squares in Figure 5.6 (a)). The positions of the reference areas are defined with respect to the centre of the hole, which is also the spatial origin of the DIC data. Thereby, three separate load-extension curves are derived on the left, on the centreline and on the right of the specimen as shown in Figure 5.6 (a). The potential of exploiting the full-field data and of deriving several load-extension curves is a further advantage of the DIC based extensometer, which allows a more detailed assessment of the specimen deformation in comparison to a conventional extensometer which only provides an averaged deformation measurement.

The extracted displacements *u* and *v* at the top and bottom edges, denoted by the superscript 'top' and 'btm', respectively, are then used to derive the vertical extension (normal response) and the horizontal extension (shear response) as follows:

$$\Delta v_i = v_i^{top} - v_i^{btm}$$
$$\Delta u_i = u_i^{top} - u_i^{btm}$$

(5.1)

where the subscript i denotes the horizontal position of the virtual extensometer, *i.e.* left, centre and right, as illustrated in Figure 5.6 (a). The extensions are then used to plot the normal and shear load-extension curves; a typical example is shown in Figure 5.6 (b).

To extract the extensions from the DIC displacement fields, the global x, y, z position coordinates and the corresponding *u, v, w* displacements were exported from the DIC software and post-processed with a purpose-written Python code. Firstly, the position and displacement vectors were transformed so that the origin of the data corresponded to the centre of the hole (via translation transformation) and that the global z-axis was perpendicular to the specimen's surface, while the top and bottom edges were parallel to the global x- axis (via rotation transformation). In the next step, the transformed data, highlighted grey in Figure 5.7 (a), was interpolated on a grid of 0.05 mm × 0.05 mm indicated by black dots in Figure 5.7 (a) [165].
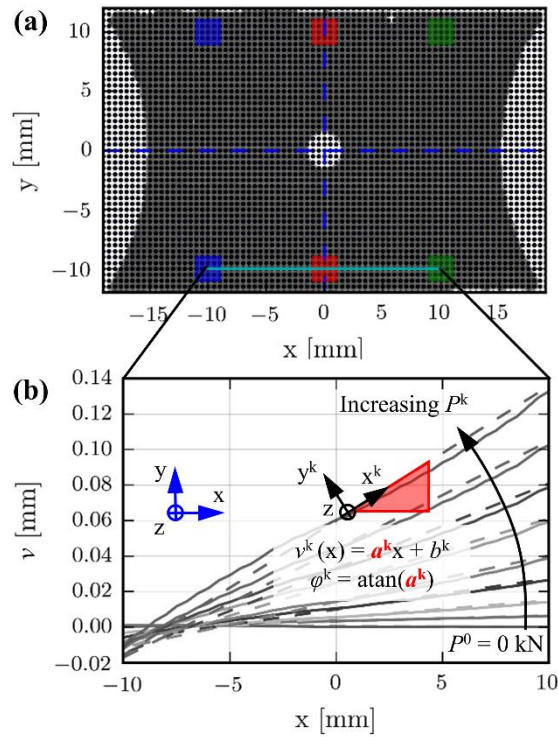
Figure 5.7, Post-processing for virtual extensometer: (a) translating, rotating and interpolating scattered data on regular grid (matrix) and (b) procedure to characterise rigid body rotation.

To use DIC as a biaxial extensometer as described above, it is essential that the kinematics of the MAF are accounted for during data post-processing. As load is applied, an in-plane rigid body rotation of the specimen occurs, so a specimen reference $x^k y^k$-coordinate system is defined that rotates with the specimen (see Figure 5.7 (b)), where k denotes the corresponding load step. At P^0 (zero loading), the specimen reference coordinate system, *i.e.* the $x^0 y^0$-coordinate system, is equivalent to the global xy-coordinate system. The rigid body rotation angle upon loading is denoted φ^k in Figure 5.7 (b) and is dependent on the applied load. The rigid body rotation angle is derived by fitting a straight line to the *v*- displacements along a line near to the bottom edge of

the specimen shown in cyan in Figure 5.7 (a). Based on the slope of the fitted line (a^k) the rigid rotation angle (φ^k) can be determined as shown in Figure 5.7 (b) for every load step, k. Corrected displacement fields in the specimen reference $x^k y^k$- frame were then obtained by superposition of the rigid body rotation fields corresponding to a rigid rotation (φ^k) and the measured fields. The corrected fields are then used to derive the load-extension curves as shown in Figure 5.7 (b). Note that the combined load case is defined solely by the MAF loading angle α and that the effect of the rigid rotation angle φ^k on the applied load case is not accounted for as it is very small.

5.5 Testing procedure

The uniaxial tension tests ($\alpha = 0°$) of Laminates 2 and 3 were conducted on an Instron Schenck 630 kN servo-hydraulic universal test machine, whereas all other tests were conducted on an Instron 8502 100 kN servo-hydraulic test machine. The following testing protocol for the MAF tests was strictly adhered to:

1) The MAF is connected to the test machine crosshead using an appropriate pair of loading holes by the aid of the pulleys as illustrated in Figure 5.3.

2) The specimen is mounted and the clamping bolts (see Figure 5.2 (b)) were torqued up to 75 Nm for $\alpha = 45°$ - $180°$ and up to 120 Nm for $\alpha = 0°$ and $15°$, respectively. The 3D printed jig, as shown in Figure 5.8 (a), is used to ensure accurate alignment of the specimen within the grips as illustrated in Figure 5.8 (b). The 3D printed alignment jig consists of a spacer (red) with a bulge, which when installed on the MAF, aligns the two MAF arms accurately and ensures that the desired specimen gauge length is met. Two 'sliders' (grey) are mounted in a groove on the spacer which hold the specimen in place while the clamping bolts are tightened. The shape of the sliders fit the gauge section shape of the specimen and ensures accurate specimen alignment in respect to the MAF arms. If other specimen shapes are tested, a new spacer or new sliders can easily be 3D printed. The alignment tool is removed prior to testing.

3) The balance weight system is installed to eliminate the spurious stresses/strains induced into the specimen by the weight of the MAF as shown in Figure 5.3.

4) The load cell is balanced. Therefore, the load reading does not include the load carried by the specimen generated by the lower half of the MAF assembly and the connected balance weight. The load reading was therefore corrected in a post-processing step.

5) The MAF is connected to the test machine actuator at the bottom and is pre-tensioned to approximately $P = 0.1$ kN to take up initial slack in the MAF assembly.

6) Five static images are taken with the calibrated stereo DIC system of the undeformed specimen.

7) Image acquisition is started at a rate of 2 Hz. The specimen was loaded in displacement control (1 mm/min) until ultimate failure.

(a)   **(b)**
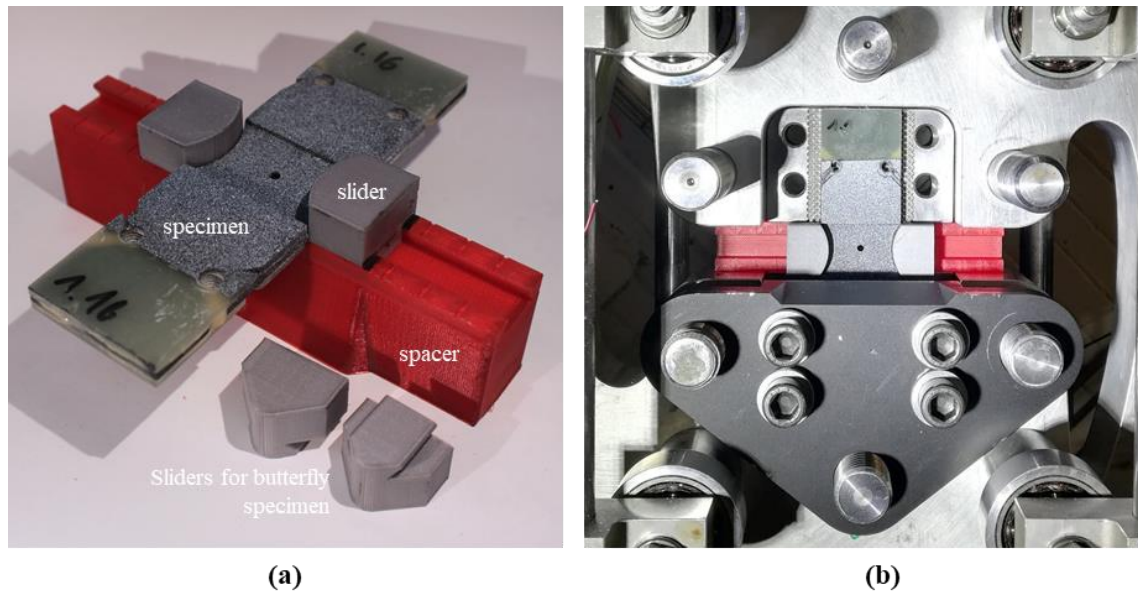
Figure 5.8, Specimen alignment tool: (a) 3D printed 'spacer' (red) and 'sliders' (grey) with a specimen installed, and (b) alignment tool and specimen mounted on the MAF.

5.6   Failure initiation and evolution

The MAF/DIC approach was used to investigate the three laminate configurations (see Figure 5.1) subjected to tension ($\alpha = 0°$), combined tension-shear ($\alpha = 15°$, $45°$), shear ($\alpha = 90°$), compression-shear ($\alpha = 135°$, $165°$) and compression ($\alpha = 180°$). Figure 5.9 shows the complex strain fields induced in specimens loaded in tension ($\alpha = 0°$) and shear ($\alpha = 90°$), obtained using DIC.
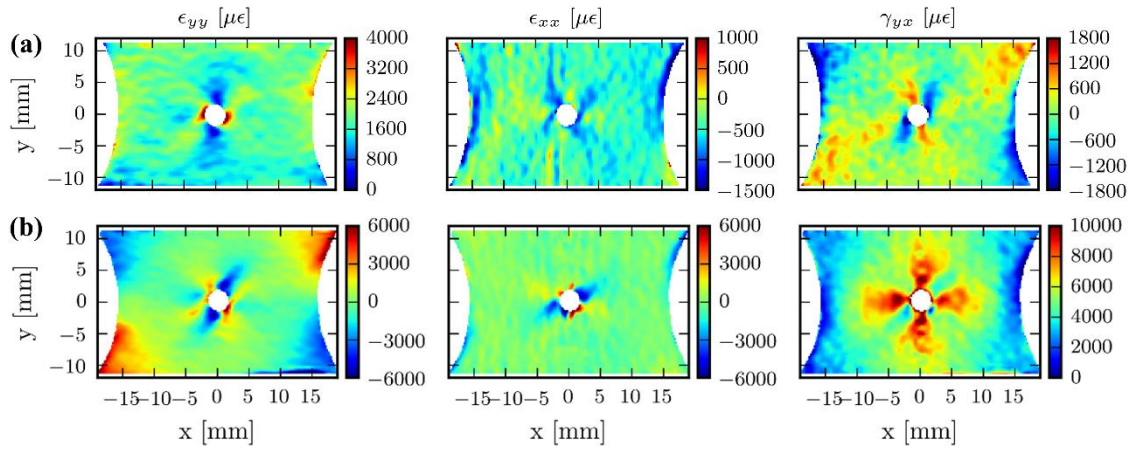
Figure 5.9, Strain fields in open-hole specimens at $P = 7.5$ *kN before initiation of failure: (a) subjected to uniaxial tensile loading, and (b) subjected to shear loading.*

In the linear elastic part of the load response, strain fields for combined load cases are simply linear superpositions of the strain fields shown in Figure 5.9. Failure modes and locations discussed later can in some cases be attributed to the strain concentrations seen in Figure 5.9. Further, the fields can be used to validate model predictions for the elastic material response before failure initiation (see Figure 6.3 and Figure 6.4 in Chapter 6).

Figure 5.9 (a) shows that in tension loaded specimens, vertical tensile normal strain concentrations ϵ_{yy} develop on both sides of the hole, while shear strain concentrations γ_{yx} are observed as a radial pattern around the hole. The strain fields agree well with similar data in the literature for open-hole tensile tests [173]. Notably γ_{xy} and ϵ_{xx} strains also develop at the curved specimen edges. Figure 5.9 (b) shows the development of high γ_{xy} shear strain concentrations in a radial pattern around the hole, while high compressive ϵ_{yy} and ϵ_{xx} normal strains are observed around the hole as well. Notably ϵ_{yy} strains also develop in the four corners of the specimen at the curved edges.

Based on the DIC results, two distinct failure events were observed across the load and lay-up configurations tested. Matrix cracks in the surface plies (+45° for Laminates 1 and 2, +22.5° for Laminate 3) can accurately be located based on the maximum principal normal strain fields (ϵ_{max}), as shown in Figure 5.10.
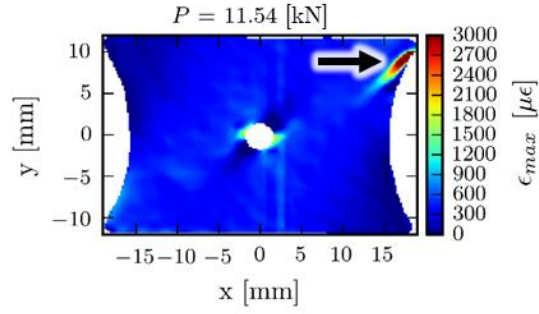
Figure 5.10, Maximum principal normal strain field used to characterise transverse cracking of the surface plies. Example shown: Laminate 1 in tension-shear loading (α = 45°).

Here the maximum principal strain is used because it is invariant to coordinate system transformation, thus simplifying comparison between specimens and with model predictions. Surface cracks indicated by high principal strain concentrations were then confirmed by visual inspection of the white-light images.

A second failure event can be determined from the out-of-plane displacement maps shown in Figure 5.11, where local out-of-plane displacement changes indicate the occurrence of sub-surface damage.
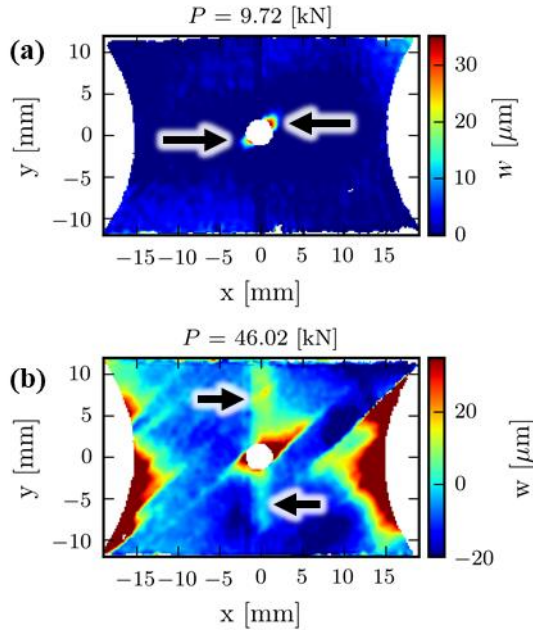
Figure 5.11, Out-of-plane w-displacement field used to characterise delamination failure: (a) delamination damage at the notch for Laminate 1 loaded in shear (α = 90°) and (b) delamination at the notch and edges for Laminate 1 loaded in tension (α = 0°).

The local surface elevation indicates the formation of a displacement discontinuity in the through-thickness direction. While the associated initial damage mode cannot be clearly determined, it is confirmed by visual inspection that the out-of-plane displacement gradients result in the initiation

of delamination (cracks at the interfaces of the plies). This can be seen through DIC camera 2 (see Figure 5.11), through which the hole and the side edges of the specimen can be observed.

In load cases with a dominant shear component, high out-of-plane displacement gradients in the vicinity of the hole aligned with the +45° fibre direction are observed as shown for example in Figure 5.11 (a) for Laminate 1 loaded in shear. Delamination cracks open further in shear and compression dominated load cases, which enhances their signature in the out-of-plane displacement plots. In the out-of-plane displacement maps for the tensile load cases shown in Figure 5.11 (b), delaminated areas can also be identified: The dark red areas are clearly associated with edge/hole induced delamination failure, verified by visual inspection of the specimen edges through DIC camera 2 (see Figure 5.3). A less pronounced change in the out-of-plane displacement is observed at the top and the bottom of the hole. Based on similar experimental data in the literature [174], this indicates delamination in the 0°/−45° ply interface between the two fibre splits typically occurring in the 0° plies of quasi-isotropic OHT specimens at both sides of the hole (see Figure 2.23).

The main failure events are chronologically identified in the load-extension plots in Figure 5.12 to Figure 5.16 for specimens loaded in tension ($\alpha = 0°$), tension-shear ($\alpha = 45°$), shear ($\alpha = 90°$), compression-shear ($\alpha = 135°$) and compression ($\alpha = 180°$), respectively.

1.1: Matrix cracks in +45 ply at hole and edges	2.1: Matrix cracks in +45 ply at top right edge	3.1: Matrix cracks in +22.5 ply at top right and bottom left corners and hole
1.2: Delamination at hole	2.2: Delamination at hole	3.2: Delamination at hole
1.3: Disintegrated gauge section (matrix cracks in +/-45, 90 plies, fibre breaks in 0 plies, delamination)	2.3: Disintegrated gauge section (matrix cracks in +/-45,90 plies, fibre breaks in 0 plies, delamination)	3.3: Disintegrated gauge section (matrix cracks in +/-22.5, +/-67.5, +/-45, 90, plies, fibre breaks in 0 plies, delamination)

Figure 5.12, Load-extension curves for Laminates 1 – 3 subjected to tension loading ($\alpha = 0°$).

1.1: Matrix cracks in +45 ply at top right corner	2.1: Matrix cracks in +45 ply at hole and top right corner edges	3.1: Delamination at hole
1.2: Delamination at hole	2.2: Matrix cracks in +45 ply at bottom left corner and hole delamination	3.2: Matrix crack in +22.5 ply at hole
1.3: Macroscopic crack from bottom left to top right corner across whole gauge	2.3: Macroscopic crack from bottom left to top right corner across whole gauge	3.3: Macroscopic crack from bottom left to top right corner across whole gauge

Figure 5.13, Load-extension curves for Laminates 1 – 3 subjected to combined tension-shear loading (α = 45°).

1.1: Delamination at hole	2.1: Delamination at hole	3.1: Delamination at hole
1.2: Matrix cracks in +45 ply at hole	2.2: Matrix cracks in +45 ply at hole	3.2: Matrix cracks in +22.5 ply at hole
1.3: Matrix cracks in +45 ply at bottom left and top right corner edges	2.3: Matrix cracks in +45 ply at bottom left and top right corner edges	3.3: Macroscopic crack from bottom left to top right corner across whole gauge
1.4: Macroscopic crack from bottom left to top right corner across whole gauge	2.4: Macroscopic crack from bottom left to top right corner across whole gauge	

Figure 5.14, Load-extension curves for Laminates 1 – 3 subjected to shear loading (α = 90°).
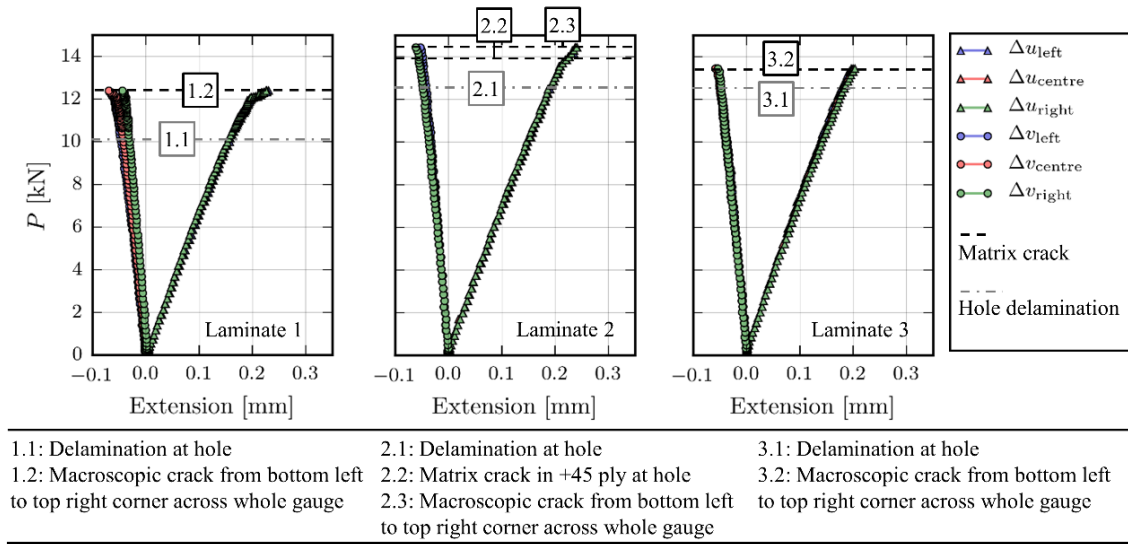
Figure 5.15, Load-extension curves for Laminates 1 – 3 subjected to combined compression-shear loading (α = 135°).
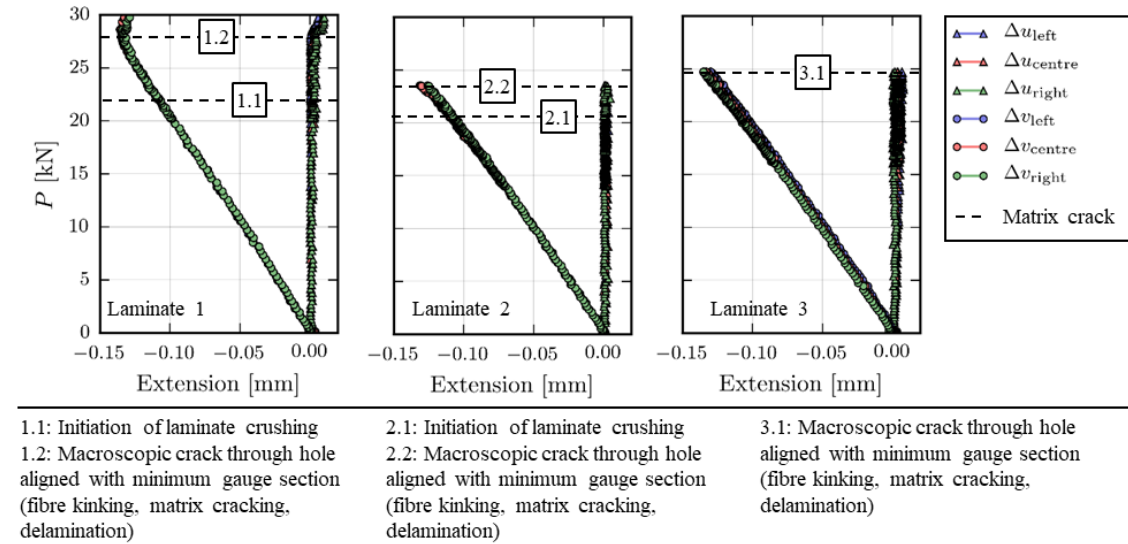
Figure 5.16, Load-extension curves for Laminates 1 – 3 subjected to compression loading (α = 180°).

All load-extension curves, as given in Figure 5.12 to Figure 5.16, display linear behaviour for most part of the load response regardless of the applied combined load case. Only the shear responses for all load cases display nonlinear behaviour close to the maximum load. It is also noted that all laminates show the same compliance within the linear elastic load regime, confirming that the homogenised elastic properties of the three laminate configurations are equivalent. Most of the load-extension curves obtained for a given specimen at the left, centre and right are in close agreement. However, for some cases, the normal load extension curves (P - Δv_i) obtained at the different horizontal locations deviate slightly (see *e.g.* Laminate 2 in Figure 5.13). This indicates that damage does not necessarily occur simultaneously on both sides of the specimens but that one side cracks first, leading to stiffness reduction on one side of the specimen.

This may be due to material variability or due to a slightly asymmetrical load introduction to the specimen. Further, it is observed that failure events detectable in the DIC fields are not necessarily reflected as a load drop in the load-extension plots, nor can the failure events be easily detected by visual inspection alone. This makes DIC an effective identification tool to characterise damage events that otherwise would be overseen. However, it should be noted that DIC is a surface-based technique, and although some internal damage events or internal nonlinearities as in [175] may be observed on the surface, not all internal failure events are detectable on the specimen surfaces. Detecting such damage events would require the use of *e.g.* x-ray CT [152], which is beyond the scope of this chapter. Nevertheless, the obtained data is useful to visualise failure locations and governing failure mechanisms of the laminate which provide means to validate failure models (see Chapter 6). By assessing initial failure events across all load and lay-up configurations, the following can be concluded:

- For tensile dominated load cases ($\alpha = 0°$, $15°$) the first detectable failure events in all laminates are inter-fibre matrix cracks in the surface plies starting at the hole and the edges (Figure 5.12). The cracks initiating at the hole can clearly be attributed to the high tensile vertical normal strain concentrations shown in Figure 5.9 (a).

- For tension-shear ($\alpha = 45°$) loading, the first failure initiation in Laminates 1 and 2 are inter-fibre matrix cracks on the surface whereas Laminate 3 delaminates at the hole (Figure 5.13).

- For shear ($\alpha = 90°$) and combined compression-shear ($\alpha = 135°$, $165°$) loading, failure initiates as delamination in all laminates at the hole (Figure 5.14 and Figure 5.15). The location and orientation of the delamination can clearly be attributed to the high vertical compressive normal strain concentration above and below the hole shown in Figure 5.9 (b).

- Failure in compression ($\alpha = 180°$) occurs suddenly and without any notable prior failure events on the surface of the specimen (Figure 5.16).

5.7   Ultimate multiaxial open-hole specimen strength
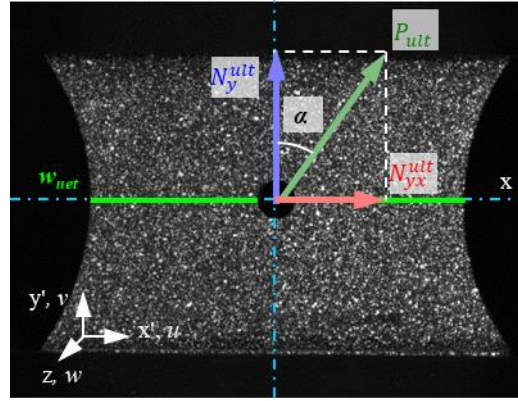
Figure 5.17, View through DIC camera and definition of the representative combined tension/compression (N_y^{ult}) and shear (N_{yx}^{ult}) load case.

To compare the ultimate multiaxial open-hole specimen strength among the three laminates with respect to the different load cases, tension/compression-shear failure envelopes were derived. Therefore, the normal, N_y^{ult}, and shear, N_{yx}^{ult}, component of the ultimate failure load (P_{ult}) were obtained using the corresponding loading angle (α) as illustrated in Figure 5.17, according to Equations (3.1). P_{ult} is expected to be influenced by the specimen shape and the hole size, which is also intrinsic to uniaxial open-hole tests [9], [120], and it has been shown in Section 5.6 that damage has not in all cases initiated at the hole. The measured ultimate failure load (or average failure stress) is therefore best regarded as the failure load (or strength) of the specimen. Furthermore, mean representative stress-based ultimate failure envelopes ($\overline{\sigma_{yy}^{ult}}$ - $\overline{\tau_{yx}^{ult}}$) were also defined according to Equations (3.1). Note that the mean stresses do not represent the actual stresses which govern failure, but instead serve as a convenient averaged (across specimen cross section) quantity to compare the performance of all laminates for different combined loading in this study.

The ultimate failure loads, P_{ult}, as measured by the load cell of the test machine and corrected for the weight of the MAF and the balance system (see Figure 5.3) are reported in Table 5.3 for all specimens.

Table 5.3, Ultimate failure loads (P$_{ult}$) sustained by each tested specimen.

Load case	$\overline{\sigma_{yy}/\tau_{yx}}$	No.	Laminate 1 P_{ult} [kN]	Laminate 2 P_{ult} [kN]	Laminate 3 P_{ult} [kN]
Tension $\alpha = 0°$	$+\infty$	1	51.58	55.16	54.84
		2	49.33	52.29	55.06
Tension-shear $\alpha = 15°$	3.732	1	30.96	43.89	45.35
		2	29.22	44.36	44.99
Tension-shear $\alpha = 45°$	1	1	16.80	22.29	22.51
		2	16.41	22.79	22.18
Shear $\alpha = 90°$	0	1	12.02	13.21	12.62
		2	11.92	13.18	12.53
Compression-shear $\alpha = 135°$	−1	1	13.52	14.44	13.46
		2	12.39	14.07	13.44
Compression-shear $\alpha = 165°$	−3.732	1	20.95	20.71	19.01
		2	20.71	20.86	19.60
Compression $\alpha = 180°*$	$-\infty$	1	21.92 / 27.52	20.34 / 23.56	24.75
		2	20.92 / 29.77	21.42 / 23.77	23.52 / 24.51

* Initiation of laminate crushing and maximum load sustained are reported if applicable.

For the case of compressively loaded specimens ($\alpha = 180°$), an additional failure load is reported which can be associated with the onset of laminate crushing which is characterised by the start of regular small load drops in the test machine load-displacement curves.

Table 5.3 shows that all laminates are strongest when loaded in tension ($\alpha = 0°$), and that the addition of shear reduces the maximum load carrying capability. The ultimate failure load increases again when compressive loading is applied and reaches about half of the ultimate tensile failure load in compression ($\alpha = 180°$). Figure 5.18 shows the tension/compression-shear failure envelopes derived using Equations (3.1) based on the ultimate failure loads in Table 5.3 in load space (a) and stress space (b), respectively.
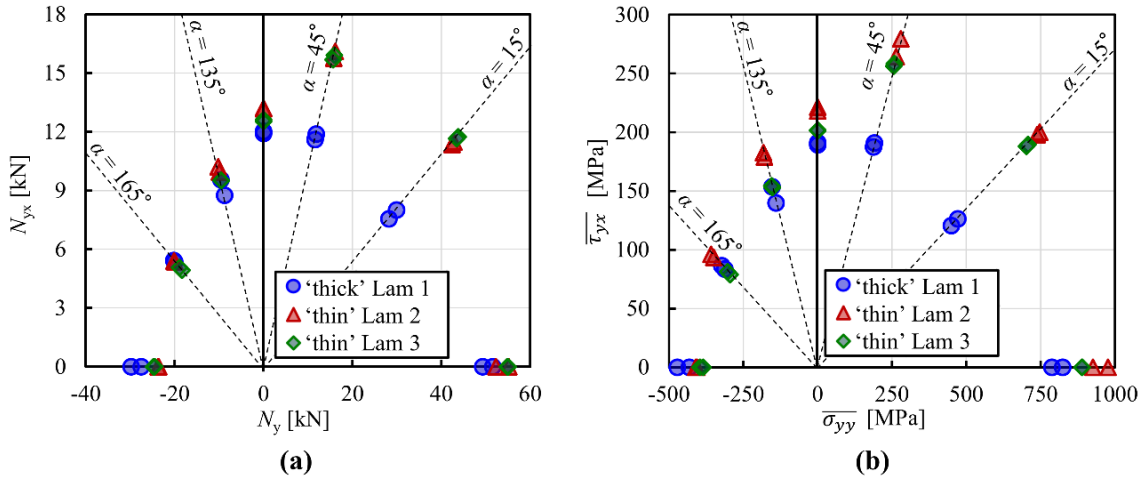
Figure 5.18, Ultimate load carrying capability of the different laminate configurations and load cases: (a) measured load-based failure envelope, (b) net cross section mean stress-based failure envelope.

Figure 5.18 reveals a strong effect of ply thickness on the load carrying capability when the specimens are subjected to tension-shear loading. The effect is most pronounced at $\alpha = 15°$, where specimens made from 'thin' ply Laminates 2 and 3 carry up to 150% of the load carried by specimens made of 'thick' ply Laminate 1. The ply thickness effect in combined tension-shear is therefore also considerably greater than for tensile loaded specimens. The observed behaviour for tension-shear loading can be related to the in-situ strength effect that states that matrix cracking in UD plies is delayed in 'thin' plies compared to 'thick' plies [77], as well as to the higher delamination onset stresses in the 'thin' plies [122]. Moreover, matrix cracking and delamination failure in open-hole tests are interacting, thus supressing matrix cracking in the 'thin' plies will also delay the onset of delamination [108] and subsequent fibre failure, which both govern the ultimate strength.
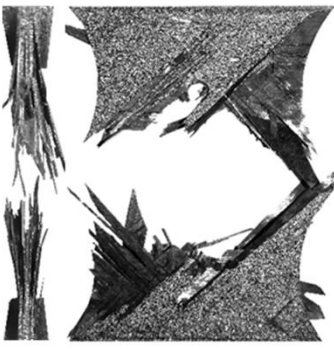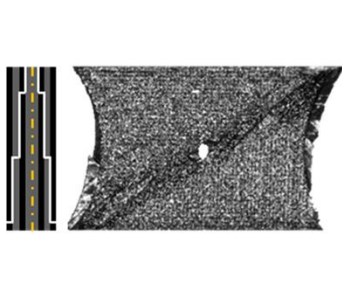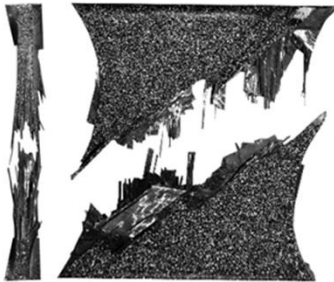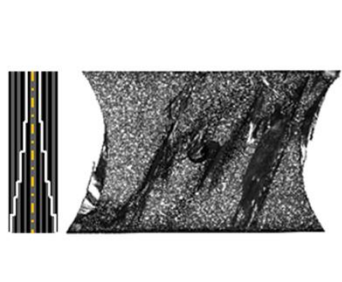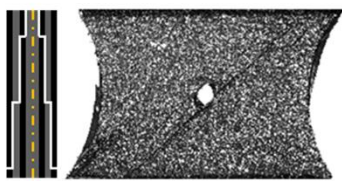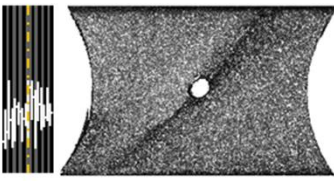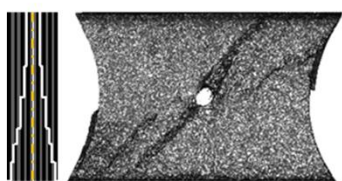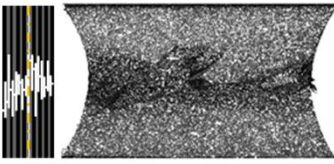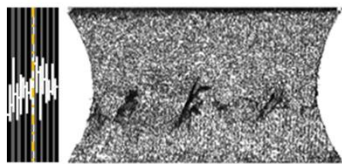
In contrast, the effect of ply thickness on the open-hole specimen strength is not evident for compression-shear loading. The in-situ effect on the transverse compressive strength is smaller than on the transverse tensile strength [176], resulting in similar crack initiation stresses for the 'thin' and 'thick' ply laminates loaded in the compressive loading regimes. Furthermore, the load-carrying capability in compression-shear of all laminates is limited by the relatively low compressive UD fibre strength. Thus, delaying the onset of matrix cracking and delamination has not such a significant effect on the ultimate open-hole specimen strength in compressive loading regimes as in the tensile loading regime where delamination dominates ultimate failure.

Furthermore, no significant effect of the relative fibre orientation angle (45° versus 22.5°) on the ultimate load carrying capability can be seen by comparing the load-based failure envelopes in Figure 5.18 (a) of the 'thin' ply Laminates 2 and 3, with an average difference in failure load of only 1% between the laminates. However, based on the mean stress-based failure envelope in

Figure 5.18 (b), Laminate 2 sustains on average 10% higher stresses than Laminate 3. This difference may at first glance indicate the existence of a minor effect of the relative ply orientation angle on the ultimate load carrying capability. However, because Laminate 2 is on average 10% thinner than Laminate 3 due to the sanded surface plies (as described in Section 5.3), it cannot be concluded that this phenomenon is attributed to the ply orientation effect alone. Instead, it is more likely that the surface 45° ply has only a minor influence on the ultimate strength of the laminate. Hence, partial removal of the Laminate 2 surface plies does not significantly reduce the ultimate failure load of Laminate 2 as evidenced in Figure 5.18 (a). However, it increases the derived mean stresses in Figure 5.18 (b) due to the reduced overall laminate thickness. It can therefore be concluded that if an effect of the relative fibre orientation on the ultimate failure load does exist, it will be much smaller than the effect of ply thickness for the laminates and load cases investigated here. Photographs of selected specimens after ultimate failure are presented in Table 5.4.

Table 5.4, Selected specimens after ultimate failure. Crack paths are highlighted as white lines in through-thickness schematics in specimens that did not break in two halves.

Laminate 1	Laminate 2	Laminate 3

Tension dominated ($\alpha = 0° - 15°$)

Tension-shear ($\alpha = 45°$)

Shear and shear with moderate compression ($\alpha = 90°-135°$)

Compression dominated ($\alpha = 165°-180°$)

Where the specimens have not fractured into two halves, schematics of the through-thickness crack paths are presented for clarity. It should be noted that, although some initial failure events can be distinguished (see Figure 5.12 - Figure 5.16), a cascade of various interacting failure events (transverse matrix cracks, fibre breaks, delamination) happen suddenly and within a fraction of a second. This means that the ultimate failure pattern is influenced by highly dynamic events inducing a considerable degree of variability in the patterns observed. Nevertheless, from

visual inspection, the following observations can be made that will facilitate the validation of predictive models:

- For tensile dominated load cases ($\alpha = 0°$, $15°$), all specimens fail in the typical open-hole tensile test pattern as reported in the literature [120]. All specimens break in two halves, indicating that final failure involves complete fracture of the $0°$ plies and in the case of Laminate 3 also the $+/−22.5°$ plies.

- For combined tension-shear loading ($\alpha = 45°$), the specimens no longer fail in the typical open-hole tensile specimen pattern [120]. Instead, macroscopic fracture planes (*i.e.* areas of major damage accumulation in the form of matrix cracks, delamination and fibre failure) run from the bottom left corner through the hole to the top right corner, where both corner areas are largely delaminated. The opposite corners instead show only little damage. Specimens of Laminate 2 break in two halves while specimens of Laminate 1 and 3 do not disintegrate completely but develop a series of through-thickness cracks forming effectively a wedge centred by the mid $0°$ plies.

- For shear and moderate combined compression-shear loading ($\alpha = 90°$ - $135°$), all specimens exhibit a macroscopic fracture plane running diagonally from bottom left to top right corners accompanied by large delamination in the same corners, while the opposite corners show little damage. For Laminates 1 and 3 a through-thickness wedge shaped crack path is evident, while Laminate 2 shows a dispersed crack pattern.

- For compressive load cases ($\alpha = 165°$-$180°$), the fracture planes align approximately with the minimum gauge section. In the through-thickness view, the cracks are dispersed, and the plies are crushed accompanied by matrix cracking, fibre breaks and delamination.

5.8   Conclusions

A novel experimental procedure based on a new MAF design developed in this thesis, stereo DIC and a lightly waisted open-hole specimen has been devised to investigate multidirectional laminates subjected to combined tension/compression-shear loading. The new MAF has enabled the characterisation of multidirectional composite laminates subjected to both combined tension-shear and compression-shear loading up to failure, which has not been possible before. Using the developed experimental procedure, three quasi-isotropic carbon/epoxy laminates were tested to investigate the effect of ply thickness and relative fibre orientation angles on the failure initiation and ultimate multiaxial open-hole specimen strength of multidirectional laminates.

Based on the DIC measurements, two macroscopic failure events were distinguished, *i.e.* matrix cracking of the surface plies and delamination at the hole. For specimens loaded in tension and combined tension-shear, initial failure events (matrix cracking in the surface ply) occurred simultaneously at the hole and the edges, while for the shear, combined compression-shear and compression load cases, the first failure events occurred at the hole. Load-extension curves were constructed based on the full-field displacement maps, which enabled the visualisation of the combined tension/compression-shear deformation and failure evolution.

The experimental data obtained showed laminate lay-up effects on failure evolution and ultimate failure. Moreover, it revealed significant dependencies of the magnitude of the laminate lay-up effect on the applied combined load case. For combined tension-shear loading, ply thickness has a strong effect on the ultimate specimen failure strength, where the 'thin' ply specimens were up to 150% stronger than the 'thick' ply specimens, while for combined compression-shear loading no significant ply thickness effect was observed. Furthermore, no significant effect of the relative fibre orientation angle on the ultimate strength was observed regardless of the combined loading regime.

The overarching conclusion from the work in the chapter impacts on the design of high-performance composite materials and structures, in that the use of laminates with thinner but increased numbers of plies may be preferential in areas of combined tension-shear loading, despite the increased manufacturing cost. However, for the material systems investigated, no significant benefit is apparent for using the 'thin' plies for laminates subjected predominantly to compression-shear loading. Moreover, according to the experiments conducted there is no significant gain of using non-standard fibre orientation angle laminates in terms of ultimate strength for the investigated load cases. However, further investigation is needed to ascertain if these findings are applicable for different hole sizes or stress raiser geometries, *i.e.* different specimen shapes.

The work conducted provides a definitive demonstration of the usefulness of the developed MAF/DIC procedure to study multidirectional composite laminates subjected to combined

tension/compression-shear loading. Based on the promising test results, it is recommended for future work to investigate the possibility for an improved specimen design to encourage failure initiation at the hole to improve comparability of the multiaxial open-hole strength. Furthermore, the use of x-ray CT in combination with the MAF test is recommended for future work which would enable the clear identification of sub-surface damage events which could be corelated against surface-based observations. Furthermore, the complex material behaviour captured in the MAF test results stemming from the various lay-up and load configurations investigated, makes the extracted high-fidelity experimental data well suited for the validation and development of novel numerical and analytical tools to predict failure in composite laminates. The data obtained in this chapter is therefore used in Chapter 6 for the validation of a state-of-the-art FE-based modelling framework developed for 'virtual testing'.

Chapter 6

Predicting ply thickness effects in composite laminates subjected to tension/compression and shear

6.1   Introduction

Efficient design and certification of FRP structures requires tools that can accurately predict the failure behaviour and strength of a wide range of composite materials and laminate lay-ups under general multiaxial loading conditions. The integration of 'virtual testing' techniques into design and certification has the potential to reduce cost and time-to-market and can accelerate the development of new composite materials and structural concepts [17], [21].

Open-hole tension (OHT) and compression (OHC) tests are commonly utilised for the validation of FE-based progressive damage models developed for 'virtual testing' (see Chapter 2, Section 2.6). These tests are ideally suited to assess the predictive capability of meso-scale progressive failure models because they offer interesting validation cases as the failure behaviour and OHT/OHC strengths are not only dependent on the UD material system but also on the laminate lay-up and hole size (see Chapter 2, Section 2.6) [121]. However, these modelling frameworks have not been rigorously assessed with respect to their ability to accurately simulate failure for more complex multiaxial loading conditions in which the interaction of failure mechanisms is different. Therefore, multiaxial experiments have been proposed for model validation (see Chapter 2, Section 2.7): cruciform specimens loaded in tension-tension, compression-compression, or tension-compression have been proposed in [41], while Tan *et al.* [7], [18] assessed model predictions against open-hole experimental data obtained in the combined tension-shear, but not in the compression-shear loading regime.

In Chapter 5, multiaxial open-hole tests were conducted using the new MAF in both the combined tension-shear and compression-shear loading regimes on out-of-autoclave carbon/epoxy laminates provided by INEOS Team UK. Three quasi-isotropic carbon/epoxy laminates with different lay-ups were studied and a significant influence of the ply thickness on the multiaxial open-hole specimen strength was observed. Therefore, in this chapter, a state-of-the-art meso-scale model is used to simulate progressive failure in quasi-isotropic carbon/epoxy laminates, with two different UD ply thicknesses subjected to combined tension/compression-shear loading

with the aim to assess the capability of the model to predict the experimentally observed ply thickness effects in Chapter 5 (Laminates 1 and 2 are considered).

In the meso-scale model, intra-laminar damage is modelled using the CDM in [17] developed at the University of Porto for 'virtual testing' (see Chapter 2, Section 2.4). Inter-laminar damage is predicted by means of mixed-mode CZMs [107], [109] native to ABAQUS (see Chapter 2, Section 2.5). The CDM was implemented in a user defined material subroutine (VUMAT) by the research group in Porto and was applied by the author to the MAF specimens. An FE modelling strategy is proposed based on structured, fibre-aligned meshes that are able to account for the interaction between inter- and intra-laminar damage for all of the investigated combined load cases.

To the knowledge of the author, the capability of a meso-scale model to predict failure of multidirectional open-hole specimens in the full tension/compression-shear loading regime has not previously been studied. This research therefore provides a significant contribution in advancing the industry-readiness of predictive tools for composite laminates and informs the further direction of model development through rigorous validation against high-fidelity experimental data.

The work presented in this Chapter has led to a tentative fourth journal paper under preparation in collaboration with Prof. P. P. Camanho's research group at the University of Porto (see Chapter 7, Section 7.3).

6.2   Meso-scale finite element model

The commercial FE software ABAQUS/Explicit 6.14-3 [115] was used to simulate the MAF experiments. The physical boundary conditions imposed by the MAF on the specimens, as shown in Figure 5.2 (a), are simplified in the modelling space as shown in Figure 6.1, ignoring the clamped area of the specimen.
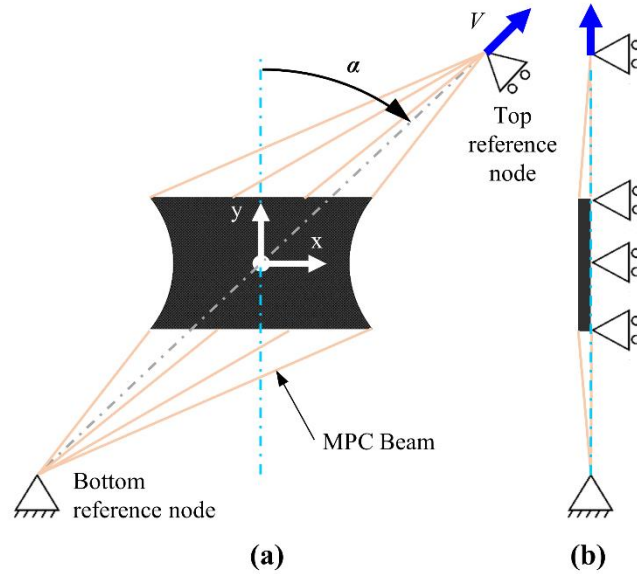
Figure 6.1, Mimicking the MAF boundary conditions in model space: (a) plane view, (b) side view.

The boomerang shaped arms of the MAF are modelled by multi point constraints (MPC) of type 'Beam', while the loading holes in the MAF arms are represented by reference nodes in the model space (see Figure 6.1 (a)). The position of the reference nodes is defined by the loading angle α and defines, like the choice of the loading hole pair in the experiment (see Figure 5.2 (a)), the combined tension/compression-shear load case applied. The bottom reference node is fixed, whereas a velocity boundary condition is imposed on the top reference node up to ultimate failure. To reduce the computational cost, the through-thickness symmetry of the lay-ups is exploited by applying symmetry boundary conditions on the mid-plane of the specimen as shown in Figure 6.1 (b). The multidirectional laminates are modelled on the meso-scale with the homogenised UD plies as the basic building block as shown in Figure 6.2.
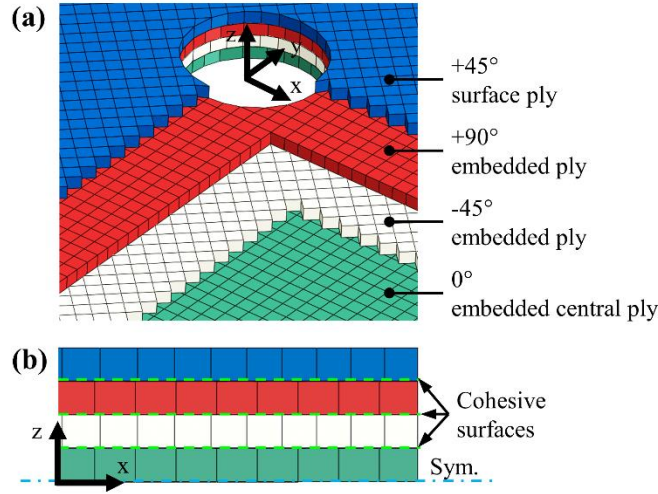
Figure 6.2, Meso-scale modelling framework illustrated on the Laminate 1 model: (a) 3D solid elements for UD plies with structured, fibre aligned mesh, and (b) cross section showing cohesive surfaces in between the solid UD plies.

Intra-laminar damage (fibre failure and in-plane matrix cracking) are modelled using a user-defined material model (VUMAT) based on the CDM proposed by Furtado *et al.* [17], which is described in more detail in Section 6.2.1. In addition, inter-laminar failure between the plies (delamination) is accounted for using cohesive surfaces placed between the plies as shown in Figure 6.1 (b), which are described in Section 6.2.2. A structured fibre aligned mesh, as shown in Figure 6.1 (a), was used to mitigate some of the mesh induced directional bias of the CDM on the prediction of intra-laminar crack propagation [15], [41], [20]. This enabled a physically more accurate prediction of subcritical inter- and intra-laminar matrix cracks and their interactions, which was deemed crucial in the prediction of the multiaxial open-hole specimen strength of the tested laminates. The plies are meshed with a single layer of linear reduced integration solid elements through the ply thickness. The mesh consists predominantly of $0.35 \times 0.35 \times t_{ply}$ mm³ brick elements (C3D8R) with some wedge elements (C3D6) along the curved edges and around the hole (see Figure 6.1 (a)). The mesh was designed in the commercial CAD software Rhino 5 [177] and was then imported into the FE software ABAQUS/Explicit [115].

A quasi-static explicit dynamic analysis was conducted to avoid convergence issues due to the nonlinear material behaviour, including strain softening and discrete cohesive failure and contact problems. To reduce the computational cost, the loaded reference node was displaced at an increased loading rate of 100 mm/s. The velocity boundary condition was applied via a smooth step loading amplitude along 1/10 of the total displacement applied. To further accelerate the analysis, variable semi-automatic mass scaling on elements with a stable time increment smaller than 1×10^{-7} s was used. To meet the typical requirements for a quasi-static analysis, the kinetic energy was ensured to be below 5% of the internal strain energy throughout the analysis [115].

6.2.1   The ply continuum damage model (CDM)

Consider a UD fibre reinforced composite ply with the x_1 axis parallel to the fibres, the x_2 axis transverse to the fibres and the x_3 axis perpendicular to the plane of the ply. Assuming transverse isotropy with respect to the fibre direction, the stress-strain relationship reads [178]:

$$
\begin{bmatrix} \epsilon_{11} \\ \epsilon_{22} \\ \epsilon_{33} \\ \gamma_{12} \\ \gamma_{13} \\ \gamma_{23} \end{bmatrix} = \begin{bmatrix} H_{11} & H_{12} & H_{13} & 0 & 0 & 0 \\ H_{12} & H_{22} & H_{23} & 0 & 0 & 0 \\ H_{13} & H_{23} & H_{33} & 0 & 0 & 0 \\ 0 & 0 & 0 & H_{44} & 0 & 0 \\ 0 & 0 & 0 & 0 & H_{55} & 0 \\ 0 & 0 & 0 & 0 & 0 & H_{66} \end{bmatrix} \begin{bmatrix} \sigma_{11} \\ \sigma_{22} \\ \sigma_{33} \\ \tau_{12} \\ \tau_{13} \\ \tau_{23} \end{bmatrix}
\tag{6.1}
$$

where **H** is the compliance matrix with its components defined as:

$$
H_{11} = \frac{1}{(1-d_1)|\sigma_{11}|}\left(\frac{\langle\sigma_{11}\rangle}{E_1} + \frac{\langle-\sigma_{11}\rangle}{E_{1c}}\right); \quad H_{22} = \frac{1}{(1-d_2)E_2}; \quad H_{33} = \frac{1}{(1-d_3)E_2}
$$

$$
H_{44} = \frac{1}{(1-d_6)G_{12}}; \quad H_{55} = \frac{1}{(1-d_5)G_{12}}; \quad H_{66} = \frac{1}{(1-d_4)G_{23}}
\tag{6.2}
$$

$$
H_{12} = -\frac{v_{12}}{|\sigma_{11}|}\left(\frac{\langle\sigma_{11}\rangle}{E_1} + \frac{\langle-\sigma_{11}\rangle}{E_{1c}}\right); \quad H_{13} = -\frac{v_{12}}{|\sigma_{11}|}\left(\frac{\langle\sigma_{11}\rangle}{E_1} + \frac{\langle-\sigma_{11}\rangle}{E_{1c}}\right); \quad H_{23} = -\frac{v_{23}}{E_2}
$$

where d_i are the damage variables, E_1 and E_{1c} are the fibre longitudinal tensile and compressive Young's moduli to account for the different response in fibre longitudinal tension and compression, and where all other variables have their usual meaning. The Macaulay bracket $\langle\bullet\rangle$ returns the argument $\bullet$ if positive or zero otherwise.

To account for the effect of crack closure under load reversal on d_1 and d_2, it is necessary to track damage caused by tension (d_{1+}, d_{2+}) separately from damage caused by compression (d_{1-}, d_{2-}) as:

$$
d_1 = d_{1+}\frac{\langle\sigma_{11}\rangle}{|\sigma_{11}|} + d_{1-}\frac{\langle-\sigma_{11}\rangle}{|\sigma_{11}|}
\tag{6.3}
$$

$$
d_2 = d_{2+}\frac{\langle\sigma_{22}\rangle}{|\sigma_{22}|} + d_{2-}\frac{\langle-\sigma_{22}\rangle}{|\sigma_{22}|}
\tag{6.4}
$$

where the sign of the corresponding normal stress defines if a damage mode is either passive or active. For shear damage only one damage variable (d_6) is defined, since shear cracks cannot close under load reversal. The damage variables d_3, d_4 and d_5 read:

$$
d_3 = 1-(1-d_{1-})(1-d_{2-}); \quad d_4 = d_6; \quad d_5 = d_{1+}
\tag{6.5}
$$

The elastic properties of the UD ply used to inform the model and the associated test methods used for their determination are reported in Table 6.1. More details on test set-ups and results are provided in Appendix C.

Table 6.1, Elastic properties of the UD ply.

E_1 [MPa] (% CoV)	143190 (1.83)	ISO 527-5 [179]
E_{1c} [MPa] (% CoV)	142620 (3.45)	ASTM D3410 [88]
E_2 [MPa] (% CoV)	7900 (0.12)	ISO 527-5 [179]
G_{12} [MPa] (% CoV)	3940 (0.33)	MAF test (Appendix C.3)
v_{12} (% CoV)	0.328 (5.6)	ISO 527-5 [179]

The domain of the elastic response (no damage) of the UD ply under a complex stress state is defined by an approximation of the LaRC03-04 failure criteria [30], [60]. The approximation consists herein in that not all failure functions considered in the LaRC03 criterion, as discussed in Chapter 2, Section 2.4), are included and that no iterative calculation is required to find the angle of the fracture plane (α), as is the case in the compressive matrix criterion in the LaRC03 criterion.

Four separate damage activation functions are defined for longitudinal fibre tensile failure (ϕ_{1+}), longitudinal fibre compressive failure (ϕ_{1-}), transverse matrix failure where the fracture plane is perpendicular (ϕ_{2+}), or not perpendicular to the mid-plane of the ply (ϕ_{2-}). Thereby, fibre tensile failure is predicted using the simple maximum stress criterion defined as:

$$\phi_{1+} = \frac{E_1}{X_T} \epsilon_{11} \tag{6.6}$$

where all variables have their usual meaning. For transverse matrix failure where the fracture plane is perpendicular to the mid-plane of the ply, two failure functions are defined for transverse tensile and moderate transverse compressive stress states defined as (see Chapter 2, Sections 2.4.2):

$$\phi_{2+} = \begin{cases} \sqrt{\left(1 - \frac{\mathscr{G}_{2+}}{\mathscr{G}_6}\right)\frac{\sigma_{22}}{Y_T} + \left(\frac{\mathscr{G}_{2+}}{\mathscr{G}_6}\right)\left(\frac{\sigma_{22}}{Y_T}\right)^2 + \left(\frac{\tau_{12}}{Y_T}\right)^2} & \text{if } \sigma_{22} \geq 0 \\ \frac{1}{S_L}\left\langle |\tau_{12}| + \eta^L \sigma_{22} \right\rangle & \text{if } \sigma_{22} < 0 \end{cases} \tag{6.7}$$

where $\mathscr{G}_{2+}$ and $\mathscr{G}_6$ are the energies associated with transverse tensile and shear fracture of the ply, and the longitudinal coefficient of influence (η^L) is defined in Equation (2.35).

Fibre compression failure is predicted using a fibre kinking model (see Chapter 2, Section 2.4.3) defined by:

$$\phi_{1-} = \frac{1}{S_L} \langle |\tau_{12}^m| + \eta^L \sigma_{22}^m \rangle \tag{6.8}$$

where failure occurs when the stresses in the coordinate system associated with the rotated (or kinked) fibres, σ_{22}^m and τ_{12}^m defined in Equations (2.40) to (2.42), reach the limit stress state for matrix cracking defined in Equation (6.7).

Transverse matrix failure under high transverse compression is also modelled based on the Mohr-Coulomb hypothesis. It is assumed that failure results from a quadratic interaction between the effective shear stresses acting on the fracture plane (τ_L^{eff} and τ_T^{eff}):

$$\phi_{2-} = \sqrt{\left(\frac{\tau_{eff}^T}{S_T}\right)^2 + \left(\frac{\tau_{eff}^L}{S_L}\right)^2} \quad \text{if } \sigma_{22} < 0 \tag{6.9}$$

where τ_L^{eff}, τ_T^{eff} are similarly defined as in Equations (2.36) and (2.37) with the addition of the sliding angle θ:

$$\tau_{eff}^T = \langle -\sigma_{22} \cos\alpha_0 (\sin\alpha_0 - \eta^T \cos\alpha_0 \cos\theta) \rangle \tag{6.10}$$

$$\tau_{eff}^L = \langle \cos\alpha_0 (|\tau_{12}| + \eta^L \sigma_{22} \cos\alpha_0 \sin\theta) \rangle \tag{6.11}$$

where the transverse shear strength (S_T) is approximated by Equation (2.39) and where θ is the angle between the resultant shear traction vector on the fracture plane and the transverse direction (x_2-axis) given by (also see Figure 2.13):

$$\theta = \arctan(\frac{-|\sigma_{12}|}{\sigma_{22} \sin\alpha_0}) \tag{6.12}$$

α_0 in Equations (6.10) and (6.11) is the angle of the fracture plane in respect to the through-thickness x_3 axis in a UD ply subjected to uniaxial transverse compression at failure stress (Y_C) assumed to be approximately 53°. Moreover, η^T, is the transverse friction coefficient defined in Equation (2.34).

Based on the failure functions given in Equations (6.6), (6.7), (6.8) and (6.9), the elastic domain thresholds, r_i ($i = 1+, 1-, 2+, 2-$), accounting for load reversal are defined as:

$$r_{1+} = \max\{1, \max_{s=0,t}\{\phi_{1+}^s\}, \max_{s=0,t}\{\phi_{1-}^s\}\} \tag{6.13}$$

$$r_{1-} = \max\{1, \max_{s=0,t}\{\phi_{1-}^s\}\} \tag{6.14}$$

$$r_{2+} = \max\{1, \max_{s=0,t}\{\phi_{2+}^s\}, \max_{s=0,t}\{\phi_{2-}^s\}\} \tag{6.15}$$

$$r_{2-} = \max\{1, \max_{s=0,t}\{\phi_{2-}^s\}\} \tag{6.16}$$

The distinction between r_{1+} and r_{1-} assumes that cracks caused by longitudinal tensile loading (ϕ_{1+}) close under load reversal, leaving the elastic domain unchanged, while kink bands formed under fibre compressive stresses (ϕ_{1-}) further inflict damage upon load reversal and thus increase the elastic domain. Similarly, transverse cracks which are perpendicular to mid-plane of the ply (ϕ_{2+}) close when compressive load is applied and therefore leave the elastic domain unchanged while cracks which are not perpendicular to the ply mid-plane (ϕ_{2-}) inflict further damage upon load reversal and thus increase the elastic domain. r_i take the value of 1 when the material is undamaged and increase with the evolution of damage: They are linked back to the damage variables in Equation (6.1) via the damage evolution laws governed by the fracture toughness ($\mathcal{G}_{1+}$, $\mathcal{G}_{1-}$, $\mathcal{G}_{2+}$, $\mathcal{G}_{2-}$, $\mathcal{G}_{6}$) associated with each damage mode and the assumed softening laws as shown in Figure 2.16.

In longitudinal tension (Figure 2.16 (a)) the initially linear elastic response is followed by a bilinear softening law after longitudinal tensile damage is identified. In longitudinal compression (Figure 2.16 (b)), the initially linear elastic ply behaviour is followed by a bilinear softening law where the first segment is associated with the formation of kink bands while the second horizontal segment is associated with kink band broadening under constant stress. The initially linear elastic stress-strain behaviour in transverse tension and compression (Figure 2.16 (c)) is followed by a simple linear softening law. Finally, the nonlinear behaviour of UD composites in shear is accounted for by assuming a bilinear shear stress-strain relationship as shown in Figure 2.16 (d), where S_L^P defines the onset of shear nonlinearity, and where K_P is the shear incremental stiffness under 'plastic' flow. After failure in shear, the elastic properties are degraded following a linear softening law (Figure 2.16 (d)). The shapes of the softening laws are described based on the fracture toughness of each failure mechanism, the shape parameters (f_{XC}, f_{XT}, f_{GT} – see Figure 2.16) and the characteristic length l^* of the finite element [103]. The strengths of the UD ply and the methods used for their determination are reported in Table 6.2. More details on test set-ups and results are provided in Appendix C.

Table 6.2, Strengths of the UD ply.

X_T [MPa] (% CoV)	2774 (1.05)	ISO 527-5 [179]
X_C [MPa] (% CoV)	1394 (2.21)	ASTM D3410 [88]
Y_T [MPa] (% CoV)	52 (8.70)	ISO 527-5 [179]
Y_C [MPa] (% CoV)	173 (0.75)	ASTM D3410 [88]
S_L [MPs] (% CoV)	81.19 (4.86)	BS EN ISO 14130 [180]
S_L^P [MPa]	60	MAF test (Appendix C.3)
K_P [MPa]	0.076	
Y_{BT} [MPa]	32	Scaled as in [17]
Y_{BC} [MPs]	410	Scaled as in [17]

Apart from the uniaxial strengths, the model requires the input of the biaxial strengths Y_{BT} and Y_{BC}. These values were scaled based on the uniaxial strengths according to [17] and are also reported in Table 6.2. The parameters for the nonlinear shear stress-strain relationship (S_L^P, K_P) were determined by a judiciously selected bilinear fit to the shear stress-strain curves obtained using butterfly specimens on the MAF as reported in Appendix C.3.

The fracture toughness values and the parameters governing the shapes of the softening laws in Figure 2.16 are given in Table 4. Due to the lack of experimental data, they were selected based on a sensitivity study reported in Appendix D, where the bounds on the toughness values were determined from values reported in the literature for the well-characterised IM7/8552 and T800/M21 carbon/epoxy material systems [17], while also considering two different bilinear shear fits. Considering seven different material parameter combinations, the average coefficient of variation in the predicted multiaxial open-hole specimen strengths for both laminates across all load cases was less than 6%. Based on the sensitivity study, the best fit (see Table 6.3) was used for the simulations presented in this chapter.

Table 6.3, UD ply fracture toughness values and softening law shape parameters [17].

$\mathscr{G}_{2+}$ [kJ/m^2]	0.28	IM7/8775 [17]
$\mathscr{G}_{2-}$ [kJ/m^2]	1.31	IM7/8775 [17]
$\mathscr{G}_{6}$ [kJ/m^2]	0.79	IM7/8775 [17]
$\mathscr{G}_{1+}$ [kJ/m^2]	340	T800/M21 [17]
f_{XT}	0.4	T800/M21 [17]
f_{GT}	0.52	T800/M21 [17]
$\mathscr{G}_{1-}$ [kJ/m^2]	61	IM7/8775 [17]
f_{XC}	0.2	IM7/8775 [17]

Furthermore, the transverse and shear strengths of a UD ply embedded in a multidirectional laminate depend on the ply thickness (t_{ply}) and on the position of the ply in the laminate stack (embedded vs. surface ply – see Chapter 2, Section 2.4.2) [49], [77], [80], [181]. Therefore, the in-situ strengths (Y_T^{is}, S_L^{is}, Y_C^{is}) are calculated for both Laminates 1 and 2 based on the fracture mechanics models presented in [17], which account for the bilinear shear stress-strain curves assumed in the model. The derived in-situ strengths are reported in Table 6.4. It is observed that the in-situ strengths for the 'thin' ply Laminate 2 are either equal or higher than the ones for the 'thick' ply Laminate 1.

Table 6.4, Calculated in-situ strengths based on the UD material properties.

	Laminate 1	Laminate 2
Embedded central ply		
t_{ply} [mm]	0.5820	0.2910
Y_T^{is} [MPa]	82.36	98.67
S_L^{is} [MPa]	99.19	99.19
Y_C^{is} [MPa]	211.35	211.35
Embedded ply		
t_{ply} [mm]	0.2910	0.1455
Y_T^{is} [MPa]	98.67	139.54
S_L^{is} [MPa]	99.19	99.19
Y_C^{is} [MPa]	211.35	211.35
Surface ply		
t_{ply} [mm]	0.2910	0.07275
Y_T^{is} [MPa]	62.10	124.19
S_L^{is} [MPa]	81.19	84.81
Y_C^{is} [MPa]	173.00	180.72

The CDM used includes modifications to account for the effect of through-the-thickness stresses on the fibre kinking failure mode as well as on the shear fracture toughness. The modifications are not critical in the predominantly plane stress problems investigated in this work. Hence, they are not described in this chapter and the reader is referred to [17] for further details.

6.2.2 Cohesive zone model

Inter-laminar failure (delamination) is modelled using the mixed-mode cohesive zone models proposed by Camanho *et al.* [109] and Turon *et al.* [107] as implemented into the surface contact algorithms native to ABAQUS/Explicit [115]. The detailed formulation of the CZM framework was given in Chapter 2, Section 2.5. Failure is identified by means of a quadratic failure criterion based on the inter-laminar normal (τ_n) and shear (τ_{sh}) strengths. Damage growth is governed by the Benzeggagh-Kenane (B-K) mixed-mode damage propagation criterion. The linear traction-separation laws are informed by the interlaminar mode I and II critical fracture energies G_{IC} and G_{IIC} respectively, and the mixed mode interaction parameter, η_{B-K}. The material input parameters informing the CZM are given in Table 6.5. K_n is selected according to recommendations in [109], τ_n is set equal to Y_T, whereas τ_{sh} was measured using the ILSS test [180]. The remaining interface properties were taken from the IM7/8552 carbon/epoxy material system as reported in the literature based on the sensitivity study conducted in Appendix D.

Table 6.5, Interface (cohesive zone) material parameters.

K_n [MPa]	10^6	[109]
τ_n [MPa]	52	Equal Y_T
τ_{sh} [MPa]	81.19	ISO 14130 [180]
G_{IC} [kJ/m2]	0.28	IM7/8552 [17]
G_{IIC} [kJ/m2]	0.79	IM7/8552 [17]
η_{B-K}	1.45	IM7/8552 [17]

6.3 Simulation results and model validation

For the prediction of progressive failure, it is crucial to assess whether the simulated stress/strain state in the specimens within the linear elastic material response, using the material properties and the simplified boundary conditions in the FE model described in Section 6.2, are accurate. Therefore, the DIC strain maps from Figure 5.9 are compared against FE predictions in Figure 6.3 and Figure 6.4 at a load level prior to failure initiation for the example of Laminate 1 loaded in tension ($\alpha = 0°$) and shear ($\alpha = 90°$), respectively. The two cases are shown as examples, because the strain fields for all other load cases within the linear elastic loading regimes are simple linear superpositions of the compared fields of Figure 6.3 and Figure 6.4.
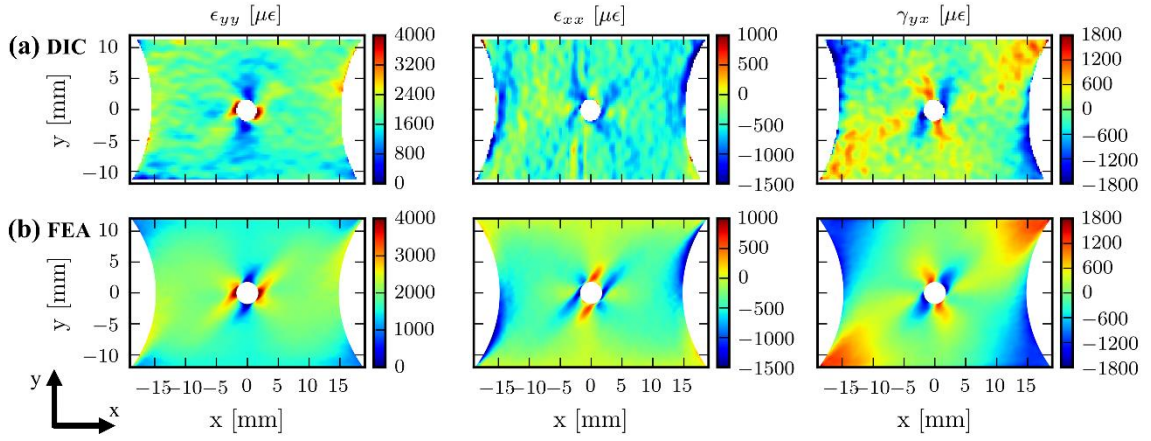
Figure 6.3, Surface strain fields in Laminate 1 specimen subjected to uniaxial tension (α = 0°) at P = 7.5 kN; (a) DIC measurements and (b) FE predictions.
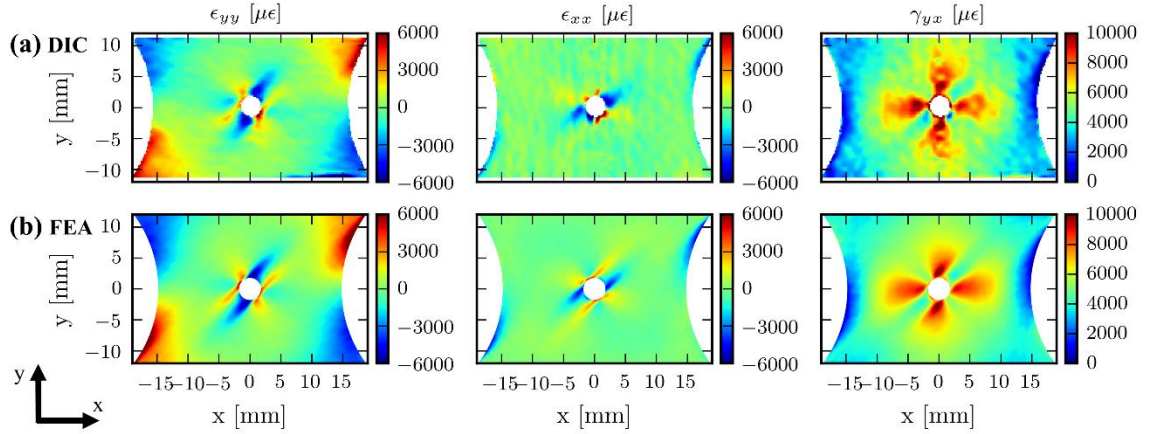
Figure 6.4, Surface strain fields in Laminate 1 specimen subjected to uniaxial shear (α = 90°) at P = 7.5 kN; (a) DIC measurements and (b) FE predictions.

It can be seen in Figure 6.3 that for the case of uniaxial tensile loading ($\alpha = 0°$), the dominant vertical strains (ϵ_{yy}) obtained from the model prediction and experiment are in good agreement, including the important strain concentrations to both sides of the hole. Even though the signal to noise ratio in the DIC horizontal (ϵ_{xx}) and shear (γ_{yx}) strain maps is poor due to low strain values recorded for this load case, it is still shown that the model predictions are generally in agreement with the DIC measurement. The predicted FE strain maps are also in good agreement with the DIC strain maps for the shear load case ($\alpha = 90°$) shown in Figure 6.4. All strain patterns as well as the magnitudes of the important strain concentrations at the hole match well. The good agreement between the predicted (FE) and experimental (DIC) strain fields confirms that the elastic properties determined for the UD plies (see Table 6.1) are accurate, and further that the assumed model space boundary conditions (see Figure 6.1) are reasonable.

6.3.1 Multiaxial open-hole specimen strength

The predicted multiaxial open-hole specimen failure envelopes for 'thick' ply Laminate 1 and 'thin' ply Laminate 2 are compared against the experimental data from Chapter 5 in Figure 6.5 in the N_y - N_{yx} load space.
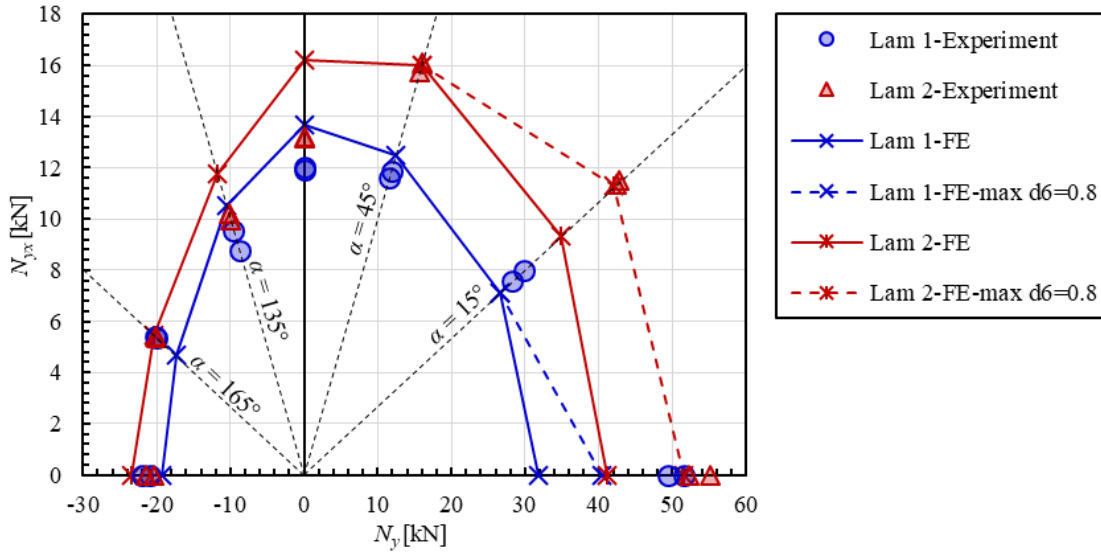
Figure 6.5, Combined tension/compression-shear open-hole specimen failure envelopes: Simulation vs. experiment (from Chapter 5).

It is observed from Figure 6.5 that the model predicts that Laminate 2 is stronger than Laminate 1 for all load cases, especially for the tensile load cases. This matches well with the experimental data and shows that the model can predict ply-thickness effects on the multiaxial open-hole specimen strength qualitatively. Ignoring the tension case for Laminate 1 and 2 ($\alpha = 0°$) and the tensile dominated tension-shear case ($\alpha = 15°$) for Laminate 2 and the associated dashed line envelopes in Figure 6.5, the average relative predictive error across all other cases is 10%. The best prediction is within 0.4% of the experimental mean value for Laminate 2 loaded in tension-shear ($\alpha = 45°$) and the worst prediction is within 21% of the mean experimental value for Laminate 2 in shear ($\alpha = 90°$). However, to predict the tensile dominated cases within acceptable accuracy (dashed line failure envelopes in Figure 6.5), an engineering solution is adopted which is described in the following. An investigation into the underpredicted tensile load cases showed that the critical failure event at ultimate load is linked to a sudden mesh instability in the plies subjected to high fibre tension and shear. An example is shown in Figure 6.6 (a) where the central 0° plies near the hole in Laminate 1 subjected to uniaxial tension ($\alpha = 0°$) is shown: A distinct 'zig-zag' pattern in the mesh near the stress/strain concentration at the hole can be observed and is identified as the critical failure event governing the ultimate load, which is severely underpredicted by over 40%.
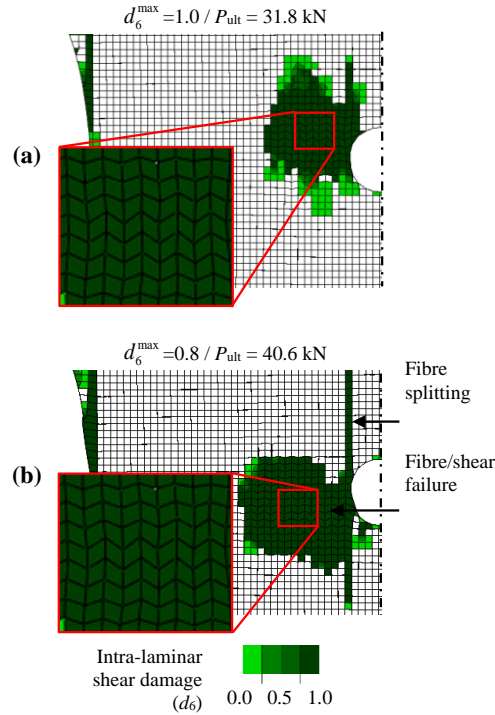
Figure 6.6, Predicted failure mechanisms of the 0° ply in Laminate 1 under tension (α = 0°) just after peak load: (a) d_6^{max} *=1.0 and (b)* d_6^{max} *=0.8.*

It was found that the mesh 'zig-zag' is associated with the intra-laminar shear damage variable d_6 as visualised in Figure 6.6. This was confirmed by limiting the maximum allowable shear damage (d_6^{max}) in the 0° ply to 0.8 which led to an increase of the predicted ultimate failure load by 24%. Limiting d_6^{max} in Laminate 2 in the 0° plies for the uniaxial tension load case ($\alpha = 0°$) and in the 0° and +45° plies for the combined tension-shear load case ($\alpha = 15°$) also improved the prediction of the ultimate failure load significantly (see dashed line failure envelopes in Figure 6.5). It is shown that the CDM used in this work cannot accurately predict fibre splitting following fibre failure in areas of high fibre tensile and shear stresses. Hence the notch blunting effect (see Chapter 2, Section 2.6) and stress redistribution is not captured well, leading to premature failure predictions. It is believed that accounting for large shear deformations within the model formulations would remedy the limitation [182], [183]. For the investigated out-of-autoclave material system, accounting for large deformations would be especially important, because it is 18% more compliant and at the same time 18% stronger in the fibre direction than *e.g.* the autoclave consolidated aerospace grade IM7/8552 carbon/epoxy material system [17] for which the CDM was originally developed. Thus, the deformations including shear (rotations) before catastrophic failure can be expected to be higher in the material system investigated in this chapter. Furthermore, the use of fibre aligned meshes has been shown to promote the 'zig-zag' instability, whereas it is suppressed to some extent in unstructured meshes. However, limiting the allowable shear damage variable (d_6^{max}) to 0.8 was found to be a practical engineering solution to mitigate this numerical instability. The final mean relative errors on the prediction of the multiaxial open-hole specimen strengths are reported in Table 6.6.

Table 6.6, Errors for each individual simulation and overall mean relative errors.

Load case (α)	Laminate 1	Laminate 2	Both
0° tension	−22% *	−4% *	**13%**
15°	−9%	−1% **	**5%**
45°	6%	0%	**3%**
90° shear	13%	21%	**17%**
135°	14%	16%	**15%**
165°	−15%	1%	**8%**
180° compression	−10%	12%	**11%**
AVG all load cases	**13%**	**8%**	**10%**
AVG tension-shear	**13%**	**7%**	**10%**
AVG compression-shear	**13%**	**12%**	**13%**

* $d_6^{\max} = 0.8$ in 0° plies

** $d_6^{\max} = 0.8$ in 0° and +45° plies

Across all the load cases and laminate configurations, the mean relative error of the predicted multiaxial open-hole specimen strength is 10% while the maximum errors are 22% (conservative) for Laminate 1 in tension and 21% (non-conservative) for Laminate 2 in shear. Considering that similar, or more advanced models, predict uniaxial OHT and OHC strengths within 10%, these are encouraging results given the more complex combined load cases and the new out-of-autoclave material system investigated in this chapter.

6.3.2   Damage visualisation

To assess the prediction of damage initiation and evolution against experimental data, ply-by-ply damage maps were plotted for both Laminates and all the investigated load cases in Appendix E. An example is shown for Laminate 1 in combined tension-shear ($\alpha = 45°$) in Figure 6.7 and in combined compression-shear ($\alpha = 135°$) in Figure 6.8. The plies are numbered from $i = 1$ (mid-ply) to $i = 4$ in Laminate 1 and $i = 8$ in Laminate 2 (outer ply), respectively. In all damage maps shown in this chapter, the intra-laminar damage (blue for fibre failure (d_1), red for matrix failure (d_2)) of the i_{th} ply is superimposed on the inter-laminar damage (black for delamination (CSDMG)) in the interface beneath, *i.e.* between ply i and ply (i-1). Furthermore, the predicted damage patterns were compared at three load steps: the first load step (failure initiation) corresponds to the first occurrence of damage that was identified using the DIC surface measurements as defined in Chapter 5. Secondly, predicted damage patterns were also compared against experimental data at the ultimate load (P_{ult}) and thirdly at post-ultimate load (post-P_{ult}). This approach does not only enable the validation of the predictions against the experiments, but also provides additional insights into the critical failure mechanisms as discussed in more detail in Section 6.4.
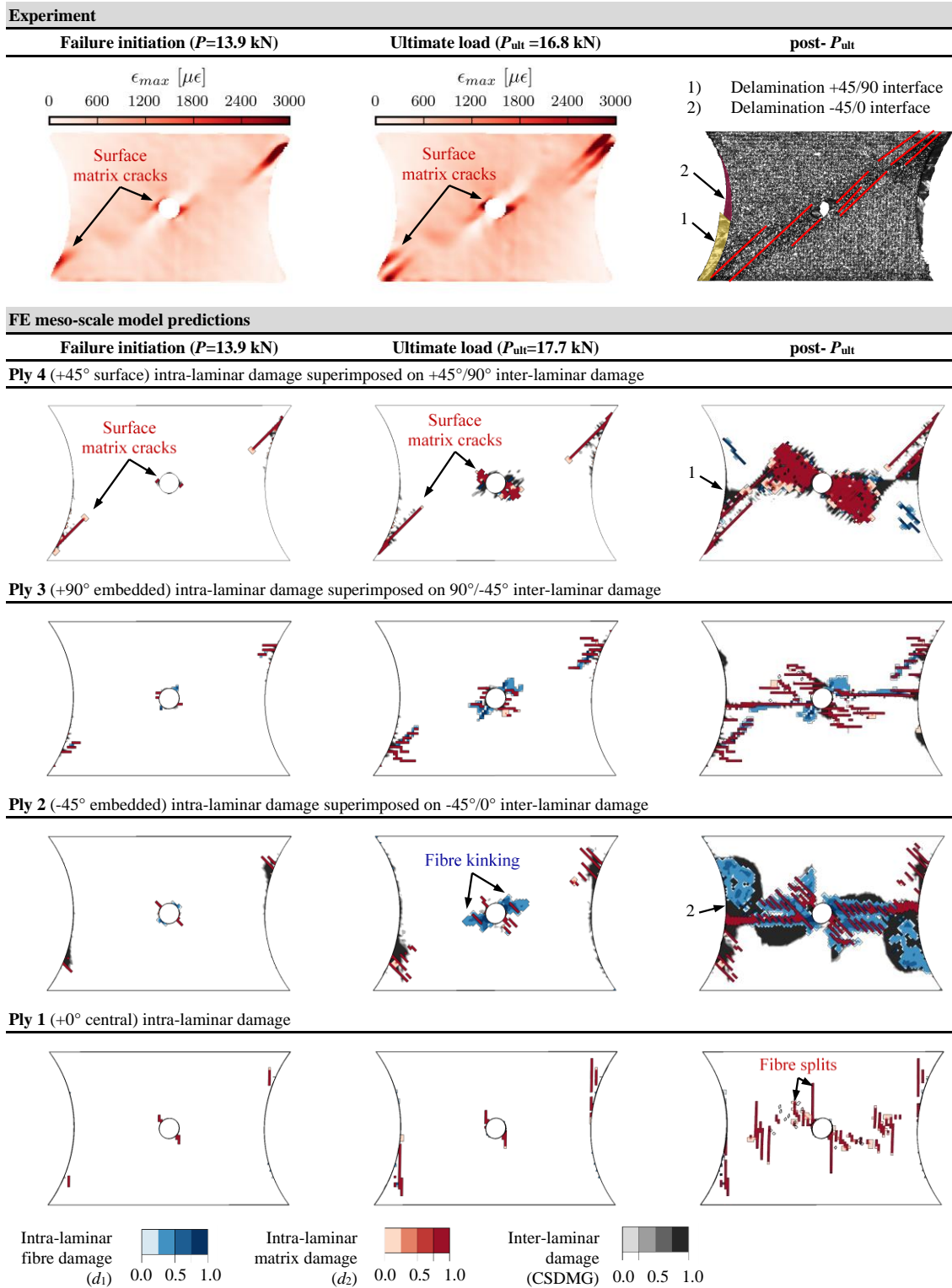
Figure 6.7, Predicted ply-by-ply damage maps compared to experimental data for Laminate 1 subjected to combined tension-shear loading (α = 45°).
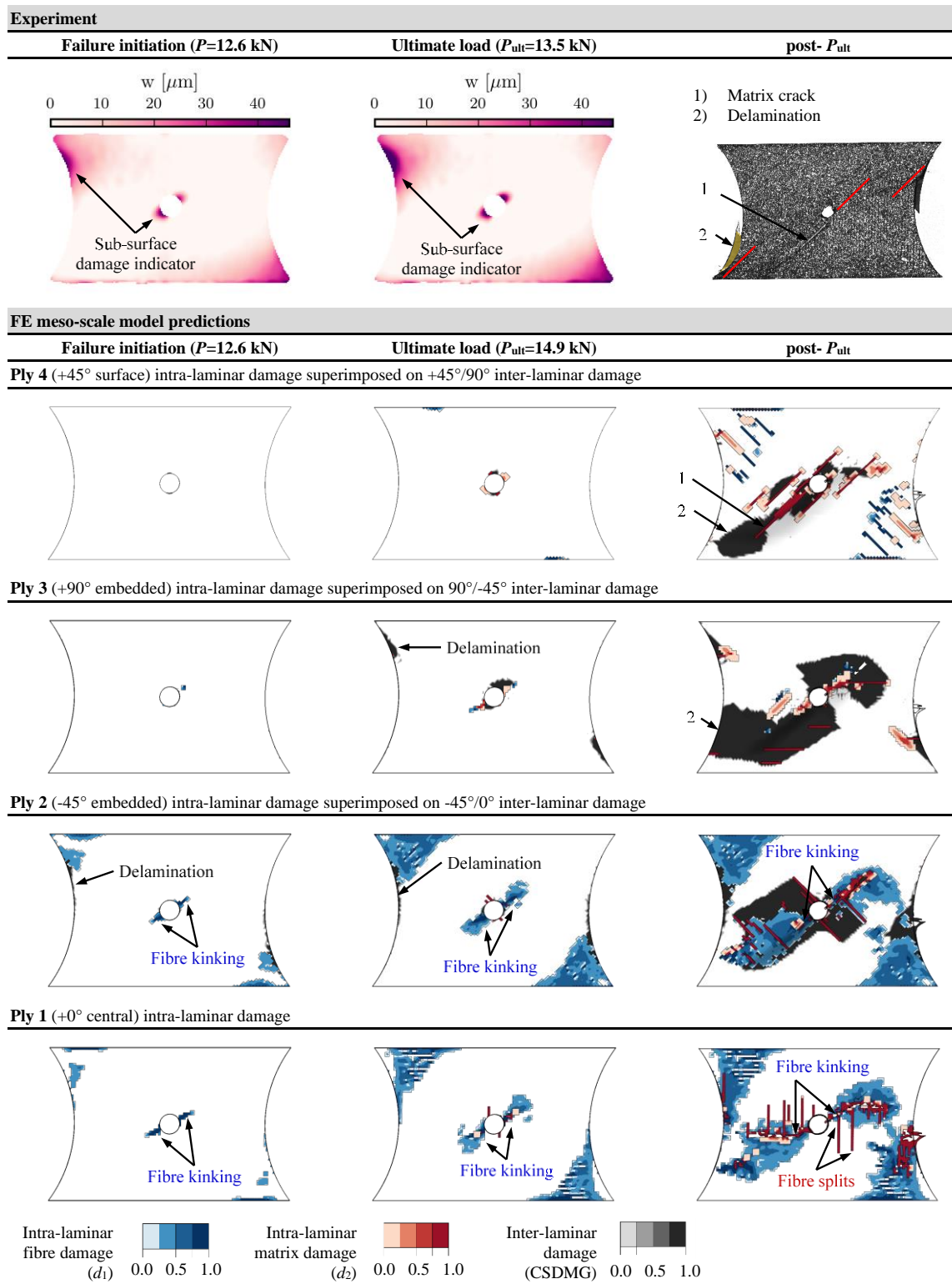
Figure 6.8, Predicted ply-by-ply damage maps compared to experimental data for Laminate 1 subjected to combined compression-shear loading (α = 135°).

The predicted damage patterns for Laminate 1 in tension-shear ($\alpha = 45°$) shown in Figure 6.7 are in agreement with the experimental observations. Thus, the high principal strain concentrations at the hole and at the top right and bottom left corners of the specimens at both the failure initiation and ultimate load orientated parallel to the fibres of the surface ply are a clear indication for surface matrix cracks. These surface cracks are also predicted by the model (labelled in Figure 6.7 at failure initiation and at P_{ult}) in the surface ply 4 and match the extent and location of the principal strain concentrations in the experiment well (labelled in Figure 6.7). Looking at the failed specimen at post-P_{ult}, it is observed that the macroscopic crack plane runs diagonally from the bottom left, through the hole, to the top right corner. This is also predicted by the model, where cracks in surface ply 4 originate at the hole and the bottom left and top right corners as well, and where major delamination at the $+45°/90°$ interface match the experimental macroscopic crack orientation. Furthermore, two distinct delamination planes (labelled in Figure 6.7 at post-P_{ult}) are observed by visual inspection of the failed specimen. In the model predictions they can be associated with delamination at the $+45°/90°$ and $-45°/0°$ interfaces, as also labelled in Figure 6.7 at post-P_{ult}. By investigating the model predictions, it can be concluded that fibre kinking at the hole in the $-45°$ ply 3, as labelled in Figure 6.7 at P_{ult}, in combination with delamination at the $-45°/0°$ interface are governing the ultimate strength of Laminate 1 in combined tension-shear. The observed failure behaviour is in agreement with observations in [152] where x-ray CT was used to investigate failure of multidirectional laminates in the combined tension-shear loading regime.

For Laminate 1 in compression-shear ($\alpha = 135°$), neither the experimental data nor the model prediction show cracks on the surface at initiation and ultimate failure load (see Figure 6.8). From visual inspection it would have been concluded that the specimen is undamaged. However, high local out-of-plane displacement gradients are observed at the hole as labelled in Figure 6.8 at failure initiation and P_{ult}. This indicates the occurrence of sub-surface damage which can be associated in the model with the prediction of fibre kinking in the $-45°$ and $0°$ ply at the hole as labelled in Figure 6.8 at failure initiation and P_{ult}. In fact, the extent and location of the predicted kinks are in very good agreement with the areas of high out-of-plane displacements in the experimental DIC maps, thus validating the predictions of the model. At ultimate load, delamination is also occurring at the $90°/-45°$ interface around the hole. Therefore, the critical failure event in Laminate 1 loaded in compression-shear is governed by fibre kinking in the $-45°$ and $0°$ plies in combination with delamination at the hole. By visual inspection of the failed specimen post-P_{ult}, it is again observed that the macroscopic fracture plane runs from the bottom left, through the hole to the bottom top right corner. Observed matrix cracks at the surface, labelled in Figure 6.8 at post-P_{ult}, are also predicted by the model. In addition, delaminated areas labelled in Figure 6.8 at post-P_{ult} can be associated with predicted delamination at the $+45°/90°$ and $90°/-45°$ interfaces.

Further observations can be made from the full set of damage maps consisting of all load cases and laminate configurations tested/simulated given in Appendix E. Firstly, matrix crack and delamination patterns often exhibit similarities, *i.e.* delaminated areas are limited by matrix cracks. An example of this behaviour is seen in Figure 6.7 in ply 4 at post-P_{ult}. This indicates that the physics of the critical interaction effects between intra- and inter-laminar failure modes can be captured by the CDM model in combination with the fibre-aligned mesh. Furthermore, damage patterns in plies with the same fibre orientation in Laminate 2 are similar. This means that only one damaged ply per fibre orientation angle for the 'thin' ply Laminate 2 can be analysed for the assessment of the laminate failure mechanisms and for comparison to the 'thick' ply Laminate 1.

6.4   Ply thickness and multiaxial loading effects

Based on the full set of predicted damage maps reported in Appendix E and as introduced in Section 6.3.2, the critical failure events as a result of the applied combined load cases and the UD ply thickness are discussed in this Section. Figure 6.9 provides an overview of the critical failure mechanisms predicted in Laminates 1 and 2. The critical failure mechanism is determined by comparing the damage patterns at P_{ult} and post-P_{ult}. In this way, the critical failure event that will eventually lead to the ultimate failure of the specimen can be separated from sub-critical events.

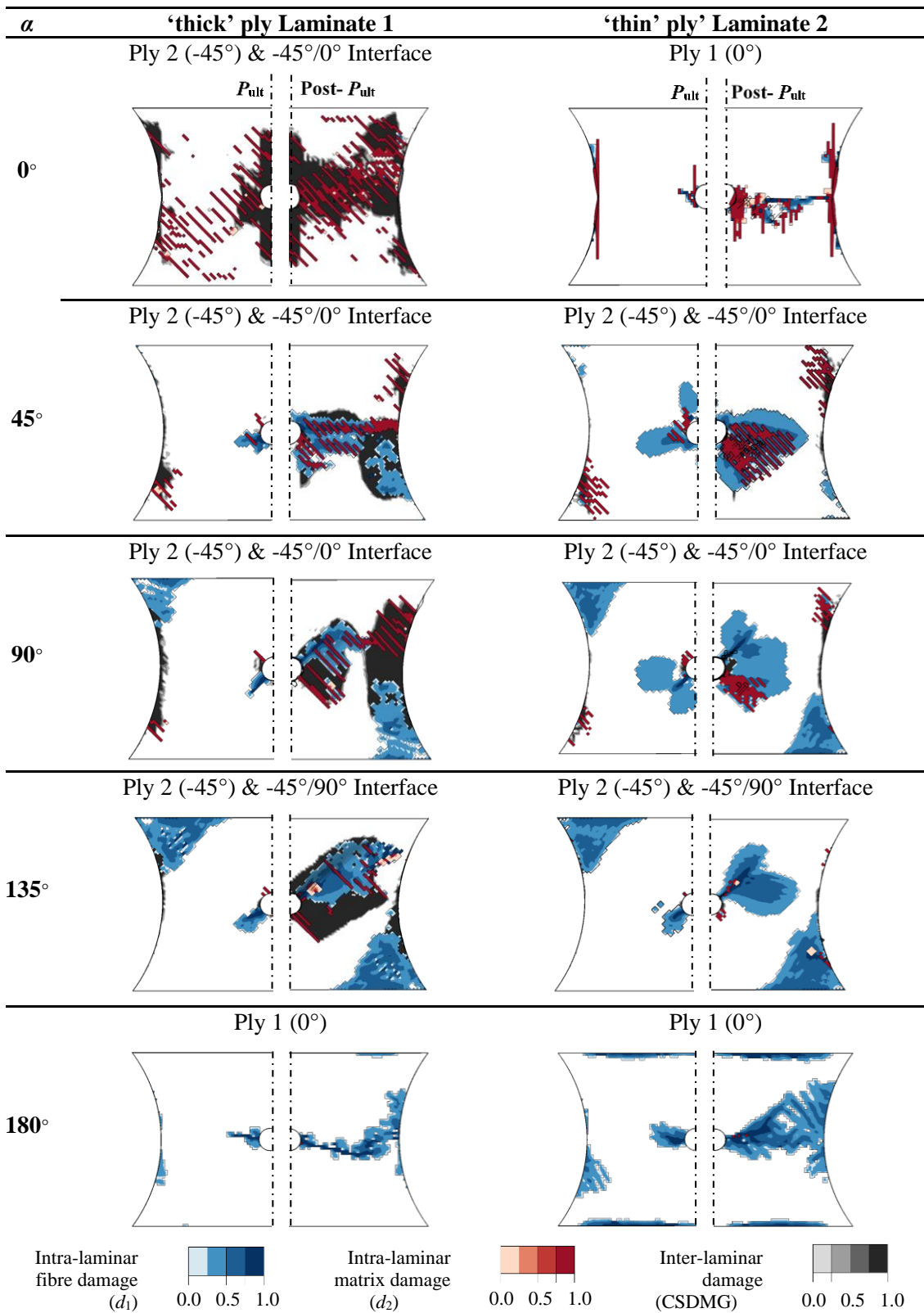| α	'thick' ply Laminate 1	'thin' ply' Laminate 2

Figure 6.9, Critical failure mechanisms in Laminate 1 (left) and Laminate 2 (right) illustrated by means of the damage pattern at ultimate load P_{ult} and post-P_{ult}.

In the tensile load case ($\alpha = 0°$) shown in Figure 6.9, the critical failure mechanism is distinctly different between Laminate 1 and 2. Laminate 1 fails due to large scale delamination, through several interfaces but mainly at the −45°/0° interface, while only minor fibre failure is observed. On the other hand, Laminate 2 exhibits only minor areas of delamination but exhibits a crack initiating at the hole perpendicular to the fibres (blue – fibre break) at P_{ult} which eventually grows across the whole gauge section at post-P_{ult}. The two different failure mechanisms observed circumstantiate the significant difference in the open-hole specimen strengths observed in Figure 6.5 between Laminate 1 and 2. The ultimate strength of Laminate 1 is dominated by the relatively low energy delamination failure mode, while delamination is supressed in the 'thin' ply Laminate 2 and its ultimate failure is governed by fibre failure, explaining the up to 150% higher open-hole specimen strength in tension-shear of Laminate 2.

Interestingly, the critical failure mechanisms for both Laminates and for all shear dominated load cases ($\alpha = 45°, 90°, 135°$) are very similar: the critical failure event in all cases is fibre kinking failure at the hole in the −45° plies. It also strikes that the model predicts Laminate 1 to be more delamination prone than Laminate 2 (compare extent of black delaminated areas in Figure 6.9), which is in agreement with related experimental studies [108]. In uniaxial compression ($\alpha = 180°$), the critical failure event changes from fibre kinking in the −45° ply to fibre kinking in the 0° plies near the hole. The similar open-hole specimen strengths for both Laminates in combined compression-shear and compression observed in Figure 6.5 can therefore be associated with the similar critical ultimate failure events.

6.5   Conclusions

In this chapter, a meso-scale modelling framework developed for 'virtual testing' was used to simulate failure in open-hole specimens of quasi-isotropic carbon/epoxy composite laminates subjected to combined tension/compression-shear loading.

The prediction of the multiaxial open-hole specimen strength and damage patterns were assessed against the multiaxial experimental data obtained in Chapter 5 using the new MAF in combination with stereo DIC. The predicted ply thickness effect on the multiaxial open-hole specimen strength were qualitatively consistent with the experimental data. The models were able to predict the open-hole specimen strength for the two different laminate lay-ups with a mean relative error of 10% across all load cases. Furthermore, the predicted ply-by-ply damage patterns were associated with failure events observed using DIC on the surface of the specimen. Based on the predicted damage maps, it was shown that the higher strength of the 'thin' ply Laminate 2 in comparison to the 'thick' ply Laminate 1, is related to different failure mechanisms, *i.e.* fibre failure in Laminate 2 and delamination failure in Laminate 1. On the other hand, the similar strengths in shear, combined compression-shear and compression are related to similar critical failure events in both 'thin' and 'thick' ply laminates, *i.e.* fibre kinking in the −45° and 0° plies, respectively.

Thus, the integrated experimental and computational analysis into the ply thickness effect has provided additional in-sight into the governing failure mechanisms and complements the experimental investigation in Chapter 5.

Nonetheless, the study has identified that the model cannot accurately predict fibre splitting and fibre breaks in areas of high fibre tensile and shear stresses for the investigated material system and underpredicts the failure strengths in tensile dominated load cases. The difficulty is related to the out-of-autoclave material simulated in this study, which is more compliant and at the same time stronger than aerospace grade, autoclave consolidated carbon/epoxy material systems for which the CDM model has been developed. It is believed that the limitation could be overcome by updating the current model to account for large shear deformations. In the present chapter, it is suggested to limit the maximum allowable shear damage as an engineering solution to overcome this limitation of the model. The revealed limitation highlights the importance for continuous and rigorous model validation against experimental data for new material systems (here an out-of-autoclave carbon/epoxy prepreg system) which challenges model assumptions that may have been legitimate for older material systems.

This chapter has contributed to the knowledge of simulating failure in multidirectional composite laminates subjected to multiaxial loading and may inform the direction of future model development and validation. The work is a step towards enabling the efficient and reliable use of 'virtual testing' techniques based on meso-scale FE modelling frameworks in the design and certification of high-performance FRP structures. The chapter also demonstrates how the experimental data in Chapter 5 can be used for model validation, and thus can serve as a guidance for other researchers aiming at validation their models against the data presented in Chapter 5.

Chapter 7

Overall conclusions and recommendations for future work

7.1   Overall conclusions

The aim of the work described in this thesis was to develop a new multiaxial testing methodology and the associated experimental procedures to enable the acquisition of high-fidelity experimental data on the damage and failure behaviour of composite laminates subjected to multiaxial loading. The acquisition of multiaxial data was aimed at addressing the limited amount of such data reported in the literature, at improving the understanding of composite failure mechanics and at advancing the development, calibration and validation of composite modelling frameworks. The defined aim has been met and several novel experimental approaches have been proposed based on which new modelling frameworks have either been developed or state-of-the-art models have been validated.

In Chapter 3, a method based on the modified Arcan fixture (MAF), combined with a butterfly-shaped specimen and DIC, was initially proposed to characterise the constitutive response (stress-strain curves and failure envelopes) of FRPs subjected to combined tension/compression and shear. Selected failure criteria (maximum stress, Tsai-Wu's, Puck's IFF and the LaRC03) implemented in a simple CLT code were assessed against the MAF test results. The analytical and experimental study has shown that the LaRC03 failure criterion is able to predict first-ply-failure and failure modes of the successfully tested laminates. However, while weak (matrix dominated) laminates were tested up to ultimate failure, strong laminates where the load response and failure behaviour was fibre dominated could not be investigated up to ultimate failure due to specimen slippage and premature failure at the grips. The observed nonuniform stress/strain state in the specimen, including stress/strain concentrations near the waist of the specimen, posed a further challenge and implied that the derived apparent stress-strain curves were only accurate when the material response is linear with respect to the applied load. The development of stress-based failure envelopes was complicated because failure did not necessarily initiate nor propagate in the representative waisted gauge section. The failure event could therefore not be directly associated with the average stresses in the gauge section. In other words, the average limit stress state in the gauge section is not truly representative of the biaxial strength and failure mode of a representative material element subjected to the combined state of stress. This limits the usefulness of the initially proposed multiaxial experimental approach.

In Chapter 4, the apparent stress-strain curves obtained in Chapter 3 were used to develop a new plasticity-based constitutive model for UD composites that accounts for their nonlinear, pressure sensitive behaviour. It has been confirmed that a non-associative flow rule must be adopted when Drucker-Prager type yield functions are used and that when an associative flow rule is used instead, non-physical plastic tensile transverse normal stresses/strains will be predicted under pure shear and moderate compression-shear stress states. Guidelines for the calibration of plasticity-based models have been established: data for only three judiciously chosen biaxial stress states are required for accurate calibration: One case needs to be in combined tension-shear, one in combined compression-shear with moderate compression and one in combined compression-shear with dominant compression. The three load cases fully determine the mathematical/geometrical shape of the yield and plastic potential ellipses and conveniently capture all three matrix failure modes of UD composites according to Puck's IFF theory. Furthermore, it is prudent to calibrate the model against both the individual transverse normal and shear stress-strain curves and not just against an on-axis stress-strain curve. This is because the individual contribution of the normal and shear plastic stress/strain components to the on-axis effective plasticity cannot be verified independently. Instead the plastic stress/strains components are obscured and may be physically inconsistent even though the on-axis nonlinearity is seemingly captured accurately.

In Chapter 5, a new multiaxial testing philosophy was proposed in which the specimen is regarded as a 'mini' structural component. A new MAF was designed which overcame the limitation of the previous MAF design used for the initial testing program. The new MAF in combination with stereo DIC enabled the investigation of laminate lay-up effects, *i.e.* the effects of UD ply thickness and fibre orientation, on the multiaxial open-hole specimen strength in quasi-isotropic carbon/epoxy laminates. The experimental results have shown that UD ply thickness has a significant effect in the tension-shear loading regime where the thin ply laminate specimens were up to 150% stronger than the thick ply laminate specimens, while only a small difference in the compression-shear loading regime was observed. The overarching conclusion impacts on the design of high-performance composite structures, in that the use of laminates with thinner but increased numbers of plies, and therefore higher manufacturing cost, may be preferred in areas of combined tension-shear loading, while no significant benefit is apparent in areas of predominantly compression-shear loading. Moreover, according to the experiments conducted, there was no significant gain in terms of ultimate open-hole specimen strength by using non-standard fibre orientation angle laminates for the investigated load and specimen configurations.

The small amount of multiaxial experimental data in the open literature implies that current composite modelling frameworks cannot be fully validated. Therefore, in Chapter 6, a 'virtual testing' framework was used to predict the ply thickness effects observed in Chapter 5. The experimental data obtained in Chapter 5 is valuable for the validation of numerical techniques because it challenges the model's ability to accurately predict strength and failure modes in

different laminate lay-ups subjected to complex loading configurations. The FE-based meso-scale model discretises the laminates at the UD ply level. Intra-laminar damage is predicted using a CDM framework, where failure is predicted using an approximation of the LaRC03/04 criteria, while inter-laminar damage is modelled using CZMs. The model captured the observed ply thickness effect qualitatively well. It correctly predicted that the thin ply laminate is considerably stronger than the thick ply laminate in combined tension-shear loading, while the difference is small for compression-shear loading. However, the model was unable to quantitatively predict the open-hole specimen strength of the thin-ply laminate in tensile dominated load cases, because it failed to accurately predict the notch blunting effect due to the occurrence of vertical matrix cracks near the hole in the 0° plies. For the present study, the limitation of the model was addressed by limiting the maximum shear damage allowed in the CDM, which improved the predictions. However, it was concluded that the model could fundamentally be improved by accounting for large shear deformation in the formulations of the model. By limiting the shear damage, the simulated open-hole specimen strength across all laminates and load cases was predicted with a mean relative error of 10%. Given that the out-of-autoclave material used for the tests is different from the aerospace grade autoclave consolidated systems for which the model was initially developed and considering the complexity of the tests and that not all model input parameters have been measured experimentally, this is a promising result. However, it also shows that further model improvements are required before 'virtual testing' techniques can be used for the design and certification of high-performance composite materials and structures.

Chapters 5 and 6 have shown that multiaxial coupon tests in which the specimen is regarded as a mini structural component are a powerful tool for the validation of 'virtual testing' techniques. They are a relatively simple way to increase the complexity of established uniaxial coupon tests to challenge and further advance the predictive capability of modelling frameworks.

7.2   Recommendations for future work

To increase the usefulness of the MAF test for the calibration of failure criteria and nonlinear constitutive models, a more uniform stress/strain state within the gauge section of the specimen is desired (see Chapters 3 and 4). Therefore, it is recommended for future work to optimise the specimen's shape to mitigate some of the restrictions imposed by the nonuniform stress/strain state. The objectives would be a more uniform biaxial stress/strain state, while avoiding premature failure outside of the gauge section. Similar studies have been conducted on cruciform specimens [137]–[140], but never on Arcan type specimens. An FE-based optimisation would require a material model that accounts for the nonlinear stress/strain relationship and the various FRP failure modes as well as accurate material properties to inform the model. Another possible direction for the development of novel nonlinear constitutive model calibration methodologies,

would be the further exploitation of the full-field data in the design of 'heterogeneous' tests [184], [185].

Guidelines for the calibration of plasticity-based nonlinear material models for UD composites have been established in Chapter 4 based on the MAF. It would be recommended for future work to apply these recommendations to on-axis tests, *i.e.* DIC could be used to derive the transverse normal and shear stress-strain curves in off-axis tests used for the calibration of the material model. The calibrated model implemented as a user material subroutine (VUMAT) could then be applied to different stress/strain analysis problems for further validation.

The investigations into laminate lay-up effects in Chapter 5, only considered one hole size even though the open-hole specimen strength depends on the size of the hole (see Chapter 2, Section 2.6). It is therefore recommended for future work to extend the experimental investigation by including specimens with different hole sizes. Furthermore, different judiciously chosen laminate lay-ups and material systems could be studied. In the conducted experiments, the damage sequence was assessed based on visual inspection and surface-based DIC measurements. Although the surface-based measurements can be used to infer the occurrence of sub-surface damage, the use of x-ray CT in combination with the MAF tests would be recommended to gain a better understanding of the failure events and their location, allowing the clear characterisation of sub-surface failure modes. Interrupted MAF tests could be conducted where specimens were x-ray CT scanned at pre-defined load levels, or the MAF test set-up could be fit inside an x-ray CT scanner for in-situ scanning. The scan data would be very useful for further validation of state-of-the art failure models. It is further recommended that the potential use of out-of-plane-displacement maps for the identification of sub-surface damage, which to the authors knowledge has never been attempted before, is further explored. The out-of-plane displacements maps are often obtained but ignored for the assessment of failure, even though it has been shown that localised features in the out-of-plane displacements maps corelated well with sub-surface damage events.

Based on the findings in Chapter 6, it is recommended for future work to account for large shear deformation in the used CDM model and to re-assess the updated model against the experimental data. Furthermore, other modelling approaches, *e.g.* DDM models could be validated. A comparative assessment of different modelling approaches against the experimental data would inform the future direction of the development of 'virtual testing' techniques, which would accelerate the uptake of 'virtual testing' in the design and certification of high-performance structures.

7.3   Contributions and impact

The work has led to four journal articles (three published / one in preparation) and six presentations at international/European conferences. The work presented at the 22nd International Conference on Composite Materials (ICCM) was nominated for the Tsai Award, for being one of the seven best student papers presented. The PhD project was further awarded a Stanley Gray Fellowship (GBP 6000) from the Institute of Marine Science and Technology (IMarEST). Parts of the research presented in this thesis was conducted at the University of Southampton Malaysia, Johor Bahru, Malaysia. The material used to investigate laminate lay-up effects in quasi-isotropic carbon/epoxy laminates in Chapter 5 was provided by INEOS Team UK, the British challenger for the 36th America's cup. The collaboration has been established during this PhD project and may lead to further collaborative research. The research successfully answered the initial questions of the INEOS Team UK, while in parallel important scientific challenges were addressed. The collaboration with the University of Porto on modelling the laminate lay-up effects in the quasi-isotropic laminates in Chapter 6 was also established during this PhD and may lead to further collaborative research. The collaboration combined the expertise in experimental mechanics at the University of Southampton with the expertise on modelling failure in composite materials at the University of Porto.

Journal papers

1) **T. Laux**, K.W. Gan, A. Arteiro, R.P. Tavares, C. Furtado, J.M. Dulieu-Barton, O.T. Thomsen, P.P. Camanho. Predicting ply thickness effects on the combined tension/compression and shear open-hole specimen strength of multidirectional composite laminates. *To be submitted to Composites Part A*. 2020.

   Contribution: Primary author of manuscript. Defined research question based on scientific and industrial needs. Developed FE modelling strategy. Obtained all experimental data required for model calibration and validation. Used the CDM based model developed by the group at the University of Porto for the prediction of intra-laminar damage. Run all of the models and analysed the results.

2) **T. Laux**, K.W. Gan, J.M. Dulieu-Barton, O.T. Thomsen. Ply thickness and fibre orientation effects in multidirectional composite laminates subjected to combined tension/compression and shear. *Composites Part A:* Applied Science and Manufacturing. 2020. doi.org/10.1016/j.compositesa.2020.105864.
   Contribution: Primary author of manuscript. Defined research question based on scientific and industrial needs. Developed the new MAF rig and the test set-up required to investigate the laminate lay-up effects. Conducted all experiments, analysed data and drew key conclusions.

3) **T. Laux**, K.W. Gan, J.M. Dulieu-Barton, O.T. Thomsen. A simple nonlinear constitutive model based on non-associative plasticity for UD composites – Development and validation using a Modified Arcan Fixture. *International Journal of Solids and Structures*. vol. 162, pp. 135-147. 2019. doi: 10.1016/j.ijsolstr.2018.12.004.

Contribution: Primary author of manuscript. Developed the constitutive equations and the calibration methodologies based on the MAF and off-axis experimental data. Analysed experimental and model data and derived guidelines for development of plasticity-based models and their calibration methodologies.

4) K. W. Gan, **T. Laux**, S. T. Taher, J. M. Dulieu-Barton, and O. T. Thomsen. A novel fixture for determining the tension/compression-shear failure envelope of multidirectional composite laminates. *Composite Structures*. vol. 184, pp. 662-673. 2018. doi: 10.1016/j.compstruct.2017.10.030.

Contributions: Conducted the MAF testing of the UD $[90]_{12}$ laminate at $\alpha = 0°$, $30°$, $135°$, $165°$ and $180°$ and for the $[-/+60]_{3s}$ at $\alpha = 0°$ and $180°$. Prepared the specimens for the x-ray CT imaging and analysed the results. Assisted with the analysis and interpretation of the experimental and analytical results.

Conference papers and presentations

1) **T. Laux**, K.W. Gan, J.M. Dulieu-Barton, O.T. Thomsen, Experimental characterisation and modelling of multidirectional CFRP composites subjected to combined tension/compression-shear loading. *7th Thematic Conference on the Mechanical Response of Composites* (ECCOMAS). Girona, Spain, 18-20 Sept. 2019.

2) **T. Laux**, K.W. Gan, J.M. Dulieu-Barton, O.T. Thomsen. Characterising multidirectional laminates subjected to tension/compression-shear loading using a modified Arcan fixture. *22nd International Conference on Composite Materials* (ICCM). Melbourne, Australia, 11-16 Aug. 2019.

3) **T. Laux**, K.W. Gan, J.M. Dulieu-Barton, O.T. Thomsen. *9th International Conference on Composite testing and model identification* (COMPTEST). improving the Arcan specimen for combined tension/ compression and shear testing of fibre-reinforced composites. Luleå, Sweden, 27-29 May 2019.

4) **T. Laux**, K.W. Gan, J.M. Dulieu-Barton, O.T. Thomsen. Experimental characterisation and modelling of the nonlinear, pressure sensitive behaviour of UD composites under multiaxial loading. *13th International Conference on Advanced Experimental Mechanics* (BSSM). Southampton, UK, 29-31 Aug. 2018.

5) **T. Laux**, K.W. Gan, J.M. Dulieu-Barton, O.T. Thomsen. Experimental and computational study of multidirectional glass/epoxy laminates subjected to multiaxial loading. *18th European Conference on Composite Materials* (ECCM). Athens, Greece, 24-28 June 2018.

6) <u>K. W. Gan</u>, **T. Laux**, J. M. Dulieu-Barton, and O. T. Thomsen. Biaxial testing of glass/epoxy composite laminates using a modified Arcan's fixture (MAF). *21st International Conference on Composite Materials* (ICCM). Xian, China, 20-25 Aug. 2017.

List of references

[1]   Composites Leadership Forum. The 2016 UK Composites Strategy. 2016.

[2]   I. M. Daniel and O. Ishai. *Engineering mechanics of composite materials*. Oxford University Press, 2005.

[3]   LM Windpower. Meet a record breaker: LM 88.4 P, 2016. [Online]. Available: https://www.lmwindpower.com/en/products-and-services/blade-types/longest-blade-in-the-world. [Accessed: 14-Mar-2018].

[4]   SpaceX. The worlds most powerfu rocket, 2020. [Online]. Available: http://www.spacex.com/falcon-heavy. [Accessed: 07-Feb-2020].

[5]   Airbus. Airbus unveils first A380 centre wingbox, 2003. [Online]. Available: http://www.airbus.com/newsroom/press-releases/en/2003/08/airbus-unveils-first-a380-centre-wingbox.html. [Accessed: 14-Mar-2018].

[6]   J. Rouchon. Certification of large aircraft composite structures, recent progress and new trends in compliance philosophy. in *17th ICAS Congress*. Stockholm. 1990. vol. 2. pp. 1439–1447.

[7]   J. L. Y. Tan, V. S. Deshpande, and N. A. Fleck. The effect of laminate lay-up on the multi-axial notched strength of CFRP panels: Simulation versus experiment. *Eur. J. Mech. A/Solids*. vol. 66. pp. 309–321. 2017. doi: 10.1016/j.euromechsol.2017.08.002.

[8]   P. P. Camanho, P. Maimí, and C. G. Dávila. Prediction of size effects in notched laminates using continuum damage mechanics. *Compos. Sci. Technol.* vol. 67, no. 13. pp. 2715–2727. 2007. doi: 10.1016/j.compscitech.2007.02.005.

[9]   S. R. Hallett, B. G. Green, W. G. Jiang, and M. R. Wisnom. An experimental and numerical investigation into the damage mechanisms in notched composites. *Compos. Part A Appl. Sci. Manuf.* vol. 40, no. 5. pp. 613–624. 2009. doi: 10.1016/j.compositesa.2009.02.021.

[10]   F. Laurin, N. Carrère, and J. F. Maire. A multiscale progressive failure approach for composite laminates based on thermodynamical viscoelastic and damage models. *Compos. Part A Appl. Sci. Manuf.* vol. 38, no. 1. pp. 198–209. 2007. doi: 10.1016/j.compositesa.2006.01.018.

[11]   P. Maimí, P. P. Camanho, J. A. Mayugo, and C. G. Davila. A continuum damage model for composite laminates: Part I - Constitutive model. *Mech. Mater.* vol. 39, no. 10. pp. 897–908. 2007. doi: 10.1016/j.mechmat.2007.03.005.

[12]   C. Bouvet, B. Castanié, M. Bizeul, and J. J. Barrau. Low velocity impact modelling in

laminate composite panels with discrete interface elements. *Int. J. Solids Struct.* vol. 46, no. 14–15. pp. 2809–2821. 2009. doi: 10.1016/j.ijsolstr.2009.03.010.

[13]   E. Abisset, F. Daghia, and P. Ladevze. On the validation of a damage mesomodel for laminated composites by means of open-hole tensile tests on quasi-isotropic laminates. *Compos. Part A Appl. Sci. Manuf.* vol. 42, no. 10. pp. 1515–1524. 2011. doi: 10.1016/j.compositesa.2011.07.004.

[14]   R. Higuchi, T. Okabe, and T. Nagashima. Numerical simulation of progressive damage and failure in composite laminates using XFEM/CZM coupled approach. *Compos. Part A Appl. Sci. Manuf.* vol. 95. pp. 197–207. 2017. doi: 10.1016/j.compositesa.2016.12.026.

[15]   O. Falcó, R. L. Ávila, B. Tijs, and C. S. Lopes. Modelling and simulation methodology for unidirectional composite laminates in a Virtual Test Lab framework. *Compos. Struct.* vol. 190. pp. 137–159. 2018. doi: 10.1016/j.compstruct.2018.02.016.

[16]   S. Mukhopadhyay and S. R. Hallett. A directed continuum damage mechanics method for modelling composite matrix cracks. *Compos. Sci. Technol.* vol. 176. pp. 1–8. 2019. doi: 10.1016/j.compscitech.2019.03.022.

[17]   C. Furtado, G. Catalanotti, A. Arteiro, P. J. Gray, B. L. Wardle, and P. P. Camanho. Simulation of failure in laminated polymer composites: Building-block validation. *Compos. Stuctures.* vol. 226. 2019.

[18]   J. L. Y. Tan, V. S. Deshpande, and N. A. Fleck. Prediction of failure in notched polymer laminates under multi-axial loading. *Philos. Trans. A.* vol. 374, no. 2071. 2016.

[19]   P. Maimí, P. P. Camanho, J. A. Mayugo, and C. G. Dávila. A continuum damage model for composite laminates: Part II - Computational implementation and validation. *Mech. Mater.* vol. 39, no. 10. pp. 909–919. 2007. doi: 10.1016/j.mechmat.2007.03.006.

[20]   F. Zhuang, P. Chen, A. Arteiro, and P. P. Camanho. Mesoscale modelling of damage in half-hole pin bearing composite laminate specimens. *Compos. Struct.* vol. 214. pp. 191–213. 2019. doi: 10.1016/j.compstruct.2019.01.062.

[21]   G. Davies, J. Ankersen, I. Guiamatsia, and B. Gordon. Replacement of industrial testing composite structures by simulation. *J. Aerosp. Eng.* vol. 224. p. 471. 2010. doi: 10.1243/09544100JAERO570.

[22]   P. P. Camanho, M. A. Bessa, G. Catalanotti, M. Vogler, and R. Rolfes. Modeling the inelastic deformation and fracture of polymer composites – Part II: Smeared crack model. *Mech. Mater.* vol. 59. pp. 36–49. 2013. doi: 10.1016/j.mechmat.2012.12.001.

[23]   J. Serra *et al.* Validation and modeling of aeronautical composite structures subjected to combined loadings: The VERTEX project. Part 2: Load envelopes for the assessment of panels with large notches. *Compos. Struct.* vol. 180. pp. 550–567. 2017. doi:

10.1016/j.compstruct.2017.08.055.

[24]   J. Serra, J. E. Pierré, J. C. Passieux, J. N. Périé, C. Bouvet, and B. Castanié. Validation and modeling of aeronautical composite structures subjected to combined loadings: The VERTEX project. Part 1: Experimental setup, FE-DIC instrumentation and procedures. *Compos. Struct.* vol. 179. pp. 224–244. 2017. doi: 10.1016/j.compstruct.2017.07.080.

[25]   M. Arcan, Z. Hashin, and A. Voloshin. A method to produce uniform plane-stress states with applications to fiber-reinforced materials. *Exp. Mech.* vol. 18, no. 4. pp. 141–146. 1978. doi: 10.1007/BF02324146.

[26]   A. Voloshin and M. Arcan. Failure of unidirectional fiber-reinforced materials—new methodology and results. *Exp. Mech.* vol. 20, no. 8. pp. 280–284. 1980. doi: 10.1007/BF02328412.

[27]   M. A. Sutton, J. J. Orteu, and H. Schreier. *Image correlation for shape, motion and deformation measurements*. Springer, 2009.

[28]   A. E. Scott, M. Mavrogordato, P. Wright, I. Sinclair, and S. M. Spearing. In situ fibre fracture measurement in carbon–epoxy laminates using high resolution computed tomography. *Compos. Sci. Technol.* vol. 71, no. 12. pp. 1471–1477. Aug. 2011. doi: 10.1016/j.compscitech.2011.06.004.

[29]   T. Taher, S. and T. Thomsen, O. Shear and tension or compression biaxial material testing fixture, 2012.

[30]   C. G. Dávila, P. P. Camanho, and C. A. Rose. Failure criteria for FRP laminates. *J. Compos. Mater.* vol. 39, no. 4. pp. 323–345. 2005. doi: 10.1177/0021998305046452.

[31]   P. P. Camanho and C. G. Dávila. Mixed-mode decohesion finite elements for the simulation of delamination in composite materials. 2002.

[32]   A. S. Kaddour and M. J. Hinton. Input data for test cases used in benchmarking triaxial failure theories of composites. *J. Compos. Mater.* vol. 46, no. 19–20. pp. 2295–2312. 2012. doi: 10.1177/0021998312449886.

[33]   S. Pinho, G. Vyas, and P. Robinson. Material and structural response of polymer-matrix fibre-reinforced composites: Part B. *J. Compos. Mater.* vol. 47, no. 6–7. pp. 679–696. 2013. doi: 10.1177/0021998313476523.

[34]   J. A. Sauer. Deformation, yield and fracture of polymers at high pressure. *Polym. Eng. Sci.* vol. 17, no. 3. pp. 150–164. 1977. doi: 10.1002/pen.760170304.

[35]   D. R. Mears, K. D. Pae, and J. A. Sauer. Effects of hydrostatic pressure on the mechanical behavior of polyethylene and polypropylene. *J. Appl. Phys.* vol. 40, no. 11. pp. 4229–4237. 1969. doi: 10.1063/1.1657180.

[36] A. Puck and H. Schürmann. Failure analysis of FRP laminates by means of physically based phenomenological models. *Compos. Sci. Technol.* vol. 58. pp. 1045–1067. 1996. doi: 10.1016/B978-008044475-8/50028-7.

[37] E. S. Shin and K. D. Pae. Effects of hydrostatic pressure on in-plane shear properties of graphite/epoxy composites. *J. Compos. Mater.* vol. 26, no. 6. pp. 828–868. 1992. doi: 10.1177/002199839202600604.

[38] S. R. Swanson, M. J. Messick, and Z. Tian. Failure of carbon/epoxy lamina under combined stress. *J. Compos. Mater.* vol. 21. pp. 619–630. 1987.

[39] J. P. Boehler and A. Sawaczuk. Application of representation theorems to describe yielding of transversely isotropic solids. *Mech. Res. Comun.* vol. 3. pp. 277–283. 1976.

[40] A. J. M. Spencer. Plasticity theory for fibre-reinforced composites. *J. Eng. Math.* vol. 26, no. 1. pp. 107–118. 1992. doi: 10.1007/BF00043230.

[41] U. Kureemun, M. Ridha, and T. Tay. Biaxial tensile-compressive loading of unnotched and open-hole carbon epoxy crossply laminates. *J. Compos. Mater.* vol. 49, no. 23. pp. 2817–2837. 2014. doi: 10.1177/0021998314555043.

[42] W. Ramberg and W. R. Osgood. Description of stress-strain curves by three parameters. 1943.

[43] R. Cuntze. The predictive capability of failure mode concept-based strength conditions for laminates composed of unidirectional laminae under static triaxial stress states. *J. Compos. Mater.* vol. 46, no. 19–20. pp. 2563–2594. 2012. doi: 10.1177/0021998312449894.

[44] T. A. Bogetti, C. P. R. Hoppel, V. M. Harik, J. F. Newill, and B. P. Burns. Predicting the nonlinear response and progressive failure of composite laminates. *Fail. Criteria Fibre-Reinforced-Polymer Compos.* pp. 402–428. 2004. doi: 10.1016/B978-008044475-8/50017-2.

[45] Y. He, A. Makeev, and B. Shonkwiler. Characterization of nonlinear shear properties for composite materials using digital image correlation and finite element analysis. *Compos. Sci. Technol.* vol. 73, no. 1. pp. 64–71. 2012. doi: 10.1016/j.compscitech.2012.09.010.

[46] Q. D. Yang *et al.* On crack initiation in notched, cross-plied polymer matrix composites. *J. Mech. Phys. Solids*. vol. 78. pp. 314–332. 2015. doi: 10.1016/j.jmps.2015.01.010.

[47] H. T. Hahn and S. W. Tsai. Nonlinear elastc behaviour of unidirectional composite laminae. *J. Compos. Mater.* vol. 7. pp. 102–118. 1973.

[48] P. P. Camanho, A. Arteiro, A. R. Melro, G. Catalanotti, and M. Vogler. Three-dimensional invariant-based failure criteria for fibre-reinforced composites. *Int. J. Solids Struct.* vol. 55. pp. 92–107. 2015. doi: 10.1016/j.ijsolstr.2014.03.038.

[49] P. P. Camanho, C. G. Davila, S. T. Pinho, L. Iannucci, and P. Robinson. Prediction of in situ strengths and matrix cracking in composites under transverse tension and in-plane shear. *Compos. Part A Appl. Sci. Manuf.* vol. 37, no. 2. pp. 165–176. 2006. doi: 10.1016/j.compositesa.2005.04.023.

[50] C. T. Sun and J. L. Chen. A simple flow rule for characterizing nonlinear behavior of fiber composites. *J. Compos. Mater.* vol. 23, no. 10. pp. 1009–1020. 1989. doi: 10.1177/002199838902301004.

[51] T. Yokozeki, S. Ogihara, S. Yoshida, and T. Ogasawara. Simple constitutive model for nonlinear response of fiber-reinforced composites with loading-directional dependence. *Compos. Sci. Technol.* vol. 67, no. 1. pp. 111–118. 2007. doi: 10.1016/j.compscitech.2006.03.024.

[52] K. W. Gan, M. R. Wisnom, S. R. Hallett, and G. Allegri. A simple plasticity model for predicting transverse composite response and failure. in *19th International Conference on Composite Materials (ICCM)*. Montreal, Canada. 2013.

[53] M. Vogler, R. Rolfes, and P. P. Camanho. Modeling the inelastic deformation and fracture of polymer composites-Part I: Plasticity model. *Mech. Mater.* vol. 59. pp. 50–64. 2013. doi: 10.1016/j.mechmat.2012.12.002.

[54] G. M. Vyas, S. T. Pinho, and P. Robinson. Constitutive modelling of fibre-reinforced composites with unidirectional plies using a plasticity-based approach. *Compos. Sci. Technol.* vol. 71, no. 8. pp. 1068–1074. 2011. doi: 10.1016/j.compscitech.2011.03.009.

[55] P. W. Gerbaud, F. Otero, P. Bussetta, and P. P. Camanho. An invariant based transversely-isotropic constitutive model for unidirectional fibre reinforced composites considering the matrix viscous effects. *Mech. Mater.* vol. 138. 2019. doi: 10.1016/j.mechmat.2019.103146.

[56] S. Y. Hsu, T. J. Vogler, and S. Kyriakides. Inelastic behavior of an AS4/PEEK composite under combined transverse compression and shear. Part II: Modeling. *Int. J. Plast.* vol. 15, no. 8. pp. 807–836. 1999. doi: 10.1016/S0749-6419(99)00012-1.

[57] T. J. Vogler and S. Kyriakides. Inelastic behavior of an AS4/PEEK composite under combined transverse compression and shear. Part I: experiments. *Int. J. Plast.* vol. 15, no. 8. pp. 783–806. 1999. doi: doi.org/10.1016/S0749-6419(99)00011-X.

[58] C. T. Sun, B. J. Quinn, and J. Tao. Comparative evaluation of failure analysis methods for composite laminates. 1996.

[59] P. P. Camanho. Failure criteria in fibre-reinforced-polymer composites. 2002.

[60] S. T. Pinho, C. G. Dávila, P. P. Camanho, L. Iannucci, and P. Robinson. Failure models and criteria for FRP under in-plane or three-dimensional stress states including shear non-

linearity. 2005.

[61]   S. W. Tsai and E. M. Wu. A general theory of strength for anisotropic materials. *J. Compos. Mater.* vol. 5, no. 1. pp. 58–80. 1971. doi: 10.1177/002199837100500106.

[62]   K. S. Liu and S. W. Tsai. A progressive quadratic failure criterion for a laminate. *Compos. Sci. Technol.* vol. 58. pp. 1023–1032. 1998. doi: 10.1016/S0266-3538(96)00141-8.

[63]   A. Kuraishi, S. W. Tsai, and K. K. S. Liu. A progressive quadratic failure criterion, part B. *Compos. Sci. Technol.* vol. 62. pp. 903–921. 2004. doi: 10.1016/B978-008044475-8/50031-7.

[64]   Z. Hashin. Failure criteria for unidirectional fiber composites. *J. Appl. Mech.* vol. 47, no. 2. pp. 329–334. 1980. doi: 10.1115/1.3153664.

[65]   A. Puck and W. Schneider. On failure mechanisms and failure criteria of filamentwound glass-fibre/resin composites. *Plast Polym.* pp. 33–44. 1969.

[66]   A. Puck. Calculating the strength of glass fibre/plastic laminates under combined load. *Kunstst Ger. Plast.* vol. 55. pp. 18–19. 1969.

[67]   B. Budiansky and N. A. Fleck. Compressive failure of fibre composites. *J. Mech. Phys. Solids.* vol. 41, no. 1. pp. 183–211. 1993. doi: 10.1016/0022-5096(93)90068-Q.

[68]   C. Soutis, F. C. Smith, and F. L. Matthews. Predicting the compressive engineering performance of carbon fibre-reinforced plastics. *Compos. Part A Appl. Sci. Manuf.* vol. 31, no. 6. pp. 531–536. 2000. doi: 10.1016/S1359-835X(99)00103-7.

[69]   A. Puck and H. Schürmann. Failure analysis of FRP lamninates by means of physically based phenomenological models. *Compos. Sci. Technol.* vol. 62. pp. 1633–1662. 2002. doi: 10.1016/S0266-3538(96)00140-6.

[70]   G. J. Dvorak and N. Laws. Analysis of progressive matrix cracking in composite laminates II. first ply failure. *J. Compos. Mater.* vol. 21, no. 4. pp. 309–329. 1987. doi: 10.1177/002199838702100402.

[71]   M. J. Hinton and P. D. Soden. Predicting failure in composite laminates: the background to the exercise. *Compos. Sci. Technol.* vol. 58, no. 7. pp. 1001–1010. 1998. doi: 10.1016/S0266-3538(98)00074-8.

[72]   M. J. Hinton and A. S. Kaddour. The background to the second world-wide failure exercise. *J. Compos. Mater.* vol. 46, no. 19–20. pp. 2283–2294. 2012. doi: 10.1177/0021998312449885.

[73]   A. Kaddour, M. Hinton, and P. Smith. The background to the third world-wide failure exercise. *J. Compos. Mater.* vol. 47, no. 20–21. pp. 2417–2426. 2013. doi: 10.1177/0021998313499475.

[74]   ASTM D3039/D3039M-95a, Standart test method for tensile properties of polymer matrix composite materials. ASTM International, 1995, doi: 10.1520/D3039.

[75]   P. D. Soden, M. J. Hinton, and A. S. Kaddour. Biaxial test results for strength and deformation of a range of E-glass and carbon fibre reinforced composite laminates: failure exercise benchmark data. *Compos. Sci. Technol.* vol. 62, no. 12–13. pp. 1489–1514. 2002.

[76]   D. W. A. Rees. *Mechanics of solids and structures*. McGraw-Hill, 1990.

[77]   A. Parvizi, K. W. Garrett, and J. E. Bailey. Constrained cracking in glass fibre-reinforced epoxy cross-ply laminates. *J. Mater. Sci.* vol. 13, no. 10. pp. 2131–2136. 1978. doi: 10.1007/BF00541666.

[78]   D. L. Flaggs. Experimental determination of the in situ transverse lamina strength in graphite / epoxy laminates. *J. Compos. Mater.* vol. 16. pp. 103–116. 1982.

[79]   K. Chang, S. Liu, and F. Chang. Damage tolerance of laminated composites containing an open hole and subjected to tensile loading. *J. Compos. Mater.* vol. 25. pp. 274–301. 1991. doi: 10.1177/002199839102500303.

[80]   A. Arteiro, G. Catalanotti, A. R. Melro, P. Linde, and P. P. Camanho. Micro-mechanical analysis of the effect of ply thickness on the transverse compressive strength of polymer composites. *Compos. Part A Appl. Sci. Manuf.* vol. 79. pp. 127–137. 2015. doi: 10.1016/j.compositesa.2015.09.015.

[81]   D. Roylance. Introduction to fracture mechanics: MIT lecture notes. 2001.

[82]   H. Hahn. A mixed-mode fracture criterion for composite materials. *J. Compos. Technol. Res.* vol. 5, no. 1. 1983.

[83]   ASTM-D3518/D3518M-94, Standard test method for in-plane shear response of polymer matrix composite materials by tensile test of +/- 45° laminate. ASTM International, 1994, doi: 10.1520/D3518.

[84]   ASTM D7078/D7078M-12, Standard test method for shear properties of composite materials by V-notched rail shear method. ASTM International, 2012, doi: 10.1520/D7078.

[85]   ASTM D5379/D5379M-05, Standard test method for shear properties of composite materials by the V-notched beam method. ASTM International, 2005.

[86]   ASTM D5528-01, Standard test method for mode I interlaminar fracture toughness of unidirectional. ASTM International, 2001, doi: 10.1520/D5528-01R07E03.2.

[87]   ASTM D7905/D7905M-19, Standard test method for determination of the mode II interlaminar fracture toughness of unidirectional fiber-reinforced polymer matrix composites. ASTM International, 2019.

[88] ASTM D3410/D3410M-03, Standard test method for compressive properties of polymer matrix composite mterials with unsupported gage section by shear. ASTM International, 2003, doi: 10.1520/D3410.

[89] ASTM D6641/D6641M-01, Standard test method for determining the compressive properties of polymer matrix composite laminates sing a combined loading compression (CLC) test fixture. ASTM International, 2001.

[90] ASTM D5467/D5467M-97, Standard test method for compressive properties of unidirectional polymer matrix composite materials using a sandwich beam. ASTM International, 1997, doi: 10.1520/D5467.

[91] U. Huetter, H. Schelling, and H. Krauss. An experimental study to determine failure envelope of composite materials with tubular specimen under combined loads and comparison between several classical criteria. in *AGRAD162*. Munich. 1974.

[92] E. Petersen, R. G. Cuntze, and C. Hühne. Experimental determination of material parameters in Cuntzes failure mode concept based UD strength failure condition. *Compos. Sci. Technol.* vol. 134. pp. 12–25. 2016.

[93] K. W. Gan, T. Laux, S. T. Taher, J. M. Dulieu-Barton, and O. T. Thomsen. A novel fixture for determining the tension/compression-shear failure envelope of multidirectional composite laminates. *Compos. Struct.* vol. 184. pp. 662–673. 2018. doi: 10.1016/j.compstruct.2017.10.030.

[94] P. Berbinau, C. Soutis, and I. A. Guz. Compressive failure of 0° unidirectional carbon-fibre-reinforced plastic (CFRP) laminates by fibre microbuckling. *Compos. Sci. Technol.* vol. 59, no. 9. pp. 1451–1455. 1999. doi: 10.1016/S0266-3538(98)00181-X.

[95] E. J. Barbero. *Introduction to Composite Materials Design*. Taylor & Fracis inc., 1999.

[96] P. P. Camanho and F. L. Matthews. A progressive damage model for mechanically fastened joints in composite lamiantes. *J. Compos. Mater.* vol. 33, no. 24. pp. 2248–2280. 1999.

[97] A. E.-D. A. El-Sisi, H. M. El-Emam, H. A. Salim, and H. E.-D. M. Sallam. Efficient 3D modeling of damage in composite materials. *J. Compos. Mater.* vol. 49, no. 7. pp. 817–828. 2014. doi: 10.1177/0021998314525983.

[98] J. H. S. Almeida, L. Bittrich, and A. Spickenheuer. Improving the open-hole tension characteristics with variable-axial composite laminates: Optimization, progressive damage modeling and experimental observations. *Compos. Sci. Technol.* vol. 185. 2020. doi: 10.1016/j.compscitech.2019.107889.

[99] I. Lapczyk and J. A. Hurtado. Progressive damage modeling in fiber-reinforced materials. *Compos. Part A Appl. Sci. Manuf.* vol. 38, no. 11. pp. 2333–2341. 2007. doi:

10.1016/j.compositesa.2007.01.017.

[100] S. T. Pinho, P. Robinson, and L. Iannucci. Fracture toughness of the tensile and compressive fibre failure modes in laminated composites. *Compos. Sci. Technol.* vol. 66, no. 13. pp. 2069–2079. 2006. doi: 10.1016/j.compscitech.2005.12.023.

[101] G. Catalanotti, A. Arteiro, M. Hayati, and P. P. Camanho. Determination of the mode I crack resistance curve of polymer composites using the size-effect law. *Eng. Fract. Mech.* vol. 118. pp. 49–65. 2014. doi: 10.1016/j.engfracmech.2013.10.021.

[102] G. Catalanotti, J. Xavier, and P. P. Camanho. Measurement of the compressive crack resistance curve of composites using the size effect law. *Compos. Part A Appl. Sci. Manuf.* vol. 56. pp. 300–307. 2014. doi: 10.1016/j.compositesa.2013.10.017.

[103] Z. P. Bažant and B. H. Oh. Crack band theory for fracture of concrete. *Mater Struct.* vol. 16, no. 93. pp. 155–177. 1983.

[104] N. Moes, J. Dolbow, and T. Belytschko. A finite element method for crack growth without remeshing. *Int. J. Numer. Methods Eng.* vol. 46. pp. 131–150. 1999.

[105] E. V Iarve, M. R. Gurvich, D. H. Mollenhauer, C. A. Rose, and C. G. Dávila. Mesh-independent matrix cracking and delamination modeling in laminated composites. *Int J Numer Meth Engng.* vol. 88. pp. 749–773. 2011. doi: 10.1002/nme.

[106] E. V. Iarve, K. Hoos, M. Braginsky, E. Zhou, and D. H. Mollenhauer. Progressive failure simulation in laminated composites under fatigue loading by using discrete damage modeling. *J. Compos. Mater.* vol. 51, no. 15. pp. 2143–2161. 2017. doi: 10.1177/0021998316681831.

[107] A. Turon, P. P. Camanho, J. Costa, and C. G. Dávila. A damage model for the simulation of delamination in advanced composites under variable-mode loading. *Mech. Mater.* vol. 38. pp. 1072–1089. 2006. doi: 10.1016/j.mechmat.2005.10.003.

[108] M. R. Wisnom and S. R. Hallett. The role of delamination in strength, failure mechanism and hole size effect in open hole tensile tests on quasi-isotropic laminates. *Compos. Part A Appl. Sci. Manuf.* vol. 40, no. 4. pp. 335–342. 2009. doi: 10.1016/j.compositesa.2008.12.013.

[109] P. P. Camanho, C. G. Davila, and M. F. DE Moura. Numerical simulation of mixed-mode progressive delamination in composite materials. *J. Compos. Mater.* vol. 37, no. 16. pp. 1415–1438. 2003. doi: 10.1177/002199803034505.

[110] R. M. Christensen and S. J. Deteresa. Delamination failure investigation for out-of-plane loading in laminates. *J. Compos. Mater.* vol. 38, no. 24. pp. 2231–2238. 2004. doi: 10.1177/0021998304046431.

[111] ASTM D7291/D7291M-15, Standard test method for through-thickness "flatwise" tensile strength and elastic modulus of a fiber-reinforced polymer matrix composite material. ASTM International, 2015.

[112] ASTM D2344/D2344M-16, Standard test method for short-beam strength of polymer matrix composite materials and their laminates. ASTM International, 2016.

[113] I. M. Daniel, J. J. Luo, and P. M. Schubel. Three-dimensional characterization of textile composites. *Compos. Part B Eng.* vol. 39, no. 1. pp. 13–19. 2008. doi: 10.1016/j.compositesb.2007.02.002.

[114] R. Krueger. Virtual crack closure technique: History, approach, and applications. *Appl. Mech. Rev.* vol. 57, no. 1–6. pp. 109–143. 2004. doi: 10.1115/1.1595677.

[115] Dassault System. Abaqus 6.14 Documentation. 2017.

[116] ASTM D6671/D6671M-06, Standard test method for mixed mode I-mode II interlaminar fracture toughness of unidirectional fiber reinforced polymer matrix composites. ASTM International, 2006, doi: 10.1520/D6671.

[117] T. Garulli, A. Catapano, D. Fanteria, and J. Jumel. Development and finite elements assessment of stacking sequences for interlaminar fracture toughness testing of angle-ply interfaces. in *9th International Conference on Composites Testing and Model Identification (COMPTEST)*. Luleå, Sweden. 2019.

[118] ASTM D5766/D5766M-11, Standard test method for open-hole tensile strength of polymer matrix composite laminates. ASTM International, 2011.

[119] ASTM D6484/D6484M-14, Standard test method for open-hole compressive strength of polymer matrix composite laminates. ASTM International, 2014.

[120] B. G. Green, M. R. Wisnom, and S. R. Hallett. An experimental investigation into the tensile strength scaling of notched composites. *Compos. Part A Appl. Sci. Manuf.* vol. 38, no. 3. pp. 867–878. 2007. doi: 10.1016/j.compositesa.2006.07.008.

[121] S. R. Hallett, B. G. Green, W. J. Kin, H. Cheung, and M. R. Wisnom. The open hole tensile test : a challenge for virtual testing of composites. *Int. J. Fract.* vol. 158. pp. 169–181. 2009. doi: 10.1007/s10704-009-9333-8.

[122] W. Cui and M. R. Wisnom. An experimental and analytical study of delamination of unidirectional specimens with cut central plies. *J. Reinf. Plast. Compos. Plast.* vol. 13. pp. 722–739. 1994.

[123] S. R. Hallett *et al.* The open hole tensile test: A challenge for virtual testing of composites. *Int. J. Fract.* vol. 158, no. 2. pp. 169–181. 2009. doi: 10.1007/s10704-009-9333-8.

[124] R. Olsson. A survey of test methods for multiaxial and out-of-plane strength of composite

laminates. *Compos. Sci. Technol.* vol. 71, no. 6. pp. 773–783. Apr. 2011. doi: 10.1016/j.compscitech.2011.01.022.

[125] R. Förster and W. Knappe. Spannungs- und Bruchanalyse an Glasfaser/Kunststoff-Wickelkörper. *Kunststoffe*. vol. 60, no. 12. pp. 1053–1059. 1970.

[126] H. Krauss and H. Schelling. Mehrachsige beanspruchung drei-richtungs-wickelrohre aus verstärkten kunststoffen. *Kunststoffe*. vol. 59, no. 12. pp. 911–917. 1969.

[127] S. R. Swanson and Y. Qian. Multiaxial characterization of T800/3900-2 carbon/epoxy composites. *Compos. Sci. Technol.* vol. 43. pp. 197–203. 1992.

[128] S. R. Swanson and B. C. Trask. Strength of quasi-isotropic laminates under off-axis loading. *Compos. Sci. Technol.* vol. 34, no. 1. pp. 19–34. 1989. doi: 10.1016/0266-3538(89)90075-4.

[129] S. R. Swanson and A. P. Christoforou. Response of quasi-isotropic carbon/epoxy laminates to biaxial stress. *J. Compos. Mater.* vol. 20, no. 5. pp. 457–471. 1986. doi: 10.1177/002199838602000504.

[130] S. R. Swanson, A. P. Christoforou, and G. E. Colvin. Biaxial testing of fiber composites using tubular specimens. *Exp. Mech.* vol. 28, no. 3. pp. 238–243. 1988. doi: 10.1007/BF02329017.

[131] C. S. Lee, W. Hwang, H. C. Park, and K. S. Han. Failure of carbon/epoxy composite tubes under combined axial and torsional loading 1. Experimental results and prediction of biaxial strength by the use of neural networks. *Compos. Sci. Technol.* vol. 59. pp. 1779–1788. 1999. doi: 10.1016/S0266-3538(99)00038-X.

[132] E. S. Shin and K. D. Pae. Effects of hydrostatic pressure on the torsional shear behavior of graphite epoxy composites. *J. Compos. Mater.* vol. 26, no. 4. pp. 462–485. 1992.

[133] J. P. Boehler, S. Demmerle, and S. Koss. A new direct biaxial testing machine for anisotropic materials. *Exp. Mech.* vol. 34, no. 1. pp. 1–9. 1994.

[134] J. S. Welsh, J. S. Mayes, and A. C. Biskner. 2-D biaxial testing and failure predictions of IM7/977-2 carbon/epoxy quasi-isotropic laminates. *Compos. Struct.* vol. 75, no. 1–4. pp. 60–66. 2006. doi: 10.1016/j.compstruct.2006.04.049.

[135] L. Mailly and S. S. Wang. Recent development of planar cruciform experiment on biaxial tensile deformation and failure of unidirectional glass/epoxy composite. *J. Compos. Mater.* vol. 42, no. 13. pp. 1359–1379. 2008. doi: 10.1177/0021998308092203.

[136] D. Van Hemelrijck *et al.* Biaxial testing of fibre reinforced composites. in *16th International Conference on Composite Material (ICCM)*. Kyoto, Japan. 2007.

[137] C. Ramault, A. Makris, D. Van Hemelrijck, E. Lamkanfi, and W. Van Paepegem.

Comparison of different techniques for strain monitoring of a biaxially loaded cruciform specimen. *Strain*. vol. 47, no. SUPPL. 2. pp. 210–217. 2011. doi: 10.1111/j.1475-1305.2010.00760.x.

[138] M. R. L. Gower and R. M. Shaw. Towards a planar cruciform specimen for biaxial characterisation of polymer matrix composites. *Appl. Mech. Mater.* vol. 24–25. pp. 115–120. 2010. doi: 10.4028/www.scientific.net/AMM.24-25.115.

[139] A. Makris, T. Vandenbergh, C. Ramault, D. Van Hemelrijck, and E. Lamkanfi. Shape optimisation of a biaxially loaded cruciform specimen. *Polym. Test.* vol. 29, no. 2. pp. 216–223. 2010. doi: 10.1016/j.polymertesting.2009.11.004.

[140] A. Smits, D. Van Hemelrijck, T. P. Philippidis, and A. Cardon. Design of a cruciform specimen for biaxial testing of fibre reinforced composite laminates. *Compos. Sci. Technol.* vol. 66, no. 7–8. pp. 964–975. 2006. doi: 10.1016/j.compscitech.2005.08.011.

[141] K. W. Gan, M. R. Wisnom, and S. R. Hallett. Effect of high through-thickness compressive stress on fibre direction tensile strength of carbon/epoxy composite laminates. *Compos. Sci. Technol.* vol. 90. pp. 1–8. 2014. doi: 10.1016/j.compscitech.2013.10.010.

[142] K. W. Gan, S. R. Hallett, and M. R. Wisnom. Measurement and modelling of interlaminar shear strength enhancement under moderate through-thickness compression. *Compos. Part A Appl. Sci. Manuf.* vol. 49. pp. 18–25. 2013. doi: 10.1016/j.compositesa.2013.02.004.

[143] J. French. Numerical and experimental design of a cruciform specimen for a novel cryobiaxial test. in *7th International Conference on Composites Testing and Model Identification (COMPTEST)*. Leuven, Belgium. 2017.

[144] A. Rashedi, I. Sridhar, and K. J. Tseng. Fracture characterization of glass fiber composite laminate under experimental biaxial loading. *Compos. Struct.* vol. 138. pp. 17–29. 2016. doi: 10.1016/j.compstruct.2015.11.029.

[145] S. C. Hung and K. M. Liechti. An evaluation of the arcan specimen for determining the shear moduli of fiber-reinforced composites. *Exp. Mech.* vol. 37, no. 4. pp. 460–468. 1997. doi: 10.1007/BF02317314.

[146] P. B. Gning, D. Delsart, J. M. Mortier, and D. Coutellier. Through-thickness strength measurements using Arcan's method. *Compos. Part B Eng.* vol. 41, no. 4. pp. 308–316. 2010. doi: 10.1016/j.compositesb.2010.03.004.

[147] R. El-Hajjar and R. Haj-Ali. In-plane shear testing of thick-section pultruded FRP composites using a modified Arcan fixture. *Compos. Part B Eng.* vol. 35, no. 5. pp. 421–428. 2004. doi: 10.1016/j.compositesb.2003.12.004.

[148] R. Erio Ramos De Sousa Junior, J. R. Gouveia, N. M. Ito, D. Etrio, and J. Dos Santos. Failure prediction of hybrid composite using Arcan's device and Drucker-Prager model. vol. 58. pp. 256–261. 2017. doi: 10.1016/j.polymertesting.2017.01.001.

[149] A. E. Oskui, N. Choupani, and M. Shameli. 3D characterisation of mixed mode fracture thougness of materials using new loading device. *Lat. Am. J. Solids Struct.* vol. 13. pp. 1464–1482. 2016.

[150] S. M. J. Razavi and F. Berto. A new fixture for fracture tests under mixed mode I/II/III loading. *Fatigue Fract. Eng. Mater. Struct.* vol. 42, no. 9. pp. 1874–1888. 2019. doi: 10.1111/ffe.13033.

[151] S. T. Taher, O. T. Thomsen, J. M. Dulieu-Barton, and S. Zhang. Determination of mechanical properties of PVC foam using a modified Arcan fixture. *Compos. Part A Appl. Sci. Manuf.* vol. 43, no. 10. pp. 1698–1708. 2012. doi: 10.1016/j.compositesa.2011.11.010.

[152] J. L. Y. Tan, V. S. Deshpande, and N. A. Fleck. Failure mechanisms of a notched CFRP laminate under multi-axial loading. *Compos. Part A Appl. Sci. Manuf.* vol. 77. pp. 56–66. 2015. doi: 10.1016/j.compositesa.2015.06.005.

[153] PRF Composites Materials. Product data prepreg systems RP-528. [Online]. Available: http://www.prfcomposites.com/. [Accessed: 20-Sep-2016].

[154] Gurit. SA 80 thoughened epoxy adhesive film. [Online]. Available: http://www.gurit.com/files/documents/sa-80pdf.pdf. [Accessed: 22-Sep-2016].

[155] T. E. Oliphant. A guide to NumPy. 2006.

[156] LaVision. DaVis 10.0 Software: Product Manual. Göttingen, 2018.

[157] J. Van Blitterswyk, L. Fletcher, and F. Pierron. Image-Based Inertial Impact Test for Composite Interlaminar Tensile Properties. *J. Dyn. Behav. Mater.* vol. 4, no. 4. pp. 543–572. 2018. doi: 10.1007/s40870-018-0175-1.

[158] C. A. Schneider, W. S. Rasband, and K. W. Eliceiri. ImageJ 1.x NIH Image to ImageJ; 25 years of image analysis. *Nat. Methods.* vol. 9, no. 7. pp. 676–682. 2012.

[159] F. Pierron and A. Vautrin. Measurement of in-plane shear strengths of unidiectional composites with the iosipescu test. *Compos. Sci. Technol.* vol. 57. pp. 1653–1660. 1997.

[160] K. D. Pae and K. Y. Rhee. Effects of hydrostatic pressure on the compressive behavior of thick laminated 45° and 90° unidirectional graphite-fiber/epoxy-matrix composites. *Compos. Sci. Technol.* vol. 53. pp. 281–287. 1995. doi: 10.1016/0266-3538(94)00080-8.

[161] S. Laustsen, E. Lund, L. Kuhlmeier, and O. T. Thomsen. Interfibre failure characterisation of unidirectional and triax glass fibre non-crimp fabric reinforced epoxy laminates. *Appl.*

Compos. Mater. vol. 22. pp. 51–79. 2014. doi: 10.1007/s10443-014-9391-6.

[162] D. C. Drucker and W. Prager. Soil mechanics and plastic analysis or limit design. *Q. Appl. Math.* vol. 10, no. 2. pp. 157–165. 1952. doi: 10.1090/qam/48291.

[163] P. J. Hine, R. A. Duckett, A. S. Kaddour, M. J. Hinton, and G. M. Wells. The effect of hydrostatic pressure on the mechanical properties of glass fibre/epoxy unidirectional composites. *Compos. Part A Appl. Sci. Manuf.* vol. 36, no. 2 SPEC. ISS. pp. 279–289. 2005. doi: 10.1016/j.compositesa.2004.06.004.

[164] E. de S. Nato, D. Peric, and O. DRJ. *Computational methods for plasticity-theory and applications*. Wiley, 2008.

[165] E. Jones, T. Oliphant, and P. Peterson. SciPy Open source scientific tools for Python. 2001.

[166] T. Laux, K. W. Gan, J. M. Dulieu-Barton, and O. T. Thomsen. A simple nonlinear constitutive model based on non-associative plasticity for UD composites: Development and calibration using a Modified Arcan Fixture. *Int. J. Solids Struct.* vol. 162. pp. 135–147. 2019. doi: 10.1016/j.ijsolstr.2018.12.004.

[167] Verein Deutscher Ingenieure (VDI). VDI 2230 Systematische Berechnung hochbeanspruchter Schraubenverbindungen - Zylindrische Einschraubenverbindungen. 2003.

[168] BS EN ISO 898-1. 2009. Mechanical properties of fasteners made of carbon steel and alloy steel, Part 1: Bolts, screws and studs with specified property classes - Coarse thread and fine pitch thread. BSI, 2009.

[169] V. J. Muhs D., Wittel H., Becker M., Jannasch D. *Bolzen-, Stiftverbindungen, Sicherungselemente. In: Roloff/Matek Maschinenelemente Formelsammlung*. 2003.

[170] E. M. C. Jones and M. A. Iadicola. *A good practices guide for digital image correlation*. 2018.

[171] Aquarius Plastics. TUFNOL Rods, Sheets & Tubes. [Online]. Available: https://www.aquariusplastics.co.uk/. [Accessed: 07-May-2019].

[172] Huntsman. Araldite 2000+ Adhesives Data sheet. [Online]. Available: http://www.huntsman.com/advanced_materials/Media Library/global/files/US 2000%2B Adhesives Selector Guide for Bonding_Assembly_Repair_Araldite.pdf. [Accessed: 07-May-2019].

[173] F. Pierron, B. Green, and M. R. Wisnom. Full-field assessment of the damage process of lamianted composite open-hole tensile speciemns. Part I: Methodology. *Compos. Part A Appl. Sci. Manuf.* vol. 38. pp. 2307–2320. 2007.

[174] O. J. Nixon-Pearson, S. R. Hallett, P. J. Withers, and J. Rouse. Damage development in

open-hole composite specimens in fatigue. Part 1: Experimental investigation. *Compos. Struct.* vol. 106. pp. 882–889. 2013. doi: 10.1016/j.compstruct.2013.05.033.

[175] F. Pierron, B. Green, M. R. Wisnom, and S. R. Hallett. Full-field assessment of the damage process of lamianted composite open-hole tensile speciemnspart. Part II: Experimental results. *Compos. Part A Appl. Sci. Manuf.* vol. 38. pp. 2321–2332. 2007.

[176] A. Arteiro, G. Catalanotti, J. Reinoso, P. Linde, and P. P. Camanho. Simulation of the mechanical response of thin-ply composites: from computational micro-mechanics to structural analysis. *Arch. Comput. Methods Eng.* vol. 26. pp. 1445–1487. 2019. doi: 10.1007/s11831-018-9291-2.

[177] Robert McNeel & Associates. Rhinoceros 3D. 2020.

[178] P. Maimí Vert. PhD Thesis: Modelizacion constitutiva y computacional del daño y la fractura de materiales compuestos, 2007.

[179] BS EN ISO 527-5:2009: Plastics — Determination of tensile properties, Part 5: Test conditions for unidirectional fibre-reinforced plastic composites. BSI, 1996.

[180] BS EN ISO 14130: Fibre-reinforced plastic composites Determination of apparent interlaminar shear strength by short-beam method. BSI, 1998.

[181] F. Chang and M. Chen. The in situ ply shear strength distributions in graphite/epoxy laminated composites. *J. Compos. Mater.* vol. 21. pp. 708–733. 1986.

[182] B. H. A. . Tijs, T. A, and B. Chiara. The importance of accounting for large shear deformations on modelling matrix failure of hermoplastic and thermoset composites. in *7th Thematic Conference on the Mechanical Response of Composites (ECCOMAS).* Girona, Spain. 2019.

[183] S. Eskandari, F. M. A. Pires, and P. P. Camanho. An analytical solution to incorporate finite fiber rotation in continuous damage model. in *2nd International conference on mechanics of composites (MECHCOMP).* Porto, Portugal. 2016.

[184] N. Souto, S. Thuillier, and A. Andrade-Campos. Design of an indicator to characterize and classify mechanical tests for sheet metals. *Int. J. Mech. Sci.* vol. 101–102. pp. 252–271. 2015. doi: 10.1016/j.ijmecsci.2015.07.026.

[185] N. Souto, A. Andrade-Campos, and S. Thuillier. A numerical methodology to design heterogeneous mechanical tests. *Int. J. Mech. Sci.* vol. 107. pp. 264–276. 2016. doi: 10.1016/j.ijmecsci.2016.01.021.

[186] G. M. Vyas and S. T. Pinho. Computational implementation of a novel constitutive model for multidirectional composites. *Comput. Mater. Sci.* vol. 51, no. 1. pp. 217–224. 2012. doi: 10.1016/j.commatsci.2011.07.038.

[187] Abaqus. Writing user subroutines with Abaqus. [Online]. Available: https://imechanica.org/files/Writing User Subroutines with ABAQUS.pdf. [Accessed: 07-Feb-2020].

[188] J. Huang and D. V. Griffiths. Return mapping algorithms and stress predictors for failure analysis in geomechanics. *J. Eng. Mech.* vol. 135, no. 4. pp. 276–284. 2009. doi: 10.1061/(ASCE)0733-9399(2009)135:4(276).

[189] ASTM D4255/D4255M-15a, Standard test method for in-plane shear properties of polymer matrix composite materials by the rail shear method. ASTM International, 2015.

Appendices

Appendix A

Experimental raw data to Chapter 3

Figure 3.6
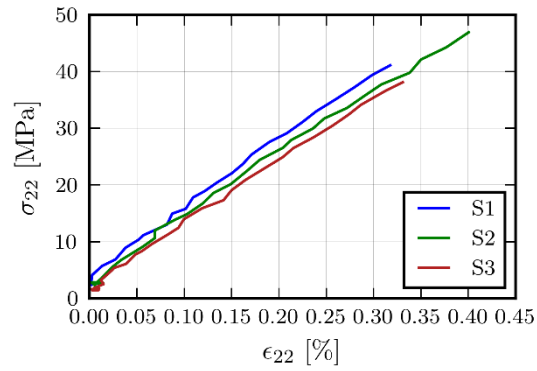
(a) Stress-strain curves for tension ($\alpha = 0°$)
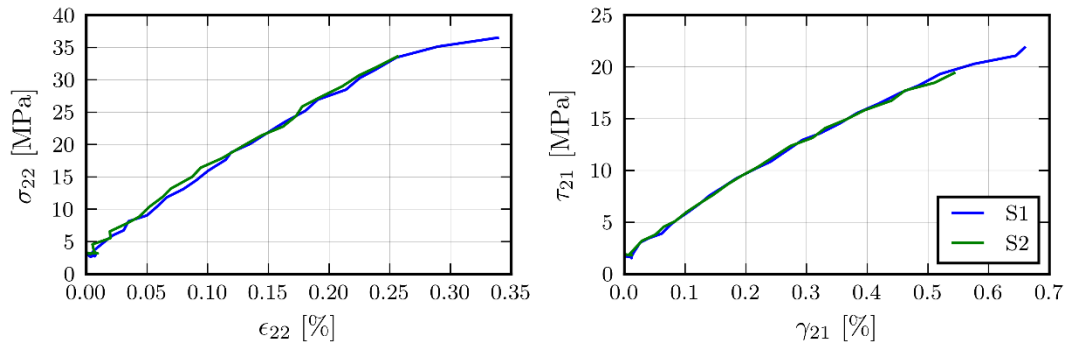
(b) Stress-strain curves for combined tension-shear ($\alpha = 30°$)
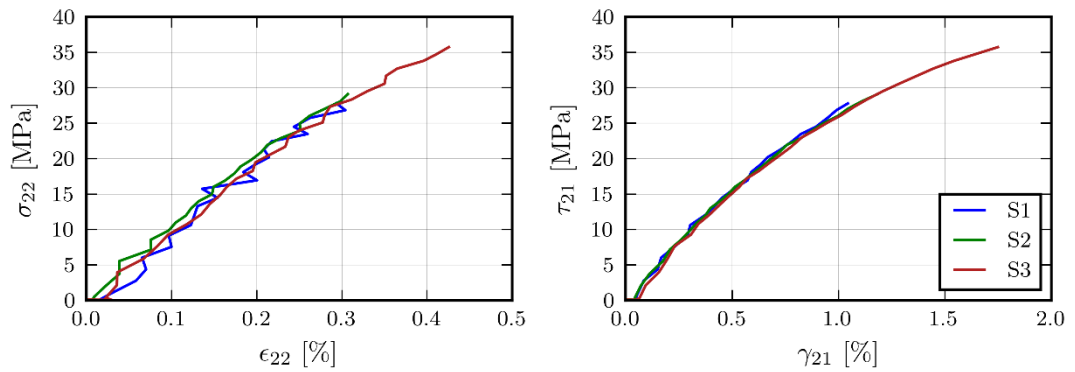
(c) Stress-strain curves for combined tension-shear ($\alpha = 45°$)
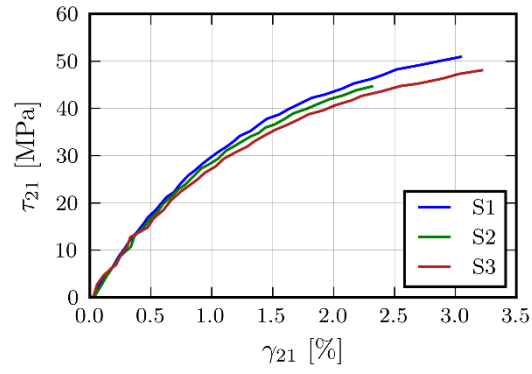
(d) Stress-strain curves for shear ($\alpha = 90°$)
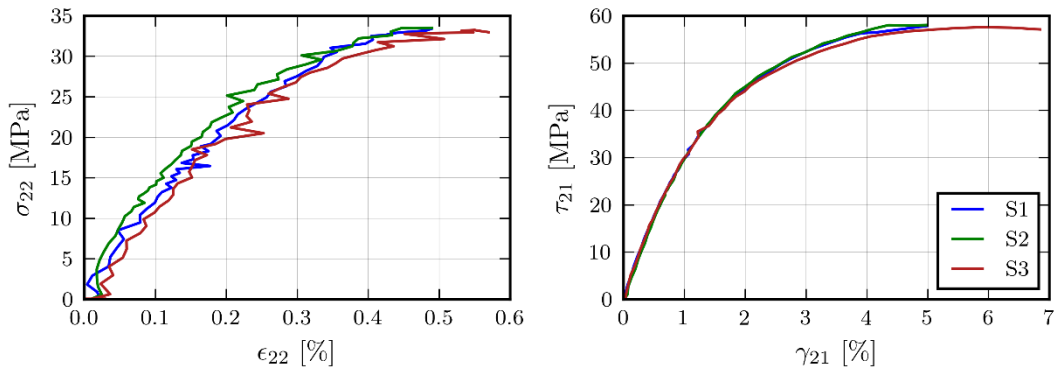
(e) Stress-strain curves for combined compression-shear ($\alpha = 120°$)
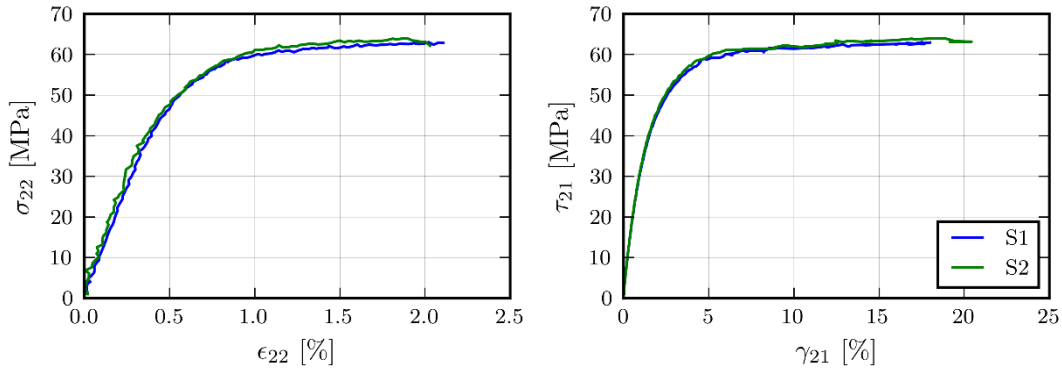
(f) Stress-strain curves for combined compression-shear ($\alpha = 135°$)
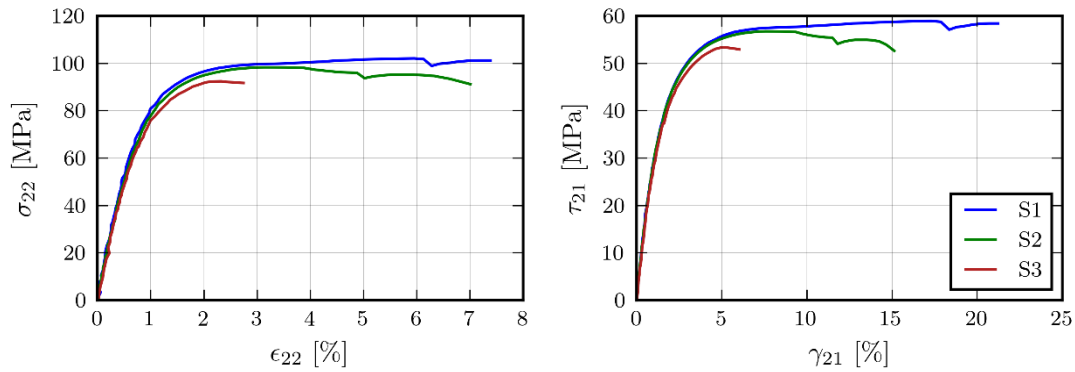
(g) Stress-strain curves for combined compression-shear ($\alpha = 150°$)
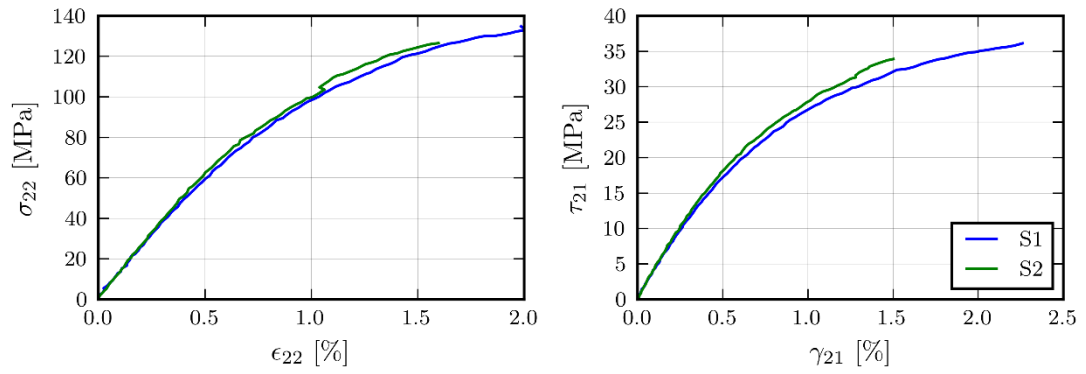
(g) Stress-strain curves for combined compression-shear ($\alpha = 165°$)
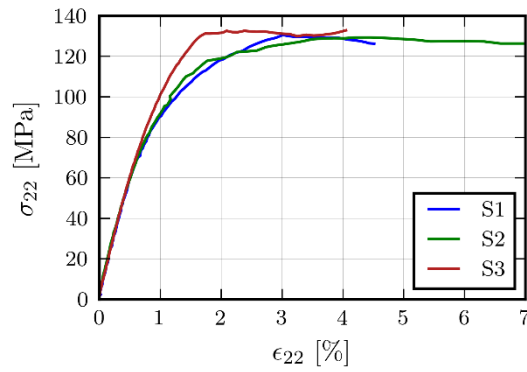
(e) Stress-strain curves for compression ($\alpha = 180°$)

Figure A.1, Experimental raw data for Figure 3.6 in Chapter 3: transverse normal and shear stress-strain curves for RP-528 UD glass/epoxy composite tested on the MAF.

Appendix B

FE implementation of nonlinear constitutive model

B.1 Constitutive model algorithm

The non-associative plasticity based nonlinear constitutive model described in Section 4.3 was implemented as a user material (VUMAT) subroutine in the commercial Finite Element (FE) software ABAQUS [115]. An explicit implementation is utilised to overcome convergence difficulties normally associated with an implicit scheme where the computation of the stiffness matrix (or Jacobian matrix) is necessary at every stress/strain increment as a function of the constitutive properties [186]. The problem is considered to be strain driven where the strain tensor variable ϵ is a function of time. Tensor variables are in the following given in bold font. Firstly, the continuous time scale is discretised into incremental time steps Δt:

$$t_{n+1} = t_n + \Delta t \tag{B.1}$$

Then, the time dependent strain and stress tensor variables ϵ and σ are discretised accordingly:

$$\begin{aligned} \epsilon_{n+1} &= \epsilon_n + \Delta\epsilon \\ \sigma_{n+1} &= \sigma_n + \Delta\sigma \end{aligned} \tag{B.2}$$

where $\Delta\epsilon$ and $\Delta\sigma$ are the incremental strain and stress tensors respectively between time steps n and n+1. The role of the VUMAT within the ABAQUS FE framework is the following [187]: Given the stress σ_n, the total strain increment $\Delta\epsilon$ and the user defined state variables (here the effective plastic strain $\bar{\epsilon}_n^p$) at time step n (all provided by the FE code), find the new stress σ_{n+1} and effective plastic strain $\bar{\epsilon}_{n+1}^p$ at the next time step n+1. In a one-dimensional stress problem, the challenge is to find the new stress at time step n+1, which lies on the nonlinear stress-strain curve. In a three-dimensional stress problem, the challenge is to find the new stress state at timestep n+1 which lies on the yield surface defined by the constitutive model. Numerically, this is iteratively solved using a return mapping algorithm consisting of an initial elastic step (trial or predictor step) followed by a plastic step (corrector step) [164]. Here the well-known cutting-plane algorithm (CPA) [188] is utilised, which is illustrated in Figure B.1.
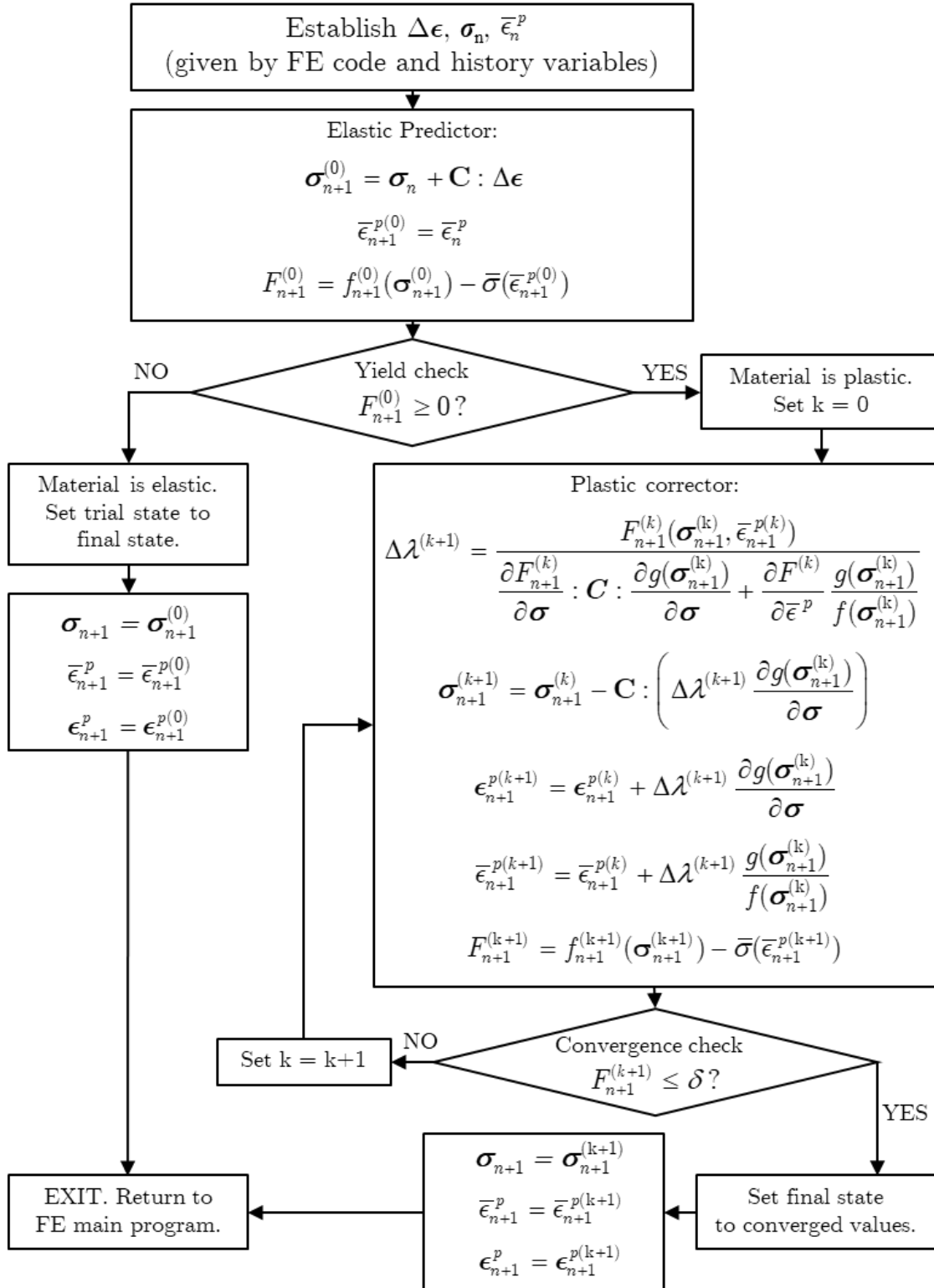
Figure B.1, VUMAT flow chart for non-associative plasticity-based material model.

(i) Setting the scene

Firstly, recall the definition of the yield function f for the three-dimensional stress state from Equation (4.4). Dropping the pressure sensitive term, following the two-dimensional version in Equation (4.7), the plastic potential for the three-dimensional case is:

$$g(\sigma_{ij}) = \sqrt{H(\sigma_{22} - \sigma_{33})^2 + L\tau_{23}^2 + M(\tau_{12}^2 + \tau_{13}^2)} \tag{B.3}$$

The hardening rule in Equation (4.14) can be rearranged for the effective stress as follows:

$$\bar{\sigma}(\bar{\epsilon}^p) = K(\bar{\epsilon}^p)^m \tag{B.4}$$

Based on the yield function in Equation (4.4) and the hardening rule in (B.4), a function F can be define as follows for checking if the material behaves elastic or plastic:

$$F_{n+1}^{trial} = f_{n+1}^{trial}(\sigma_{n+1}^{trial}) - \bar{\sigma}(\bar{\epsilon}_{n+1}^p) < 0 \Rightarrow elastic$$
$$F_{n+1}^{trial} = f_{n+1}^{trial}(\sigma_{n+1}^{trial}) - \bar{\sigma}(\bar{\epsilon}_{n+1}^p) \geq 0 \Rightarrow plastic \tag{B.5}$$

where the stress state is elastic when F is smaller than zero and plastic when F is equal or larger than zero.

(ii) Elastic predictor step

In the initial elastic predictor step, $\Delta\epsilon$ provided by ABAQUS for each timestep n+1 is assumed to be fully elastic. The new stress at n+1 is therefore assumed to be fully elastic and is called the elastic trial stress defined as:

$$\sigma_{n+1}^{trial} = \sigma_n + \mathbf{C} : \Delta\epsilon \tag{B.6}$$

where $\mathbf{C}$ is the stiffness matrix of an orthotropic material. Following Hooke's law, the compliance matrix $\mathbf{H}$ is given by:

$$\mathbf{C}^{-1} = \mathbf{H} = \begin{bmatrix} 1/E_1 & -v_{12}/E_1 & -v_{13}/E_1 & 0 & 0 & 0 \\ & 1/E_2 & -v_{23}/E_2 & 0 & 0 & 0 \\ & & 1/E_3 & 0 & 0 & 0 \\ & & & 1/G_{12} & 0 & 0 \\ & sym. & & & 1/G_{23} & 0 \\ & & & & & 1/G_{13} \end{bmatrix} \tag{B.7}$$

It follows, that the new effective plastic strain at time n+1 can be set to the effective plastic strain at the previous time step n, as the trial step is assumed to be fully elastic *i.e.* there is no increase in effective plastic strain, thus:

$$\bar{\epsilon}_{n+1}^p = \bar{\epsilon}_n^p \tag{B.8}$$

Using the trial stress σ_{n+1}^{trial} and the effective plastic strain $\bar{\epsilon}_{n+1}^p$ at the new time step n+1, the yield condition F in Equation (5.6) is checked. If the trial stress state lies within the elastic domain,

then the new stress and state variables can be set equal to the trial state and the VUMAT can return to the FE main program because the trial stress state is already admissible.

$$\sigma_{n+1} = \sigma_{n+1}^{trial}$$

$$\bar{\epsilon}_{n+1}^{p} = \bar{\epsilon}_{n+1}^{p(k=0)}$$

$$\epsilon_{n+1}^{p} = \epsilon_{n+1}^{p(k=0)}$$

(B.9)

where (k = 0) indicates that no iterative solution was required to find the new stress state *i.e.* the CPA in the plastic corrector was not invoked.

If the stress state lies outside the elastic domain according to the yield condition F in Equation (B.5), then plastic deformation must occur and the plastic corrector step is invoked. In the plastic corrector step, the elastic trial stress state which lies outside of the yield surface is iteratively returned to the yield surface to satisfy the yield condition in Equation (B.5).

(iii) Plastic corrector step

Using the CPA algorithm (other algorithms may be used), the elastic trial stress is iteratively returned to the yield surface in k sub-steps indicated by the superscripts. Using Hooke's law and the strain decomposition theorem from Equation (4.1) and substituting the discretised plastic strain $\epsilon_{n+1}^{p} = \epsilon_{n}^{p} + \Delta\epsilon^{p}$, the new stress $\sigma_{n+1}^{(k+1)}$ at sub-step k+1 is obtained as:

$$\sigma_{n+1}^{(k+1)} = \mathbf{C}:(\epsilon_{n+1} - \epsilon_{n+1}^{p})$$
$$\sigma_{n+1}^{(k+1)} = \mathbf{C}:(\epsilon_{n+1} - \epsilon_{n}^{p}) - \mathbf{C}:\Delta\epsilon^{p}$$

(B.10)

Substituting the flow rule given in Equation (4.8) into Equation (B.10), the new stress becomes:

$$\sigma_{n+1}^{(k+1)} = \mathbf{C}:(\epsilon_{n+1} - \epsilon_{n}^{p}) - \mathbf{C}:\left(\Delta\lambda^{(k+1)}\frac{\partial g(\sigma_{n+1}^{(k)})}{\partial\sigma}\right)$$

(B.11)

Expressing the new strain ϵ_{n+1} based on the previous stain and the strain increment as in (B.2) and upon rearranging the new stress is expressed as:

$$\sigma_{n+1}^{(k+1)} = \mathbf{C}:\left(\epsilon_{n} + \Delta\epsilon - \epsilon_{n}^{p}\right) - \mathbf{C}:\left(\Delta\lambda^{(k+1)}\frac{\partial g(\sigma_{n+1}^{(k)})}{\partial\sigma}\right)$$

$$= \mathbf{C}:(\epsilon_{n} - \epsilon_{n}^{p}) + \mathbf{C}:\Delta\epsilon - \mathbf{C}:\left(\Delta\lambda^{(k+1)}\frac{\partial g(\sigma_{n+1}^{(k)})}{\partial\sigma}\right)$$

(B.12)

Substituting the trial stress given in Equation (B.6) into Equation (B.10) the new stress becomes:

$$\sigma_{n+1}^{(k+1)} = \sigma_{n+1}^{trial} - \mathbf{C}:\left(\Delta\lambda^{(k+1)}\frac{\partial g(\sigma_{n+1}^{(k)})}{\partial\sigma}\right)$$

(B.13)

where $-\mathbf{C}:\left(\Delta\lambda^{(k+1)}\dfrac{\partial g(\boldsymbol{\sigma}_{n+1}^{(k)})}{\partial\boldsymbol{\sigma}}\right)$ is called the plastic corrector, which returns the trial stress back to

the yield surface F along a path perpendicular to the potential function g.

The only unknown in the calculation of the new stress in Equation (B.13) at timestep n+1 is the scalar plastic multiplier $\Delta\lambda^{(k+1)}$. It can be solved by linearizing the yield condition in Equation (B.5) using Taylor's expansion around $\boldsymbol{\sigma}_{n+1}^{(k+1)}$:

$$
F_{n+1}^{(k+1)}(\boldsymbol{\sigma}_{n+1}^{(k+1)},\overline{\epsilon}_{n+1}^{p(k+1)}) =
$$
$$
F_{n+1}^{(k)}(\boldsymbol{\sigma}_{n+1}^{(k)},\overline{\epsilon}_{n+1}^{p(k)}) + \frac{\partial F_{n+1}^{(k)}}{\partial\boldsymbol{\sigma}}\underbrace{(\boldsymbol{\sigma}_{n+1}^{(k+1)}-\boldsymbol{\sigma}_{n+1}^{(k)})}_{\Delta\boldsymbol{\sigma}_{n+1}^{(k+1)}}\frac{\partial F_{n+1}^{(k)}}{\partial\overline{\epsilon}^{p}}\underbrace{(\overline{\epsilon}_{n+1}^{p(k+1)}-\overline{\epsilon}_{n+1}^{p(k)})}_{\Delta\overline{\epsilon}_{n+1}^{p(k+1)}}
\tag{B.14}
$$

where the stress increment $\Delta\boldsymbol{\sigma}_{n+1}^{(k+1)}$ is equal to the plastic corrector step when setting $\boldsymbol{\sigma}_{n+1}^{trial}=\boldsymbol{\sigma}_{n+1}^{(k=0)}$ to allow for the iteration procedure beyond the initial trial stress state:

$$
\Delta\boldsymbol{\sigma}_{n+1}^{k+1} = -\mathbf{C}:\Delta\lambda^{(k+1)}\frac{\partial g(\boldsymbol{\sigma}_{n+1}^{k})}{\partial\boldsymbol{\sigma}}
\tag{B.15}
$$

where the effective plastic strain increment is defined according to Equation (4.12) as:

$$
\Delta\overline{\epsilon}_{n+1}^{p(k+1)} = \Delta\lambda^{(k+1)}\frac{g(\boldsymbol{\sigma}_{n+1}^{(k)})}{f(\boldsymbol{\sigma}_{n+1}^{(k)})}
\tag{B.16}
$$

The consistency condition states that in the plastic domain the plastic multiplier is larger than zero and the yield function is zero ($d\lambda>0\Rightarrow dF=0$), while in the elastic domain the yield function is smaller than zero and the plastic multiplier is zero ($dF<0\Rightarrow d\lambda=0$). This leads to the consistency equation [164]:

$$
d\lambda dF = 0
\tag{B.17}
$$

Substituting Equations (B.15) and (B.16) into (B.14) and forcing $F_{n+1}^{(k+1)}(\boldsymbol{\sigma}_{n+1}^{(k+1)},\overline{\epsilon}_{n+1}^{p(k+1)})$ to zero, because $dF = 0$, which follows from the consistency equation, the following expression is obtained:

$$
0 = F_{n+1}^{(k)}(\boldsymbol{\sigma}_{n+1}^{(k)},\overline{\epsilon}_{n+1}^{p(k)}) - \frac{\partial F_{n+1}^{(k)}}{\partial\boldsymbol{\sigma}}(\mathbf{C}:\Delta\lambda^{(k+1)}\frac{\partial g(\boldsymbol{\sigma}_{n+1}^{(k)})}{\partial\boldsymbol{\sigma}}) + \frac{\partial F_{n+1}^{(k)}}{\partial\overline{\epsilon}^{p}}\frac{g(\boldsymbol{\sigma}_{n+1}^{(k)})}{f(\boldsymbol{\sigma}_{n+1}^{(k)})}\Delta\lambda^{(k+1)}
\tag{B.18}
$$

The plastic multiplier $\Delta\lambda^{(k+1)}$ can then be found upon rearranging Equation (B.18) as follows:

$$
\Delta\lambda^{(k+1)} = \frac{F_{n+1}^{(k)}(\boldsymbol{\sigma}_{n+1}^{(k)},\overline{\epsilon}_{n+1}^{p(k)})}{\dfrac{\partial F_{n+1}^{(k)}}{\partial\boldsymbol{\sigma}}:\mathbf{C}:\dfrac{\partial g(\boldsymbol{\sigma}_{n+1}^{(k)})}{\partial\boldsymbol{\sigma}} + \dfrac{\partial F^{(k)}}{\partial\overline{\epsilon}^{p}}\dfrac{g(\boldsymbol{\sigma}_{n+1}^{(k)})}{f(\boldsymbol{\sigma}_{n+1}^{(k)})}}
\tag{B.19}
$$

With $\Delta\lambda^{(k+1)}$, the new stresses, plastic strains and the effective plastic strains are updated for time step n+1:

$$\boldsymbol{\sigma}_{n+1}^{(k+1)} = \boldsymbol{\sigma}_{n+1}^{(k)} - \mathbf{C} : \left(\Delta \lambda^{(k+1)} \frac{\partial g(\boldsymbol{\sigma}_{n+1}^{(k)})}{\partial \boldsymbol{\sigma}} \right) \tag{B.20}$$

$$\epsilon_{n+1}^{p(k+1)} = \epsilon_{n+1}^{p(k)} + \Delta \lambda^{(k+1)} \frac{\partial g(\boldsymbol{\sigma}_{n+1}^{(k+1)})}{\partial \boldsymbol{\sigma}} \tag{B.21}$$

$$\overline{\epsilon}_{n+1}^{p(k+1)} = \overline{\epsilon}_{n+1}^{p(k)} + \Delta \lambda^{(k+1)} \frac{g(\boldsymbol{\sigma}_{n+1}^{(k)})}{f(\boldsymbol{\sigma}_{n+1}^{(k)})} \tag{B.22}$$

The iterative procedure is repeated k times until the plastic yield condition in Equation (B.14) converges to a prescribed tolerance δ (here $\delta = 10^{-6}$):

$$F_{n+1}^{(k+1)} = f_{n+1}^{(k+1)}(\boldsymbol{\sigma}_{n+1}^{(k+1)}) - \overline{\sigma}(\overline{\epsilon}_{n+1}^{p(k+1)}) \leq \delta \tag{7.23}$$

Upon convergence, the VUMAT can return to the FE main program.

B.2 Verification of FE implementation

A simple single element FE model was subjected to pure tension, shear and compression using the VUMAT developed above for model verification. The element type used was an 8-noded brick with reduced integration and hour glass control (C3D8R). The simulated stress-strain curves were then compared in Figure B.2 against the linear elastic material model and the nonlinear analytical constitutive model described in Chapter 4 to verify the model implementation. The VUMAT stress-strain curves for tension (Figure B.2 (a)), shear (Figure B.2 (b)), and compression (Figure B.2 (c)), as well as the associated effective plastic stress-strain curves (Figure B.2 (d)) agree well with the analytical model.
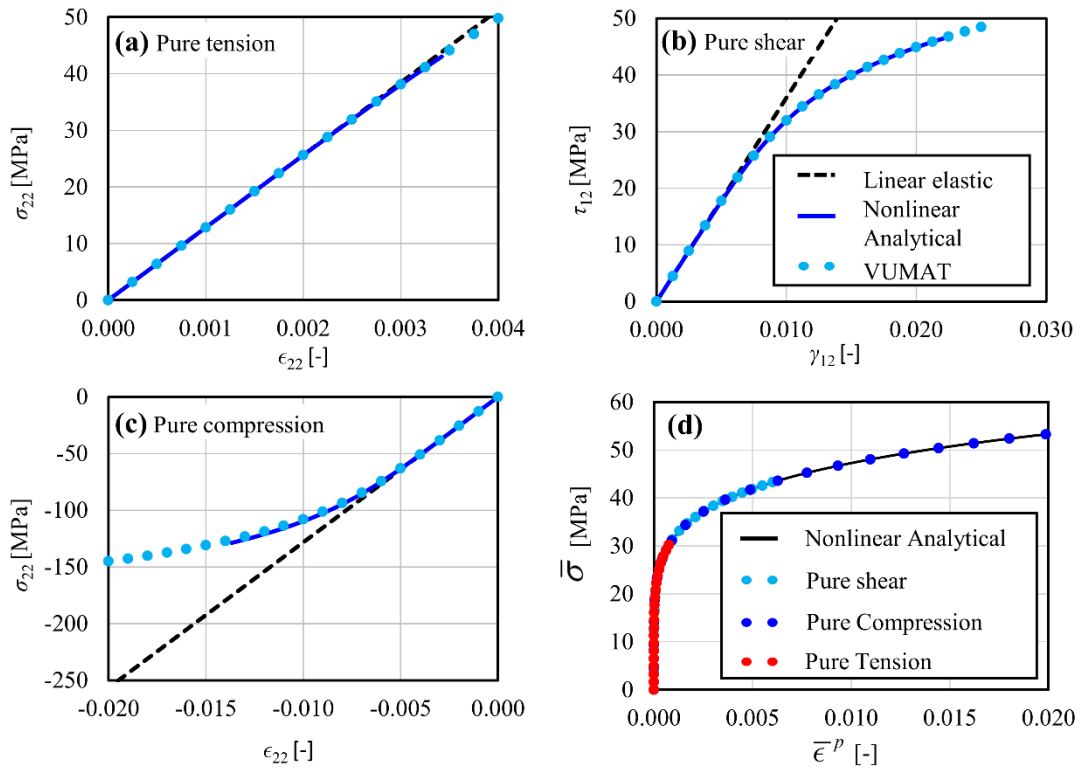
Figure B.2, Stress-strain curves as predicted by the single element FE model using the VUMAT in comparison to the linear elastic and nonlinear analytical material models: (a) uniaxial tension, (b) pure shear, (c) uniaxial compression, and (d) effective plastic stress-strain curves associated with tension, compression and shear.

The same single element FE model was also run for combined tension-shear (Figure B.3) and compression-shear (Figure B.4) load cases. Good agreement between the VUMAT transverse and shear stress-strain curve with the analytical model predictions were found for both cases.
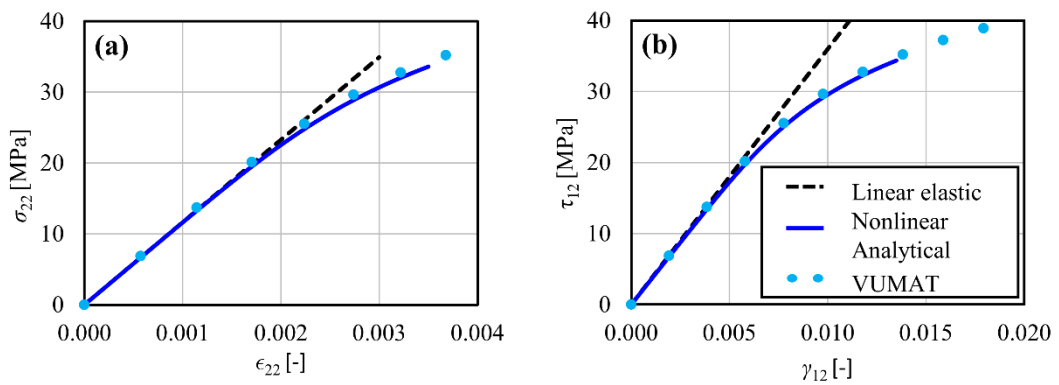
Figure B.3, (a) transverse and (b) shear stress-strain curves as predicted by the single element FE model using the VUMAT in comparison with the linear elastic and nonlinear analytical model for combined tension-shear (α = 45°).
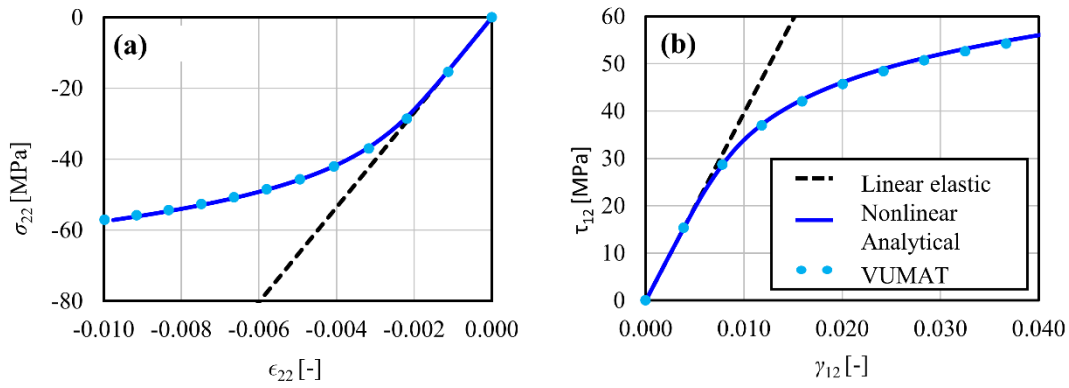
Figure B.4, (a) transverse and (b) shear stress-strain curves as predicted by the single element FE model using the VUMAT in comparison with the linear elastic and nonlinear analytical model for combined compression-shear (α = 135°).

The section has shown that the nonlinear material model for UD composites developed in Chapter 4 has been implemented accurately into a user material subroutine (VUMAT). The VUMAT can be used for nonlinear stress/strain analyses in FRP composites.

Appendix C

Experimental characterisation of the uniaxial mechanical properties of UD carbon/epoxy prepreg system

C.1 Longitudinal tensile test (ISO 527-5)
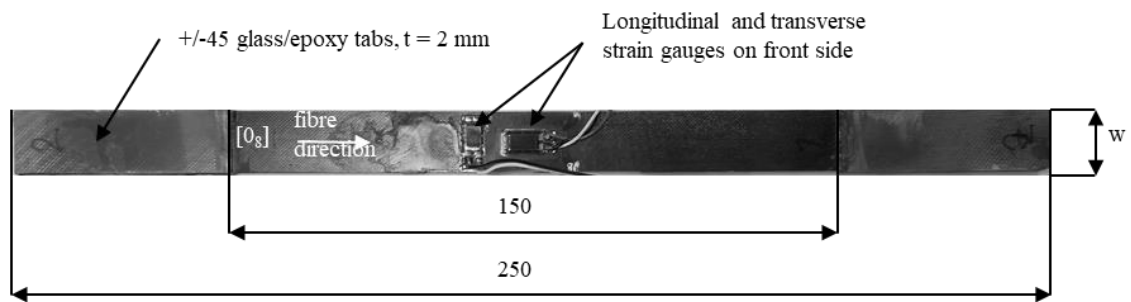
Figure C.1, Longitudinal tensile specimen with a longitudinal and a transverse linear strain gauge mounted on the front side.
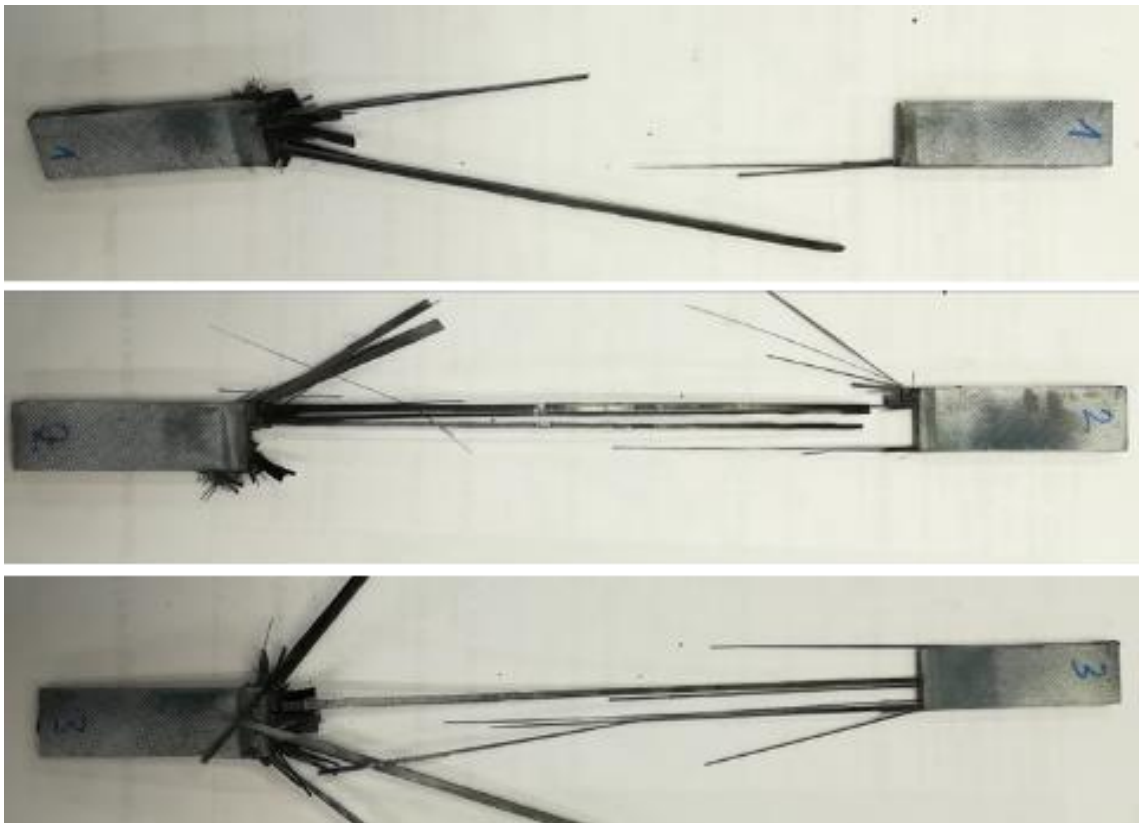
Figure C.2, Failed specimens showing fibre splitting and fibre breaks.
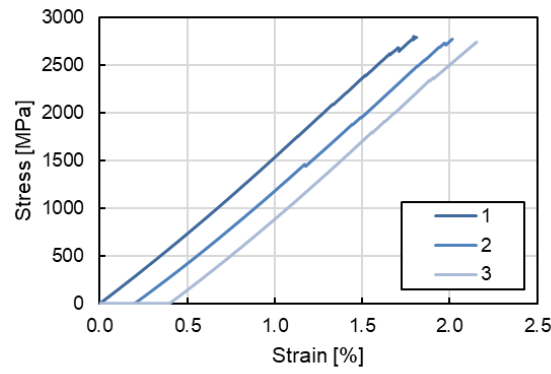
Figure C.3, Longitudinal tensile stress-strain curves.

Table C.1, Longitudinal tensile test results.

Test No.	w [mm]	t [mm]	E_1* [GPa]	v_{12}* [-]	X_T [MPa]	ϵ_{11}^T [%]	Failure modes
1	15.14	1.22	144.93	0.312	2802	1.81	Combined fibre splitting and breaking
2	15.12	1.22	140.18	0.324	2775	1.81	Combined fibre splitting and breaking
3	15.15	1.22	144.45	0.348	2743	1.90	Combined fibre splitting and breaking
AVG	**15.13**	**1.22**	**143.19**	**0.328**	**2774**	**1.84**	
STD	**0.02**	**0.00**	**2.62**	**0.018**	**29**	**0.05**	
COV	**0.10%**	**0.32%**	**1.83%**	**5.60%**	**1.05%**	**2.92%**	

* Extracted in the strain range of 0.1 – 0.3%.

C.2 Transverse tensile test ISO 527-5
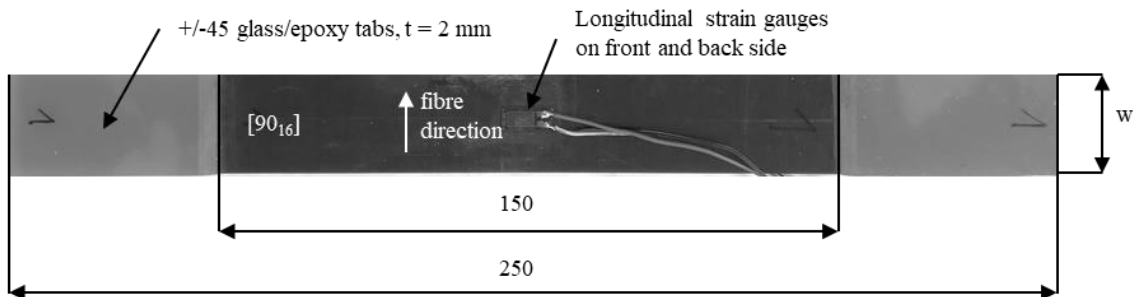
Figure C.4, Transverse tensile specimen with a longitudinally mounted strain gauge on the front and the back side of the specimen.

Figure C.5, Failed specimens showing transverse matrix cracks in the gauge area.
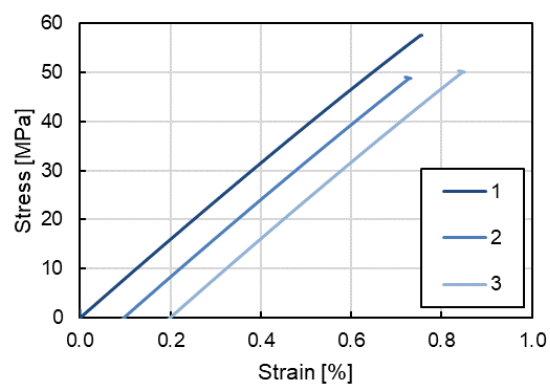
Figure C.6, Transverse tensile stress-strain curves. Strains are taken as the average of the front and backside strain gauge measurement.

Table C.2, Summary of results for the transverse tensile Young's modulus E_2, the transverse tensile strength Y_T and the transverse tensile strain to failure ϵ_{22}^T.

Test No.	w [mm]	t [mm]	E_2 [GPa]	Y_T [MPa]	ϵ_{22}^T [%]	Failure mode
1	25.18	2.46	7.90	58	0.76	Two transverse fracture planes in the gauge section
2	24.32	2.46	7.91	49	0.63	One transverse fracture plane in gauge section
3	25.00	2.48	7.90	50	0.65	One transverse fracture plane in gauge section
AVG	**24.83**	**2.47**	**7.90**	**52**	**0.68**	
STD	**0.45**	**0.01**	**0.01**	**5**	**0.07**	
COV	**1.83%**	**0.47%**	**0.12%**	**8.70%**	**9.86%**	

* Extracted in the strain range of 0.1 – 0.3%.

C.3 Shear testing using Modified Arcan Fixture and DIC

C.3.1   Introduction

No consensus has been reached on how to best obtain the shear modulus and strength of strongly anisotropic materials such as UD carbon/epoxy composites. This is reflected in the existence of several methods for determining the shear response of FRP composites which includes tensile tests of +/−45 laminates [83], the V-notched beam method [85], also called Iosipescu test, the two (or three) rail shear method [189] or the V-notched rail shear method [84], which is similar to the Arcan test. Both the V-notched beam and the V-notched shear method use similar butterfly specimens where the shear strains used to derive the shear stress-strain curve is typically measured using a strain gauge rosette at the centre of the waisted gauge section, although the stress/strain state is nonuniform and a function of not only the butterfly geometry but also of the anisotropy of the material. The nonuniformity leads to an under- or overprediction of the slope of the shear stress-strain curves depending on the material tested. To overcome this drawback, correction factors were suggested which can be determined by FE model updating. Despite the time and effort needed in FE modelling, a further disadvantage is that all material elastic constants need to be determined beforehand, which is not normally the case. In the following, it is shown that by using the full-field strain measurement technique DIC, which is nowadays widely available in materials research laboratories, an accurate shear stress/strain response can be obtained without the need for correction factors. The proposed methodology is validated by testing two types of UD carbon/epoxy specimens where the fibres are parallel and perpendicular to the waisted gauge section, respectively. Based on the fundamentals of solid mechanics for transversely isotropic materials, the in-plane shear moduli derived from the two specimens must be the same $(G_{12} = G_{21})$.

The following work demonstrates that by using the average shear strains in the gauge section obtained using DIC, instead of the strains measured with a strain gauge at the centre of the gauge section, the two obtained shear moduli only differ by 3.5%, which is less and therefore more accurate than when strain gauges at the centre of the waisted gauge line were used.

C.3.2   Experimental set-up and data reduction

The shear tests were conducted on the MAF using the experimental set-up proposed in Chapter 3. The two types of specimen geometries tested are shown in Figure C.7. In the $[0_{16}]$ specimen shown in Figure C.7 (a), the fibres are aligned perpendicular to the gauge section whereas in the $[90_{16}]$ specimen shown in Figure C.7 (b) they are aligned parallel to the gauge section.
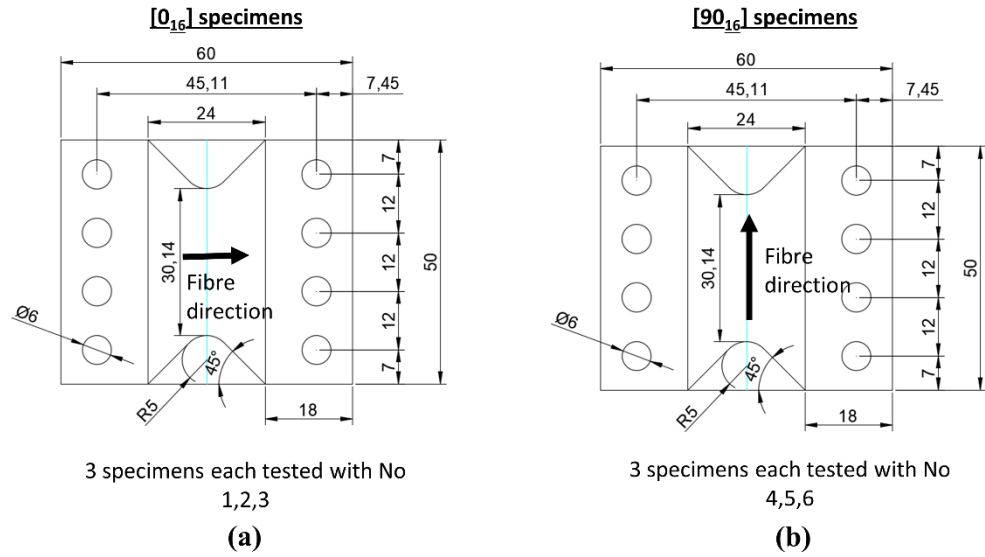
Figure C.7, Butterfly specimen configurations used for shear testing on the MAF: (a) specimen with fibre perpendicular [0$_{16}$], and specimen with the fibres parallel [90$_{16}$] to the waisted gauge section.

Characteristic DIC shear strain maps and gauge section strain profiles for both specimen types obtained on both sides are shown in Figure C.8 and Figure C.9, respectively. Note, that in case of the [0$_{16}$] specimen, the strain gauge used according to standard procedures sits in a strain minimum (Figure C.8 (a)) and in case of the [90$_{16}$] specimen in a strain maximum (Figure C.8 (b)). Also note the similarity of the front and back side strain fields which proofs symmetry of loading. The areas of the DIC strain maps used to extract the average gauge section shear strains are highlighted with black boxes in Figure C.8.
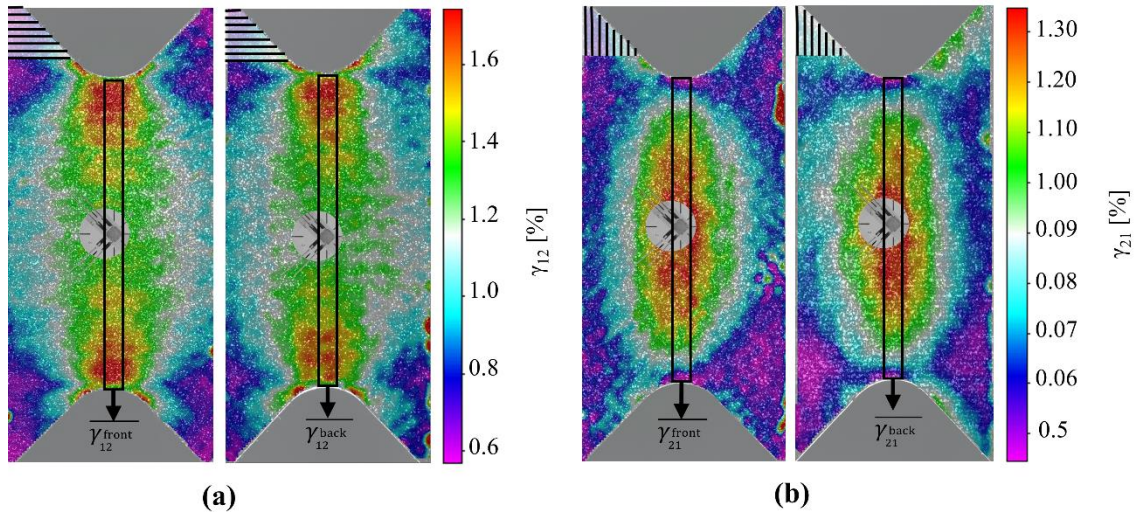
Figure C.8, Shear strain maps obtained using DIC in the linear/elastic part of the material response for (a) the [0$_{16}$] specimen and (b) the [90$_{16}$] specimen on the front and back side.
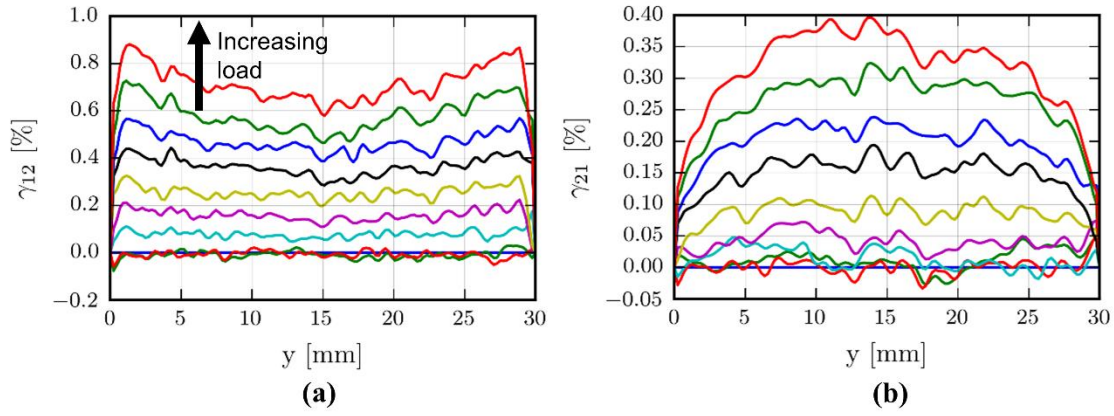
Figure C.9, Shear strain profiles at the gauge section for (a) a [0₁₆] specimen and (b) a [90₁₆] specimen.

C.3.3   Results

The derived stress-strain curves on the front (blue) and back (green) side of the $[0_{16}]$ specimens are shown in the top row and of the $[90_{16}]$ specimens in the bottom row of Figure C.10. Photographs of the failed $[0_{16}]$ specimens are shown in Figure C.11 and the failed $[90_{16}]$ specimens are shown in Figure C.12.
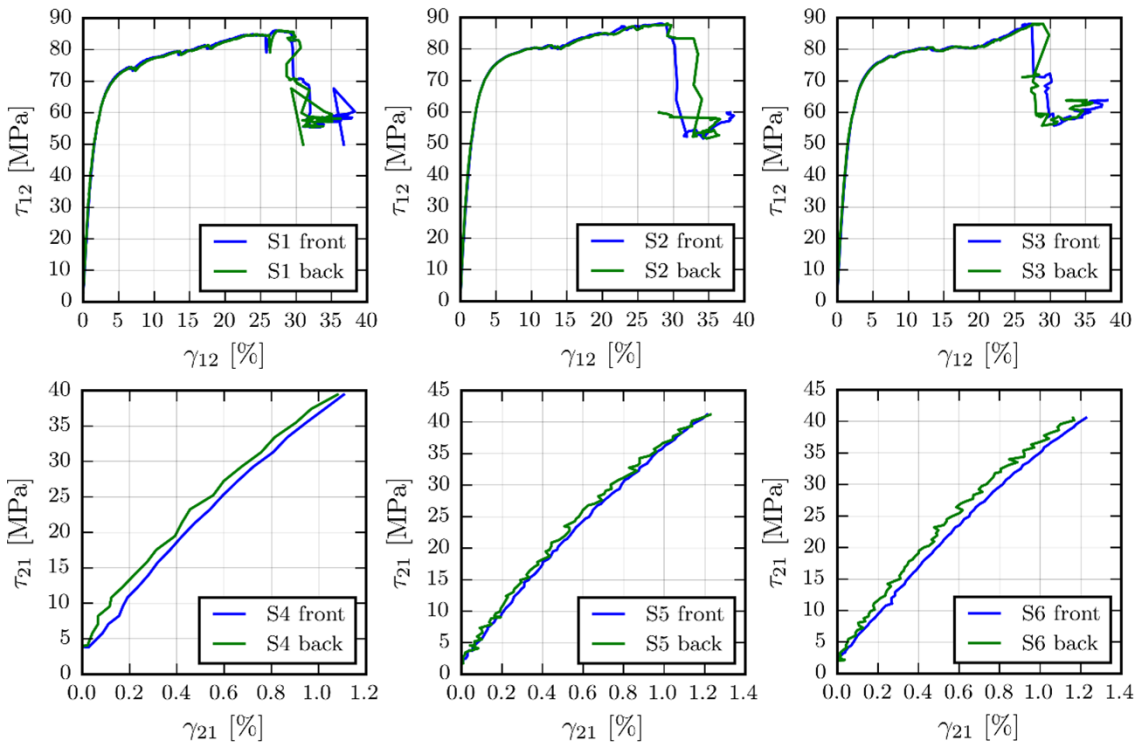
Figure C.10, Shear stress-strain curves derived using DIC on the front (blue) and back (green) side of the [0₁₆] (top row) and a [90₁₆] (bottom row) specimens.

Figure C.11, Failed [0$_{16}$] specimens.

Figure C.12, Failed [90$_{16}$] specimens.

The stress-strain curves derived on the front side of the specimens are plotted in Figure C.13 . Three shear failure strengths are defined. The first is the lower bound shear strength $S_L^{90°}$, obtained as the maximum stress carried by the [90$_{16}$] specimens. These types of specimens fail at the notches under a combined transverse tensile and shear stress state and fail prematurely due to the low transverse tensile strength of the UD composite (also see Chapter 3). Another shear strength is defined as the 0.2% offset shear strength of the [0$_{16}$] specimens which marks the initiation of nonlinear behaviour. The ultimate shear strength is than defined as the maximum stress carried by the [0$_{16}$] specimens. Further the inter laminar shear strength (ILSS) obtained by an independent material characterisation laboratory using a short beam shear test [112] is also plotted for comparison.
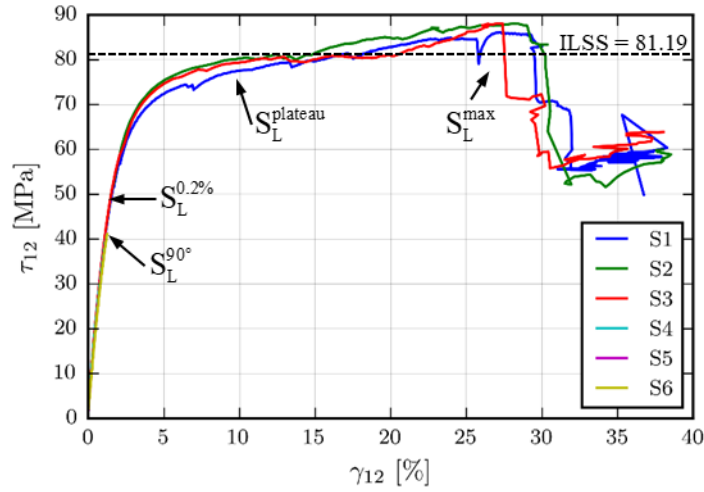
Figure C.13, All shear-stress-strain curves overlaid, definition of three distinct failure points.

The shear moduli and strengths extracted from the stress-strain curves are summarised in Table C.3 for the [0_{16}] specimens and in Table C.4 for the [90_{16}] specimens.

Table C.3, Summary of results obtained on the [0_{16}] specimens.

Specimen No.	G_{12}^{front} * [GPa]	G_{12}^{back} * [GPa]	G_{12}^{avg} [GPa]	$S_L^{0.2\%}$ [MPa]	$S_L^{plateau}$ [MPa]	S_L^{max} [MPa]	γ_{12}^{fail} [%]
1	3.839	3.935	3.953	47.683	73.810	86.111	29.450
2	3.751	4.129	3.940	48.978	80.690	88.064	29.348
3	3.724	4.130	3.927	49.892	77.430	88.089	28.2
Mean	**3.771**	**4.065**	**3.940**	**48.851**	**77.310**	**87.421**	**28.999**
Std	**0.060**	**0.112**	**0.013**	**1.110**	**3.442**	**1.135**	**0.694**
CoV	**1.59%**	**2.76%**	**0.33%**	**2.27%**	**4.45%**	**1.30%**	**2.39%**
	* Extracted in the strain range of 0.1 – 0.5%.						

Table C.4, Summary of results obtained on the [90_{16}] specimens.

Specimen No.	G_{21}^{front} * a[GPa]	G_{21}^{back} * [GPa]	G_{21}^{avg} [GPa]	$S_L^{90°}$ [MPa]	γ_{21}^{fail} [%]
4	3.946	3.682	3.814	39.432	1.093
5	3.776	3.850	3.813	41.190	1.221
6	3.685	3.881	3.783	41.071	1.197
Mean	**3.803**	**3.804**	**3.804**	**40.564**	**1.170**
Std	**0.132**	**0.107**	**0.017**	**0.982**	**0.068**
CoV	**3.48%**	**2.82%**	**0.46%**	**2.42%**	**5.82%**
* Extracted in the strain range of 0.1 – 0.5%.					

The two average moduli obtained from $[90_{16}]$ and $[0_{16}]$ type specimens differ by 3.5%. Due to the more uniform strain state in the shear modulus obtained from the $[0_{16}]$, G_{12}^{avg} is judged to be more accurate than G_{21}^{avg} and is therefore used to inform the meso-scale model in Chapter 6. The definition of the shear strength which should be used to calibrate failure criteria is ambiguous. By comparing the different shear strength definitions, it is concluded that the ILSS strength and the plateau onset strength $(S_L^{plateau})$ are good estimates of the true shear strength and that $S_L^{90°}$ underestimates (also see Chapter 3) and S_L^{max} overestimates the true shear strength. Therefore, ILSS will be used to inform the in-plane failure criterion used in Chapter 6.

C.4 Longitudinal compression test (ASTM D 3410M)
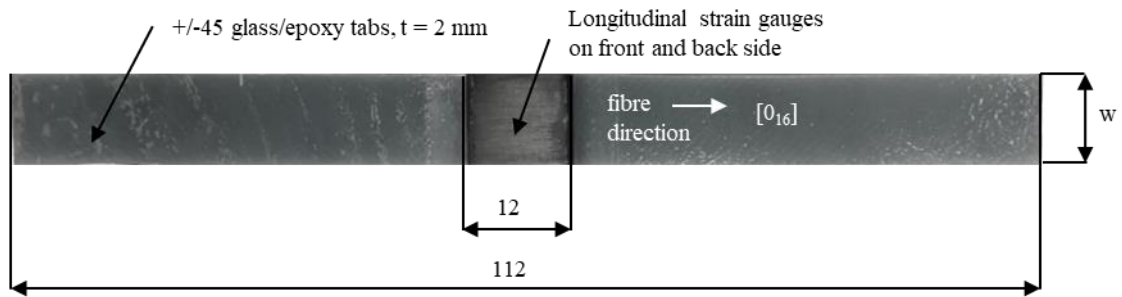
Figure C.14, Longitudinal compression specimen with a longitudinal strain gauge mounted on the front and backside.
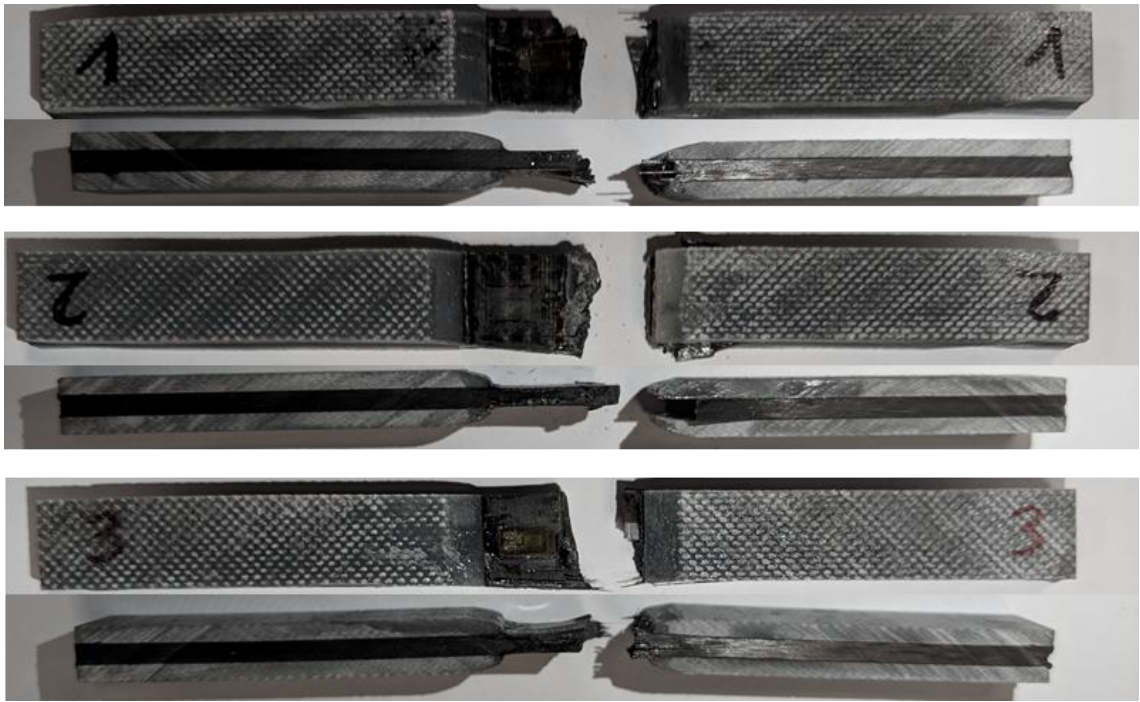
Figure C.15, Failed specimens longitudinal compression specimens.
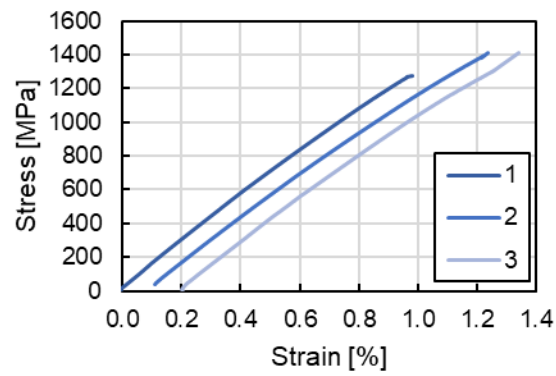
Figure C.16, Longitudinal compression stress-strain curves.

Table C.5, Summary of results for the longitudinal compression test.

Test No.	w [mm]	t [mm]	$E_{1c}*$ [GPa]	X_C [Mpa]	ϵ_{11}^C [%]	Failure modes
1	10.38	2.27	148.59	1358	0.98	TAT -Transverse shear at grip top
2	10.41	2.24	142.55	1414	1.14	SGV - splitting at gage
3	10.44	2.26	136.72	1408	1.14	TAT -Transverse shear at grip top
AVG	**10.41**	**2.26**	**142.62**	**1394**	**1.09**	
STD	**0.03**	**0.01**	**5.93**	**31**	**0.09**	
COV	**0.29%**	**0.52%**	**4.16%**	**2.21%**	**8.31%**	

* Extracted in the strain range of 0.05 – 0.15%.

C.5 Transverse compression test (ASTM D 3410M)
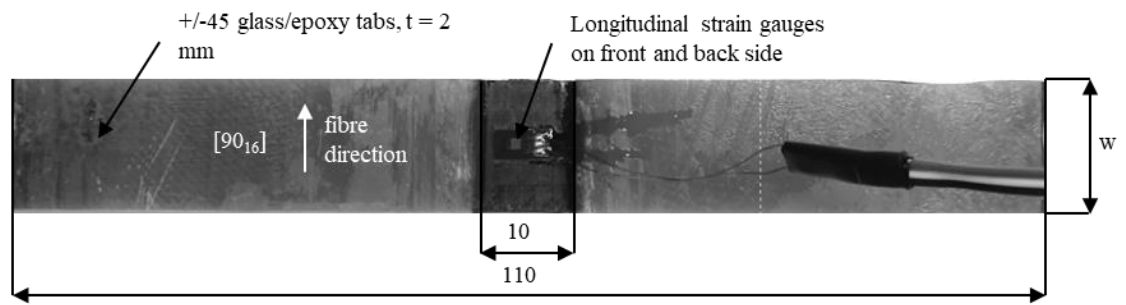
Figure C.17, Transverse compression specimen with longitudinal strain gauges mounted on front and backside.

Figure C.18, Failed transverse compression specimens.
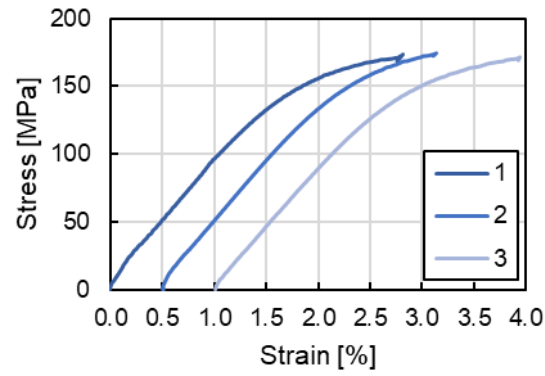
Figure C.19, Transverse compressive stress-strain curves.

Table C.6, Summary of results for the transverse Young's modulus obtained under compressive loading E_{2c}, the transverse compressive strength Y_c and the transverse compressive strain to failure ϵ_{22}^{C}.

Spec. No.	w [mm]	t [mm]	E_{2c}* [Gpa]	Y_C [Mpa]	ϵ_{22}^{C} [%]	Failure mode
1	15.38	2.29	8.62	174	2.81	Puck's IFF Mode C
2	15.43	2.32	8.50	174	2.64	Puck's IFF Mode C
3	15.38	2.33	8.64	172	2.94	Puck's IFF Mode C
AVG	**15.40**	**2.31**	**8.59**	**173**	**2.80**	
STD	**0.03**	**0.02**	**0.08**	**1**	**0.15**	
COV	**0.20%**	**0.97%**	**0.91%**	**0.75%**	**5.47%**	

* Extracted from strain range of 0.15 – 0.35%.

Appendix D

Meso-scale modelling – sensitivity study

Two main uncertainties regarding the input parameters for the meso-scale model used in Chapter 6 were identified: the first is the bilinear shear-fit adopted and the second one is the uncertainty associated with the fracture energies assumed from different material systems reported in the literature. Therefore, a sensitivity analysis was run on judiciously selected combinations of material parameters to establish a feel for the sensitivity of the predicted open-hole specimen strength on the investigated parameters.

The shear stress-strain curves shown in Figure D.1 were obtained using the method described in Chapter 3 and are presented in Appendix C.3.
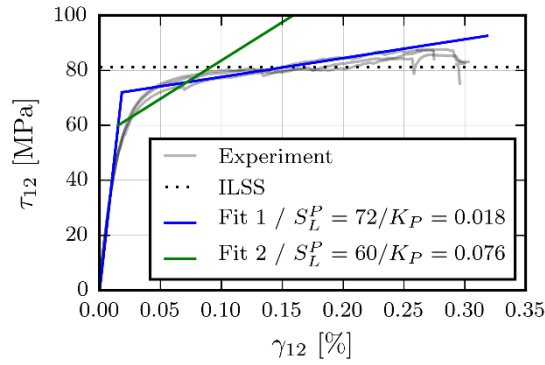
Figure D.1, Shear stress-strain curves: Experimental versus two different bilinear shear fits.

Due to the bilinear nature of the fit, the model cannot accurately predict the stress-strain curves over the whole range of shear deformation. A choice can be made between an overall best fit (shear fit 1) and a fit that fits the experimental data better in the initial part of the stress-strain curves, while losing accuracy at high strains (shear fit 2) as shown in Figure D.1. In addition, the stress-strain curve at very large strains may only approximate the 'true' material stress-strain curves due to structural effects in the experiment. For these reasons two shear-fits were considered.

Fracture toughness values were taken from the IM7/8552 (referred to as IM7) and T800/M21 (referred to as T800) carbon/epoxy prepreg material systems as reported in [17]. The fracture toughness values were grouped into toughness of the fibre, the matrix and the interface, and different combinations of these groups were analysed as illustrated in Figure D.2.
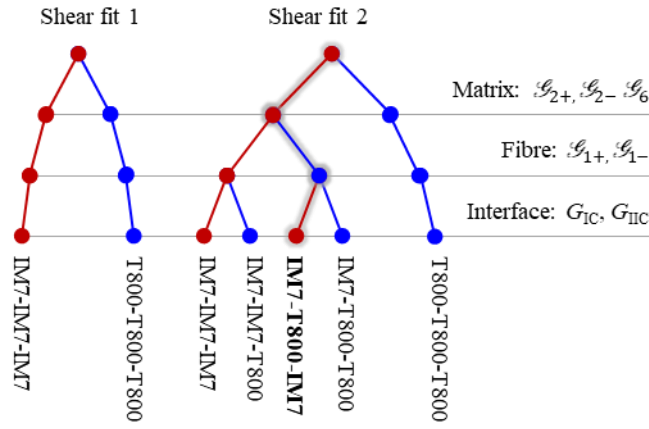
Figure D.2, Shear-fit and fracture toughness combinations included in the sensitivity analysis.

The simulated failure envelopes for the investigated sets of material properties are compared against each other and against the experimental data for Laminates 1 and 2 tested in Chapter 5 in Figure D.3.
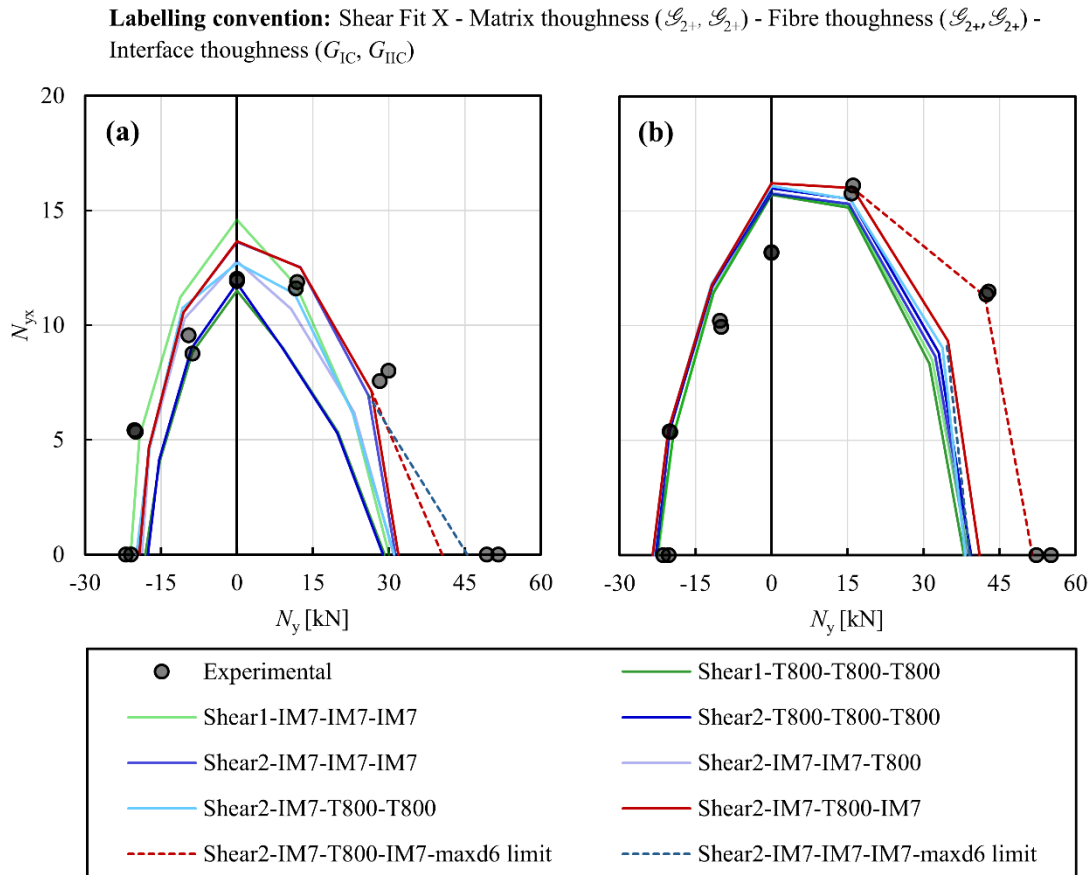

Figure D.3, Predicted failure envelopes in comparison to experimental data: (a) thick ply Laminate 1 and (b) thin ply Laminate 2.

It is observed from Figure D.3 that the predictions for Laminate 1 are more sensitive to the selection of different material parameters. This is also confirmed in Table D.1 where the variance in the predicted strengths across all load cases and laminate configurations are compared.

Table D.1, Mean open-hole specimen strength predictions and CoV for Laminates 1 and 2 and all combined load cases for the seven sets of material properties investigated.

	Laminate 1		Laminate 2		
α [deg]	mean strength [kN]	% CoV	mean strength [kN]	% CoV	Both Laminates %CoV
0	30.45	4%	39.10	3%	
15	23.83	11%	33.88	4%	
45	15.53	14%	21.82	2%	
90	12.95	8%	15.90	1%	
135	14.38	9%	16.50	1%	
165	17.62	8%	20.72	2%	
180	19.12	6%	22.92	2%	
Total		**9%**		**2%**	**5.32%**

Overall the variance in Laminate 1 and 2 are 9% and 2%, respectively, and the average variance is less than 6%. The larger variance for Laminate 1 may be due to the reduced number of through-thickness elements (4 instead of 8 for the half-models used), indicating that 4 through-the-thickness elements may be too few. However, in the model used, individual plies are inherently meshed with a single through-thickness element and no through-thickness refinement is possible. It was further observed that for Laminate 2, the engineering solution of limiting the maximum allowable shear damage (see Chapter 6) only had the intended effect in combination with the T800 fibre fracture toughness values (red dashed lines vs blue dashed line in Figure D.3). Moreover, shear-fit 1 either under or over predicted the failure envelopes in Laminate 1 (see green envelopes in Figure D.3), hence shear fit 2 was considered further. From the models combining shear-fit 2 with the T800 fibre fracture toughness, the *Shear2-IM7-T800-IM7* model is in reasonable agreement (excluding cases were the engineering solution was employed, *i.e.* $\alpha = 0°$ for Laminate 1 and $\alpha = 0°$, 15° for Laminates 2) with experimental data (mean relative error of 10% across all the load cases) and was therefore selected for the analysis in Chapter 6.

Appendix E
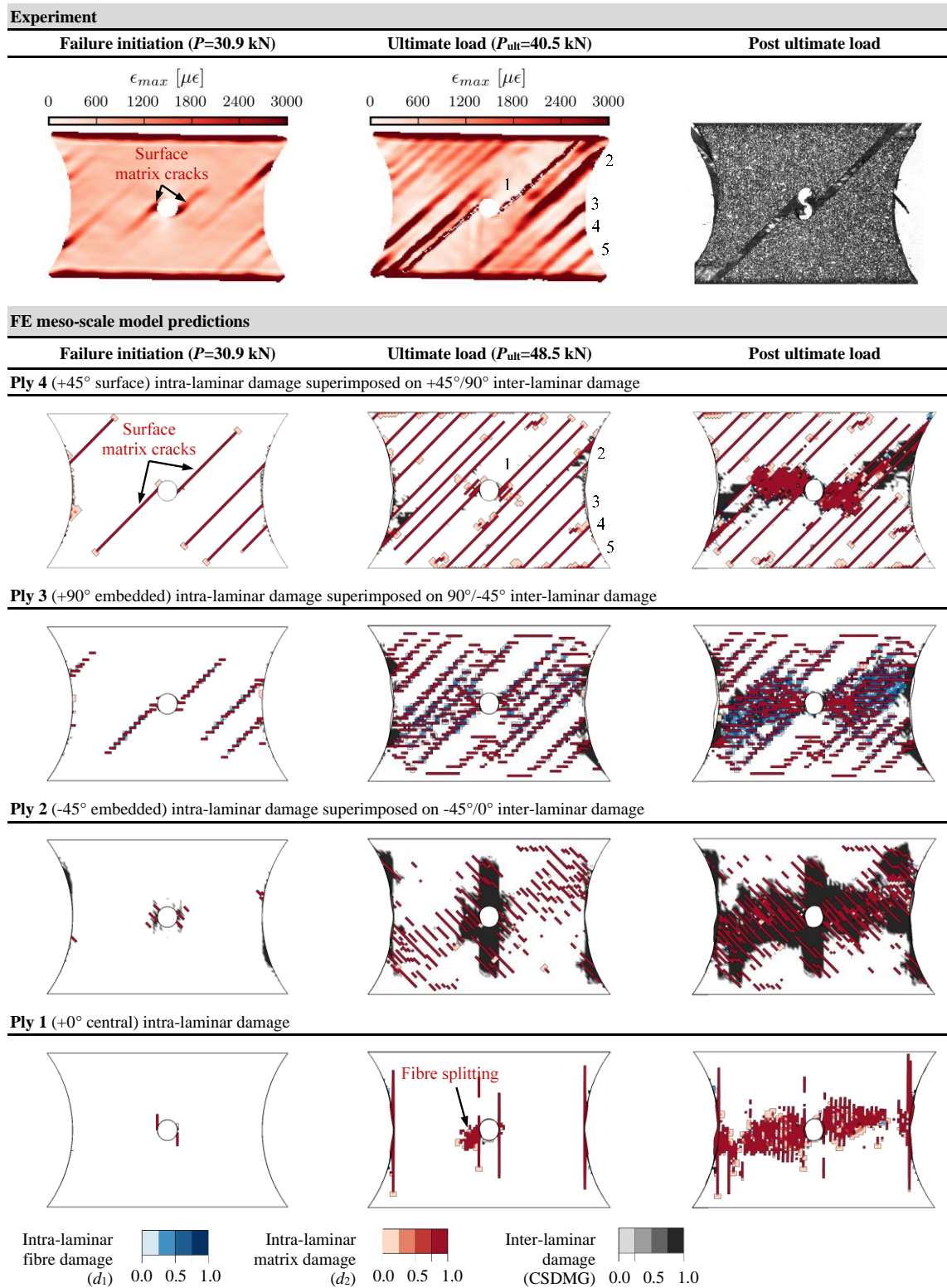
Meso-scale modelling – additional damage maps

Experiment

Failure initiation (P=30.9 kN)	Ultimate load (P_{ult}=40.5 kN)	Post ultimate load

FE meso-scale model predictions

Failure initiation (P=30.9 kN)	Ultimate load (P_{ult}=48.5 kN)	Post ultimate load

Ply 4 (+45° surface) intra-laminar damage superimposed on +45°/90° inter-laminar damage

Ply 3 (+90° embedded) intra-laminar damage superimposed on 90°/-45° inter-laminar damage

Ply 2 (-45° embedded) intra-laminar damage superimposed on -45°/0° inter-laminar damage

Ply 1 (+0° central) intra-laminar damage

Intra-laminar fibre damage (d_1) 0.0 0.5 1.0	Intra-laminar matrix damage (d_2) 0.0 0.5 1.0	Inter-laminar damage (CSDMG) 0.0 0.5 1.0

Figure E.1, Damage maps for Laminate 1 subjected to tension ($\alpha = 0°$).

Experiment

Failure initiation (*P*=9.7 kN)	Ultimate load (*P*ult=12.0 kN)	Post ultimate load

FE meso-scale model predictions

Failure initiation (9.7 kN)	Ultimate load (*P*ult=13.7 kN)	Post ultimate load

Ply 4 (+45° surface) intra-laminar damage superimposed on +45°/90° inter-laminar damage

Ply 3 (+90° embedded) intra-laminar damage superimposed on 90°/-45° inter-laminar damage

Ply 2 (-45° embedded) intra-laminar damage superimposed on -45°/0° inter-laminar damage

Ply 1 (+0° central) intra-laminar damage

Figure E.2, Damage maps for Laminate 1 subjected to shear (α = 90°).
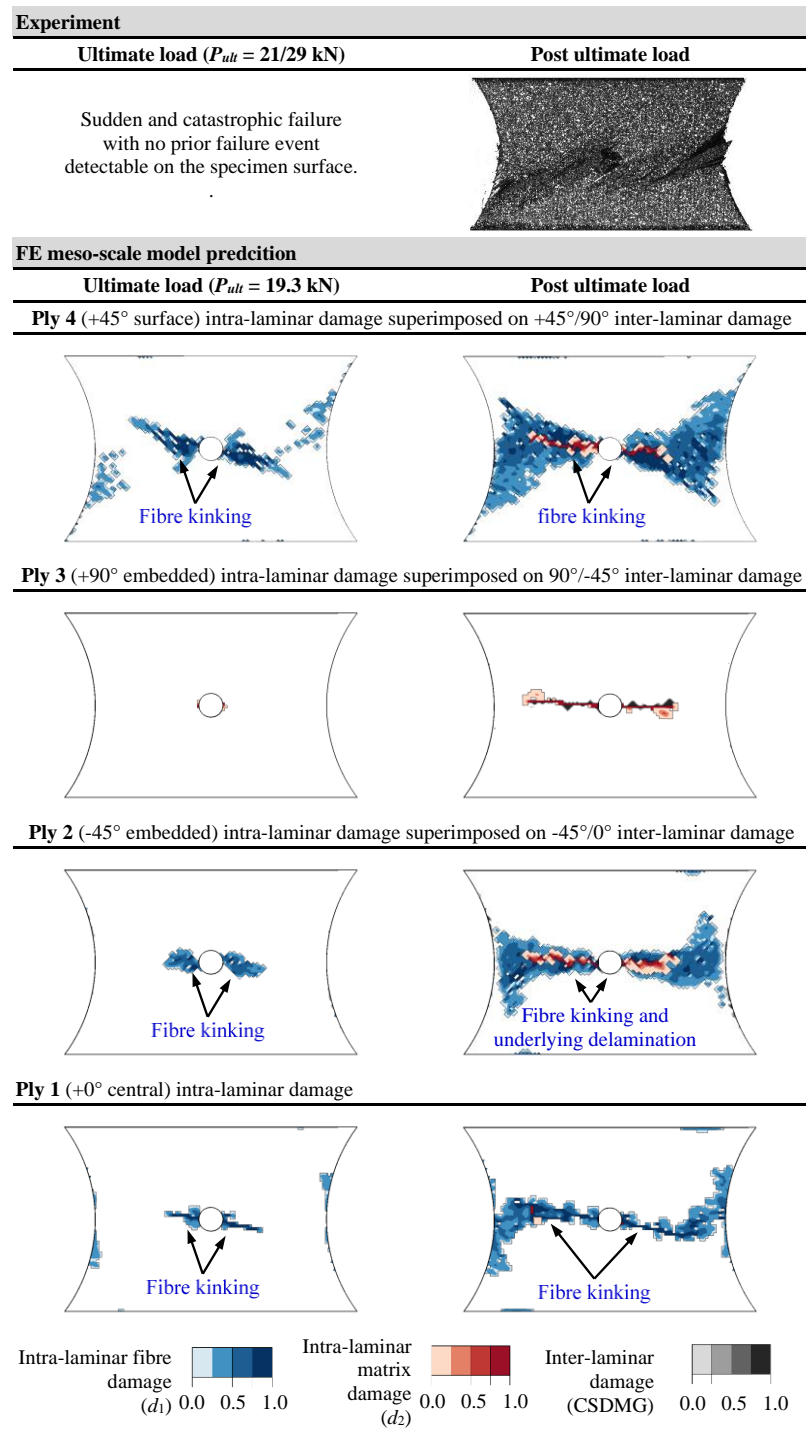
Figure E.3, Damage maps for Laminate 1 subjected to compression (α = 180°).
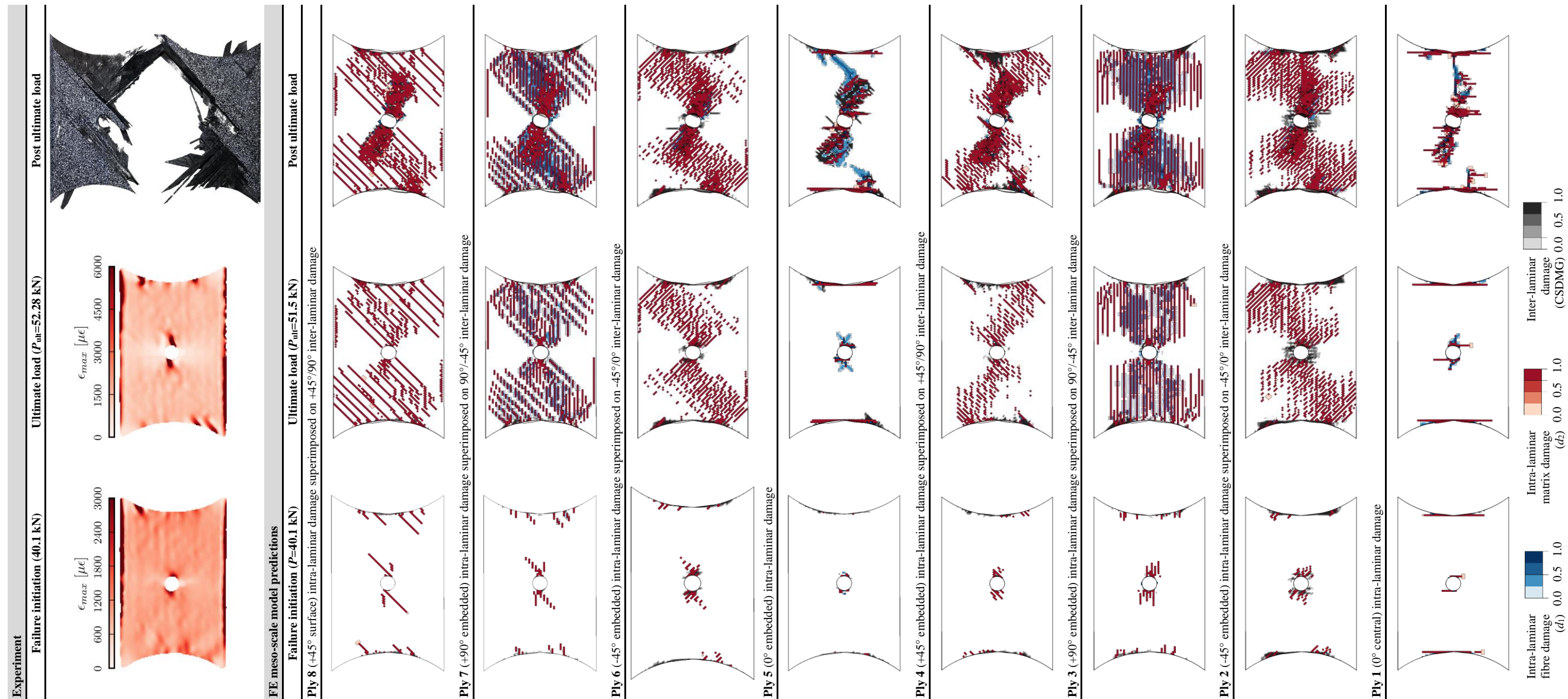
Figure E.4, Damage maps for Laminate 2 subjected to tension (α = 0°).
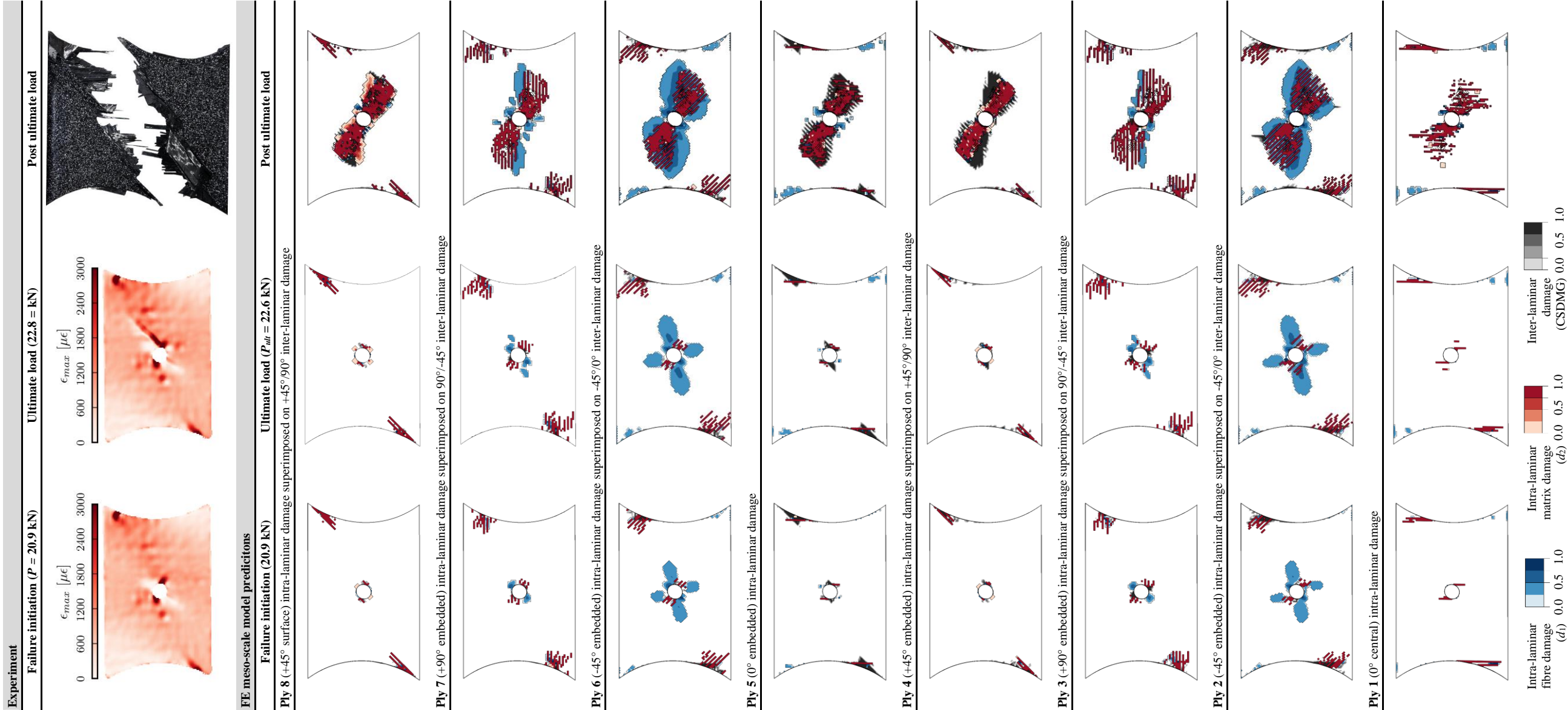
Figure E.5, Damage maps for Laminate 2 subjected to combined tension-shear (α = 45°)
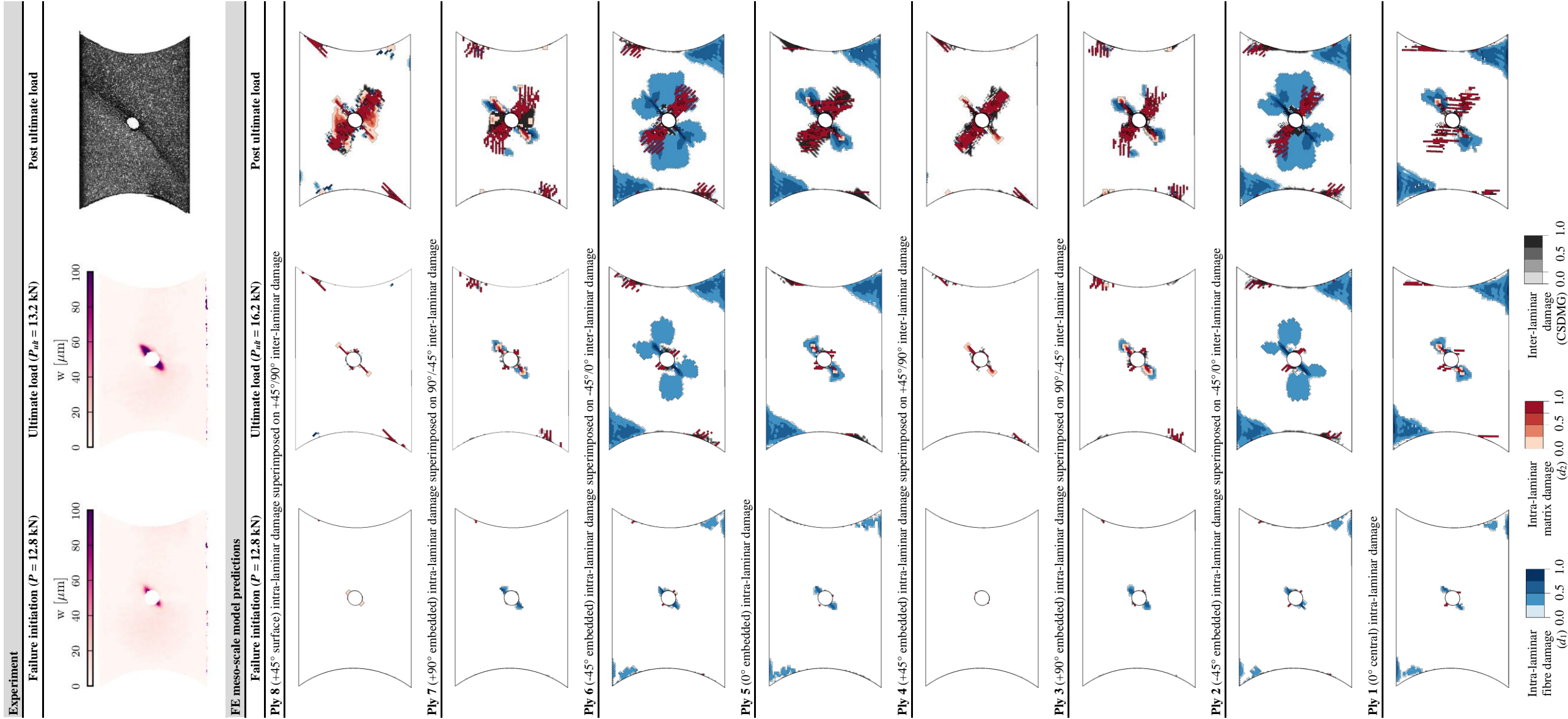
*Figure E.6, Damage maps for Laminate 2 subjected to shear (*α = 90°*).*
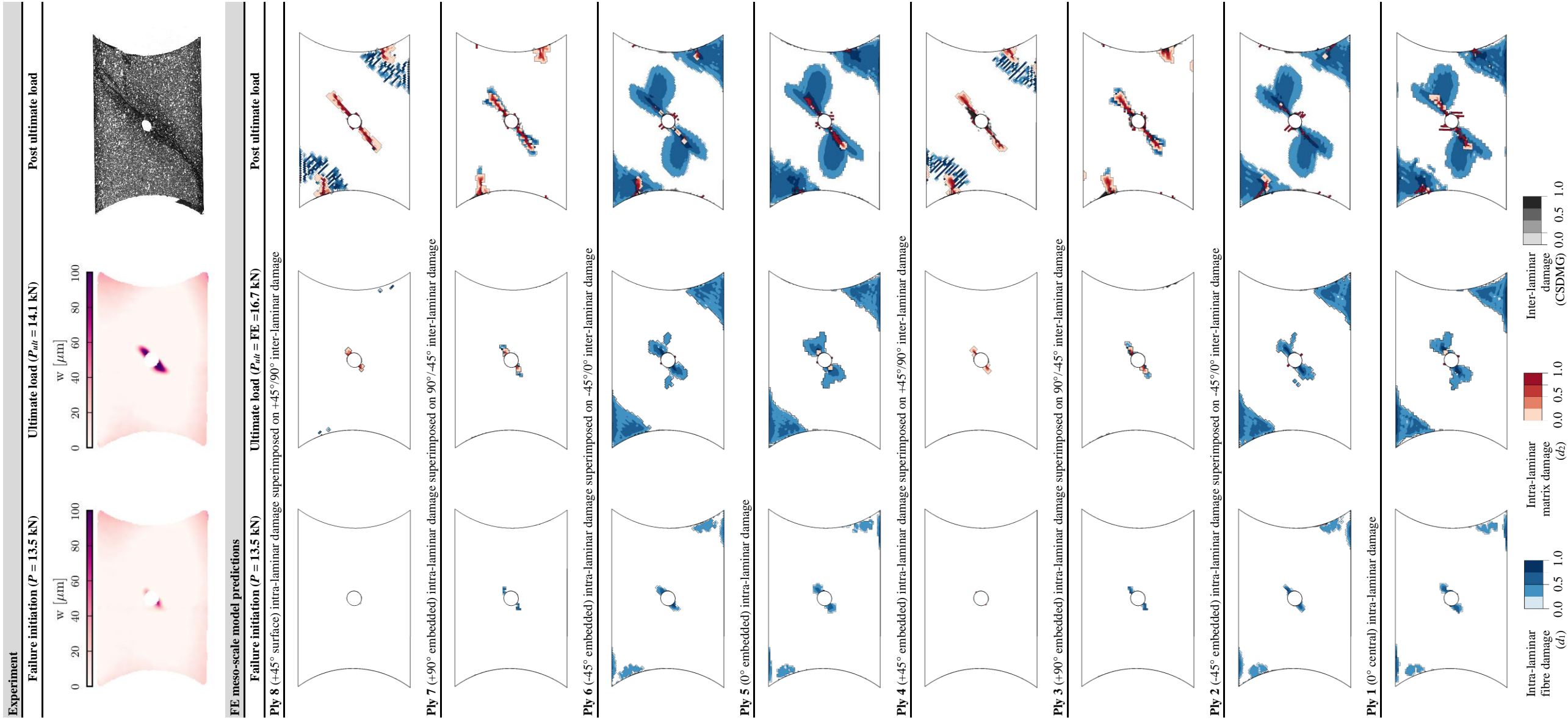
Figure E.7, Damage maps for Laminate 2 subjected to combined compression-shear (α = 135°).
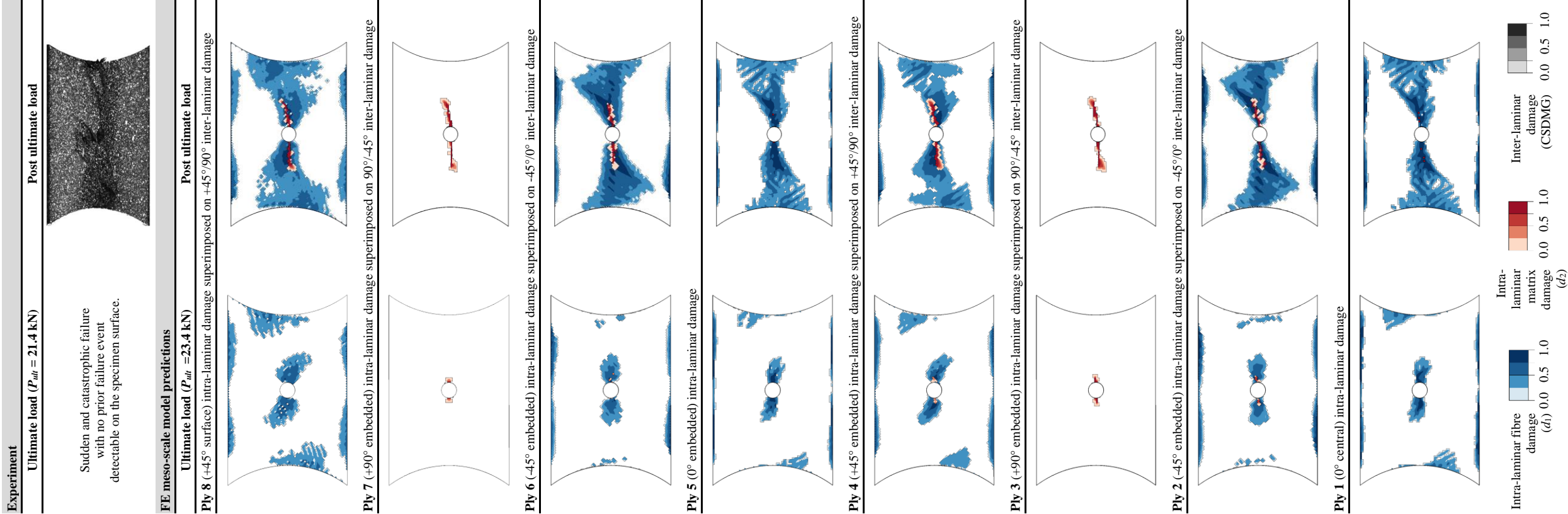
Figure E.8, Damage maps for Laminate 2 subjected to compression (α = 180°).

Appendix F

Drawings for the new Modified Arcan Fixture (MAF)
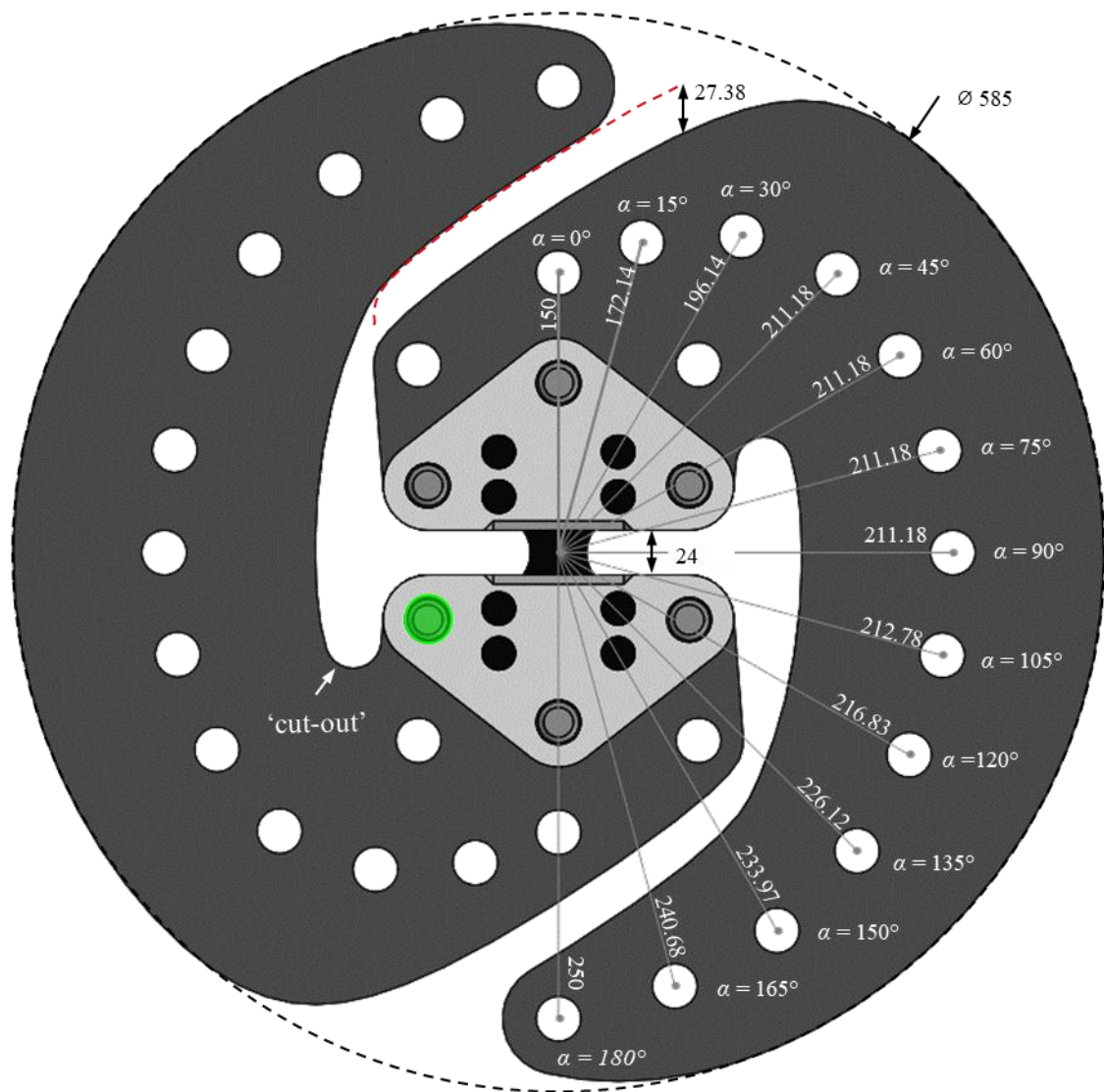
Figure F.9, The geometry of the new MAF. Dimensions are given in mm.

The geometry of the new MAF arms is shown in Figure F.9. The MAF is designed to test FRP specimens with a gauge section length l_g of 24 mm. However, specimens with longer gauge sections could be tested. Care must be taken in the design of new specimens due to the maximum allowable extension which is limited by the MAF geometry in tensile dominated load cases up to $\alpha = 45°$ (see red dashed line in Figure F.9), while after the length of the anti-buckling rails are the limiting design feature. If specimens with gauge lengths different from 24 mm are used on the MAF, then the positions of the loading hole pairs change and the associated loading angles (α) need to be re-calculated. Figure F.9 allows to check the feasibility of new specimen geometries and the re-calculation of the loading angles α. The 'cut-out' in the inner perimeter of the boomerang shaped arm is a consequence of a detailed FE analysis: they are required to reduce the stresses occurring around the grip attachment bolt nearest to the cut-out (green in Figure F.9) when the rig is loaded in shear dominated load cases. The cut-out decouples the stress field generated by the global loading (load applied through the loading holes) from the locally induced contact stress field arising around the grip attachment bolt, reducing the critical von Misses stress.

Drawing 1: MAF Assembly

Drawing 2: MAF Connector Assembly

Drawing 3: MAF Arm

Drawing 4: MAF Grip Front

Drawing 5: MAF Grip Back
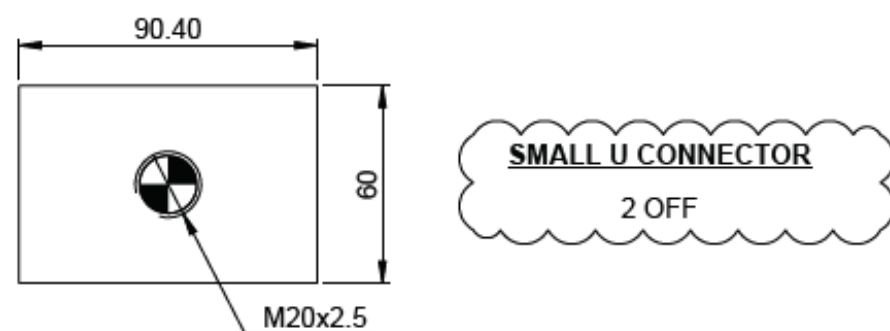
Drawing 6: MAF Grip Attachment Bolt

SEE CONNECTOR ASSEMBLY SHEET 2

SLIDING FITS TO GRIPS
TIGHT FIT TO ARM

M24X1.5

Ø1000

270

880.36
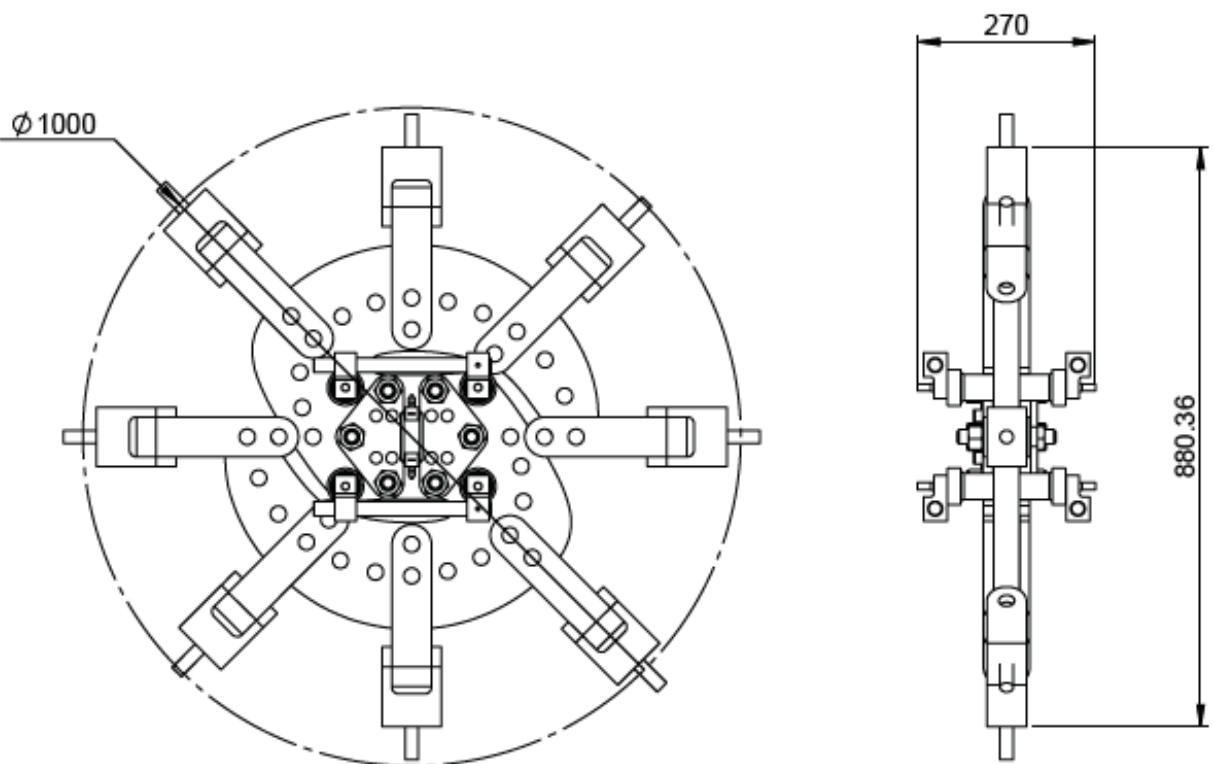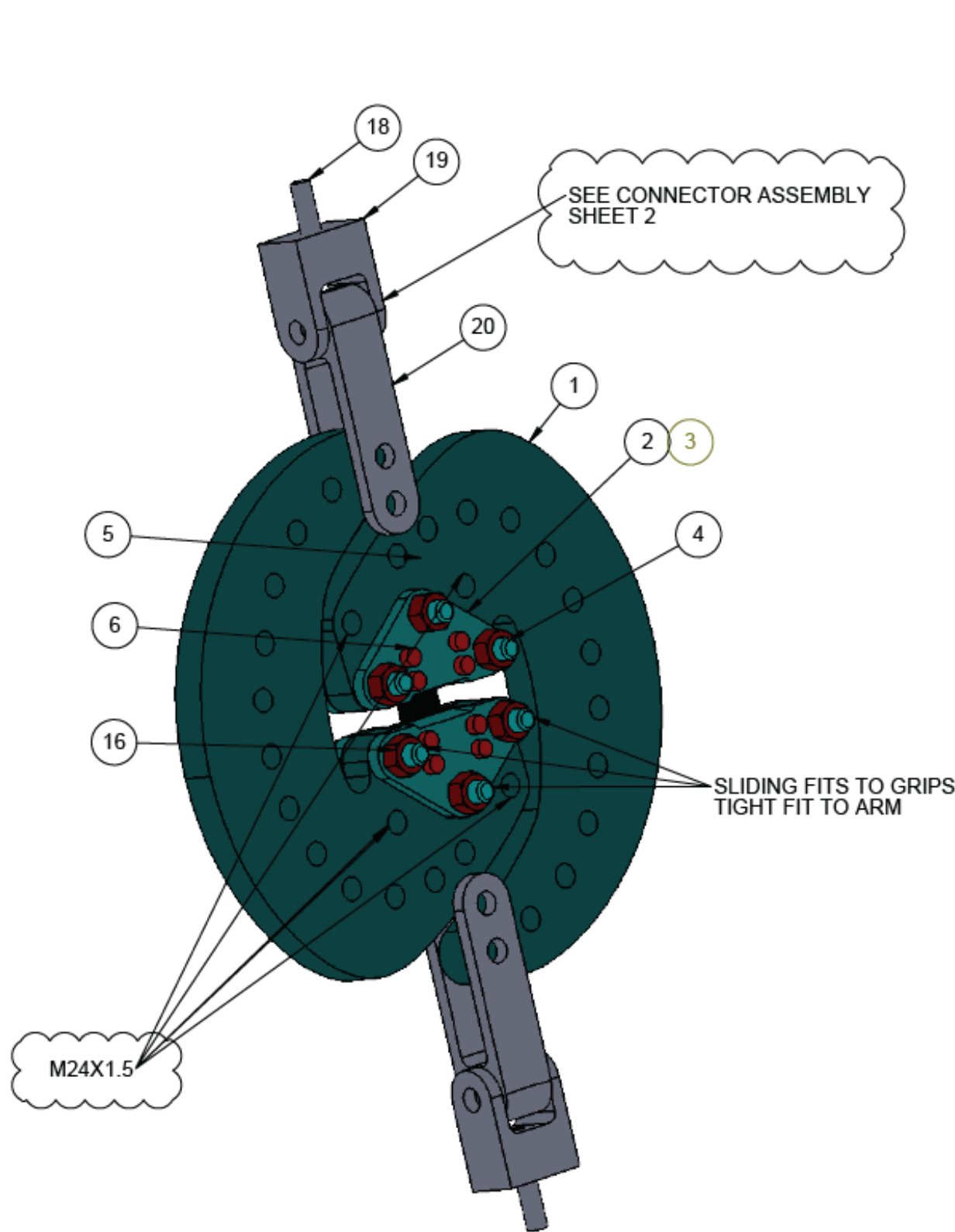
NOTE: RIG AND CONNECTORS FIN IN A 1 M CIRCLE

ITEM NO.	PART NUMBER	DESCRIPTION	QTY.
1	Arm	ALUMEC 89	2
2	Grip front	STANINLESS STEEL P 17-4 H900	2
3	Grip back	STANINLESS STEEL P 17-4 H900	2
4	Grip Attachment Bolt	STANINLESS STEEL P 17-4 A	6
5	Shoulder screws with collar ISO 7379-24-M20-70	STEEL GRADE 12.9	2
6	M12x70 Socket screw	STEEL GRADE 12.9	8
16	M24 NUTS	-	12
18	Connector to test machine	STEEL GRADE 10.9 (OR HIGHER)	1
19	small U connector	P20 STEEL	2
20	large U connector	P20 STEEL	2

DO NOT SCALE

A3

EDMC JOB No
XXXX

DRAWN BY
T.LAUX

DESIGNED BY
T.LAUX

DEPARTMENT
MATERIALS

DATE
21/09/2018

SCALE
NA

TOLERANCES UNLESS OTHERWISE STATED
LINEAR DIMENSIONS
X = +/- 0.5mm
X.X = +/- 0.25mm
X.XX = +/- 0.1mm
ANGULAR DIMENSIONS
X = +/- 0.5mm
X.X = +/- 0.25mm
ALL DIMENSIONS IN mm UNLESS OTHERWISE STATED

PROJECT
MAF REDESIGN

SUPERVISOR
K.W. GAN

MATERIAL
NA

TEXTURE
XXXX
XXXX

SURFACE FINISH
1.5/ ALL OVER UNLESS OTHERWISE STATED

UNIVERSITY OF
Southampton
Faculty of Engineering and the Environment

TITLE
MAF ASSEMBLY

REMOVE ALL SHARP EDGES

IF IN DOUBT PLEASE ASK

THE INFORMATION CONTAINED IN THIS DOCUMENT IS THE PROPERTY OF THE UNIVERSITY OF SOUTHAMPTON DO NOT COPY WITHOUT WRITTEN PERMISSION.

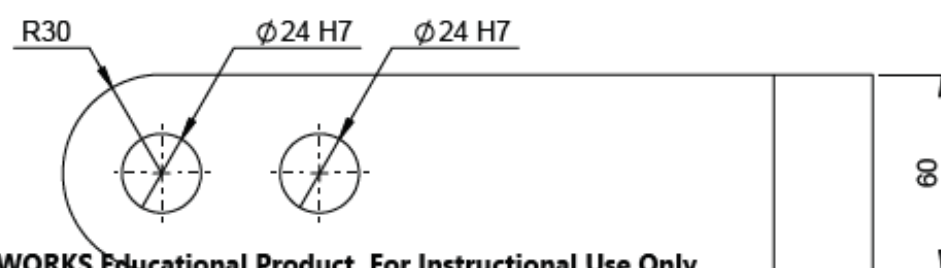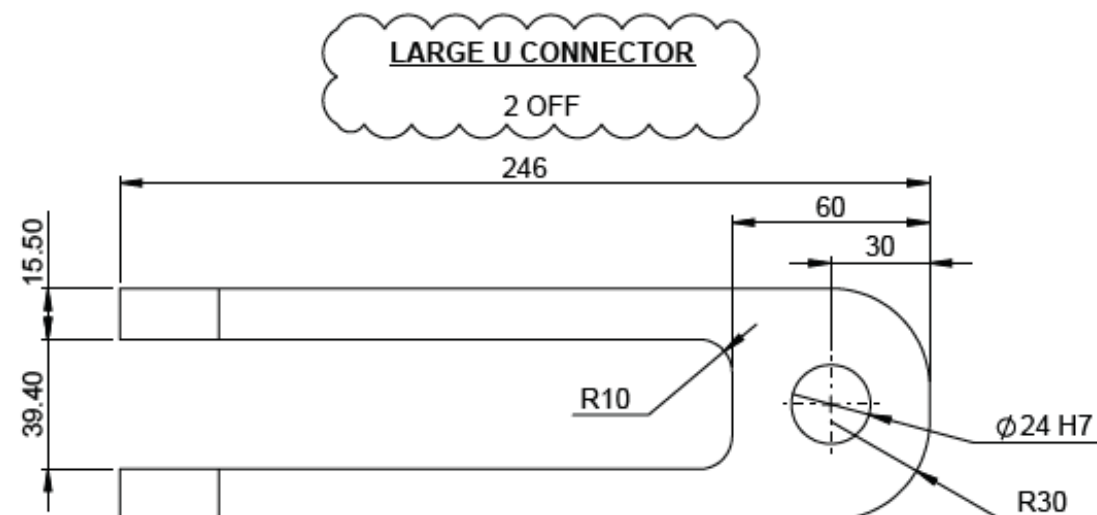| SHEET	No OFF	ASSEMBLY NUMBER	DRAWING NUMBER	REVISION
1 of 6	XX	XXX/XXX	XXX/XXX	C

90.40

60

SMALL U CONNECTOR
2 OFF

M20x2.5

A

50

121

71

Ø24 H7

R30

60.40   15

SECTION A

A

CONNECTOR TO TEST MACHINE

1 OFF
MATERIAL: STEEL GRADE 10.9 (OR HIGHER)

M20X2.5

100

LARGE U CONNECTOR
2 OFF

246

60

30

15.50

39.40

R10

Ø24 H7

R30

R30   Ø24 H7   Ø24 H7

60

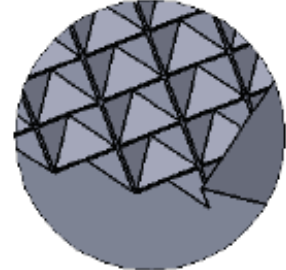SOLIDWORKS Educational Product. For Instructional Use Only

1

M20x2.5

2

3

SLIDE FIT
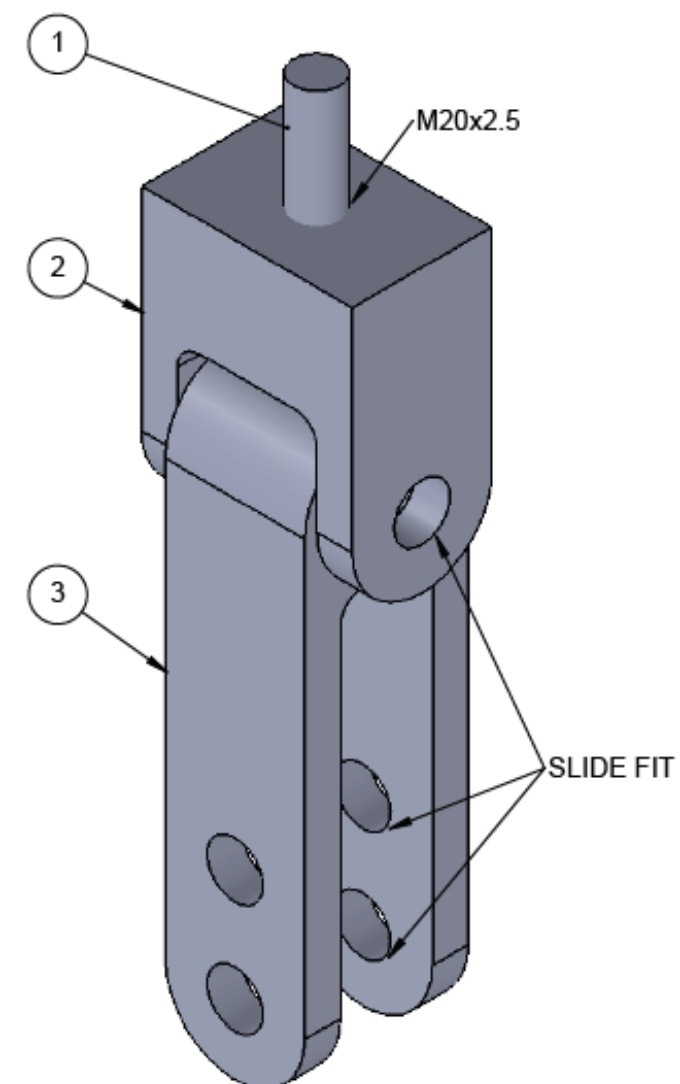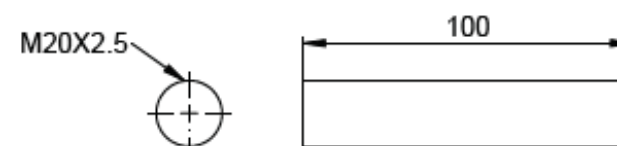
NOTE: TWO CONNECTOR ASSEMBLIES REQUIRED

ITEM NO.	PART NUMBER	DESCRIPTION	QTY.
1	Connector to test machine	STEEL GRADE 10.9 (OR HIGHER)	1
2	small U connector	P20 STEEL	1
3	large U connector	P20 STEEL	1

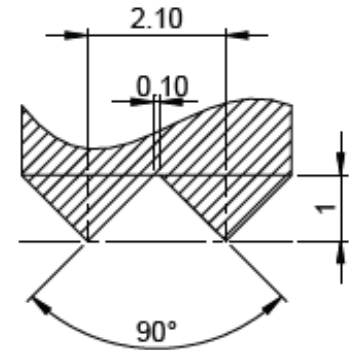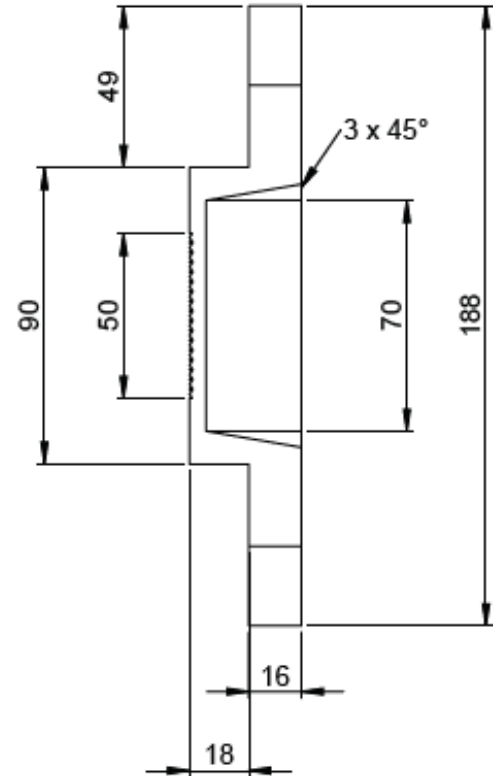| DO NOT SCALE	DRAWN BY T.LAUX	TOLERANCES UNLESS OTHERWISE STATED	UNIVERSITY OF **Southampton**
A3	DESIGNED BY T.LAUX	LINEAR DIMENSIONS X = +/-0.5mm X.X = +/-0.25mm X.XX = +/-0.1mm	Faculty of Engineering and the Environment
EDMC JOB No XXXX	DEPARTMENT MATERIALS	DATE 21/09/2018	SCALE 1:2	ANGULAR DIMENSIONS X = +/- 0.5mm X.X = +/- 0.25mm ALL DIMENSIONS IN mm UNLESS OTHERWISE STATED	TITLE MAF Connector Assembly
PROJECT MAF REDESIGN	SUPERVISOR K.W. GAN	MATERIAL P20 STEEL	TEXTURE XXXX XXXX	SURFACE FINISH 1.6 ALL OVER UNLESS OTHERWISE STATED	
REMOVE ALL SHARP EDGES	THE INFORMATION CONTAINED IN THIS DOCUMENT IS THE PROPERTY OF THE UNIVERSITY OF SOUTHAMPTON DO NOT COPY WITHOUT WRITTEN PERMISSION.	SHEET 2 of 6	No OFF 2	ASSEMBLY NUMBER XXX/XXX	DRAWING NUMBER XXX/XXX	REVISION C
IF IN DOUBT PLEASE ASK					

525.92

138

88.75

79

24

39

TIGHT FIT WITH
GRIP ATTACHMENT BOLT Ø24
REMOVABLE WITH RUBBER HAMMER

M24X1.5

R30

Ø24 H7

ALL BOLT HOLES
(IF NOT STATED OTHERWISE)
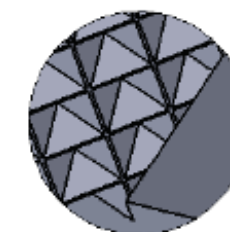SLIDING FIT WITH 24 MM
SHOULDER BOLT

150

140

92

56

R14

391.08

SOLIDWORKS Educational Product. For Instructional Use Only
QUANTITY: 2

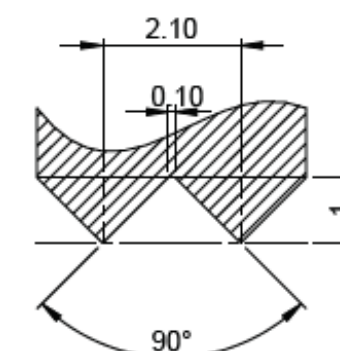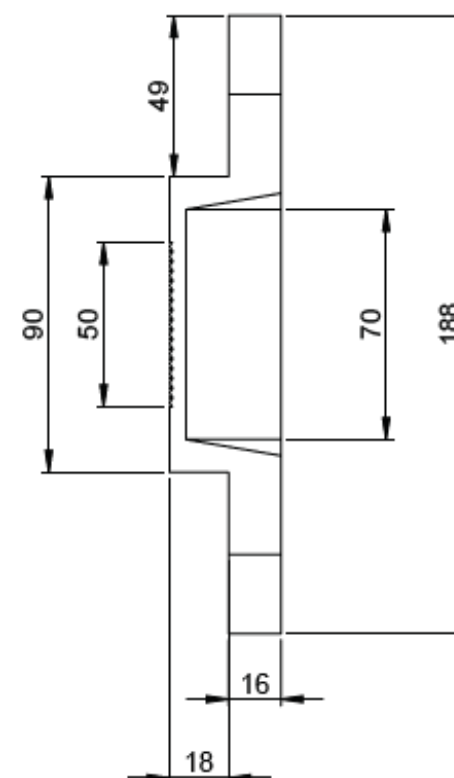| DO NOT SCALE	DRAWN BY T.LAUX	TOLERANCES UNLESS OTHERWISE STATED	UNIVERSITY OF
A3	DESIGNED BY T.LAUX	LINEAR DIMENSIONS X = +/-0.5mm X.X = +/-0.25mm X.XX = +/-0.1mm	Southampton
EDMC JOB No XXXX	DEPARTMENT MATERIALS	DATE 21/09/2018	SCALE 1:2	ANGULAR DIMENSIONS X = +/-0.5mm X.X = +/-0.25mm ALL DIMENSIONS IN mm UNLESS OTHERWISE STATED	Faculty of Engineering and the Environment
PROJECT MAF REDESIGN	SUPERVISOR K.W. GAN	MATERIAL ALUMEC 89	TEXTURE XXXX XXXX	SURFACE FINISH 1.6 ALL OVER UNLESS OTHERWISE STATED	TITLE MAF ARM
REMOVE ALL SHARP EDGES		THE INFORMATION CONTAINED IN THIS DOCUMENT IS THE PROPERTY OF THE UNIVERSITY OF SOUTHAMPTON DO NOT COPY WITHOUT WRITTEN PERMISSION.	SHEET 3 of 6	No OFF 2	ASSEMBLY NUMBER XXX/XXX	DRAWING NUMBER XXX/XXX	REVISION C
IF IN DOUBT PLEASE ASK						

QUANTITY: 2

SECTION A

5

5

103

DETAIL O
SCALE 5 : 1

TO FIT M12
SOCKET HEAD CAP SCREW
NO THREAD HERE.
THREAD IN PART "GRIP BACK"
Ø12

R24

Ø24 H7

TO SUIT GRIP ATTACHMENT BOLTS
IN SLIDING FIT

IN PLANE GRIPPING
SURFACE ORIENTATION

Ø24 H7

R24

3 x 45°

45°

GRIPPING SURFACE DETAIL
10:1

2.10

0.10

32

A   A

90

50

70

188

1

70

ALIGN GRIP TEETH WITH FRONT
EDGE (THIS EDGE). AT ALL OTHER
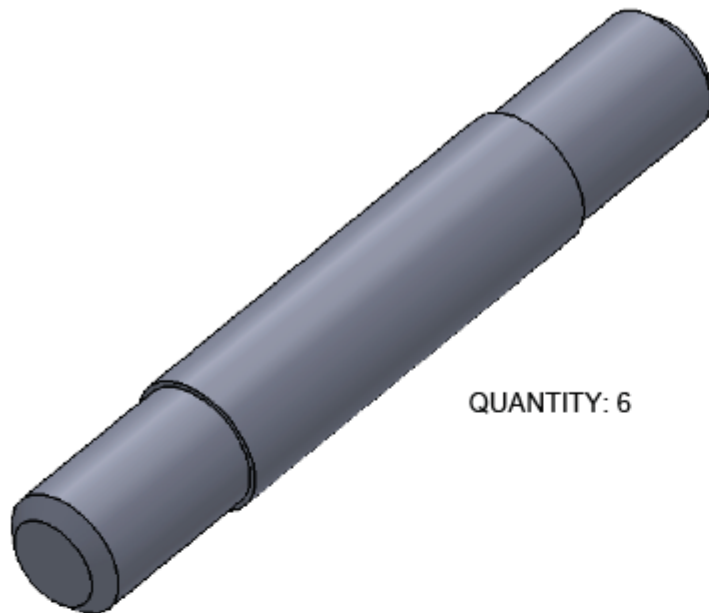EDGES, GRIPPING SURFACE CAN
FADE OUT.

90°

R13

18

Ø24 H7

24

16

NOTES:
1) PITCH: 2.1 MM WITH 0.1 MM FLATS BETWEEN TEETH
2) DENT HIGHT: 1MM

42

55

18

79

SOLIDWORKS Educational Product. For Instructional Use Only

QUANTITY: 2

SECTION A

5

103

5

DETAIL O
SCALE 5 : 1

R24

TO FIT M12
SOCKET HEAD CAP SCREW
M12 X 1.75 THREAD

Ø 24 H7
TO SUIT GRIP ATTACHMENT BOLTS
IN SLIDING FIT

GRIPPING SURFACE DETAIL
10:1

Ø 24 H7

R24

IN PLANE GRIPPING
SURFACE ORIENTATION

2.10

0.10

45°

32

A

A

90

50

70

188

1

70

R13

ALIGN GRIP TEETH WITH FRONT
EDGE (THIS EDGE). AT ALL OTHER
EDGES, GRIPPING SURFACE CAN
FADE OUT.

90°

18

Ø 24 H7

24

42

16

NOTES:
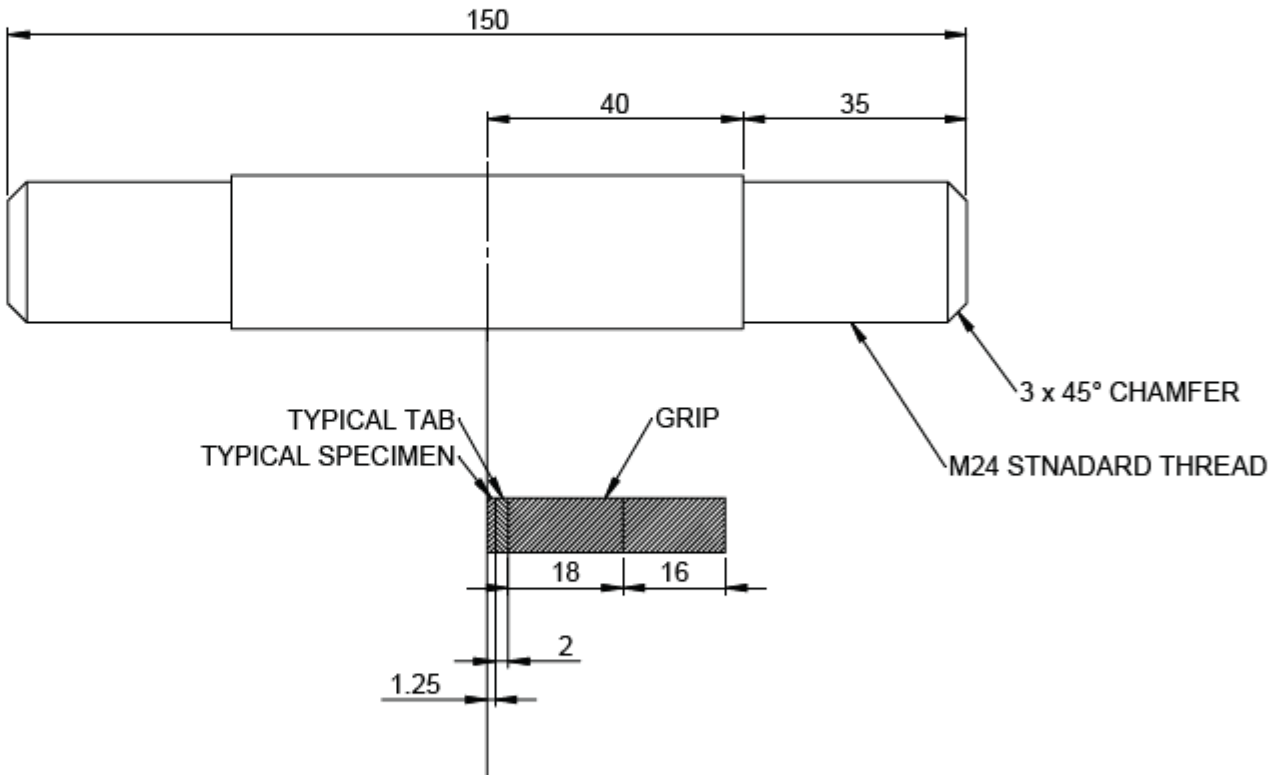1) PITCH: 2.1 MM WITH 0.1 MM FLATS BETWEEN TEETH
2) DENT HIGHT: 1MM

55

18

79

DO NOT SCALE	DRAWN BY T.LAUX	TOLERANCES UNLESS OTHERWISE STATED	UNIVERSITY OF
A3	DESIGNED BY T.LAUX	LINEAR DIMENSIONS	Southampton
EDMC JOB No XXXX	DEPARTMENT MATERIALS ENGINEERING	DATE 21/09/2018	SCALE 1:2	ANGULAR DIMENSIONS	Faculty of Engineering and the Environment
PROJECT MAF REDESIGN	SUPERVISOR K.W. GAN	MATERIAL P17-4 H900	TEXTURE XXXX XXXX	SURFACE FINISH	TITLE MAF GRIP BACK
REMOVE ALL SHARP EDGES	THE INFORMATION CONTAINED IN THIS DOCUMENT IS THE PROPERTY OF THE UNIVERSITY OF SOUTHAMPTON DO NOT COPY WITHOUT WRITTEN PERMISSION.	SHEET 5 of 6	No OFF 2	ASSEMBLY NUMBER XXX/XXX	DRAWING NUMBER XXX/XXX	REVISION C
IF IN DOUBT PLEASE ASK				

QUANTITY: 6

150

40   35

⌀24
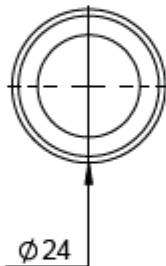
TIGHT FIT TO MAF ARM
SLIDING FIT TO GRIP FRONT AND GRIP BACK

3 x 45° CHAMFER

TYPICAL TAB
TYPICAL SPECIMEN

GRIP

M24 STNADARD THREAD

18   16

2

1.25

DO NOT SCALE	DRAWN BY T.LAUX	TOLERANCES UNLESS OTHERWISE STATED	UNIVERSITY OF
A3	DESIGNED BY T.LAUX	LINEAR DIMENSIONS X = +/- 0.5mm X.X = +/- 0.25mm X.XX = +/- 0.1mm	**Southampton**
EDMC JOB No XXXX	DEPARTMENT MATERIALS	DATE 21/09/2018	SCALE 1:1	ANGULAR DIMENSIONS X = +/- 0.5mm X.X = +/- 0.25mm ALL DIMENSIONS IN mm UNLESS OTHERWISE STATED	Faculty of Engineering and the Environment
PROJECT MAF REDESIGN	SUPERVISOR K.W. GAN	MATERIAL P 17-4 A	TEXTURE XXXX XXXX	SURFACE FINISH 1.6 ALL OVER UNLESS OTHERWISE STATED	TITLE MAF GRIP ATTCHMENT BOLT
REMOVE ALL SHARP EDGES	THE INFORMATION CONTAINED IN THIS DOCUMENT IS THE PROPERTY OF THE UNIVERSITY OF SOUTHAMPTON DO NOT COPY WITHOUT WRITTEN PERMISSION.	SHEET 6 of 6	No OFF 6	ASSEMBLY NUMBER XXX/XXX	DRAWING NUMBER XXX/XXX	REVISION C
IF IN DOUBT PLEASE ASK					

SOLIDWORKS Educational Product. For Instructional Use Only